

---

# **Methane Dehydro Aromatization: Thermodynamics, Catalysts, Kinetics and Potential of Membrane Reactors**

Dissertation for Submission to the Faculty of Process and Systems

Engineering for the award of degree of

**Doktoringenieurin (Dr.-Ing.)**

From: PhD Degree, **Kaidi Gao**

Birth: 10. 10. 1987 in Liaoning, China

Approved by the Faculty of Process and Systems Engineering of Otto-  
von-Guericke-University Magdeburg

Promotion Commission:

**Prof. Dr. rer. nat. habil. Helmut Wieß (Vorsitz)**

**Prof. Dr.-Ing. Andreas Seidel-Morgenstern**

**Prof. Dr. Jürgen Caro**

**Prof. rer. nat. Ingolf Voigt**

Date of Submission: 30. 04. 2015

Date of Colloquium: 08. 07. 2015



# Table of Contents

<b>TABLE OF CONTENTS .....</b>	<b>I</b>
<b>ABSTRACT .....</b>	<b>V</b>
<b>ZUSAMMENFASSUNG .....</b>	<b>VII</b>
<b>ACKNOWLEDGEMENTS .....</b>	<b>IX</b>
<b>1. INTRODUCTION.....</b>	<b>1</b>
1.1 METHANE CONVERSION .....	1
1.1.1 <i>Oxidative versus non-oxidative</i> .....	5
1.1.2 <i>Direct versus indirect</i> .....	5
1.2 MDA REACTION SYSTEM .....	6
1.2.1 <i>Catalysts</i> .....	8
1.2.1.1 Active metal loading .....	8
1.2.1.2 Catalyst support.....	9
1.2.1.3 Molybdenum species in zeolite .....	11
1.2.2 <i>Reaction mechanisms</i> .....	13
1.2.3 <i>Approaches to improve MDA</i> .....	16
1.2.4 <i>Conclusions</i> .....	18
1.3 MOTIVATION AND AIM OF THIS WORK .....	18
<b>2. THERMODYNAMIC STUDY .....</b>	<b>21</b>
2.1 <i>Chemical reaction equilibrium</i> .....	21
2.1.1 Equilibrium constants .....	21
2.1.2 Single reactions .....	22
2.1.3 Multiple reactions .....	24
2.1.4 Calculation of equilibrium compositions.....	25
2.2 <i>Equilibrium constant of MDA</i> .....	27
2.3 <i>Effect of hydrogen removal in MDA</i> .....	28
2.4 <i>Conclusions</i> .....	29
<b>3. SYNTHESIS AND CHARACTERIZATION OF CATALYST .....</b>	<b>31</b>
3.1 CHEMICALS AND EQUIPMENT .....	31
3.2 CATALYST SYNTHESIS .....	31
3.3 CHARACTERIZATION OF CATALYST .....	32
3.4 CONCLUSIONS .....	37
<b>4. EXPERIMENTAL TECHNIQUES .....</b>	<b>39</b>
4.1 CHEMICALS AND MATERIALS.....	39
4.2 CONFIGURATIONS AND EQUIPMENT .....	40
4.2.1 <i>Fixed bed reactor (FBR) runs</i> .....	40
4.2.2 <i>Characterizing mass transfer in carbon membranes</i> .....	43
4.2.2.1 Single gas permeation .....	44
4.2.2.2 Binary gas mixture permeation .....	44

4.2.2.3	Ternary gas mixture permeation.....	45
4.2.3	<i>Coupling reaction and hydrogen removal in a membrane reactor (MR)</i> .....	46
4.3	PROCEDURES.....	49
4.3.1	<i>Experimental procedures: FBR</i> .....	49
4.3.1.1	Methane feed.....	49
4.3.1.2	Ethylene feed.....	50
4.3.2	<i>Experimental procedures: characterizing mass transfer parameters</i> .....	51
4.3.2.1	Single gas permeation.....	51
4.3.2.2	Binary gas mixture permeation.....	52
4.3.2.3	Ternary gas mixture permeation.....	52
4.3.3	<i>Experimental procedures: coupling reaction and hydrogen removal by MR</i> .....	52
<b>5.</b>	<b>INVESTIGATIONS IN A FIXED BED REACTOR (FBR)</b> .....	<b>55</b>
5.1	GENERAL OBSERVATION.....	55
5.2	KINETIC MEASUREMENTS.....	55
5.2.1	<i>Methane feed (total network)</i> .....	56
5.2.1.1	Influence of temperature on MDA.....	57
5.2.1.2	Influence of methane feed volumetric fraction on MDA.....	65
5.2.1.3	Influence of W/F on MDA.....	68
5.2.1.4	Effect of stepwise temperature rise on MDA.....	71
5.2.1.5	Stepwise W/F changing on MDA.....	73
5.2.2	<i>Ethylene feed (sub-network)</i> .....	74
5.2.2.1	Influence of temperature on sub-network.....	74
5.2.2.2	Influence of ethylene feed volumetric fraction on sub-network.....	80
5.2.3	<i>Summary regarding kinetic measurements</i> .....	82
5.3	SIMPLIFIED MODELS TO QUANTIFY REACTION KINETICS.....	82
5.3.1	<i>Reactor modelling and reaction kinetics</i> .....	83
5.3.1.1	Reactor modelling.....	83
5.3.1.2	Reaction kinetics.....	85
5.3.2	<i>Methodology for kinetic investigations</i> .....	86
5.3.2.1	Parameter estimation.....	87
5.3.2.2	Preliminary estimation.....	87
5.3.2.3	Objective function and final optimization.....	89
5.3.3	<i>Postulated reaction network 1</i> .....	89
5.3.3.1	Preliminary estimation of reaction network 1.....	90
5.3.3.2	Final optimize of reaction network 1.....	92
5.3.4	<i>Postulated reaction network 2</i> .....	93
5.3.4.1	Parameter estimation of sub-network 2.....	94
5.3.4.1.1	Preliminary estimation of sub-network 2.....	95
5.3.4.1.2	Final optimization of sub-network 2.....	96
5.3.4.2	Parameter estimation of reaction network 2.....	97
5.3.4.2.1	Preliminary estimation of reaction network 2.....	98
5.3.4.2.2	Final optimization of reaction network 2.....	99
5.3.5	<i>Postulate reaction network 3</i> .....	102
5.3.5.1	Preliminary estimation of reaction network 3.....	103



---

5.3.5.2	Final optimization of reaction network 3.....	105
5.4	CONCLUSIONS.....	108
<b>6.</b>	<b>INVESTIGATION IN MEMBRANE REACTORS (MR) .....</b>	<b>111</b>
6.1	INTRODUCTION INTO MEMBRANE REACTOR AND THEORY OF MASS TRANSFER.....	111
6.1.1	<i>Application of membrane reactor in heterogeneous reaction.....</i>	<i>112</i>
6.1.2	<i>Application of inorganic membrane reactor in MDA system.....</i>	<i>114</i>
6.1.3	<i>Fundamentals of mass transfer.....</i>	<i>117</i>
6.2	RESULTS FOR DENSE MEMBRANE (PALLADIUM).....	120
6.3	RESULTS OF GAS PERMEATION FOR CARBON MEMBRANES.....	122
6.3.1	Single gas permeation.....	122
6.3.2	Binary gas mixture permeation.....	123
6.3.3	Ternary gas mixture permeation.....	125
6.4	QUANTIFICATION OF PERMEABILITY OF CARBON MEMBRANES.....	126
6.4.1	<i>Carbon membrane No. 1.....</i>	<i>127</i>
6.4.2	<i>Carbon membrane No. 2.....</i>	<i>129</i>
6.5	FEASIBILITY OF MEMBRANE REACTOR (CARBON MEMBRANE).....	132
6.6	EXPERIMENTS IN MDA-MR USING A CARBON MEMBRANE.....	134
6.7	CONCLUSIONS.....	137
<b>7.</b>	<b>DEACTIVATION INVESTIGATION.....</b>	<b>139</b>
7.1	INTRODUCTION.....	139
7.2	MODELLING OF CATALYST DEACTIVATION.....	139
7.3	OBSERVED DEACTIVATION IN FBR AND DESCRIPTION.....	143
7.3.1	<i>Experimental tendency of deactivation of FBR.....</i>	<i>143</i>
7.3.2	<i>Preliminary estimation of FBR.....</i>	<i>144</i>
7.3.3	<i>Deactivation parameters (FBR).....</i>	<i>146</i>
7.4	OBSERVED DEACTIVATION IN MR AND DESCRIPTION.....	149
7.4.1	<i>Experimental tendency of deactivation of MR.....</i>	<i>149</i>
7.4.2	<i>Preliminary estimation of MR.....</i>	<i>149</i>
7.4.3	<i>Deactivation parameters (MR).....</i>	<i>151</i>
7.5	CONCLUSIONS.....	154
	<b>SUMMARY AND CONCLUSIONS.....</b>	<b>155</b>
	<b>NOMENCLATURE.....</b>	<b>157</b>
	<b>APPENDIX.....</b>	<b>161</b>
	<b>REFERENCE.....</b>	<b>169</b>
	<b>LIST OF FIGURES.....</b>	<b>181</b>
	<b>LIST OF TABLES.....</b>	<b>189</b>
	<b>CURRIULUM VITAE.....</b>	<b>191</b>



---

## Abstract

Natural gas conversion remains one of the essential technologies for current energy demands. Investigations of transforming methane to benzene have been carried out already in order to verify and complement earlier reported data, on the basis of which it was not yet possible to estimate industrial perspectives of methane aromatization, main challenges and barriers. Methane-Dehydro-Aromatization (MDA) has been intensively investigated for its potential in the conversion of methane into chemicals and liquid fuels. Numerous achievements have been reported regarding catalyst development, reaction mechanisms and understanding of coke formation. MDA under nonoxidative condition, a simple straightforward and economic pathway from methane to aromatic hydrocarbons, can avoid deep oxidation of hydrocarbons to carbon dioxide and water, and offers easy separation of benzene from other products by condensation. The effects of Mo content in the most promising catalysts, temperature, space velocity, and the presence of CO<sub>2</sub>, CO, H<sub>2</sub>O, C<sub>2</sub>H<sub>4</sub>, C<sub>2</sub>H<sub>6</sub> in the feed have been studied. The effectiveness of catalyst regeneration in air streams was also examined. However, many problems inhibiting the MDA process from industrialization still remain unsolved, namely low methane conversion and reduced target product selectivity, as well as severe catalyst deactivation.

MDA into hydrogen and aromatics under nonoxidative conditions is a process severely limited by thermodynamics. However, the movement from the present era of fossil fuels into the coming hydrogen age makes it an interesting and important approach compared with the direct conversion of methane under the aid of oxidants. The concept of membrane reactors (MR) is seen as a perfect solution to tackle such thermodynamic limitations. By withdrawing hydrogen from the reaction zone, the thermodynamic equilibrium can be shifted to the product side, which will improve the reactant conversion and eventually also the products yield.

In this work, MDA has been experimentally studied over Mo/MCM-22 catalysts under non-oxidizing conditions in a fixed-bed continuous-flow reactor (FBR) for both methane and ethylene feeds. At the same time, the understanding of MDA over Mo/MCM-22 catalysts for the simultaneous formation of hydrogen and light aromatics and regarding the catalyst bi-functionality was improved with respect to both academic and industrial viewpoints. The influence of operating conditions (e.g. temperature, feed volumetric fraction and space velocity) was examined and discussed. The results were compared with literature data and evaluated from a technological point of view. Hydrogen, ethylene and ethane have been directly detected in the product streams using gas chromatographs. The experimental results show that benzene is not the only hydrocarbon product of MDA. A benzene selectivity of 9% could be achieved at 6% of methane conversion over Mo/MCM-22 at 973K with a volumetric methane feed fraction of 90% and a space velocity of 2160 kgs m<sup>-3</sup>. This selectivity is relatively low compared with available literature data. However, the catalyst was found to have a better resistance against carbon deposition.

Kinetic studies of MDA over Mo/MCM-22 catalysts have been carried out aiming at a better understanding of this reaction and to provide opportunities for process intensification and optimization. Various possible technological schemes were analysed and simplified kinetic models taking into account several side reactions were derived. The models allow evaluating the

---

MDA system under various reacting conditions. The parameters in the model were estimated based on experimental data obtained in a FBR under various conditions. The developed model described the experimentally observed MDA performance over a wide range of operating conditions, temperatures from 923 to 1023 K, space velocity between 720 and 2160 kgs m<sup>-3</sup>, and methane inlet molar fractions from 0.3 to 0.9. A simple deactivation function was used to describe deactivation phenomena.

The potential of hydrogen removal via membrane reactor was evaluated for a Pd membrane available in literature with the estimated kinetic parameters and transport kinetics. The results predict a significant increase in the production of benzene due to the hydrogen removal. This implies promising potential of MR application to intensify the equilibrium limited MDA system. Two tubular carbon membranes (from Fraunhofer Institute IKTS, Hermsdorf) was tested experimentally. The transport of various gases (N<sub>2</sub>, He, H<sub>2</sub>, CH<sub>4</sub>) was studied for different temperatures. The hydrogen selectivity of the carbon membrane was lower than expected. Around 50% of methane from the feed also permeated out of the reaction zone, which lowered the methane conversion compared to the process using a conventional FBR. The observed diffusion behaviour could be described by configurational diffusion for membrane No. 1 and a second order polynomial function for membrane No. 2. The parameters in the diffusion models were estimated and validated. The theoretical and practical results of MDA using this “carbon MR” are not comparable with the result of FBR due to the insufficient hydrogen selectivity.

Catalyst deactivation is a very serious problem for MDA. The deactivation behavior of hierarchical Mo/MCM-22 is described in this work by a simple deactivation function which is used in simulating FBR and “carbon MR”. The deactivation simulation in FBR is in very good agreement with experimental data. The deactivation simulations for the “carbon MR” are less accurate.

It can be concluded that chances for industrial application of non-oxidative MDA would depend largely on further advancements in cost-effective catalysts, the identification of optimized operating conditions and new concept of reactors. The MDA concept was also compared with other methane conversion processes. The results indicate that the catalyst used in this work (Mo/MCM-22) has a distinguished tolerance against carbon deposition, but only moderate benzene selectivity. A higher methane conversion is possible when the bed temperature is raised at atmospheric pressure. The derived kinetic model can be used for MDA performance predictions for this catalyst. The carbon membrane tested is capable to remove the hydrogen produced during the MDA but is not sufficiently hydrogen selective.

## Zusammenfassung

Die Umwandlung von Erdgas ist eine der wesentlichen Technologien, um den aktuellen und künftigen Energiebedarf zu decken. Untersuchungen über die Umwandlung von Methan zu Benzol bisher wurden mit dem Ziel durchgeführt, vorhandene Berichte und Daten zu stützen und Perspektiven für die industrielle Umsetzung des Methan-Aromatisierungskonzeptes, sowie bestehende Grenzen aufzuzeigen. Die Methan-Dehydro-Aromatisierung (MDA) wurde intensiv hinsichtlich des Potenzials für die Umwandlung von Methan in wertvolle Plattformchemikalien und flüssige Brennstoffe untersucht. Dabei wurden zahlreiche Fortschritte hinsichtlich der Entwicklung aktiver Katalysatoren, des Verständnisses der Reaktionsmechanismen und zur Deaktivierung durch Koksbildung erzielt. Die MDA unter nicht-oxidativen Bedingungen kann einen einfachen und attraktiven Weg von Methan zu aromatischen Kohlenwasserstoffen ohne Zwischenschritte eröffnen. Die Totaloxidation der Reaktanden zu Kohlendioxid und Wasser kann vermieden werden und das Hauptprodukt Benzol kann von den anderen Produkten durch Kondensation abgetrennt werden. Effekte des Mo-Gehaltes im Katalysator, der Temperatur, der Raumgeschwindigkeit und der Partialdrücke von  $\text{CO}_2$ ,  $\text{CO}$ ,  $\text{H}_2\text{O}$ ,  $\text{C}_2\text{H}_4$ ,  $\text{C}_2\text{H}_6$  im Feed auf die MDA wurden bereits studiert. Zusätzlich wurde die Effektivität einer Katalysatorregenerierung mit Luft untersucht. Viele ungelöste Herausforderungen stehen der großtechnischen Umsetzung der MDA jedoch weiterhin im Weg, wie geringe Methanumsätze, niedrige Produktselektivitäten und starke Katalysatordeaktivierungen.

Die MDA zu Wasserstoff und Aromaten unter nicht-oxidativen Bedingungen ist ein thermodynamisch limitierter Prozess. Unter Berücksichtigung des Wechsels von fossilen Brennstoffen zu Wasserstofftechnologien ist die MDA ein interessanter und wichtiger Ansatz, verglichen mit der direkten oxidativen Umsetzung von Methan. Das Membranreaktor-konzept erscheint als ideale Lösung für das Problem der thermodynamischen Limitierung. Durch selektives Entfernen von Wasserstoff aus der Reaktionszone kann das thermodynamische Gleichgewicht in Richtung der Produkte beeinflusst werden, wodurch der Methanumsatz und eventuell auch die Produktselektivität positiv verändert werden.

In dieser Arbeit wurde die MDA auf einem Mo/MCM-22 Katalysator unter nicht-oxidativen Bedingungen in einem kontinuierlich betriebenen Festbett Rohrreaktor (FBR) mit Methan oder Ethylen als Rohgas detailliert experimentell untersucht. Damit wurde das Verständnis der MDA auf Mo/MCM-22 Katalysatoren für die simultane Bildung von Wasserstoff und leichten Aromaten, sowie zur Bifunktionalität des Katalysators unter akademischen und industriellen Gesichtspunkten verbessert. Der Einfluss verschiedener Prozessparameter (Temperatur, Feedzusammensetzung und Raumgeschwindigkeit) wurde untersucht und diskutiert. Alle Resultate wurden mit dem aktuellen Stand des Wissens verglichen und hinsichtlich technologischer Gesichtspunkte analysiert. Wasserstoff, Ethylen und Ethan wurden in den Experimenten durch gaschromatographische Analyse nachgewiesen. Die experimentellen Ergebnisse zeigen, dass Benzol bei allen Temperaturen nicht das einzige Kohlenwasserstoffprodukt der MDA ist. Eine Selektivität zu Benzol von 9 % konnte bei einem Methanumsatz von 6 % mit Mo/MCM-22, einer Temperatur von 973 K, einem Methangehalt im Feed von 90 % und einer Raumgeschwindigkeit von  $2160 \text{ kg s}^{-1} \text{ m}^{-3}$  erreicht werden. Die erzielten Selektivitäten und Umsätze sind geringer, als die in der Literatur berichteten. Dafür

---

wurde eine geringere Koksbildung auf dem verwendeten Katalysator beobachtet.

Im weiteren Verlauf der Arbeit wurden kinetische Untersuchungen für die MDA mit Mo/MCM-22 Katalysator durchgeführt, um das Verständnis dieser Reaktion zu erweitern und eine Prozessintensivierung und Optimierung zu ermöglichen. Verschiedene technologische Möglichkeiten wurden analysiert und vereinfachte kinetische Modelle, die auch mehrere Nebenreaktionen beinhalten, wurden entwickelt, um die MDA unter verschiedenen Reaktionsbedingungen abbilden zu können. Die Werte der kinetischen Parameter wurden anhand experimenteller Daten, die im FBR unter prozessrelevanten Bedingungen erzeugt wurden, abgeschätzt. Die entwickelten Modelle konnten die experimentellen Beobachtungen adäquat beschreiben und breite Prozessparameterbereiche abdecken: Temperaturspannen von 923 – 1023 K, Raumgeschwindigkeiten von 720 – 2160 kg s m<sup>-3</sup> und Methankonzentrationen im Feed von 30 – 90 %. Die Katalysatordeaktivierung über längere Standzeiten wurde mit einer einfachen Deaktivierungsfunktion erfolgreich beschrieben.

Das Potenzial des Einsetzens einer wasserstoffselektiven Membran wurde mit dem entwickelten reaktionskinetischen Modell und einem kinetischen Membranstofftransportmodell aus der Literatur evaluiert. Die Ergebnisse zeigen eine signifikante Steigerung in der Benzolproduktion durch selektiven Abzug von Wasserstoff, was das vielversprechende Potenzial dieses Membranreaktor-Konzeptes hinsichtlich der Beeinflussung der Gleichgewichtslimitierung der MDA unterstreicht. Eine zylindrische Kohlenstoffmembran (Fraunhofer Institut, Hermsdorf) wurde mit verschiedenen Gasen (N<sub>2</sub>, He, H<sub>2</sub>, CH<sub>4</sub>) bei verschiedenen Temperaturen charakterisiert. Das Diffusionsverhalten kann mit konfigurationeller Diffusion für Membran Nr. 1 und für Membran Nr. 2 mit einem angepassten Polynom 2. Ordnung beschrieben werden. Die Diffusionsmodellparameter wurden abgeschätzt, das Diffusionsverhalten experimentell validiert und das MR-Verhalten konnte vorhergesagt werden.

Zusammenfassend konnte in dieser Arbeit gezeigt werden, dass eine industrielle Umsetzung der MDA stark von der Entwicklung besserer, kosteneffektiver Katalysatoren, dem Auffinden optimierter Prozessparameter und der Entwicklung von Reaktorkonzepten abhängt. Das MDA Konzept wurde mit anderen Methankonvertierungsprozessen verglichen. Die Ergebnisse dieses Vergleiches deuten darauf hin, dass der in dieser Arbeit verwendete Katalysator (Mo/MCM-22) eine erhöhte Koksbildungstoleranz, sowie eine moderate Benzolselektivität bei hohen Methanumständen aufweist, wenn unter atmosphärischem Druck die Temperatur angehoben wird. Das entwickelte kinetische Modell kann genutzt werden, um die MDA auf dem verwendeten Katalysator unter anderen Reaktionsbedingungen abzubilden. Die verwendete Kohlenstoffmembran kann genutzt werden um den in der MDA produzierten Wasserstoff zu entfernen, ist allerdings nicht in ausreichendem Maße wasserstoffselektiv.

---

## Acknowledgements

This thesis presents the results of research work performed between October 2010 and December 2014 at the Otto-von-Guericke University and the Max Planck Institute for Dynamics of Complex Technical System in Magdeburg, Germany. I would like to thank the Max Planck Society and the Otto-von-Guericke University. Furthermore, I thank Dalian University of Technology and Chinese Scholarship Council for establishing and financing this German-Chinese Cooperation project.

As it is the case with all theses, this is work not only of the person mentioned on the cover. Hence I would also like to thank all people who helped me in realizing this thesis.

Personally, I would like to thank at first Prof. Andreas Seidel-Morgenstern, for providing me possibility of a promotion and supervising my study and research at the Max Planck Institute. His enthusiasm, suggestions and unwavering ideas were always very stimulating and instructive experience. It has been a valuable experience to be part of his group, seeing people working on a broad spectrum of problems in process engineering. Full commitment to the engineering sciences and willingness to move beyond personal boundaries and those of the discipline is the most important lecture I learnt from him.

I met Prof. Christof Hamel first in 2010 when I came to Germany to do my Master thesis. Working with him has been a shaping experience in many ways. He has encouraged me to enforce this project and to fight the mission through. I appreciate his illuminating discussion and encouragement concerning not only scientific work. His confidence, patience and amicability in dealing with people and an unambiguous but unpretentious attitude of leadership has become an anchor point in my own coordinate system. I admire his cyclopaedic knowledge and practical operational dexterity, like the Iron Man. It was always my pleasure and fun to work with him even, when he was facing the problems from the totally different angle.

Now many thanks for my Chinese support, Prof. Jianhua Yang. It was always pleasure to cooperate and to work with her. I am grateful for her suggestions on scientific matters and for always helpful advices concerning my future.

Then, I would like to thank Andreas Jörke, who help me a lot, e.g. with my German abstract. Jan Protzmann, Jutta Wilke, Tanya Wolff and Luise Borchert, who supported me in the laboratory. Christian Kocheler, Yuan Xu and Alberto Carrillo deserve many thanks for making the kinetic of MDA and membranes investigation in this thesis and for very collaborative support, useful discussions and the possibility to learn more about data fitting, optimization tools and membrane diffusion phenomena.

Working as a PhD requires a stimulating and productive atmosphere. In this respect I am particularly grateful to whole group for Physical and Chemical Fundamentals of Process Engineering. Special thanks go to my brilliant office mates, Gregor Kiedorf, Thomas Munkelt and Marielle Huebener, who do not only support me with scientific thing but also train my German. Then thanks to colleagues and friends Erik Temmel, Matthias Eicke and Kamila Galan.

I stays also to thank all friends who are outside the PhD unity which have made their contributions through parties, weekends and other activities necessary for the derivation of this thesis.

Finally, I want to express my deepest thank to my parents Xiuqin and Deyin and my sister Kaiman for the encouragement, understanding and the unconditional support.





## 1. Introduction

With the development of industrial progress, the world's energy situation is undergoing profound changes. Coal was the main energy for human to store, transport and make use of in early time. With oil is gradually developed in modern time, it generally replaces coal as the blood of modern industry and flows to every corner of the world. However, with the depleting of coal and oil resources in recent decades, the conflict between worldwide energy shortage and the growing energy needs of human is more and more prominent. According to the experts' prediction, the demand of energy will increase by 54% from 2001 to 2025. The exploitation rates of coal and oil have far exceeded the growth rates of their reserves. Energy issues will be the common problems faced by the entire planet. In the last decades, with the rapid decreasing of crude oil reserves, advanced techniques are being developed to obtain alternative energy sources. So the third largest reserved energy, natural gas, which is only second to coal and oil, are attracting more and more attention. The proven reserves of natural gas increase rapidly recent years, whose rate is much faster than the exploitation rate. The discovery of recently reported "combustible ice", which is hydrates of natural gas, attracts more attention of development and utilization of natural gas. Many geographic reports have shown that abundant reserves of nature gas exist in the earth, especially with the deposits in continental North America and in the sediments of the ocean floors. The worldwide existing reservation of natural gas is about 152 trillion cubic meters, which can be continuously exploited for more than 65 years. According to the prediction of authoritative experts, the increase of consumption of natural gas will be among the first of energy in the next three decades. Developing new technology to utilize methane has a significant strategic importance since methane is abundant reserves, high H/C ratio and clean.

### 1.1 Methane conversion

Methane, which is the most abundant compound in nature gas, is considered to contain twice the amount of carbon compared to all other known fossil fuel reserves [1]. Decades ago, methane has been considered as the world's third most important energy following coal and oil. The world reserve of natural gas is estimated as 187.3 trillion cubic meters according to the 2013 world energy structure analysis [2], which is greater than the sum of coal and oil together. With the gradual depletion of coal and oil, natural gas highly effective utilization has a significant impact on the world's energy balance [3]. Thus, converting methane into more practical significance chemicals would be the purport of natural gas industry and its related areas. On one hand, methane is a non-polar molecule with a similar stable structure of inert gas. The bond energy of C-H is as large as 435kJ/mol, which indicates very thermodynamic stability. On the other hand, methane is the most stable linear symmetric molecule at the same time, which means it is very difficult to avoid deep reacting once methane is activated. Its high chemical and thermodynamic stability is really a great challenge for developing new useful pathways of applying methane, which hindered its wider application. How to effectively activate this stable molecule and to achieve a reasonable conversion, has not only of great practical significance but poses also important theoretical problems. Scientists paid a lot of efforts on the field of methane catalysis, including methane partial oxidation, steam reforming oxidative dimerization, aromatization etc. A summary of main process routes is given in Figure 1. 1.

—Steam reforming (StR) is currently the major route of methane conversion and has been extensively reviewed [4]. It can be represented as eq. (1. 1). This highly endothermic process results in the formation of synthesis gas (with a  $H_2/CO=3/1$  composition) that can be further processed, e.g. into methanol and ammonia. Alternatively, synthesis gas can be directly processed into hydrocarbons via the Fischer-Tropsch (FT) process [5].

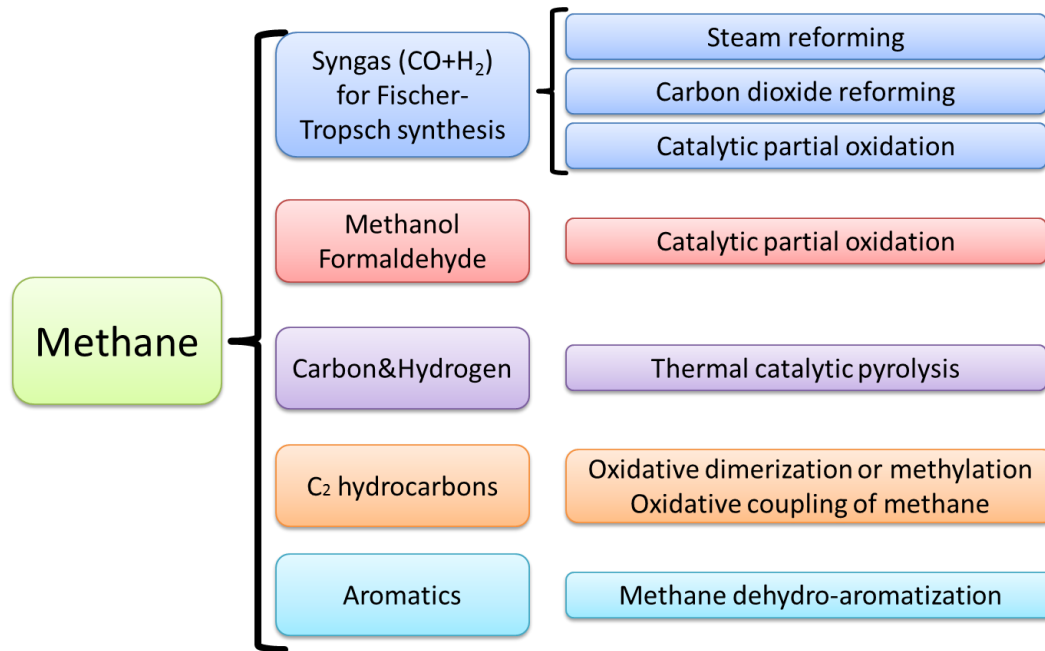
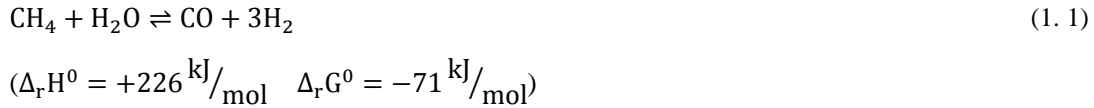
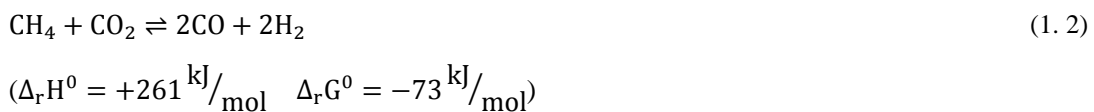
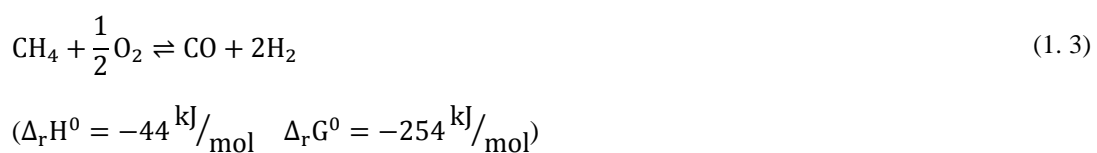


Figure 1. 1: Main processes and respectively products for methane processing

—Catalytic  $CO_2$  reforming ( $CO_2R$ ) of methane to syngas in the presence of steam and oxygen has also been extensively investigated [3, 6, 7].  $CO_2R$  make it possible to produce syngas with the composition  $H_2/CO=1/1$ , which can be directly use to synthesis formaldehyde.



—Catalytic partial oxidation of methane (POM) is thermodynamically favorable in the whole temperature range (see eq. (1. 3)). However, reaction conditions have to be carefully controlled in order to avoid methane deep or total oxidation. The aimed products composition of  $H_2/CO=2/1$ , which is required of methanol and olefins production. But the cost and explosion risk is relatively high because the presence of pure oxygen.



POM can also directly produce methanol and formaldehyde. The best performance of POM to

methanol is obtained at 350-550°C and 3-10 MPa [8] under Fe oxide catalysts with methane conversion less than 5% whereas methanol selectivity is about 70% [9]. Methanol is widely used as a fundamental chemical material and the consumption of methanol is more than 22 million tons every year. Thus, the potential of POM to produce methanol is very promising, since it is relatively easy to realize. But up to now, this reaction is not industrialized because methanol is much more reactive than methane, which induces the very low selectivity with respect to methanol since the produced methanol is oxidized faster than the oxidation of methane occurs. So, to suppress the oxidation of methanol is the bottleneck of this reaction.



$$(\Delta_r H^0 = -126 \text{ kJ/mol} \quad \Delta_r G^0 = -112 \text{ kJ/mol})$$

POM to formaldehyde is usually carried out at 550-650°C and atmosphere. Methane conversion of this process is not higher than 3-4% with selectivity around 80% [10]. Work on these processes is still at the laboratory scale.



$$(\Delta_r H^0 = -285 \text{ kJ/mol} \quad \Delta_r G^0 = -290 \text{ kJ/mol})$$

—Thermal catalytic pyrolysis (TCP): decomposition of methane to produce hydrogen has been proposed as an economical process to produce hydrogen since methane has the highest H/C ratio [11, 12]. The products of this process are filamentous carbon and hydrogen that does not contain CO and CO<sub>2</sub> impurities. Carbon obtained by this process can be used as the catalyst support, whereas hydrogen can be applied in the low temperature fuel cells [13]. The process is carried out at 600-1000°C in the presence of iron group metal loading catalysts [14]. Numerous articles, dealing with methane decomposition on single crystal surface, have provide important, fundamental insights into the dynamics of methane decomposition.



$$(\Delta_r H^0 = +74.8 \text{ kJ/mol} \quad \Delta_r G^0 = +50.8 \text{ kJ/mol})$$

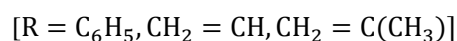
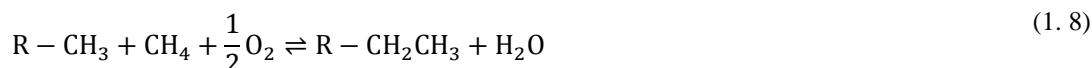
—Oxidative dimerization (OD) results in coupling of two methane molecules in the presence of oxygen or other oxidizing agents to form C<sub>2+</sub> hydrocarbons. This process is normally carried out at 700-850°C and atmosphere with methane conversion not exceed 40% whereas ethane selectivity is less than 80% [15].



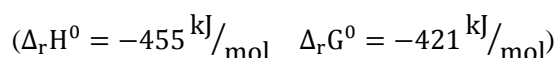
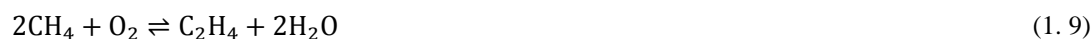
$$(\Delta_r H^0 = -350 \text{ kJ/mol} \quad \Delta_r G^0 = -223 \text{ kJ/mol})$$

—Oxidative methylation (OM) is a thermodynamically feasible reaction as shown in eq. (1. 8).

These reactions are normally carried out at 650-750°C, which is relatively high [16].



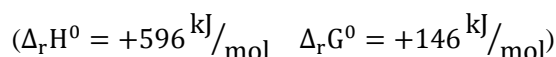
—Oxidative coupling of methane (OCM): in 1982, Keller and Bhasin [17] first reported the direct conversion of methane into ethylene, which received considerable excitement in the scientific world since hydrocarbon production via synthesis gas is expensive and rather circuitous. Most research of OCM focus on the development of high activity and selectivity catalyst.



Following this pioneering work, OCM became one of the most pursued topics of research in methane conversion [18-20]. Normally OCM is carried out at 600-950°C under atmosphere on basic oxides promoted with alkali metal salts or alkaline earth metal salts as important catalysts [21-23]. Usually the C<sub>2</sub> hydrocarbon yields are less than 25-30% because the selectivity of desired products is hampered by the undesired CO<sub>x</sub> formation due to the presence of oxygen in the feed and the high reaction temperature. Applications of new reactor concepts [24-28] are proposed, but economic considerations and commercial viability still prohibit the large scale implementation of such reactors.

—Methane dehydro-aromatization (MDA): Benzene and its derivatives are very important basic chemicals, which are necessary in plastics, fibers, rubber, pharmaceutical and other industries. With the growth of global economy, the demand of benzene is rising by years as well. Today the traditional method of producing benzene is based on petroleum industry. With the rapid depleting and increasing price of crude oil, the production costs of benzene remain at a high expensive level. So there is an urgent requirement to open up some new routes without oil as raw material instead of traditional crafts.

MDA takes place both under oxidative and non-oxidative conditions. With the presence of oxygen, MDA is more thermodynamically favored but benzene selectivity over zeolite catalysts was found to be only 3% at 600°C [29] because of strong production of CO and CO<sub>2</sub>. In 1993, Wang et al [30] firstly reported MDA under non-oxidizing conditions in a fix bed reactor with a molybdenum loaded zeolite catalyst (HZSM-5) capable to form aromatics (mainly benzene) and hydrogen. Thermodynamically, non-oxidative MDA to benzene is not very favorable. But the case of product separation and the low amount of by-product attracts many scientific activities.



Methane conversion processes can be classified by different categories, as oxidative versus non-oxidative and direct versus indirect.

### 1.1.1 Oxidative versus non-oxidative

From the aspect of oxidation, there are two major routes to produce available chemicals from methane: (1) oxidative treatment, most widely used, including indirect conversion (e.g. synthesis gas) and direct conversion (e.g. methanol); and (2) non-oxidative treatment, mostly direct conversion, that are shown in Figure 1.2 [31]. Until now, methane non-oxidative treatment technique has no significant breakthrough and is not easy to be commercialized. In contrast, oxidative treatment of methane has already been utilized in several larger plants, including the Sasol plants near Johannesburg, the PetroSA plant at Mossel Bay, the Shell SMDS (Shell Middle Distillate Synthesis) plant in Malaysia, the Oryx GTL (gas-to-liquid) plant in Qatar, as well as a GTL plant in Nigeria [31].

Some obvious advantages of oxidative treatment of methane led to industrialization. As mentioned above, methane is an extremely stable molecule, in which C–H bond requires strongly activation energy. In oxidative treatment, with introducing of oxidative species, C–H bond can be break down relatively easily. With adjusting the ratio of methane and oxidative species in the feed, we can obtain synthesis gas of different composition. However, during oxidative treatment, the oxidative species in the feed should be strictly controlled, because deep oxidation of carbon monoxide into carbon dioxide could occur. Great efforts are needed in controlling deep oxidation during oxidative treatment of methane. Consequently, many scientists started to study non-oxidative treatment of methane in recent years, which can overcome disadvantages of oxidative treatment.

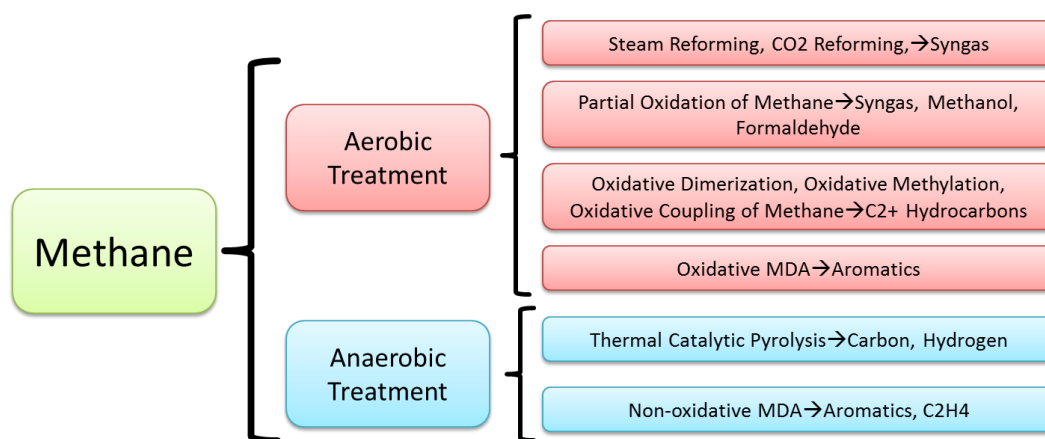


Figure 1.2: Comparison of oxidative and non-oxidative routes for methane conversion

### 1.1.2 Direct versus indirect

The routes applied currently in natural gas industry can be generally classified into direct and indirect routes, as shown in Figure 1.3. Direct means methane is directly converted to basic chemicals such as ethylene or aromatics under certain conditions without producing an intermediate, e.g. POM to methanol or formaldehyde [32], OCM to ethylene or ethane [25, 33-35], MDA [30, 36, 37], TCP. Since Keller and Bhasin et al [17] reported synthesis of ethylene via oxidative coupling of methane at 1982, methane direct conversion has been extensively investigated. The products of

direct conversion can be ethylene, aromatics or oxygenate hydrocarbons. Overall, direct conversion of natural gas has broad application prospects, but the products of direct conversion are usually much more active than methane under reaction condition and easily react further, which leads to low conversion of methane and low selectivities of target products. So far, methane direct conversion technique has no breakthrough and is not easy to industrialize in a short time.

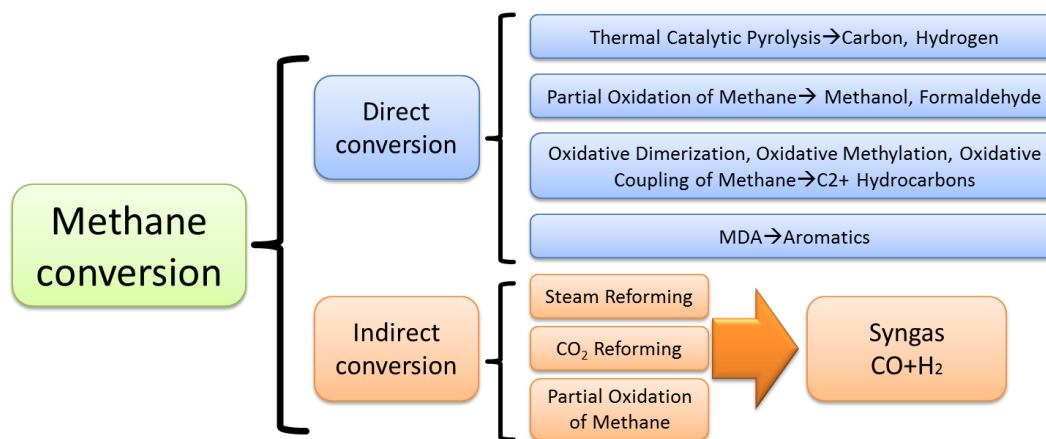


Figure 1.3: Comparison of direct and indirect routes for methane conversion

Indirect conversion indicates firstly converting methane to syngas with a certain ratio of carbon monoxide and hydrogen by reforming or partial oxidation under certain reaction conditions, and then further converting the products to alkenes or oxygenates with catalysts. The technology of indirect conversion is rather mature and the productions of ammonia and methanol are already industrialized a long time. The main pathways of indirect conversion are POM, StR and CO<sub>2</sub>R [38]. The reforming reaction is highly endothermic, which needs vast heating supply units. StR has been industrialized decades ago, but the H<sub>2</sub>/CO ratio of produced syngas is too high for direct methanol production. Also the costs of facilities are very high. The deactivation of nickel catalysts is very fast and heavy. POM is a slightly exothermic reaction, and the application of oxygen aggregates the catalyst deactivation and increase the risk of explosion at the same time. So the operation of POM must be strictly controlled. 60% of the energy of methane indirect conversion is consumed at the step of reforming to syngas. The procedure is relatively cumbersome and complicated. So methane direct conversion is most focused on saving energy and reducing investment costs as well as simplifying facilities and process operation.

## 1.2 MDA reaction system

Without producing syngas intermediates via steam reforming or partial oxidation, direct methane conversion has huge economically attraction. In the conversion of methane, oxygen is usually in response, which provides the thermodynamic driving force and then leaves the reaction free energy to be negative. However, there will be a large number of non-target CO<sub>2</sub> in the products due to the dynamics, which limits the yield of target products. Thus, as mentioned above, non-oxidation of methane to aromatics attracted wide attention. The non-oxidative MDA can validly avoid deep oxidation of methane to carbon dioxide, and it will produce abundant hydrogen at the same time. The products of MDA are liquid aromatics and gaseous hydrogen, which are easy to separate. Thus,

an increasing number of scientists studied MDA reaction system. Methane produce aromatics is thermodynamically favorable than the other hydrocarbons.

MDA can be separated into oxidative [36, 39-41] and non-oxidative [30, 37, 42-47]. 1983, Shepelev and Lone [36] firstly reported oxidative MDA with the feed of methane and N<sub>2</sub>O mixture (CH<sub>4</sub>/N<sub>2</sub>O=10) at 673K on the Fe<sub>2</sub>O<sub>3</sub>/HZSM-5 catalyst with methane conversion of 44.4% and aromatics selectivity of 90%. However, when oxygen is used instead of nitrous oxide, methane is almost completely oxidized to CO, CO<sub>2</sub> and H<sub>2</sub>O. Otsuka and Komatsu [39] reported oxidative MDA on the oxidative coupling catalyst Na/MnO<sub>2</sub> and Ga/HZSM-5 in series at 1023K and 973K respectively with aromatic yield of 5.5%. Abasov et al. [48] found oxidation of methane under solution adsorption method on Ni/γ-Al<sub>2</sub>O<sub>3</sub> catalyst with aromatics yields of 8.5%. While Claridge et al. [40] realized oxidative MDA on K/BaCO<sub>3</sub> and NaCl/MnO<sub>3</sub> catalysts and Yu et al. [41] also observed the aromatics formation of methane and carbon dioxide mixture on the Pt filament. Even though the presence of oxygen makes MDA thermodynamically favorable, but the deep oxidation of products, which low down the selectivity of aimed product and also waste nature gas resource, is inevitable just because of oxygen is presented. So the non-oxidative MDA attracted huge interests of scientists.

Non-oxidative MDA process can almost completely avoid deep oxidation of methane to carbon dioxide, and abundant hydrogen can be expected as valuable byproduct at the same time. The products of MDA are liquid aromatics and gaseous hydrogen, which are really easy to separate.

In 1989, Inui et al [42] reported non-oxidative MDA at 973K on Pt/Ga-silicates catalyst with methane conversion of 4.2% and aromatics selectivity of 90%. Murata and Ushijima [49] reported non-oxidative MDA on amorphous-like carbons which are get form the pyrolysis of triphenylphosphine. The reaction starts at 1000K and they get methane conversion of 40.5% and benzene yield of 23% at 1323K. They pointed out methane pyrolysis to CH<sub>3</sub> first at high temperature, where after CH<sub>3</sub> dimerization to ethylene and further cyclization to benzene. Marczewski et al [50-52] utilized MnO<sub>x</sub>-Na/SiO<sub>2</sub>-HZSM-5 as the two stage catalyst to investigate non-oxidative MDA. They found methane coupled with MnO<sub>x</sub>-Na/SiO<sub>2</sub> at 1073K reacted to ethylene, which cyclized to benzene on HZSM-5 at 873K with benzene yield of 6.5%. They figured out that the performance of MDA is closely relative to Si/Al ratio of HZSM-5 (low Si/Al ratio is better for CH<sub>4</sub> activation), and further proposed that the acidity of zeolite plays a crucial role in MDA.

1993, Wang et al reported MDA on Mo/HZSM-5 catalyst in a continuous flow model, which is identified as a milestone to non-oxidative MDA system. Since than many global scientific research groups or institutes [37, 43, 44, 46, 53-61] did plenty of investigation of MDA on transition metal loaded zeolite catalyst system and got some achievements. Most of the works are focused on the following aspects: selection of catalyst system, optimization of reaction system, the location of molybdenum, the interaction of Mo and zeolite, identification of reactive species, investigation of reaction mechanism and the improvement of catalyst performance.

Here are some consensuses of non-oxidative MDA on metal loaded zeolite catalysts: (1) Mo/HZSM-5 is a bi-functional catalyst; (2) there is an induction period at the early reacting stage, during which

MoO<sub>x</sub> species is reduced by CH<sub>4</sub> to Mo<sub>2</sub>C or MoO<sub>x</sub>C<sub>y</sub>; (3) it's very easy to have carbon deposit during reaction process, which induce the deactivation of catalyst; (4) Mo interacts with alumina in the zeolite framework and acid sites of zeolite, which impacts the performance of catalyst; (5) the shape selectivity of zeolite channels significantly affect the distribution of products.

Non-oxidative MDA reacts on Mo based catalysts at relatively low temperature (975K) with low carbon deposit and tar yields, because active sites activate methane within shape-selectivity which restrict chain growth and produce aromatic polymer. The conversion nature of MDA is highly endothermic and leads to very low equilibrium conversions and to benzene yields of only ~ 7% at 950K. The coupling of hydrogen permeating through the membrane would lead to higher methane reaction rates and conversion as a result of the breaking down of thermodynamic constraints.

## 1.2.1 Catalysts

Non-oxidative MDA is a very important pass way of natural gas direct conversion, which is considered as a very challenging complex reaction in catalytic field. After decades' of investigation, some attainments have been achieved. But low methane conversion and catalyst stability prohibit the further development and application of MDA. For the development of MDA reaction catalyst, research mainly focused on two aspects, the active metal component and carrier.

### 1.2.1.1 Active metal loading

Since 1993 non-oxidative MDA on Mo/HZSM-5 catalyst was reported, numerous research activities was dedicated to investigating this catalyst system [30]. Most of the researchers use impregnation method to synthesis catalyst, which means that mixing the soluble active component and the insoluble support components together, and then soaking the excess liquid, after drying, calcining and forming, comes the loading type catalyst [62]. For a heterogeneous catalyst, active metal loading, support and aids are normally the breakthrough points. Many metal ions dispersed on various supports have been investigated including Mo, Zn [63, 64], W [65-69], Re [70], Cu, Mn [71], Ni, Cr, V, and Ga. For instance Xu et al. [72] in Dalian institute of chemical physics, studied the performance of Mo, Zn, Cu, Pt, Ni and other metal ions loading on HZSM-5 to MDA system. Results are presented in Table 1. 1.

Table 1. 1: The catalytic results of methane dehydro-aromatization under non-oxidative condition over different catalysts [62]

Catalyst	Conv. of CH <sub>4</sub> (%)	Select. to aromatics (%)
Mo/HZSM-5	7.2	100
Zn/HZSM-5	1.0	79.1
Cu/HZSM-5	0.6	52.5
Pt/HZSM-5	0.03	0
Ni/HZSM-5	0.01	0

(Operating condition: T=973K, P=115kPa, F/W=1500mL/gh)



As can be seen from Table 1. 1, under the operating condition from the literature, molybdenum performs best. Weckhuysen et al. [44] compared the performance of Mo, Fe, V, Cr and W loaded on HZSM-5 in MDA reaction, the results show that at 1023K with methane space velocity (SV) 800mL/gh, Mo/HZSM-5 still performed the best. Ohnishi et al. [73] reported that Re/HZSM-5 possess the same catalytic performance as Mo/HZSM-5 with the condition of 1023K and 3 atm, but Re is much less than Mo at 973K.

Table 1. 2 shows the performances of different catalysts in terms of the selectivity of aromatics and conversion of methane [31]. We can conclude that Mo-based catalyst exhibits the highest activity in the conversion of methane to aromatics, meanwhile both W and Co-Ga based catalysts also perform well. However, other metal ions show only low activity for methane aromatization.

Table 1. 2: Comparison of MDA activities of various supported metals on HZSM-5 zeolite

Active metals	Reaction conditions		CH <sub>4</sub> conversion (%)	Selectivity (%)		Benzene yield (%)
	T (°C)	F/W (mL g <sup>-1</sup> h <sup>-1</sup> )		benzene	naphthalene	
Mo [30]	730	1500	16.7	60.4	8.1	10.09
Zn [63, 64]	700	1500	1.0	69.9	<sup>b</sup>	0.70
W [65-68]	800	1500	13.3	52.0	<sup>b</sup>	6.92
Re [70]	750	1440	9.3	52.0	0	4.84
Co-Ga	700	1500	12.8	66.5	7.2	8.51
Fe	750	800 <sup>a</sup>	4.1	73.4	16.1	3.01
Mn[71]	800	1600	6.9	75.6	11.9	5.22
V	750	800 <sup>a</sup>	3.2	32.6	6.3	1.04
Cr	750	800 <sup>a</sup>	1.1	72.0	3.7	0.79

<sup>a</sup> GHSV/h<sup>-1</sup> ; <sup>b</sup> Not reported

### 1.2.1.2 Catalyst support

The support is an important component of a catalyst, which has functions of dispersing, stabilizing, supporting and aid-catalysis to the active component. Therefore, MDA performance of Mo-based catalyst supported on different types of zeolites has also been deeply studied.

Solylmosi [74] tested many kinds of oxides instead of ZSM-5 as the catalyst of MDA and the results showed that the performance of Mo loaded SiO<sub>2</sub>, MgO, Al<sub>2</sub>O<sub>3</sub> and TiO<sub>2</sub> are far worse than ZSM-5. Lin[75] studied many kinds of zeolites as the carrier of MDA catalyst and the resulted catalytic activity rank is: Mo/HZSM-11 > Mo/HZSM-5 > Mo/HZSM-8 > Mo/Hβ > Mo/MCM-41 > Mo/HSAPO-34 > Mo/H-mordenite > Mo/HX > Mo/HY > Mo/HSAPO-5 > Mo/HSAPO-11. Regarding to this aspect, Liu [76] made a detailed summary given in Table 1. 3. According to Table 1. 3, pore openings of the internal channels close to the kinetic diameter of benzene are an important factor of well performed catalyst. Based on this, in order to improve the selectivity of aromatics, a variety of zeolite supports were studied, including MCM-22 [58, 77-81], MCM-49 , MCM-36 [82], NU-87, HZRP-1 [83], ITQ- 2 [84], ITQ-13, and MCM-56 [85] and the results are

listed in Table 1. 4 [31].

Table 1. 3: The effect of the zeolite supports on the catalytic performances of Mo-based catalysts in the methane dehydro-aromatization under non-oxidative condition [76]

Catalyst	Pore structure	Conv. of CH <sub>4</sub> (%)	Select. to C <sub>6</sub> H <sub>6</sub> (%)
HZSM-5	10 ring CC	6.9	90.8
HZSM-8	10 ring 2-D SC	4.1	86.7
HZSM-11	10 ring 2-D SC	8.0	90.9
HSAPO-5	12 ring SC	0	0
HSAPO-11	10 ring SC	0	0
HSAPO-34	8 ring sc with CS	0.6	72.9
HX	12 ring sc with SCS	0.7	0
HY	12 ring sc with SCS	0.7	0
H $\beta$	12 ring sc and CuC	3.1	80.4
MCM-41	Mesoporous	0.9	80.1
H-mordenite	12 ring and 8 ring SC	7.3	53.2
ESR-7	8 ring RC	1.2	0
JQX-1	12 ring RC	2.8	3.4
SBA-15	Mesoporous	5.6	6.3
HZRP-1	10 ring CC	10	56.2
MCM-22	10 ring CuC and 12 ring SCS	10.5	78
MCM-49	10 ring CuC and 12 ring SCS	5.6	95

CC: cross channel, SC: straight channel, CS: cage structure, SCS: super cage structure, CuC: curved channel, RC: ring channel,

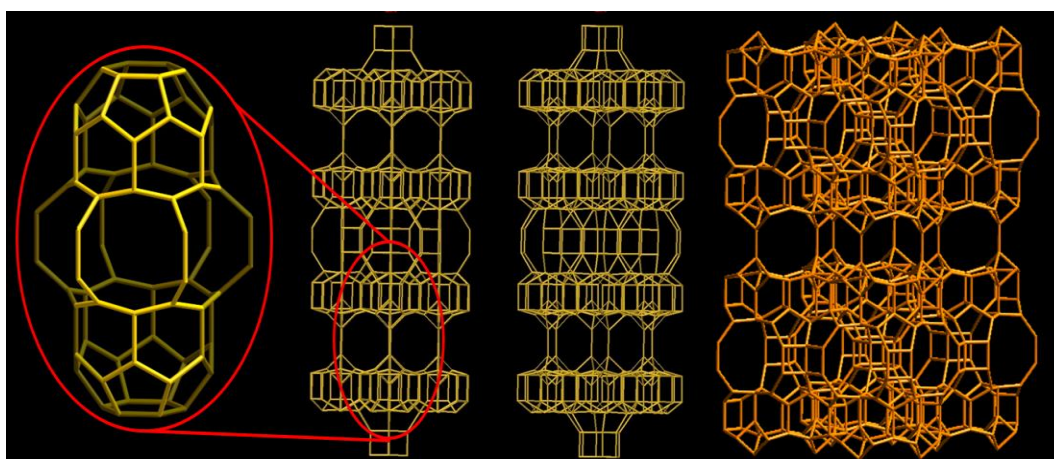


Figure 1.4: Pore structure of MCM-22 zeolite [86]

Table 1. 4 shows us the characters and performances of different supporters at 973K, which exhibit that HZSM-5, MCM-22 and MCM-49 are all suitable supports for MDA process. In addition to HZSM-5, MCM-22 is another support that has been widely used for its better tolerance against

carbon deposition during research of MDA process and is also the catalyst support we use in this thesis. As shown in Figure 1.4 MCM-22 possesses a unique pore architecture with two independent pore systems: a smaller, 2D (two-dimensional) 10-ring sinusoidal pore system ( $4.1 \times 5.1 \text{ \AA}$ ), and a larger, 3D 12-ring super-cage system inter connected with 10-ring windows ( $4.0 \times 5.5 \text{ \AA}$ ). This pore structure and the presence of supercages are responsible for the high coke accommodation ability of MCM-22, at the same time retaining shape selectivity is necessary for the formation of aromatics [31]. These two vital factors ensure the selectivity to benzene and stability of the catalyst under methane aromatization reaction conditions.

Table 1. 4: Comparison of activities zeolite supports for Mo-based MDA catalyst [87]

Zeolites	Pore size( $\text{\AA}$ )	MR	flow(mL $\text{g}_{\text{cat}}^{-1} \text{ h}^{-1}$ )	CH <sub>4</sub> conversion (%)	Selectivity (%)		
					C <sub>6</sub> H <sub>6</sub>	C <sub>10</sub> H <sub>8</sub>	coke
HZSM-5	5.4*5.6,5.4*5.5	10	1500	10.0	58.2	18.2	16.5
			1600	5.9	91.3 <sup>a</sup>	—	—
HZSM-8	5+	10	1600	8.0	90.1 <sup>a</sup>	—	—
HZSM-11	5.1*5.5	10	1600	4.1	86.7 <sup>a</sup>	—	—
HZSM-22	4.0*5.5,4.1*5.1, 7.1*7.1	10,1	1500	9.9	72.8	5.9	13.0
		2					
HZSM-41	4.0		1600	0.9	80.1 <sup>b</sup>	0	—
HZSM-36			1500	11.5	47.4	0.31	28.5
HZSM-49	4.0*5.9,4.0*5.4	10	1500	13.0	76.9	5	3.54
NU-87	4.8*5.7	10,1	1500	11.0	22.9	10.9	62.7
		2					
HZRP-1	5.0*5.3,5.0*5.4	10	1500	9.7	48.6	27.0	13.9
ITQ-2		6,10	1500	7.1	70	20	10
ITQ-13	4.0*4.9,4.8*5.7, 4.7*5.1	9,10	1500	2.0	72 <sup>b</sup>	12	—
		,10					
MCM-56			1320	6.5	52	—	30
IM-5	5.5*5.6,5.3*5.4,		1500	11.5	39.3	14.6	5.2
	5.3*5.9						
	4.8*5.4,5.1*5.3						
TNU-9	5.2*6.0,5.1*5.5,	10,1	1500	11.3	81.2	16.6	—
	5.4*5.5,7.2*7.2	2					

### 1.2.1.3 Molybdenum species in zeolite

Many papers are devoted to investigate of the state of molybdenum in the zeolite matrix. The most widely used molybdenum source is  $(\text{NH}_4)_6\text{Mo}_7\text{O}_{24}$  impregnation, which decomposed to  $\text{MoO}_3$  during calcination from 514 to 616K [14]. Xu et al [88] conducted XRD and BET measurements on

a Mo/HZSM-5 catalyst. The different BET specific surface area of different Mo loading percentage results showed that Mo is highly dispersed on both the outer surface and the internal channels of HZSM-5.

Chen et al. [89] studied HZSM-5 with different Mo loading percent by means of XRD, IR, UV diffuse reflectance spectroscopy, TPR and NH<sub>3</sub>-TPR. The results showed that with increasing Mo load, both BET specific surface area and acidity of catalyst are decreasing. Most molybdenum species are located in the channels of zeolite when Mo loading is less than 5 wt%. Above that, molybdenum oxides phase appears and decreases the catalyst surface area dramatically.

Lunsford et al. [44, 90, 91] investigate the connection between Mo species and zeolite by FTIR, XPS and ISS. They found after impregnation, Mo species mainly dispersed on the outer surface of zeolite. Some Mo species will migrate into the zeolite channel during calcination. When molybdenum is impregnated onto HZSM-5, the three stretch peaks at 3747, 3611, 3670cm<sup>-1</sup> are weakened, especial the peak at 3670cm<sup>-1</sup>. This shows that the introduction of Mo strongly affects the Si-OH terminal group and the Brønsted acid sites of zeolite. The state of molybdenum was shown by FTIR spectroscopy that after the zeolite impregnation with ammonium heptamolybdate ((NH<sub>4</sub>)<sub>6</sub>Mo<sub>7</sub>O<sub>24</sub>·4H<sub>2</sub>O) solution and drying in air at 100°C with mixing for 24h, molybdenum remained in the form of ammonium heptamolybdate crystallites. Calcination at 400–500°C led to the formation of molybdenum oxides in Mo/ZSM-5. At higher calcination temperature (700°C) aluminum molybdate Al<sub>2</sub>(MoO<sub>4</sub>)<sub>3</sub> was formed in addition to MoO<sub>3</sub>. These changes in the zeolite structure composition take place only in the catalysts with relatively high molybdenum concentrations (around 10-15%). Meanwhile, at low molybdenum concentration of 2-6%, molybdenum exists in the form of finely dispersed oxide structures [89].

Lv studied the influence of Si-OH group and Al-OH bridge on the surface of zeolite to the chemical and dispersive state of Mo species by XPS, H<sub>2</sub>-TPR and NMR. The results showed that Si-OH group can help Mo species dispersion and promote Mo oxide to be reduced, while Al-OH bridge will inhibit Mo dispersion and form Mo/Al compound further suppress Mo reduction. And Lv considered only a small portion of Mo migrates into the channel and the major is on the external surface [92].

Howe et al. [93] conducted XPS, <sup>27</sup>Al, <sup>29</sup>Si MAS-NMR, IR, EXAFS measurements on Mo/ZSM-5 catalyst. Their results showed that Mo have the tendency to migrate into the zeolite channel, interact with the Brønsted acid sites and lead to the formation of non-framework aluminum at 773K calcination temperature. If raise the temperature to 973K, there will form Al<sub>2</sub>(MoO<sub>4</sub>)<sub>3</sub> crystals which is induced by the Mo migration and resulted in heavy dealumination of zeolite.

Bao et al. [59, 94-96] proved Mo interacted with Brønsted acid sites on the surface and in the zeolite channel during impregnation and calcination by NH<sub>3</sub>-TPD, <sup>1</sup>H MAS NMR measurements. They found after loading Mo species, the strength of the peak represents for acid sites of NH<sub>3</sub>-TPD and the one at 3.8ppm chemical shift of <sup>1</sup>H MAS NMR are reduced. And this reduction is more obvious with more Mo loading weight. Mo species inside the channels were described as [Mo<sub>5</sub>O<sub>12</sub><sup>6+</sup>], while other Mo are present as oxides on the external surface. Both Mo species are converted to a mixture

---

of  $\text{MoO}_x\text{C}_y$ ,  $\text{Mo}_2\text{C}$  and  $[\text{Mo}_5\text{O}_x\text{C}_y^{n+}]$  during MDA induction period.

Ma et al. [77, 97] reported that Mo ions interact with the zeolite lattice during both impregnation and calcination. Molybdenum ions become adhesive to the zeolite framework near aluminum ions via oxygen bond because of Brønsted acid sites serve as powerful traps, causing molybdenum ions migrating into the internal channels of the zeolite where they react preferentially. When this kind of interaction is very strong, formation of octahedral, non-framework aluminum ions and  $\text{Al}_2(\text{MoO}_4)_3$  crystallites take place, which led to a decrease in the zeolite crystallinity. The EPR [57, 97] results showed that prolonging calcination time at 773K favors the diffusion of Mo species on the external surface and their migration in the channels. Mo on the external surface are readily reduced to  $\text{Mo}_2\text{C}$ , while those in the channels are partially converted into  $\text{MoO}_x\text{C}_y$  closely associated with framework Al ions ( $\text{Al}(\text{I})-\text{MoO}_x\text{C}_y$  or  $\text{Al}(\text{II})-\text{MoO}_x\text{C}_y$ ). Mo species associated with Brønsted acid sites in the zeolite channels are more active and stable for the formation of aromatics. Both Mo species play key roles in non-oxidative MDA process.

Nagai [98] found that three forms of Mo carbides in the carburized catalysts:  $\alpha\text{-Mo}_2\text{C}_{1-x}$ ,  $\beta\text{-Mo}_2\text{C}$  and  $\eta\text{-Mo}_3\text{C}_2$ .  $\eta\text{-Mo}_3\text{C}_2$  has more selectivity of pyrolytic carbon formation than benzene compared with  $\alpha\text{-Mo}_2\text{C}_{1-x}$  and  $\beta\text{-Mo}_2\text{C}$ .

Tessonier et al. [99, 100] reported an innovation approach to quantify both the amount and the localization of Mo species as well as the role of Brønsted acid sites in Mo/ZSM-5. They found the anchoring mode of Molybdenum with Brønsted acid sites is strongly influenced by Si-Al ratios of ZSM-5. Mononuclear bidentate Mo species ( $\text{MoO}_2^{2+}$ ) predominate at low Si/Al ratios while dinuclear ones prevalent at high Si/Al ratios. However, when the loading of Mo species was increased to 4 wt%, the number of Brønsted acid sites is too few to allow all Mo species to adopt binuclear structure, and the formation of extra-framework polymolybdates or alumino-molybdate species cannot be avoided. One different opinion about the active Mo species is from Zaikovskii [101], who concluded that methane is mainly activated on oxidized molybdenum cluster located in the zeolite channels.

The widely-held opinion regarding molybdenum impregnation catalyst is that Mo is dispersed on both external and internal surface of zeolite. Mo will migrate into zeolite channel interact with Brønsted acid sites by ion exchange after calcination. There are two key Mo species in the catalyst, which are fully reduced,  $\text{Mo}_2\text{C}$  on the external surface and the partial reduced  $\text{MoO}_x$  in the channels.

### 1.2.2 Reaction mechanisms

Dehydro-aromatization of  $\text{CH}_4$  on Mo/zeolite catalyst under non-oxidative condition mainly produces aromatics and hydrogen, but with the formation of ethylene (considered as an intermediate), ethane and carbonaceous deposit at the same time. The detailed elementary steps of MDA are very complicated, which include activation of C-H bonds, formation, oligomerization and cyclization of intermediate [60]. It's a great challenge in catalytic field to clarify the real detail process from one carbon atom of methane into six or even more carbon atoms molecular products, but also has a very realistic and practical importance. It is widely accepted now that the mechanism

for methane dehydro-aromatization over Mo/zeolite is bi-functional [62, 74, 91, 102, 103]. Methane is activated by Mo sites with hydrogen radicals release to gas phase and formation of  $\text{CH}_x$ . Then the  $\text{C}_2\text{H}_y$  species oligomerize to form aromatics on Brønsted acid sites. The schematic reaction mechanism is shown in Figure 1.5. Lunsford et al. [90, 91, 104, 105] analyzed Mo/HZSM-5 at different reaction stage with XPS and found that there is an obvious induction period in the early stage of MDA reaction. In this induction period,  $\text{Mo}^{6+}$  ions are reduced to  $\text{Mo}_2\text{C}$  by methane accompanied by carbonaceous deposit on the surface of  $\text{Mo}_2\text{C}$ , which become to be the active center of methane reacting to ethylene. Most of the produced  $\text{Mo}_2\text{C}$  were higher dispersed on the outer surface of HZSM-5, only a few of them migrated into zeolite channels. They pointed out that the intermediate ethylene, produced by methane activation, moved into zeolite channels and reacted at Brønsted acid sites. That means  $\text{Mo}_2\text{C}$  is active center of methane and the acid sites in zeolite are the further reacting center of the subsequent ethylene aromatizing. The schematic reaction mechanism is shown in Figure 1.5.

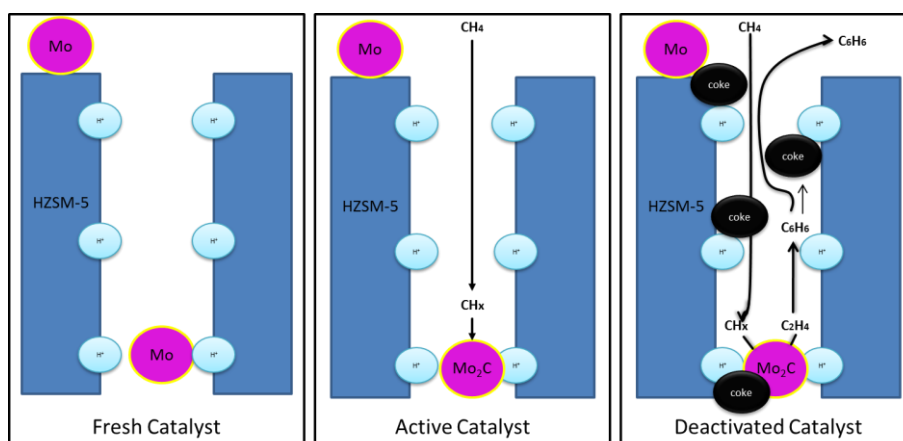
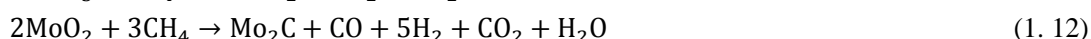
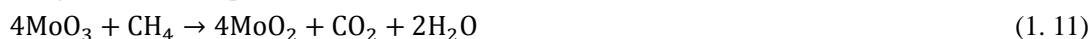


Figure 1.5: Schematic representation of the MDA reaction over the Mo/HZSM-5 catalyst

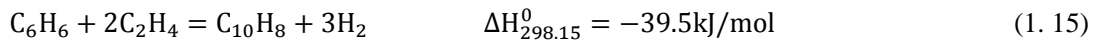
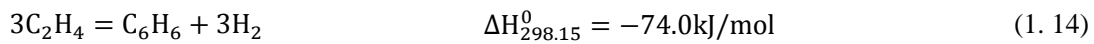
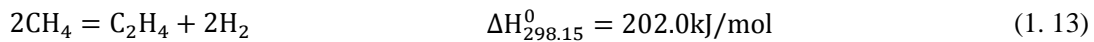
Bao et al. [30, 94, 95, 97, 106] found that Mo species on the surface of zeolite can interact with Brønsted acid sites in the channels, i.e. the Brønsted acid sites attracted Mo species to migrate into the channels. The Mo species in the channels anchored on the aluminum sites by oxygen-bridge, formed Mo reacting center with  $\text{C}_{2v}$  symmetry. And the free Brønsted acid sites are the further reacting center for aggregation, cyclization and aromatization. That is the bi-functional catalytic mechanism (Figure 1.5). They also investigated MDA induction period and found three stages for product formation, as a function of increasing reaction temperature. (1) Temperatures from 547 to 687 °C, methane is converted to  $\text{CO}_2$  and  $\text{H}_2\text{O}$ . (2) Formation of  $\text{CO}$ ,  $\text{H}_2$ ,  $\text{CO}_2$ , and  $\text{H}_2\text{O}$  from 687 to  $\sim 777$  °C. (3) Benzene formation occurs near the end of  $\text{CO}$  and  $\text{CO}_2$  production at  $> \sim 777$  °C. The first two stages constitute the induction period. They also deduced the following reactions happened during the induction period.



Solymosi et al. [74, 107-109] studied MDA performance with catalysts of different molybdenum precursors and zeolite supports ( $\text{MoO}_3/\text{SiO}_2$ ,  $\text{K}_2\text{MoO}_4/\text{ZSM-5}$ ,  $\text{MoO}_2/\text{ZSM-5}$ ,  $\text{MoO}_3/\text{ZSM-5}$ ,  $\text{Mo}_2\text{C}/\text{ZSM-5}$  and unsupported  $\text{MoO}_3$ ,  $\text{MoO}_2$  and  $\text{Mo}$  etc.). They found that highly dispersed molybdenum oxide on the surface of zeolite reacted to  $\text{Mo}_2\text{C}$  during methane activation, which is

the reacting center of methane to ethylene. The isolated Mo<sub>2</sub>C only catalyzed methane to carbon and hydrogen. And the acid site of zeolite is the reacting center of ethylene polymerization and cyclization to aromatics. While Ma et al. [106] found that ethylene and benzene were produced at the same time and the amount of ethylene is much smaller than benzene by TPSR.

The methane aromatization process is very complex. There are many theories about the reaction mechanism. It was reported that cyclopentadiene is the most important intermediate of methane cyclization [110]. They exhibited a cyclopentadiene mechanism with 44 elementary reactions concerning 25 species when methane conversion is under 1%. Wang [91] proposed H extraction and acetylene additive mechanism, which could be applied under high methane conversion, but still no accurate enough. According to the report of Li Lin [111], the following reversible reactions (1. 13)-(1. 15) are possible in the reaction process under temperature 950K and CH<sub>4</sub> partial pressure at 0.5 bar with different W/F.



Li Zuoan [112] simulated MDA system in a fixed bed reactor and a membrane reactor by investigating the reaction kinetics, mass transport and fluid dynamics. The reaction network under consideration is quite simple which contains only two reactions as shown in eq. (1. 16) and (1. 17).



An elementary steps-based kinetic model was developed for the steady state reaction kinetics of MDA by Guy B. Marin [60]. The reaction network proposed for MDA over Mo/MCM-22 includes 23 elementary steps as shown in Figure 1.6.

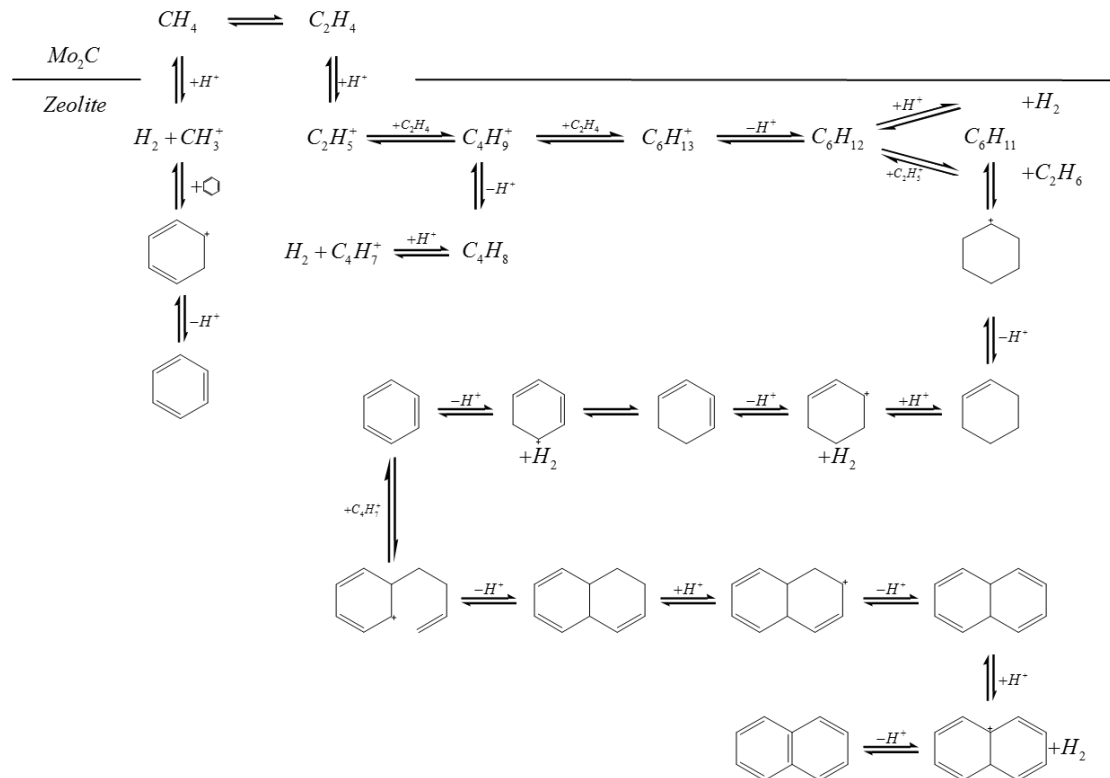


Figure 1.6: Schematic reaction network of the MDA reaction over the Mo/MCM-22 catalyst

After nearly a certain decades of investigation, the majority of scientists found the following important features and reached consensuses about MDA reaction [53, 113-115]:

- i. Mo/zeolite is bi-functional catalysts; Mo species as well as the acid sites in zeolite have the same importance.
- ii. There is an induction period at the beginning, in which  $\text{MoO}_x$  is reduced to  $\text{Mo}_2\text{C}$  or  $\text{MoO}_x\text{C}_y$  by methane.
- iii. The interactions of Mo species with Al in the frame of zeolite and also with acid site on the zeolite are determining factors of catalytic activity.
- iv. The open-framework structure of the channel in the catalyst has a shape-selectivity and will affect the species of products.
- v. During the reaction process there are significant carbon depositions, which are the main reason of catalyst deactivation.

### 1.2.3 Approaches to improve MDA

Much efforts have been devoted in the area of MDA reaction system optimization, especially in the direction of coupling other reactions and introducing reactor design improvements to enhance catalyst lifetime, methane conversion and aromatics selectivity.

#### ➤ Coupling other reactions

Various attempts have been dedicated to suppress carbonaceous deposit and improve methane conversion. Coupling MDA with other reactions (e.g. Boudouard reaction, StR,  $\text{CO}_2\text{R}$  and OCM) has been studied. However, it's not always easy to identify which reaction is occurring due to the complex nature of MDA.

Ichikawa et al. [54, 73, 116, 117] studied coupling MDA with Boudouard reaction by adding a small amount of CO or  $\text{CO}_2$  in the feed. They found 1.6%-12% CO co-feed can suppress carbonaceous deposit and prolong the catalyst life time up to more than 30h. Addition of  $\text{CO}_2$  can also improve the catalyst stability in a narrow range of  $\text{CO}_2$  concentration. 2.0 vol%  $\text{CO}_2$  greatly suppresses methane conversion and 12 vol%  $\text{CO}_2$  completely inhibits the formation of aromatics [118]. These authors also tested the effect of coupling StR with MDA. The results showed that a small amount of water (concentration between 1.7% and 2.2%) also improved catalyst stability at 1023K. Excess water (concentration >2.6%) sharply dropped the catalyst activity after several hours on-stream [119].

Addition of hydrogen (3% to 6%) was found to be effective in hydrogasification of deposited coke but the presence of hydrogen does not favor the conversion of methane [120-125]. It's also reported that Mo zeolite catalyst was dramatically stabilized by co-addition of both 5.4% hydrogen and 1.8% water, compared with the single addition of either hydrogen or water [126, 127]. Li et al. [128, 129] studied coupling of OCM and MDA in a single-pass reactor. The resulted aromatics yield is 5% with methane conversion of 9.6% even at 72h on-stream, which is a significant improvement compared with the conventional MDA process. However, the amount of oxygen have to be precisely controlled,



otherwise there could be no yield of aromatics [120].

Many researches dedicated their work to optimize the reaction system in order to increase the aromatics selectivity and methane conversion. A large amount of experimental results showed that different pretreatment of the catalyst, different operation temperature, pressure and space velocity can affect the performance significantly [88, 130-132]. Some researchers also investigated the influence of adding other light hydrocarbon into the feed. Choudhary et al. [133] added gas olefin or C2-C4 alkane into MDA feed (catalyst is HGaAl-MFI) and got higher methane conversion (45%) and higher aromatics selectivity (92%) under low temperature (673-873K). These authors believe that the activation of methane could be realized by coupling hydrogen transfer reactions in a new reaction system.

### ➤ Application of membrane reactor

Both thermodynamic and kinetic constraints limit the performance of MDA process [38]. MDA performance can be enhanced by either higher reaction temperature or lower system pressure. Neither of these conditions is economically suitable for MDA industrialization. Development of catalysts can improve the kinetic constraint with shape-selective channels, but it cannot solve the thermodynamic problem. If hydrogen could be selectively removed, chemical equilibrium of MDA will be shifted towards the products side. This can be eventually achieved by a membrane reactor with a suitable hydrogen selective membrane, which possess the kinetic compatibility of hydrogen permeation rate and formation rate.

Iglesia et al. [134-136] applied inorganic membrane ( $\text{SrZr}_{0.95}\text{Y}_{0.05}\text{O}_3$ , 10-100 $\mu\text{m}$ ) to carry out MDA. Unfortunately the performance was not ideal because of the slow hydrogen removal rate (only 7%  $\text{H}_2$  were removed at 950 K). Even though, membrane reactor is still as a very promising way under investigation. Grandjean, Larachi and Ichikawa et al. [55, 136-141] used Pd or Pd/Ag alloy membrane reactor to carry out MDA and got some good outcome (product formation rates were enhanced 2-10 times by membrane reactor). However the high membrane cost and low thermal stability limited all these studies to low temperatures (max. 873K). While methane conversion is strongly affected by temperature, so methane conversion was very low under low temperature. Therefore, lowering the membrane cost and improving the thermal stability is the crucial problem of applying membrane reactor to MDA system.

Using a hydrogen selective membrane, the methane conversion could be increased, however, hydrogen removal resulted in accelerated coking. Thermodynamically favorable is the substitution of the non-oxidative MDA by the oxidative MDA ( $6\text{CH}_4 + \frac{9}{2}\text{O}_2 \leftrightarrow \text{C}_6\text{H}_6 + 9\text{H}_2\text{O}$ ), which has been demonstrated to be efficient in suppressing the coke formation in the presence of oxygen and steam additionally [142]. However, the presence of stoichiometric amount of oxygen inhibits the formation of molybdenum carbide, which is supposed to be the active catalyst component required for the formation of aromatic compounds [143]. As a result, side reactions (such as POM, OCM) can become predominant, which will decrease the target product selectivity. Caro et al. [61] recently applied an oxygen selective membrane (asymmetric  $\text{Ba}_{0.5}\text{Sr}_{0.5}\text{Co}_{0.8}\text{Fe}_{0.2}\text{O}_{3-\delta}$  perovskite membrane)

for the oxidative MDA to control oxygen dosing. The experimental results showed that membrane reactor improved methane conversion from 9% to 11% and benzene selectivity was raised from 10% to 30% in contrast to conventional co-feeding gaseous oxygen into a fixed-bed reactor.

### 1.2.4 Conclusions

After decades of research, the majority of scientists found some important features and reached some consensuses about MDA reaction:

- i. Mo/HZSM-5 is a bi-functional catalyst; Mo species as well as the acid sites in HZSM-5 have the same importance.  $\text{MoO}_3$  is reduced to  $\text{MoC}_2$  or  $\text{Mo}_x\text{C}_y$  by methane at first which is called induction period, followed by transformation of methane to  $\text{C}_2\text{H}_y$  ( $y < 4$ ) intermediates on the resulting active sites. At last,  $\text{C}_2\text{H}_y$  is oligomerized and cyclized to aromatics on the Brønsted acid sites of the zeolite.
- ii. Regarding to catalyst, the zeolites HZM-5 and MCM-22 contain molybdenum exhibit higher  $\text{CH}_4$  conversion and selectivity to benzene than other types of zeolites.
- iii. During the reaction process there is very easy to have heavily carbon deposit, which is the main reason of catalyst deactivate and an important factor to the development of practical application of the process.
- iv. The interactions of Mo species with Al in the frame of zeolite and also with acid site on the zeolite are determined factors of catalytic activation of the catalysts.
- v. The structure of the channel in the catalyst has a shape-selectivity and will affect the species of products.
- vi. The stability of Mo-based zeolite catalyst can be improved by co-feeding small amounts of other reactants (e.g. alkenes [133]), or by coupling MDA reaction with other reactions (e.g. Boudouard reaction and methane reforming [53, 54, 73, 116, 144, 145], Oxidative coupling of methane [43, 128])

## 1.3 Motivation and aim of this work

The understanding of a complex reaction system like the MDA is the prerequisite for rational improvements. This requires appropriate experimental investigations and realistic models. Temperature, feed fraction and residence time are important operating parameters in MDA system. The aim of this work is to provide experimental data applying a commonly used Mo/MCM-22 catalyst under various operating conditions. Furthermore, kinetic models of different complexity as well as their parameters should be provided and applied in fixed bed reactor (FBR) and a membrane reactor (MR) model. Experiments for a MR should be done. In particular, this involves the settlement of the following questions:

- How are the thermodynamic limits given by nature for the MDA? What can be done to overcome the thermodynamic limitations?

- 
- How do temperature, feed fraction and residence time influence separately and coupled the performance of MDA in FBR?
  - What kind of models can be applied to quantify the course of MDA in a FBR?
  - How do temperature, feed fraction and sweep gas ratio influence the performance of MDA in a MR?
  - What kind of models can be applied to simulate mass transfer of a carbon membrane and what are the values of the parameters within the models?
  - What is the expected MDA performance in this “carbon MR” and in other MRs?
  - How do these three parameters (temperature, feed fraction and residence time) influence the carbon deposit rate and catalyst deactivation rate?
  - Which models can be used to simulate the deactivation behavior?

The basics of the MDA reaction were just reviewed in Chapter 1, which also gives below the motivation and goal of this work. Chapter 2 will then describe a thermodynamic study, which outlines limitations of the MDA and motivates to explore potential solutions. In Chapter 3, synthesis and characterization of the Mo/MCM-22 catalyst are presented, which is used for all the experimental reaction studies in this work. Chapter 4 gives the experimental techniques in FBR and MR, which also includes the applied procedures. Experimental and simulated investigations in FBR are given in Chapter 5. It describes the detailed influence of temperature, feed fraction and residence time on total network and sub-network of MDA experimentally. Based on the experimental obtained results, 3 kinetic models with different complexity will be proposed. The parameters in these models are then estimated and simulation results are compared with experimental observations. Chapter 6 studies the mass transfer through a carbon membrane and the course of MDA in a MR using the characterized membrane exploiting results of the theoretical study of Chapter 3. MDA reactions, with the kinetics model described in Chapter 5, are simulated in the “carbon MR” and also in a “Pd MR”. Based on the results of these simulations, an ideal and extreme case is analyzed (“Ideal membrane”). For validation of the membrane mass transfer model, simulation and experiments are compared for the “carbon MR”. Finally catalyst deactivation is independently quantified in Chapter 7. A deactivation function is used to describe the catalyst deactivation rate.

Clearly, there are numerous other questions in MDA process engineering which are not addressed here. The important subject of catalyst activation simulation and concentration related deactivation functions for example are not discussed. Models that derive the elementary reaction steps or even elementary reaction rates from the micro-kinetics are not a topic of this work. The complex interaction between the reactant or intermedia and the reactive sites on the catalyst is not matter of concern.



## 2. Thermodynamic study

Thermodynamics tell us in which direction a reaction system will develop and how far it is from its equilibrium state. The state of a system characterized by properties such as temperature, pressure, density, composition, etc. is referred to the thermodynamic state of the system. These properties do not depend on the past history of the system nor on the means by which it has reached a given state. They depend only on the present conditions. The corresponding properties are known as state properties or functions.

An important concept in thermodynamics is the equilibrium state. General characteristics of an equilibrium state are that: the state does not vary with time; the system is uniform (i.e. there are no internal temperature, pressure, velocity, or concentration gradients) or is composed of subsystems each of which is uniform; all flows of heat, mass or work between the system and its surroundings are zero; and the net rate of all chemical reactions is zero [146]. Equilibrium requires that the rates of all possible reactions between the components of the system are zero. This state is often not reached in industrially applied chemical reactors.

### 2.1 Chemical reaction equilibrium

In this section the equilibrium composition of reacting systems is considered. The criterion for equilibrium in a closed system at constant temperature  $T$  and pressure  $P$  is that the Gibbs free energy of the system attains its minimum value.

#### 2.1.1 Equilibrium constants

The feasibility (i.e. direction and extent of the chemical change) and mechanism (i.e. study of rate and factors effecting it) are two important aspects, which should be distinguished clearly while considering a chemical reaction. Chemical reactions approach to an equilibrium, when the product and reactant concentrations do not change anymore. A reacting system is in chemical equilibrium if the reaction rates of the forward and backward reactions are equal. The basic quantity required to identify the equilibrium state is the Gibbs free enthalpy of reaction, which is also considered as a measure of the spontaneity of a reaction. In turn, this thermodynamic parameter measures a combination of changes in heat, work, and entropy that occur during a reaction. The change of this quantity becomes zero when the equilibrium is reached. The Gibbs free energy of reaction is defined by Gibbs Helmholtz equation as:

$$\Delta_r G^0 = \Delta_r H^0 - T\Delta_r S^0 \quad (2.1)$$

where  $\Delta_r H^0$  and  $\Delta_r S^0$  are the standard reaction enthalpy and entropy, respectively.

The equilibrium constant  $K_P$  does not depend on concentrations but depends on temperature. At the given temperature, if the equilibrium concentrations of products are higher than those of reactants and indicates high value of  $K_P$ , then reactants have reacted to a considerable extent. On the other hand, if  $K_P$  is small, there will be little of products at equilibrium. Thus, the extent of chemical reaction is determined by equilibrium constant and is not related in any simple way to the rate or velocity of reaction with which the chemical change takes place. The reaction between two reactants may occur to almost completion, but the time for even very small fraction of the molecules to react may be extremely long. The theory of equilibrium is treated on the basis of thermodynamics

considering only the initial and final states. Time or intermediate states have no concern. However, there is a close relationship between the theory of rates and the theory of equilibria, in spite of there being no general relation between equilibrium and rate of reaction. A good approximation of equilibrium can be regarded between the reactants and activated by ordinary equilibrium theory and probability of decomposition of activated complex and hence the rate of reaction can be known.

By rearranging eq. (2. 1) and using the relation in eq. (2. 17), one can obtain

$$\ln K_P = -\frac{\Delta_r H^0}{RT} + \frac{\Delta_r S^0}{R} \quad (2. 2)$$

Thus, if one measures  $K_P$  as a function of temperature, a plot of  $\ln K_P$  versus  $1/T$  should yield a straight line with a slope of  $-\Delta_r H^0/R$  and an intercept of  $\Delta_r S^0/R$  as shown in Figure 2. 1.

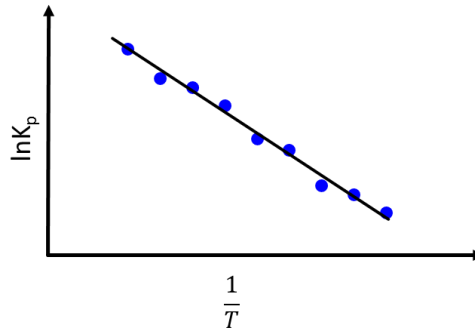


Figure 2. 1: Schematic illustration of  $\ln K_P$  versus  $1/T$  plot

This relationship can be expressed as a differential equation describing the temperature dependence of the equilibrium constant  $K_P$ :

$$\frac{d(\ln K_P)}{dT} = -\frac{\Delta_r H^0}{RT^2} \quad (2. 3)$$

Even though  $\Delta_r H^0$  is also a function of temperature, for small temperature differences,  $\Delta_r H^0$  can be assumed to be constant, and then

$$\ln K_P(T) = \ln K_P(T^0) - \frac{\Delta_r H^0}{R} \left( \frac{1}{T} - \frac{1}{T^0} \right) \quad (2. 4)$$

Eq. (2. 4) is known as the van't Hoff equation, and by performing a van't Hoff analysis, the reaction enthalpy and entropy can be extracted.

### 2.1.2 Single reactions

The free Gibbs enthalpy of reaction can be defined relating to the temperature, pressure and composition changes for a single phase system using the following equation:

$$dG_R = -S_R dT + V dP + \sum_{i=1}^{N_C} \mu_i dn_i \quad (2. 5)$$

Consider the case of a single chemical reaction occurring in a single phase in a closed system at constant temperature and pressure. The mole number of component  $i$  ( $n_i$ ) out of a number of  $N_C$  components, present at any time can be calculated from the initial mole number  $n_i^0$ , according to the following mass balance:

$$n_i = n_i^0 + \nu_i \xi \quad i=1, \dots, N_C \quad (2. 6)$$

where  $\xi$  denotes the reaction extent; and  $\nu_i$  is the stoichiometric coefficient for component  $i$  (positive for products and negative for reactants). Taking the differential of eq. (2. 6) yields the relation between a differential change in the number of moles of a reacting component and a differential change of the extent of reaction:

$$dn_i = \nu_i d\xi \quad i=1, \dots, N_C \quad (2. 7)$$

Using eq. (2. 6) and (2. 7) holds:

$$dG_R = -S_R dT + V dP + \sum_{i=1}^{N_C} \nu_i \mu_i d\xi \quad (2. 8)$$

Thus, for constant pressure and temperature the change of the free Gibbs enthalpy of reaction can be described as follows:

$$dG_R = \sum_{i=1}^{N_C} \nu_i \mu_i d\xi \quad (2. 9)$$

Or

$$\left(\frac{dG_R}{d\xi}\right)_{T,P} = \sum_{i=1}^{N_C} \nu_i \mu_i \quad (2. 10)$$

The basic quantity to identify the equilibrium state is the change of Gibbs free enthalpy of reaction  $G_R$  is zero. Hence it follows at the equilibrium state, that

$$\Delta G_R = dG|_{T,P} = \left(\frac{dG_R}{d\xi}\right)_{T,P} = 0 \quad (2. 11)$$

The slope of the Gibbs energy with respect to  $\xi$  represents the Gibbs energy of reaction. It is zero as the reaction system approaches the equilibrium composition at constant  $p$  and  $T$ . It can be used as the calculation basis for determining equilibria, especially for complex systems consisting of a large number of components and phases. Combination of eq. (2. 10) and eq. (2. 11), the condition of chemical reaction equilibrium can be written:

And the equilibrium can be characterized by:

$$\sum_{i=1}^{N_C} \nu_i \mu_i = 0 \quad (2. 12)$$

Eq. (2. 12) shows that for a chemical reaction at constant temperature  $T$  and pressure  $P$ , the net chemical potential of the reactants (weighted by the stoichiometric coefficients) must be equal to the net chemical potential of the products at equilibrium. This equilibrium equation is also a general formulation of the law of mass action. It follows from this that at equilibrium the chemical potential of a particular component is the same in all phases of the system. The following equation shows the relation of the chemical potential of a component in mixture to that of the component in its standard state. The chemical potential  $\mu_i$  is defined as follows:

$$\mu_i(T, p) = \mu_i^\Phi(T) + RT \ln \frac{p_i}{p^0} \quad i=1, \dots, N_C \quad (2. 13)$$

The superscript  $\Phi$  characterizes the standard pressure condition ( $p^0 = 1\text{bar}$ ), and  $p_i$  stands for the partial pressure of component  $i$ . With eq. (2. 12) holds:

$$\sum_{i=1}^{N_C} \nu_i \mu_i^\phi(T) + RT \sum_{i=1}^{N_C} \nu_i \ln \frac{p_i}{p^0} = 0 \quad (2.14)$$

The standard chemical potential  $\mu_i^0$  (which is characterized by temperature  $T^0$  and pressure  $P^0$ ) of component  $i$  corresponds to the standard Gibbs free energy of its formation  $\Delta G_{f,i}^0$ . Thus,

$$\sum_{i=1}^{N_C} \nu_i \mu_i^0 = \sum_{i=1}^{N_C} \nu_i \Delta G_{f,i}^0(T^0) \equiv \Delta_r G^0(T^0) \quad (2.15)$$

with  $\Delta G_r^0$  being the standard Gibbs free energy change of reaction. It is the different between the Gibbs free energies of formation of the products and reactants (weighted by their stoichiometric coefficients) when each is in its standard state as a pure substance at the system temperature and at a fixed pressure. Thus, the value of  $\Delta G_r^0$  is fixed for a given reaction once the temperature is established, and is independent of the equilibrium pressure and composition [147]. Extensive tabulations of values of the Gibbs free energies of formation for common compounds in the standard state,  $\Delta G_{f,i}^0$ , can be found in handbooks and in most thermodynamics texts. Combining eq. (2.14) and (2.15) gives:

$$\Delta_r G^0(T^0) + RT \sum_{i=1}^{N_C} \ln \left( \frac{p_i}{p^0} \right)^{\nu_i} = 0 \quad (2.16)$$

The following relationship between  $\Delta G_R^\phi = \sum_{i=1}^{N_C} \nu_i \mu_i^\phi(T)$  and the equilibrium constant  $K_P$  can be derived:

$$\Delta G_R^\phi = -RT \ln K_P \quad \text{with} \quad K_P(T) = \prod_{i=1}^{N_C} \left( \frac{p_i}{p^0} \right)^{\nu_i} \quad (\text{mass action law}) \quad (2.17)$$

$\Delta G_R^\phi$  is the temperature dependent Gibbs free reaction enthalpy for the standard pressure of 1 bar. By means of mass action law expression and eq. (2.17) the equilibrium constant  $K_P$  for ideal gases can be calculated as follows.

$$K_P(T) = \exp \left( -\frac{\Delta G_R^\phi}{RT} \right) = \prod_{i=1}^{N_C} \left( \frac{p_i}{p^0} \right)^{\nu_i} \quad (2.18)$$

Thus, in chemical equilibrium the ratio of product and reactant concentrations is a temperature dependent constant. The equilibrium constant  $K_P$  is valid for ideal gases.

### 2.1.3 Multiple reactions

For the case that there are several chemical reactions occurring in a single phase in a closed system at constant temperature and pressure, the mass balance of component  $i$  is:

$$n_i = n_i^0 + \sum_{j=1}^{N_R} \nu_{ij} \xi_j \quad i=1, \dots, N_C \quad (2.19)$$

where  $N_R$  is the number of independent reactions  $j$ ;  $\nu_{ij}$  is the stoichiometric coefficient of component  $i$  for reaction  $j$ ; and  $\xi_j$  is the extent of reaction  $j$ . since the stoichiometric coefficients



are constant, differentiation of eq. (2. 19) gives:

$$dn_i = \sum_{j=1}^{N_R} \nu_{ij} d\xi_j \quad i=1, \dots, N_C \quad (2. 20)$$

Substituting eq. (2. 20) into eq. (2. 5) yields:

$$dG = VdP - SdT + \sum_{i=1}^{N_C} \sum_{j=1}^{N_R} \nu_{ij} \mu_i d\xi_j \quad (2. 21)$$

At constant temperature and pressure, eq. (2. 21) becomes:

$$dG|_{T,P} = \sum_{i=1}^{N_C} \sum_{j=1}^{N_R} \nu_{ij} \mu_i d\xi_j \quad (2. 22)$$

The condition for chemical equilibrium in this multi-reaction system is that  $dG=0$  for all variations consistent with stoichiometry at constant temperature, pressure and total mass. For the present case, this implies:

$$\frac{\partial G}{\partial \xi_j} \Big|_{T,P,\xi_{k \neq j}} = 0 \quad j=1, \dots, N_R \quad (2. 23)$$

Thus

$$\frac{\partial G}{\partial \xi_j} \Big|_{T,P,\xi_{k \neq j}} = 0 = \sum_{i=1}^{N_C} \nu_{ij} \mu_i \quad j=1, \dots, N_R \quad (2. 24)$$

As discussed above for the case of a single reaction, a separate equilibrium constant is evaluated for each reaction in the present case, eq. (2. 18) then becomes:

$$K_{P,j} = \prod_{i=1}^{N_C} \left( \frac{P_i}{P^0} \right)^{\nu_{ij}} \quad j=1, \dots, N_R \quad (2. 25)$$

In the next section, a few aspects regarding the calculation of equilibrium compositions of systems containing an active multi-component mixture are presented.

### 2.1.4 Calculation of equilibrium compositions

The equilibrium state for multiple reactions occurring in a single phase system at constant temperature and pressure is identified by finding the state for which

$$\sum_{i=1}^{N_C} \nu_{ij} \mu_i = 0 \quad j=1, \dots, N_R \quad (2. 26)$$

subject to the mole balances

$$n_i = n_i^0 + \sum_{j=1}^{N_R} \nu_{ij} \xi_j \quad i=1, \dots, N_C \quad (2. 27)$$

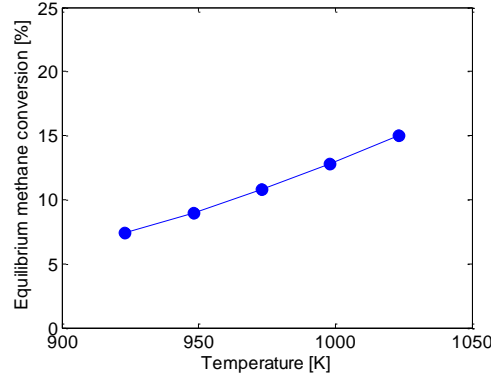


Figure 2. 2: Calculated equilibrium methane conversion at different temperatures [148]1

Recalling eq. (2. 25), one can write the equilibrium constant expressions for each reaction in the gas phase as follow:

$$K_{P,j}(T) = \prod_{i=1}^{N_C} \left(\frac{P_i}{P^0}\right)^{v_{ij}} \quad j=1, \dots, N_R \quad (2. 28)$$

The partial pressure of component  $i$   $P_i$  can be write in the form of molar fraction:

$$P_i = x_i * P_{tot} \quad i=1, \dots, N_C \quad (2. 29)$$

and  $x_i$  can be write in the form of molar number:

$$x_i = \frac{n_i}{n_{tot}} \quad i=1, \dots, N_C \quad (2. 30)$$

Eq. (2. 30) together with eq. (2. 27), (2. 28) and (2. 29) represents a nonlinear system of algebraic equations with the unknown  $\xi_j$ . The equilibrium composition of MDA can be calculated with  $\xi_j$  from eq. (2. 27) at the temperature range of normal used. Then the equilibrium methane conversion can be calculated from eq. (2. 31).

$$X_{CH_4} = \frac{n_{CH_4}^0 - n_{CH_4}}{n_{CH_4}^0} \times 100\% \quad (2. 31)$$

Figure 2. 2 shows the equilibrium methane conversion of MDA ( eq. (1. 10)) with the thermodynamic data from handbook [148] at different temperature with  $n_{CH_4}^0 = 1\text{mol}$ , which are calculated numerically by Matlab. At 650°C (923.15K) the equilibrium methane conversion is only 7.53%, and at 750°C (1023.15K) the equilibrium methane conversion is 15.59%.

Product selectivity and relative selectivity are also important properties in a multiple reaction system. Selectivity shows the percentage of converted reactant to the aimed product as shown in eq. (2. 32).

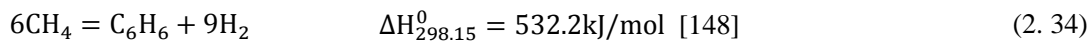
$$S_i = \frac{n_i/v_i}{(n_k^0 - n_k)/v_k} \times 100\% \quad i=C_6H_6, C_2H_4, C_2H_6, C_xH_y \text{ for MDA} \quad (2. 32)$$

The relative selectivity in some cases is also important to evaluate the reaction performance. It shows how many percentage of product  $i$  among all the aimed products. For the case of MDA, the relative selectivity can be calculated according to eq. (2. 33).

$$S_i^R = \frac{S_i}{\sum S_{aim}} = \frac{S_i}{S_{C_6H_6} + S_{C_2H_4} + S_{C_2H_6}} \times 100\% \quad i=C_6H_6, C_2H_4, C_2H_6 \quad (2. 33)$$

## 2.2 Equilibrium constant of MDA

Wider application of methane is hindered by its high chemical and thermodynamic stability. Consequently, computational analysis of the thermodynamic equilibrium limits in MDA reaction system, which can provide some essential theoretical guidelines for MDA study. Recent advances in equilibrium analysis permit the rapid calculation of the equilibrium composition of a complex reacting mixture [149]. There are two basic approaches for computing chemical equilibria to thermodynamically analysis the complex systems. In the first one, the equilibrium constants of chemical reactions and the mass balance equations are employed to determine equilibrium composition. The second approach is based on minimization of the Gibbs free energy with the mass balances of the elements as constraints. The first approach was used in this work for thermodynamic estimation. Several chemical reactions occurring simultaneously in MDA system, but the general overall reaction equation is (2. 34).



The standard molar reaction indicates that this reaction is a strongly endothermic reaction. According to eq. (2. 35) to (2. 37), the thermodynamic equilibrium constant for different temperature can be calculated.  $\Delta G_f$  is the formation Gibbs free energy of each component,  $\Delta G_R$  is the reaction Gibbs free energy,  $K_p^{\text{TD}}$  is the thermodynamic equilibrium constant, and A, B and C (values are shown in Table 2. 1) are the parameters of  $\Delta G_f$ .

$$\Delta G_f(T) = A + B \cdot T + C \cdot T^2 \quad (2. 35)$$

$$\Delta G_R(T) = \sum v_i \cdot \Delta G_{fi}(T) \quad (2. 36)$$

$$K_p(T) = \exp\left(\frac{-\Delta G_R(T)}{RT}\right) \quad (2. 37)$$

Table 2. 1: The Gibbs enthalpy parameters of components [148]

Comp.	A	B	C
CH <sub>4</sub>	-75.262	7.5925E-02	1.8700E-05
C <sub>6</sub> H <sub>6</sub>	81.512	1.5282E-01	2.6522E-05
H <sub>2</sub>	0	0	0

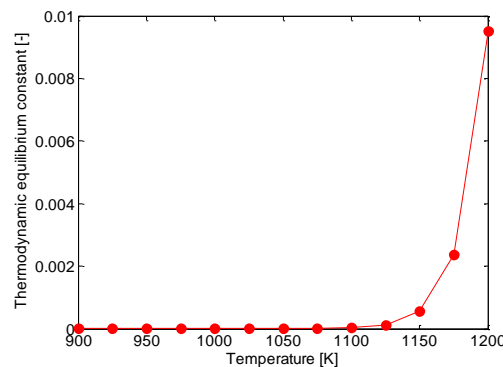


Figure 2. 3: Thermodynamic equilibrium constants over different temperatures

The calculated thermodynamic constants at different temperature are plotted in Figure 2. 3. As shown in the figure,  $K_p$  is  $5.67E-10$  at  $950K$ , which means the reaction rate constant of forward reaction (methane to benzene) is extremely small. Even though the temperature reaches  $1200K$ , equilibrium constant is still not large enough,  $K_p=9.5E-03$ . This shows that this reaction is limited by thermodynamics, which have to be overcome in order to improve the reaction performance.

Unfavorable thermodynamics restrict equilibrium aromatics yields in non-oxidative methane conversion reactions (12% benzene at  $973 K$  and  $1\text{bar CH}_4$  [33]). Thermodynamic estimates show that high temperatures and low  $H_2$  concentrations can increase aromatics yields, but they also lead to increasingly unsaturated products ( $C_xH_y$ ,  $x>2y$ ) and the formation of carbon [150]. The effects of  $H_2$  concentration are complicated, which must be described more in detail in order to design optimum practical processes. On one hand removal of hydrogen can break the thermodynamic equilibrium to increase the selectivity of benzene. On the other hand removal of hydrogen will aggravate carbon deposition as hydrogen contributes to reduction of deposit carbon. Thus, there could be a solution to use hydrogen-selective transport membranes to change the hydrogen concentration in the reaction system to optimize the performance of MDA system.

### 2.3 Effect of hydrogen removal in MDA

Continuous with-drawl of hydrogen from the reaction can shift, through the so-called drain-off effect, the equilibrium location of the dehydrogenation reactions, which is also optimistic for non-oxidative MDA reaction system. At low temperature, methane conversion is severely limited because of its endothermic and equilibrium controlled features. Therefore, temperatures in excess of  $973K$  are required to boost to meaningful levels methane conversion to aromatics within the traditional fixed bed catalytic reactors. Most of the experimental studies reported by the research community in the open literature were performed at  $973K$  or above. But as shown in Figure 2. 3, even at high temperature, the equilibrium constant of MDA is still very small, which implies that MDA is strongly limited by thermodynamics. However, if  $H_2$  is selectively removed, chemical equilibrium in MDA is shifted towards the products, as shown in Figure 2. 4. The left one of Figure 2. 4 (a) shows the hydrogen removal effects to equilibrium methane conversion at  $883K$  and  $0.5\text{MPa}$  and the author achieved that by Pd membrane with  $50-70\%$  of hydrogen removed [55]. The right one of Figure 2. 4 (b) is the calculated result of hydrogen removal effect at  $973K$  and  $0.1\text{MPa}$ , which is the normal used reaction condition.

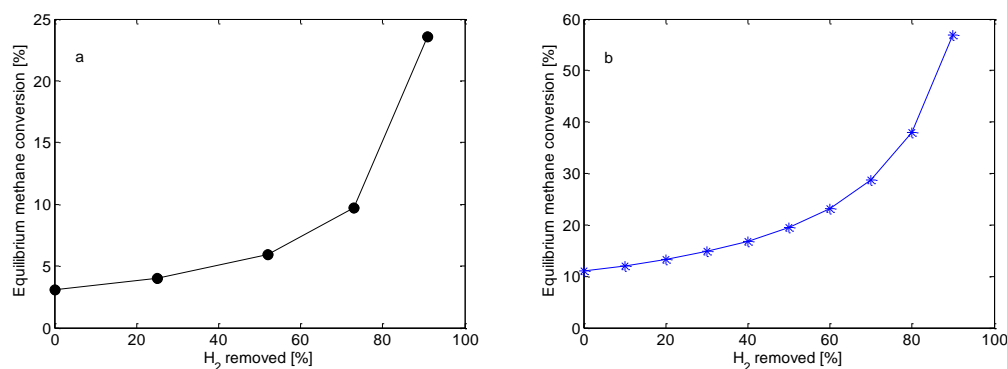


Figure 2. 4: Calculated equilibrium methane conversion as a function of  $H_2$  removal (%) during MDA, a: at  $883K$  and  $0.5\text{MPa}$  [55]; b: at  $973K$  and  $0.1\text{MPa}$  [148]

---

Compared with the case without H<sub>2</sub> removal (points H<sub>2</sub> removed = 0%), it is obvious that removing hydrogen from the reacting system can improve the equilibrium methane conversion. And this can be achieved with a suitable membrane that has a H<sub>2</sub> penetration rate comparable to the rate of its formation in the catalytic reaction.

Nonetheless, high temperature operation leads to serious deactivation of Mo based catalysts by coke deposition and or by Mo loss through volatilization. And with removing hydrogen, the coke deposition can be further more heavy since hydrogen is a reductive gas and has a protective effect to the catalyst against coke. Coke deposition is one important drawback to methane aromatization that is responsible for the decrease in conversion into useful products. Much of the current work has been targeting improved conversion into aromatics and reduction in coke formation.

## 2.4 Conclusions

In this chapter, the thermodynamics of MDA were studied. The results show that MDA is strongly limited by thermodynamics. Theoretically, the removal of hydrogen should be an option to increase methane equilibrium conversion. This indicates potential for membrane reactor application (see chapter 6). Practically, it should be kept in mind, that hydrogen removal could also accelerate catalyst deactivation (see chapter 7).



### 3. Synthesis and characterization of catalyst

The most widely used method for synthesis of Mo-zeolite catalysts is impregnation of various zeolites with ammonium heptamolybdate  $(\text{NH}_4)_6\text{Mo}_7\text{O}_{24}\cdot 4\text{H}_2\text{O}$  solution [104]. Impregnation method is to mix the soluble active component and the insoluble support components together at first, and then keep on stirring for a certain time, afterwards go through drying, calcinating and forming the loading type catalyst (Mo/MCM-22 in this thesis). The support of the catalyst is MCM-22 in this work. The synthesis and characterization of the catalyst is introduced in this chapter.

#### 3.1 Chemicals and equipment

In order to get more accurate and useful experimental data, the detailed chemicals, equipment and procedures (including operation steps and conditions) used in this work are presented here. The chemicals used for the zeolite synthesis are supplied by different chemical companies. Type and purity of the chemicals are given in Table 3. 1. Tap water was deionized and filtered by an ion exchange unit and a 2-stage reverse osmosis unit in Dalian University of Technology China.

Table 3. 1 Materials and Reagents [45]

Reagents	Specification	Supplier (China)
Sodium hydroxide (NaOH)	96 wt%	Tianjin Bodi Chemical Co., Ltd.
Sodium metaaluminate ( $\text{NaAlO}_2$ )	45 wt% $\text{Al}_2\text{O}_3$	Tianjin Chemical Reagents Institute
Ludox (Ludox,AS-40)	40 wt% $\text{SiO}_2$	Aldrich
Hexamethyleneimine (HMI)	99.9 wt%	Aldrich
Ammonium nitrate ( $\text{NH}_4\text{NO}_3$ )	Analytical purity	Shenyang New Reagent Plant
Ammonium molybdate ( $(\text{NH}_4)_6\text{Mo}_7\text{O}_{24}\cdot 4\text{H}_2\text{O}$ )	>99.0 wt%	Tianjin No. 4 Chemical Reagent Plant
Deionized water		Dalian University of Technology

#### 3.2 Catalyst synthesis

In cooperation with Prof. Yang in Dalian University of Technology China, the catalyst (Mo/MCM-22) used in the work was synthesized, analyzed and characterized in Dalian. Hydrothermal crystallization method in a high pressure autoclave is applied using hexamethyleneimine (HMI) as a structure direction agent. First, a certain amount of sodium metaaluminate ( $\text{NaAlO}_2$ ), sodium hydroxide (NaOH) and deionized water were mixed and vigorously agitated in a vessel until solid compounds are totally solved, afterwards HMI and ludox ( $\text{SiO}_2$ ) were dropped into the clear solution sequentially. The recipe of the precursor is  $1\text{Al}_2\text{O}_3: 30\text{SiO}_2: 1.8\text{Na}_2\text{O}: 900\text{H}_2\text{O}: 15\text{HMI}$  as reported by Chu [47]. After mixing for 24h with stirring and aging for 24h without stirring at room temperature, the resultant mixture was introduced into a stainless-steel autoclave with a Teflon bottle

lining, followed by heating to 423K for 7 days under the condition of rotating crystallizer. After crystallization, the autoclave need to quench in the cold water until room temperature. The powder-liquid mixed got from the autoclave need to be separated centrifugally and washed by deionized water until pH=8-9. The sample need to dry under 383K for 12h and calcinate at 823K for 5h. After washing, drying and calcining, the Na/MCM-22 was obtained. For ion exchanging, dissolve  $\text{NH}_4\text{NO}_3$  in water first and then put Na/MCM-22 into the solution with stirring at 363K with cold backflow, with the recipe: mass of Na/MCM-22: mass of  $\text{NH}_4\text{NO}_3$ : volume of deionized water=1g: 8g: 100ml. After 4h, stop the stirring and settle the mixture for 1h at 363K. And then discard the upper clear liquid and get the left liquid with plastic dropper. This is one loop of ion exchange. After three or four loops of ion exchange, the resulted powder need to dry at 373K for 12h and calcinate at 823K for 6h. The acid form of MCM-22 was obtained after successive exchanging with  $\text{NH}_4\text{NO}_3$  aqueous solution and calcinations. The last part is loading molybdenum onto the zeolite to compose the Mo-containing catalyst. The Mo/MCM-22 was prepared by incipient wetness impregnation of MCM-22 with an aqueous solution of ammonium molybdate ( $(\text{NH}_4)_6\text{Mo}_7\text{O}_{24}$ ) for 24h with stirring, and followed by drying 6h at 373K and calcining 6h at 823K.

### 3.3 Characterization of catalyst

Figure 3. 1 to Figure 3. 4 illustrate the scanning electron microscope (SEM) and transmission electron microscope (TEM) images of conventional and hierarchical aggregated (HA) MCM-22 without loading molybdenum, which is used as the catalyst support in this paper.

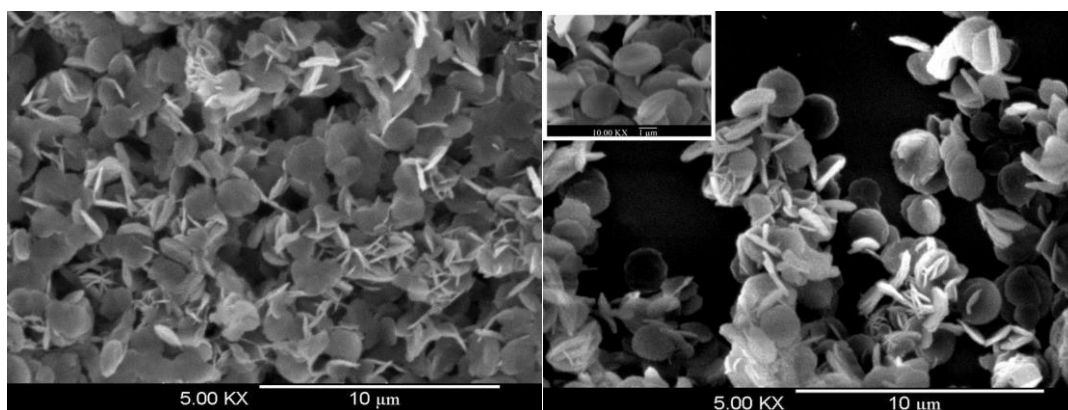


Figure 3. 1 SEM images of conventional zeolite MCM-22

From Figure 3. 1 we can see that, the conventional MCM-22 is uniform flaky crystal with the diameter around  $2\mu\text{m}$ , which is consisted with the report of Shu [151]. Figure 3. 2 shows an irregular aggregates morphology, which is assembled by the intergrowth of many small flaky crystals (which can be clearly seen from the zoom magnified picture). Figure 3. 3 is the TEM pictures of conventional MCM-22, which show the independent or isolated flaky crystals with high crystallinity. The TEM images (Figure 3. 4) proves the MCM-22-HA we used is hierarchical, which is consisted with SEM results. Moreover, lattice fringes can be observed in the high resolution TEM image of the selected part marked by the red circle, which reveals that this zeolite possesses high crystallinity as well. This MCM-22 hierarchical aggregates (MCM-22-HA) is used as the support of catalyst in this work.



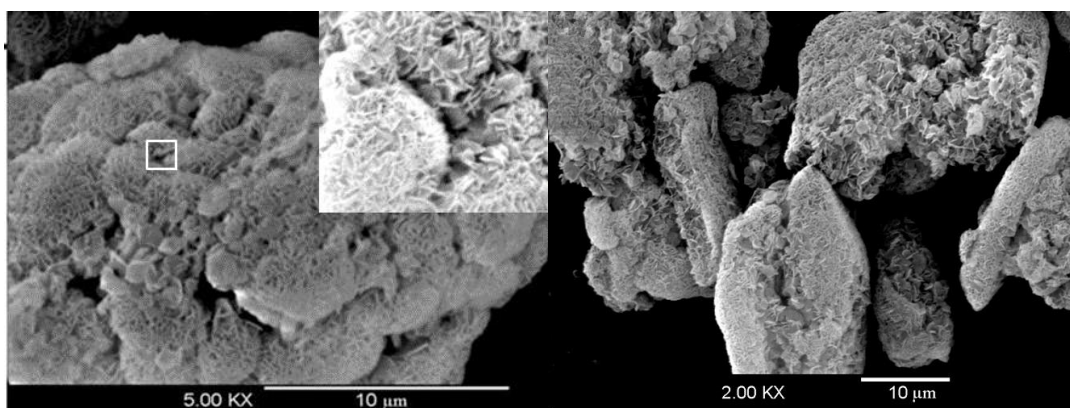


Figure 3. 2 SEM images of the zeolite MCM-22-HA

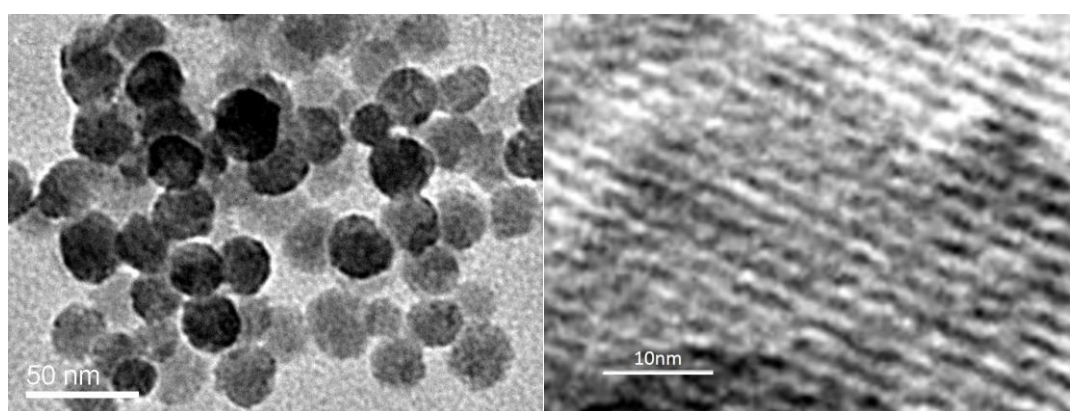


Figure 3. 3 TEM images of conventional zeolite MCM-22

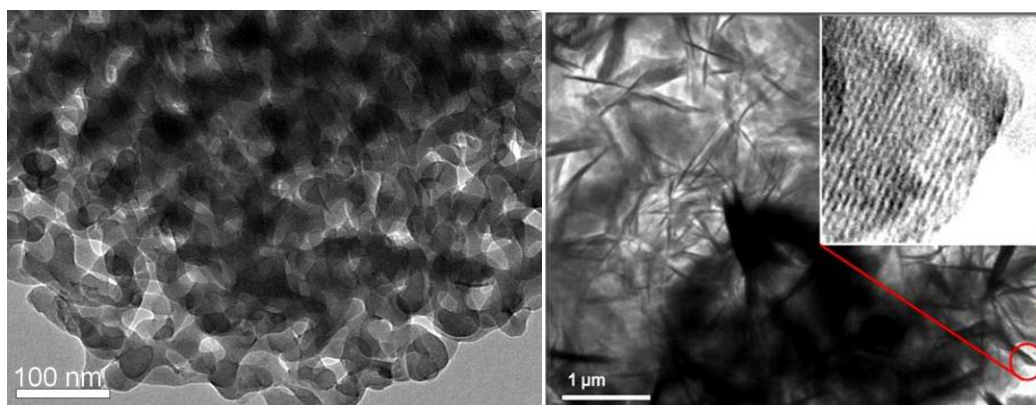


Figure 3. 4 TEM images of the zeolite MCM-22-HA

The powder X-ray diffraction (XRD) patterns for MCM-22-HA, the conventional MCM-22 and Mo/MCM-22-HA are shown in Figure 3. 5. The XRD patterns show the typical MCM-22 structure and high crystallinity of both MCM-22 zeolite. The 6 wt% Mo loaded MCM-22-HA also shows a typical MCM-22 structure pattern, which is completely corresponding to MCM-22-HA pattern, and no any other diffraction peaks (e.g.  $\text{MoO}_3$  crystal diffraction peak), which means there is no  $\text{MoO}_3$  crystal in the catalyst. However, because loading of molybdenum, the intensity of Mo/MCM-22-HA diffraction peaks are weaker than of MCM-22-HA. That means loading molybdenum slightly

decreases the crystallinity of zeolite, which implies that the loaded Mo are highly dispersed onto the zeolite support [151].

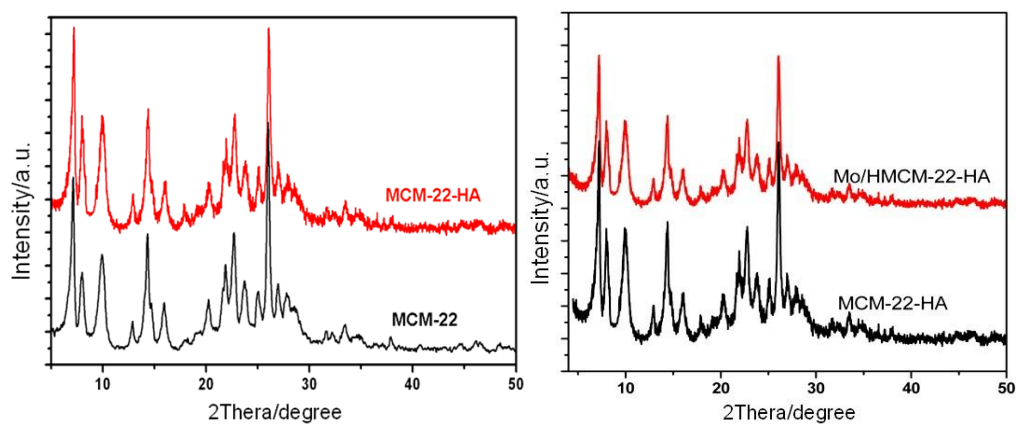


Figure 3. 5 Powder XRD patterns for MCM-22-HA, the conventional MCM-22 zeolites and Mo/MCM-22-HA catalyst

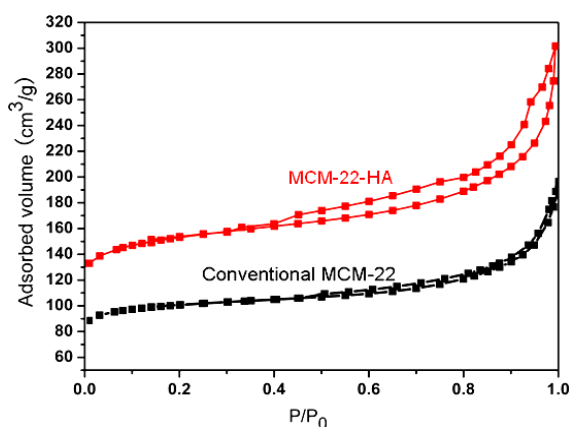


Figure 3. 6 Nitrogen adsorption and desorption isotherms for MCM-22-HA and the conventional MCM-22 zeolites

Table 3. 2 BET surface areas, pore volumes and average pore diameters of traditional MCM-22 and MCM-22-HA

Sample	Si/Al ratio	Surface Area (m <sup>2</sup> /g)	Micropore Area (m <sup>2</sup> /g)	Micropore Volume (cm <sup>3</sup> /g)	Average Pore Diameter (nm)*
MCM-22	15	448	356	0.16	1.93
MCM-22-HA	15	518	361	0.17	4
MCM-22 [152]	15	453	335	0.15	-

\* Calculated from BJH method based on the desorption branch of the isotherm

The N<sub>2</sub> adsorption-desorption isotherms for MCM-22-HA and conventional MCM-22 are plotted in Figure 3. 6. The isotherms of MCM-22-HA possess an obvious hysteresis loop in the relative pressure range of 0.4-1.0, which means there are mesopores in MCM-22-HA. The existence of mesopores in MCM-22-HA is also proved by the BJH analysis, which gives the average pore diameter of 4nm. The detailed BET analysis data are listed in Table 3. 2.

In order to better detailed compare the different catalyst supports, we keep the same Si/Al ratio and Mo loading, as well as synthesis procedure and conditions. Table 3. 3 listed the X-ray fluorescence (XRF) analytic results of these two kinds of catalysts. It's clear that the molybdenum loading and Si/Al ratio, which determine the acidity of the support, are similar. This implies that there is no big difference of the catalytic performance induced by different Mo loading.

Table 3. 3 Results of XRF analysis of the Mo/MCM-22 and Mo/MCM-22-HA catalysts

Catalysts	Mo (wt%)	SiO <sub>2</sub> (wt%)	Al <sub>2</sub> O <sub>3</sub> (wt%)	[SiO <sub>2</sub> /Al <sub>2</sub> O <sub>3</sub> ]
Mo/MCM-22	5.9	85.3	5.1	28.4
Mo/MCM-22-HA	6.2	84.9	5.03	28.7

Two kinds of supports with and without Mo loading are compared by NH<sub>3</sub>-TPD. From Figure 3. 7 we can see that, the NH<sub>3</sub>-TPD characterization of these two catalysts are similar with the literature result [151], which is a typical double-peak structure refers to a bi-functional feature. The low temperature peak (Peak L) is attribute to physical adsorbed NH<sub>3</sub> or NH<sub>3</sub> desorbed from Lewis acid sites; while the high temperature peak (Peak H) is the NH<sub>3</sub> desorption peak from the Brønsted acid sites in the zeolite channel, which is considered as the active aromatization center [151, 153]. As can be seen, before loading Mo species (curve No. 1 and No. 2), two zeolites have comparable acidity; after loading Mo species (curve No. 3 and No. 4), the acidity of both zeolites are lowered, especially the Brønsted acidity. This implies loaded Mo species associated with Brønsted acid sites and occupied some of the acid center by calcination. Comparatively speaking, the reduction in Peak H of Mo/MCM-22-HA is larger than of Mo/MCM-22, which means Mo species may associate with Brønsted acid sites better and more efficient, that is beneficial for benzene yield.

The results of NH<sub>3</sub>-TPD indicate that hierarchical MCM-22-HA is beneficial for the interaction of Mo species and Brønsted acid sites to generate more reactive sites. During induction period, faster carbonate species production rate of MCM-22-HA compared with conventional MCM-22 further proves that Mo/MCM-22-HA can generate more catalytic reactive sites, which results in higher methane conversion and benzene yield.

On the other hand, in contrast with conventional Mo/MCM-22, Mo/MCM-22-HA possess less excess Brønsted acid sites, which is also benefit for higher benzene selectivity. Actually, the major difference of these two catalyst is different structure (Table 3. 2). MCM-22-HA have bigger surface area and mesoporous structure, which tolerate naturally more carbon deposit and improve the stability of the catalyst [154-156].

Figure 3. 8 is the TEM image and energy dispersive X-ray (EDX) spectrum of calcined Mo/MCM-22-HA. From the TEM image we can observe that there are lots of small inter-grown flaky MCM-22 crystals and no MoO<sub>3</sub> particle. This means the active MoO<sub>3</sub> species doesn't aggregate obviously, which stands for no catalyst deactivation induced by active species aggregation. EDX spectrum was got by scanning along with the dotted line A in the TEM image. The results show that the content

of Mo species (around 6 wt%) and the Si/Al ratio of the zeolite (about 15) are very uniform. The results of EDX consist with the XRF results, which could be attributed to the superior diffusion properties of substances of hierarchical Mo/MCM-22-HA.

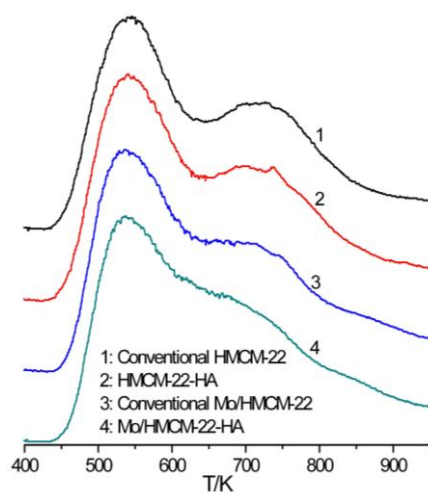


Figure 3. 7  $\text{NH}_3$ -TPD spectra of the MCM-22 (1), MCM-22-HA (2) zeolites, the calcined Mo/MCM-22 (3) and Mo/MCM-22-HA (4) catalysts

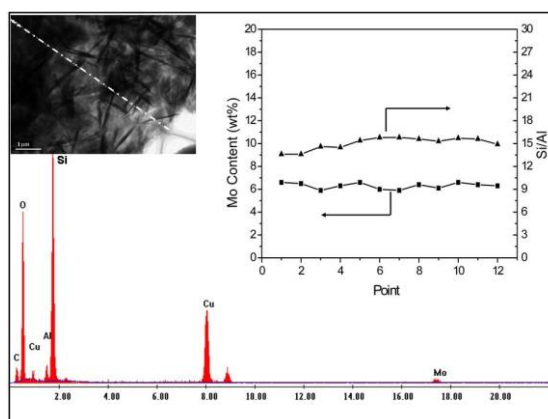


Figure 3. 8 TEM image and element distribution of the calcined Mo/MCM-22-HA catalyst

In order to investigate the catalytic performance and coke formation behavior of Mo/MCM-22-HA and Mo/MCM-22 (conventional), a group of testing experiments were carried out with the catalyst mass of 0.5g at 973K and space velocity of 1500ml/(g·h).

Table 3. 4 Catalytic performance of various catalysts (Mo-based MCM-22 catalysts) being subjected to MDA reaction for 24 h

Catalyst	Temperature (K)	$\text{CH}_4$ conversion (%)	$\text{C}_6\text{H}_6$ yield (%)
Mo/MCM-22 [151, 157]	973	9-14	6.1-8
Mo/MCM-22 [45]	973	8.5-12.5	4.7-6.8
Mo/MCM-22-HA [45]	973	10.5-20	8.7-9

Table 3. 4 listed out the catalytic performance of Mo/MCM-22 catalyst within 24h of literature results and ours. It's clearly that the Mo/MCM-22-HA possess the highest methane conversion and benzene yield. More important is that within the same reaction time, the variation of benzene yield refers to Mo/MCM-22-HA is very small, which implies a superior catalytic stability.

The conventional Mo/MCM-22 catalyst after 24h MDA reaction and hierarchical Mo/MCM-22-HA after 72h reaction are analyzed by derivative thermo-gravimeter (TG/DTG). As can be seen from Figure 3. 9, the weight loss of Mo/MCM-22-HA is more than Mo/MCM-22, which accounts for the mass of carbon deposit on Mo/MCM-22-HA is larger than on Mo/MCM-22.

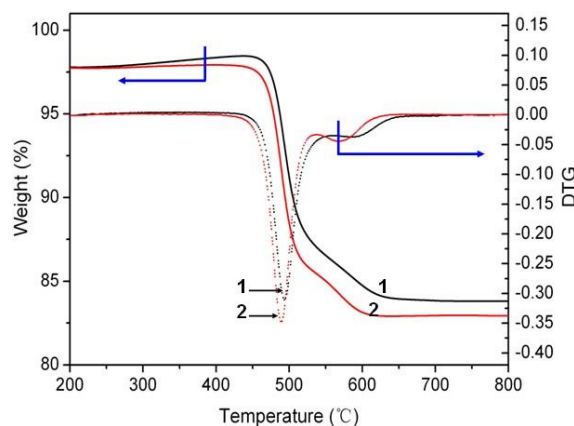


Figure 3. 9 The TG/DTG curves recorded from the coked conventional Mo/MCM-22 catalyst (1) and Mo/MCM-22-HA catalyst (2) being subjected to MDA reaction for 24h and 72h respectively

This result implies that under the same reaction condition, hierarchical Mo/MCM-22-HA got more carbon deposit but much longer lifetime (with methane conversion of 10% at 72h), compared with conventional Mo/MCM-22 (with methane conversion of 5.5% at 24h).

### 3.4 Conclusions

In this chapter, a simple procedure to synthesis Mo/MCM-22 catalyst for MDA is introduced. This procedure avoids cumbersome post-treatment. It was developed essentially in Dalian University of Technology by Chu [45] and will be exploited in this thesis. Compared to the conventional Mo/MCM-22, the Mo/MCM-22-HA was found in the literature to have higher activity and exceptional stability, attributed to the hierarchical structure.



## 4. Experimental techniques

In order to investigate the kinetics of MDA, experiments were performed to study influences of experimental conditions on MDA performance and to determine the model parameters. Experimental equipment used and experimental procedures are introduced in this chapter. In FBR, experiments with methane feed for whole reaction network kinetic investigation (see section 5.2.1) and with ethylene feed for sub-network kinetic investigation (see section 5.2.2) were carried out. In order to study the feasibility of MR, a carbon membrane was tested (see section 0) by gas permeation and used as the hydrogen selective membrane in MR. For validation, MDA reactions were also carried out in this MR under different operating conditions (see section 6.6).

### 4.1 Chemicals and materials

In order to get more accurate and useful experimental data, the detailed chemicals, equipment and procedures used in this work are presented in this chapter. The chemicals used for the reactions are supplied by different companies. Type and purity of the chemicals are given in Table 4. 1.

Table 4. 1: Chemicals for reactions

Reagent	Specification	Supplier (Germany)
CH <sub>4</sub> (gas, for FBR)	99.995%	Westfalen
N <sub>2</sub> (gas, for FBR)	99.999%	Air Liquide
C <sub>2</sub> H <sub>4</sub> (gas, for FBR)	99.9%	Air Liquide
He (gas, for FBR)	99.999%	Air Liquide
C <sub>6</sub> H <sub>6</sub> (gas, for GC)	5000ppm	Westfalen
H <sub>2</sub> (gas, for GC)	10%	Westfalen
Al <sub>2</sub> O <sub>3</sub> (powder, 100-200 mesh)	99%	Sigma-Alorich

The hydrogen selective carbon membrane used in this thesis was prepared by Fraunhofer institute for Keramische Technologien und Systeme (IKTS) Hermsdorf of a thin layer of carbon deposited on a porous alumina oxide support. The support was a multilayered porous material (synthesised by IKTS) of tubular geometry (OD=10mm, ID=7mm) with properties as shown in Table 4. 2. A 1.5cm length section of this membrane was covered by glass glaze via thermal treatment. The effective length of this membrane is 22cm.

Table 4. 2: Parameters of the two carbon membranes provided by IKTS institute

Layer name	Pore diameter	Porosity	Thickness [ μ m]	Tortuosity
Al <sub>2</sub> O <sub>3</sub> layer 1	3 μ m	0.33	1500	3.20
Al <sub>2</sub> O <sub>3</sub> layer 2	0.8 μ m	0.38	15	3.87
Al <sub>2</sub> O <sub>3</sub> layer 3	0.2 μ m	0.39	15	1.54
Al <sub>2</sub> O <sub>3</sub> layer 4	70nm	0.4	15	1.33
Carbon layer	5nm	0.45	1.2	8.20

This work used two carbon membrane (named as membrane No. 1 and membrane No. 2) which are synthesised from the same batch with the same condition and are supposed to have the same properties. Membrane No. 1 was damaged during gases testing, so membrane No. 2 was used to composite the MR for MDA reaction.

## 4.2 Configurations and equipment

The experiments in this thesis can be classified as 3 categories: MDA experiments in FBR for kinetics investigation, membrane permeation experiments for membrane characterization and MDA experiments in MR for verification. Configurations for each category is different and all of them will be introduced here.

### 4.2.1 Fixed bed reactor (FBR) runs

In this section, set-up configuration and equipment of MDA experiments in FBR for kinetics investigation will be introduced.

#### ➤ MDA process configuration

The set-up for FBR (OVGU, Magdeburg) of MDA used consists of several units: mass flow controls (MFC), reactor models and gas chromatography (GC). Fixed-bed reactor (FBR) is used as the reactor model in this part of experiment. The flow chat is shown as Figure 4. 1.

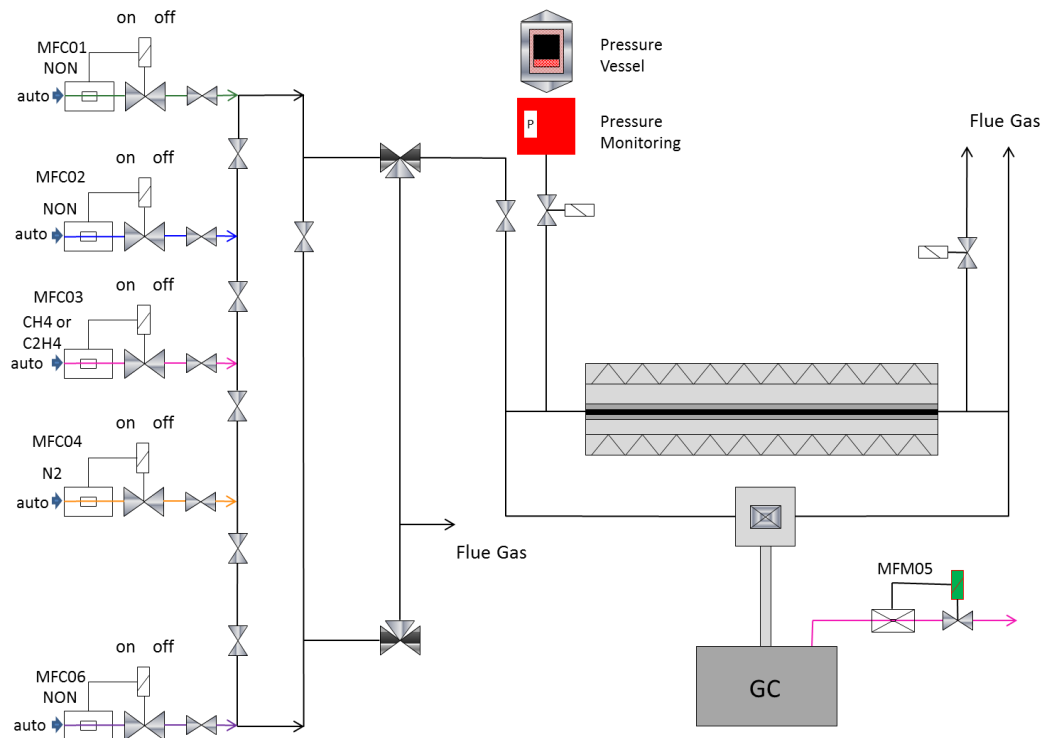


Figure 4. 1: Schematic diagram of experimental set-up

A process control system was implemented to run the unit automatically and recover all process data. Feed mixtures and flow configurations were realized by using MFCs (Bronkhorst®, EL-Flow



F-201CV). Gas samples were taken from different positions of the reactor (inlet and outlet) as described below by switching the multi-position valve. They transferred through a heated line to the sample calve of the GC-MSD to prevent condensation. All gas samples were analyzed with a GC-MSD/TCD system equipped with several columns and valves. The feed are nitrogen plus methane or ethylene entering from MFC04 and MFC03. Meanwhile, the flow rates of the feeds are controlled and monitored by the MFCs. Before the FBR, pressure is ensured to below 5 bar by pressure monitor to guarantee the safety of the experiment and the apparatus. After reaction products are analyzed by GC and recorded by computer connected with GC. A photo of the experimental set-up was taken from the lab as shown in Figure 4. 2.

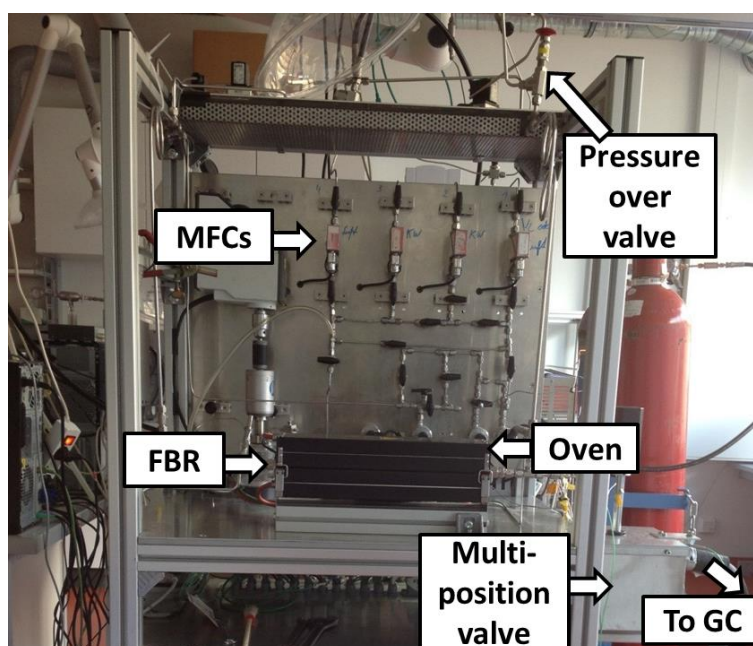


Figure 4. 2: Photograph of FBR set-up

➤ Fixed-bed reactor

The MDA reactions were carried out in a continuous flow quartz tubular fixed bed reactor with 6mm inner diameter and 250mm length at atmospheric pressure and different temperatures with a space velocity of 1500mL/(gh). The feed section composed of several gas lines and mass flow controllers, where reactant and nitrogen is premixed ( $\text{CH}_4$  and  $\text{C}_2\text{H}_4$  feed diluted by  $\text{N}_2$  with different percentages). 0.5g Mo/MCM-22 (fresh or activated) catalyst is settled in the middle tube of the reactor, and the other part of reactor is filled with inert aluminum oxide ( $\text{Al}_2\text{O}_3$ ) and settled with glass wool, as shown in Figure 4. 3. Moreover, two thermal couples are installed at the beginning of the reactor and in the middle of catalyst bed to perform the temperature monitoring and controlling with the range from  $650^\circ\text{C}$  to  $750^\circ\text{C}$  different from separated experiments.

For the experiments of methane feed, nitrogen was fed into the reaction system first and then gradually raising the temperature to the value we need. And keep on feeding with nitrogen only at the reaction temperature for 30 min to purge the other gases and components in the catalyst. Afterwards, feed is switched to the mixture of  $\text{N}_2+\text{CH}_4$  to start the reaction. Catalyst used for  $\text{C}_2\text{H}_4$  feed experiments need to be activated by methane, as explained in introduction part, at reaction temperature in advance to realize a reproducible resting scale of the catalyst.

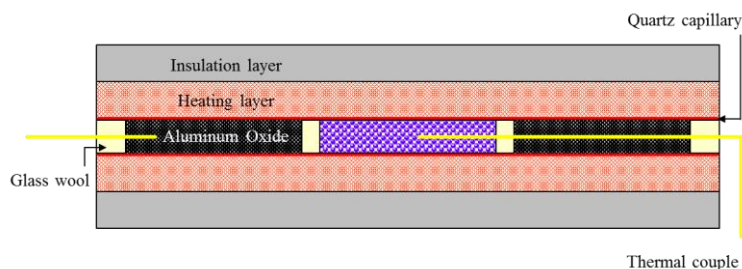


Figure 4. 3: Schematic diagram of inner structure of FBR (L=250mm)

➤ Analytical gas chromatography

GC (Agilent 6890, Version N.05.05) configuration diagram is shown in Figure 4. 4. To increase the clarity of the lines, auxiliary injector and detector gases were omitted. GC has two in parallel working analyzing channels. The first channel for separating permanent gases ( $N_2$ ) and light hydrocarbons ( $CH_4$ ,  $C_2H_4$ ,  $C_2H_6$ ,  $C_3H_6$ ,  $C_3H_8$ ,  $C_6H_6$ ) is applied over the 250  $\mu$ l gas sample loop controlled by valve 1. First, the injection of the less volatile components via a so-called "Volatile Interface" is about VI - Split ratio = 10:1. Then follows Poraplot Q column (J&W Scientific, column 2 in Figure 4. 4) which is used for separating the hydrocarbons and  $CO_2$  from the permanent gases and CO possibly formed. The separation of permanent gases and CO is realized by molecular sieve column (J&W Scientific, column 3 in Figure 4. 4), while hydrocarbons and  $CO_2$  are prohibited in the column by means of the valve 2. The compensation of the pressure drop of the column is accomplished by the built-in restrictor. At the end of this analysis channel is the thermal conductivity detector (TCD).

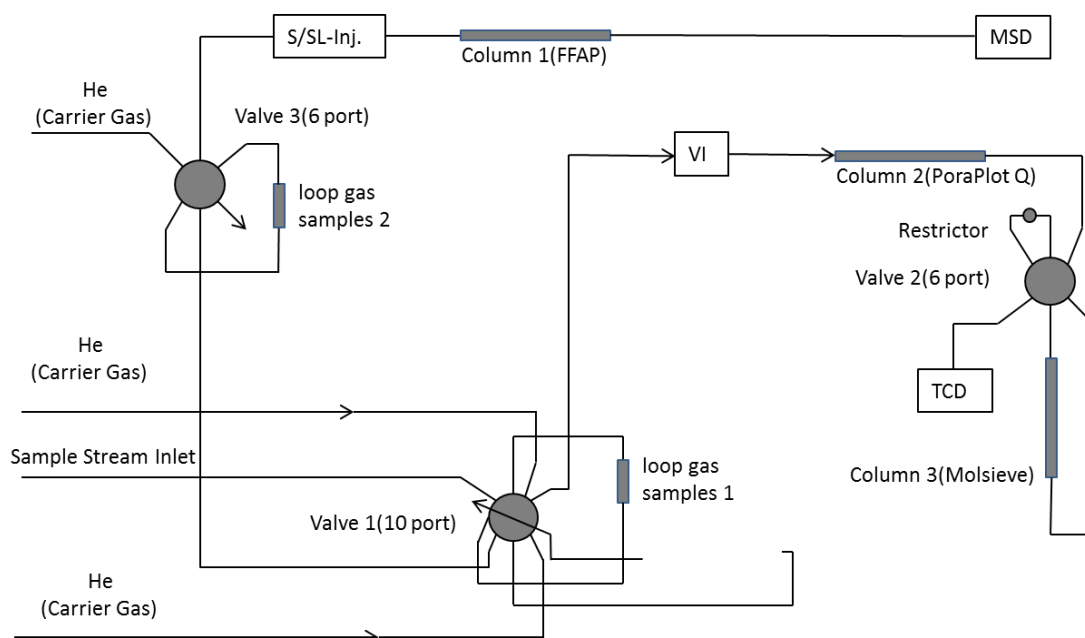


Figure 4. 4: GC configuration (from the GC instruction manual, Agilent Germany)

During the analysis, the permanent gases and CO will first be transported to the molecular sieve column, after valve 2 is switched on,  $CO_2$ , ethylene, ethane, propylene and propane can access into the TCD,

then valve 2 is again switched off so that  $O_2$ ,  $N_2$  and CO from the molecular sieve are eluted. This separation requires about 15 minutes (isothermal at 60-90 °C). The second analysis channel is supplied through the gas sample loop 2 and valve 3 via the split/splitless injector (adjusted split ratio 50:1) on FFAP column (J&W Scientific), where water and possibly formed oxygenate compounds (for example, aldehydes and carboxylic acids) may be separated and quantified from the rest of the reaction mixture. All other major components of the reaction gas will appear in one peak after detection with this column. The sequence of sampling and analysis has been automated in computer. The multi-position valve is switched to the position for the next analysis in order to ensure a sufficient rinsing time for the two gas samples loops during an analysis. Also, the peak integration for the quantification could be largely automated. Before each series of measurements the GC and the MSD were calibrated with mixtures of certified pre-mixed calibration gases and technical nitrogen. The corresponding concentration response curves signal form the basis can be used for the subsequent calculation of conversion and selectivity.

### 4.2.2 Characterizing mass transfer in carbon membranes

Before the MDA reaction, the hydrogen permeability of a fresh carbon membrane was measured by single, binary and ternary gas permeation tests under different temperatures and pressures. The mass transport quantification of single gas and gas mixtures through our carbon membrane at different temperatures have to be determined in advance.

The prediction of diffusion rates through porous media is difficult but of great practical importance. There are a number of different techniques available and capable of measuring diffusive transport. Graham [158] designed a tube with the rubber membrane on the top, which contains gas and is immersed in water bath. Gas in the tube diffuses out with a different rate from the one of surrounding gas diffuses in. The diffusion rate can be measure from the water level in the tube. Barrer [159] introduced the variable pressure method (also named time-lag method), which is based on the continuous monitoring the amount of penetrant diffusing through a membrane into close vessel. The pressure in the vessel is read as a function of time.

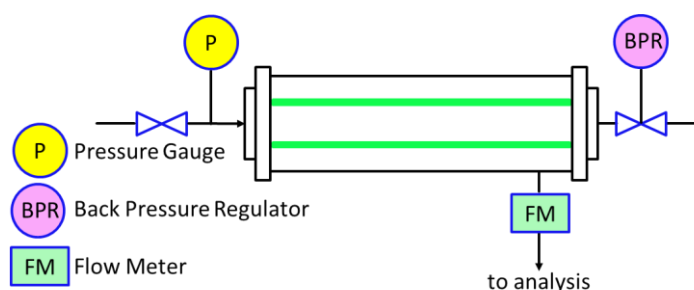


Figure 4. 5: Set-up to study single component permeation through tubular membranes [160]

The Wicke-Kallenbach cell [161] can be used for measuring diffusion coefficients in macroporous and mesoporous catalysts under steady state conditions. In this cell a catalyst pallet is mounted between two open chambers. In one chamber, component 1 is flowing through by convection and component 2 is flowing in another chamber. The molecules of one component (1 or 2) diffuse through the catalysts in opposite direction from another one (2 or 1). The flux through the pallet is

calculated by simply measuring the concentration of both components in the exit streams of two chambers.

Steady state permeation can be performed by maintaining the constant pressure difference across the membrane and measuring the permeate flow. Figure 4. 5 shows schematic set-up of typical steady state experiment for single gas permeation [160]. The feed pressure can be controlled by back pressure regulator, while the permeate pressure is usually atmospheric. For study of the pressure dependence of gas permeation, a lower permeate pressure can be imposed by vacuum pump or high pressure controlled with valve or pressure regulator. The permeate flow is analyzing usually by flow meter. For mixture permeability measurements, normally the well-known Wicke-Kallenbach cell is used.

Transient measurements can be operated with keeping one chamber open (sweep gas side), and the other one closed. The permeation through the membrane involves not only partial pressure but also total pressure changes. A modified Wicke-Kallenbach cell, based on that a temporary total pressure difference arises after input pressure change, has been used in this thesis under transient conditions. The data observed in the experiments were analyzed by the “Dusty Gas Model” for quantification of gas phase diffusion. The experimental schema and plan is described in the following sections.

#### 4.2.2.1 Single gas permeation

Figure 4. 6 show a sketch of the experimental setup of single gas permeation with a membrane reactor and its ancillary accessories, which consist of a membrane reactor (OD=16mm, ID=11mm) hosting the 220mm long carbon tubular membrane.

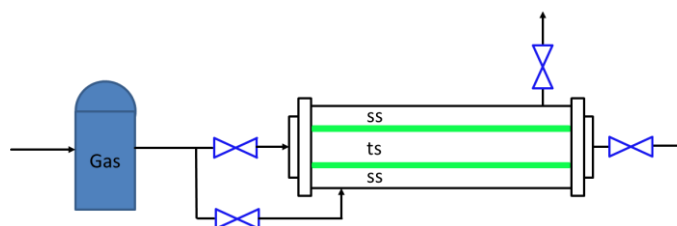


Figure 4. 6: Schematic diagram of experimental set-up for studying single gas permeation

The two gas chamber, tube side (ts) and shell side (ss), are separated by a tubular membrane (OD=10mm, ID=7mm). The sealing between compartments consisted of silicon rubber cooled by pressured air to avoid overheating. Temperature can be controlled by a heating jacket which can reach 800°C high temperature. The gases ( $N_2$ , He,  $H_2$  and  $CH_4$ ) are fed through the inlet of ts of the reactor and the outlet of ss is open to the atmosphere with closing ts outlet and ss inlet (or just the other way around); therefore the gas must diffuse through the membrane to be able to leave the reactor. The flow through the membrane was measured using a digital film flow meter. Heating jacket as well as thermal couples were used to heat/regulate the membrane cell temperature, which was measured using a thermocouple placed in the middle of the tube.

#### 4.2.2.2 Binary gas mixture permeation

One common method to validate that the chosen model and the calculated parameters can adequately model the behavior of the membrane is by carrying out binary gas mixture permeation or transient diffusion experiments with pairs of the gases in study. Figure 4. 7 shows the experimental set-up of binary gas mixture permeation experiments. The membrane reactor part is

exactly the same as in Figure 4. 6. The experiment consists in keeping the shell side of the reactor closed and flowing one gas through the tube side, which is open to the atmosphere, until the whole reactor is filled with this gas and in equilibrium. Next, the initial gas is quickly replaced by the second gas. At the inlet a four way valve was used to switch manually between different gases. This creates a transient increase or decrease in pressure in the ss of the reactor due to the diffusion of the gases. The inlet flow rates and gas compositions were measured and controlled by mass flow controllers. The absolute pressure difference between ts and ss were recorded with pressure gauge ( $p_{\max} = 2\text{bar}$ ).

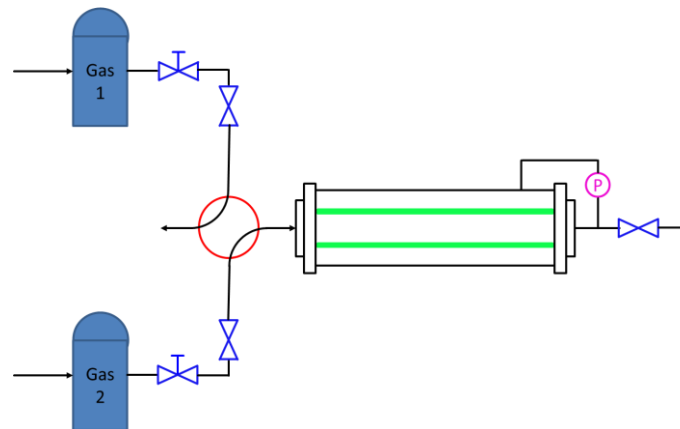


Figure 4. 7: Schematic diagram of experimental set-up for studying binary gas mixture permeation

#### 4.2.2.3 Ternary gas mixture permeation

The ternary gas mixture permeation (Figure 4. 8) is aimed to test the influence of different sweep gases to different gas mixtures. The gas mixtures were flowing through ts and the sweep gases were in ss, to experimentally simulate the reaction in membrane reactor also at different temperatures and atmospheric pressure. The exit gases from ts and ss of the reactor were analyzed by micro gas chromatograph (Agilent Technologies 490 Micro GC, described below).

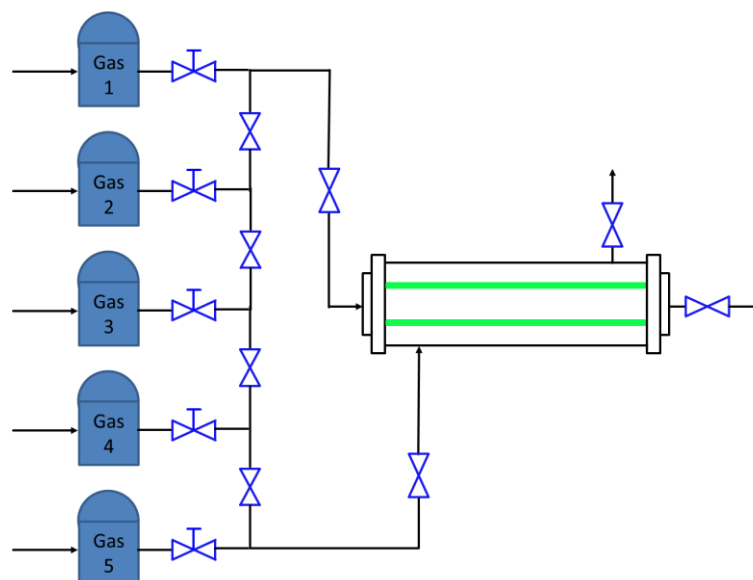


Figure 4. 8: Schematic diagram of experimental set-up for studying ternary gas mixture permeation

### 4.2.3 Coupling reaction and hydrogen removal in a membrane reactor (MR)

#### ➤ Process configuration

The set-up of membrane system (MPI, Magdeburg) used consists of several units: MFCs, membrane reactor (MR) and micro GC. The flow chart is shown as Figure 4. 9. A process control system was implemented to run the unit automatically and recover all process data. Feed mixtures and flow configurations were realized by using MFCs (Bronkhorst®, EL-Flow F-201CV). A heating jacket is placed onto the membrane reactor to control temperature. Gas samples were taken from different positions (inlet and outlet) and different chamber (ss and ts) of the reactor as described below by switching the values. They transferred through a cooled line to the sample entrance of the micro GC. All gas samples were analyzed with a Micro - TCD system equipped with two columns and several valves.

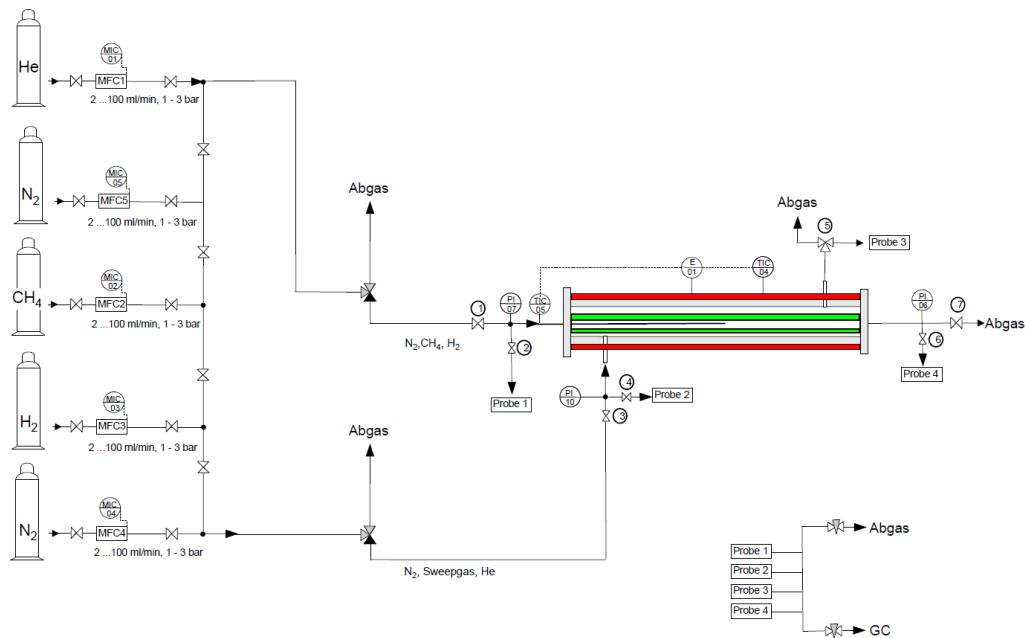


Figure 4. 9: Schematic illustration of experiment set-up in membrane system

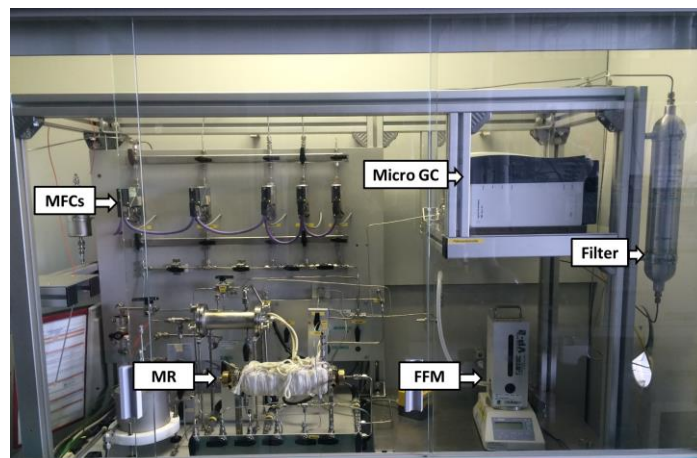


Figure 4. 10: Photograph of membrane system experimental set-up



Four pressure sensors are equipped at the inlet and outlet of ts and ss to monitor the pressure change as a function of time. For MDA reaction, the feed are nitrogen plus methane entering from MFC5 and MFC2. Meanwhile, the flow rates of the feeds are controlled and monitored by the MFCs. Before the MR, pressure is ensured to below 5 bar by pressure monitor to guarantee the safety of the experiment and the apparatus. After reaction products are analyzed by micro GC (Agilent 490) and recorded by computer connected with micro GC. A photo of the experimental set-up was taken from the lab as shown in Figure 4. 10. Figure 4. 11 is a sketch of the experimental setup of membrane reactor and its ancillary accessories, which gives more clear view of the configuration.

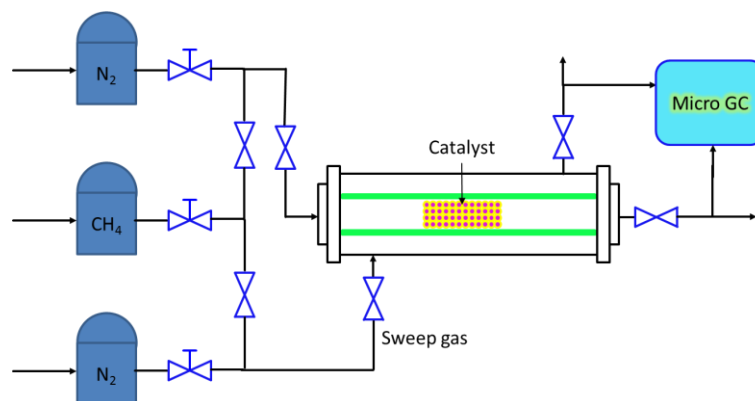


Figure 4. 11: Schematic diagram of experimental set-up for membrane reactor of MDA

#### ➤ Membrane reactor

The membrane reactor (OD=16mm, ID=11mm) was loaded with 0.5g (the same mass as used in FBR) of 5 wt% Mo/MCM-22 catalyst diluted by 20g  $Al_2O_3$  powder (as shown in Figure 4. 12 and Figure 4. 13) and was connected to gas feeding unit and analytical equipment.

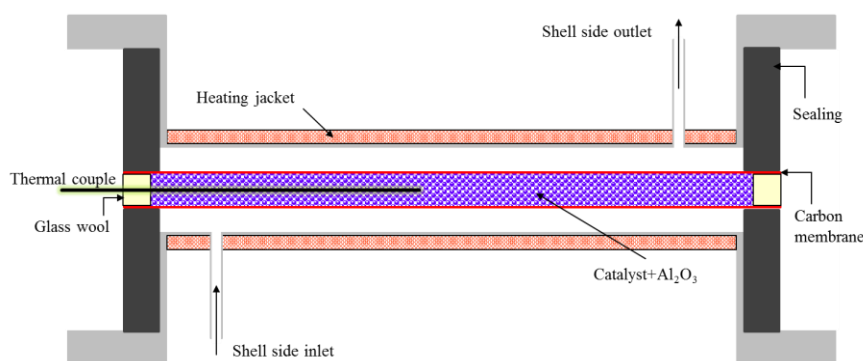


Figure 4. 12: Schematic illustration of applied membrane reactor

A thermal couple is placed in the middle of the catalyst bed to monitor the temperature inside. The rubber O-ring is used for sealing to separate gases between ts and ss at the inlet and outlet of the reactor. A heating jacket is covered onto the MR to control temperature. The temperature profile in MR is different from the one in FBR. In FBR, the catalyst (~5cm length) is packed in the middle of a quartz reactor (25cm length) placed in an oven. So the temperature in FBR can be considered as isothermal. But in MR, the catalyst/ $Al_2O_3$  mixture (~20cm length) is filled in the tube side of MR (25cm length) and heated by the heating jacket. There should be a temperature gradient along the

reactor length in MR. The reaction temperature (temperature in the middle of the catalyst bed) carried between 923 and 973K, was controlled by a sheathed thermocouple from the heating jacket. After catalyst pretreatment,  $\text{CH}_4/\text{N}_2$  mixture was fed to the reactor under atmospheric pressure. Hydrogen was swept by nitrogen from the ss. The sweep ratio varied from 1:1 to 1:3 to provide different driving force for withdrawal of hydrogen produced from the aromatization out of the reaction zone.

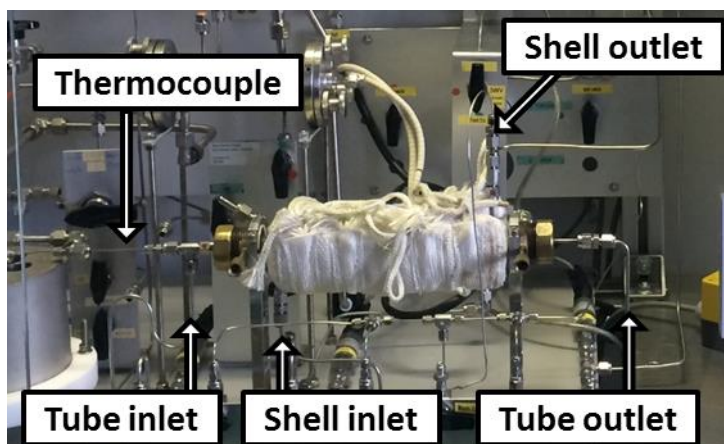


Figure 4. 13: Photograph of applied membrane reactor

➤ Micro gas chromatography

The gaseous reaction products were analyzed by a dual channel micro gas chromatograph (Agilent Technologies, 490 Micro GC) equipped with a backflush vent and a micro thermal conductivity detector (TCD) connected to a Molsive 5 column (10m length) and a  $\text{Al}_2\text{O}_3$  column (10m length) supplied by Agilent Technologies (as shown in Figure 4. 14).

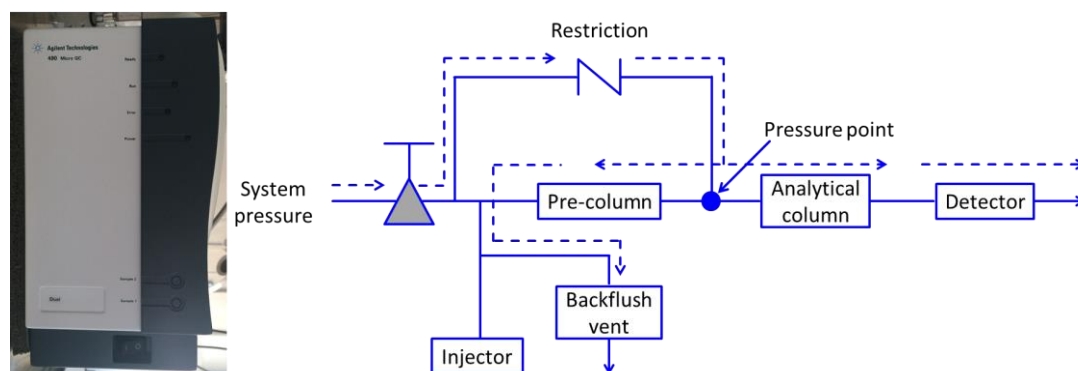


Figure 4. 14: Micro GC photograph and configuration (from the GC instruction manual, Agilent Germany)

Backflush vent is used to prevent later eluting compounds from reaching the analytical column and detector, which can keep the analytical column clean and reduced analysis time. A backflush system always consists with a pre-column and an analytical column. The two columns are coupled with a so-called pressure point, which makes it possible to invert the carrier gas flow direction through the pre-column at the “backflush time”. When all compounds which are to be quantified are transferred



to the analytical column, the backflush valve switches. Then the flow of the pre-column is inverted and all compounds left in the pre-column are back flushed to the vent. On the analytical column, the separation goes on.

All detected gaseous products in the reactor exit stream were analyzed: benzene, ethylene, ethane and hydrogen. Benzene was the aimed hydrocarbon product, whereas other aromatics (toluene, naphthalene) cannot be detected by this GC. As what have done in FBR, these aromatics and the coke on/in the catalyst were calculated as an average carbon deposit composition ( $C_xH_y$ ) from carbon and hydrogen balance calculation.

## 4.3 Procedures

### 4.3.1 Experimental procedures: FBR

In this thesis, both ethylene and methane are used as reactants in the MDA reaction based on Mo/MCM-22 zeolite catalyst. Nitrogen is also in the feed as dilution gas and internal standard for the subsequent calculation. Experiments with ethylene feed were carried out to study the ethylene sub-network separately.

Two kinds of experiments have been conducted, which are 1) step-wise temperature rising from 650°C to 750°C within 8.3 hours for feed with ethylene and 17.6 hours for feed with methane, and 2) control variable method (definition: turn multiple variable problem into many single variable problems; keep the other variables constant and only change one variable to investigate the influences of this variable) through temperature fixed with different inlet reactant concentration varying from 30% to 90% volume fraction and reactant concentration fixed with different temperature varying from 650°C to 750°C. Original data obtained from GC and MFC are product composition and volume flow rate of each reacting species, from which molar flow rate as well as selectivity of products and conversion of reactants can be calculated. With these calculated data, speculation of the behavior of the catalyst is possible.

#### 4.3.1.1 Methane feed

➤ Control variable method

For the experiments feed with methane, the inlet volume fraction of methane is fixed with 90%. There are 4 experiments with different reaction temperature shown in Table 4. 3. Just like experiments with feed with ethylene before, another series experiments also have been done for control variable method analysis (shown in Table 4. 4). Reaction temperature is fixed with changing inlet volume fraction of methane. The mass of catalyst used are still 0.5g.

Table 4. 3: Reaction conditions of methane experiments (feed 90%)

Reactant	Temperature (°C)	Volumetric fraction (%)	W/F (kg·s·m <sup>-3</sup> )
CH <sub>4</sub>	650	90.19	2.167E+03
	700	90.19	2.163E+03
	725	90.18	2.166E+03
	750	90.18	2.166E+03

Table 4. 4: Reaction conditions for fixed temperature experiments

Reactant	Temperature (°C)	Volumetric fraction (%)	W/F (kg·s·m <sup>-3</sup> )
CH <sub>4</sub>	700	30.02	2.163E+03
	700	50.06	2.162E+03
	700	70.11	2.163E+03
	700	90.19	2.163E+03

➤ Stepwise temperature rising

After two series experiments for control variable method analysis finished, another kind of experiment for stepwise temperature rising analysis (always the same catalyst, overlap of deactivation catalyst) is conducted (with the same operating error). The reaction temperature is rising for 650 °C to 750 °C step by step with W/F equals to 2160 kg·s·m<sup>-3</sup> and inlet methane volumetric fraction of 30%.

#### 4.3.1.2 Ethylene feed

As start point, feed with ethylene as instructive sub-network is discussed, because ethylene is considered as primary intermediate in MDA process and a sub-network of the MDA system can be studied for the further research of the MDA process. The catalyst should be activated by methane at the very beginning, because Molybdenum needs to react with methane forming Mo<sub>2</sub>C as reaction center. Several activation procedures were tested, and one of them is found with better performance and reproducible. The activation process sustains for about 1h with pure methane feed (5E-07 m<sup>3</sup>/s) including a temperature rising from 25 °C to 700 °C for 15 min, in order to reduce molybdenum oxide to molybdenum carbide. Afterwards the same volume flow of ethylene is introduced into the system for 20 min in order to blow methane from the line section. Thereafter, flow of nitrogen, temperature, process parameters and GC parameters were given into the automatic control. After activation, ethylene and nitrogen mixture in a certain composition is passed into the reactor. Two kinds of experiments have been conducted: 1) step-wise temperature rising and 2) control variable method. Conversion of ethylene as well as selectivity of methane, benzene and ethane will be calculated according to original data of volume flow rate of these species.

➤ Control variable method

For the experiments feed with ethylene, the inlet fraction of ethylene is fixed with 1%. There are 5 experiments (always use fresh catalyst) with different reaction temperature shown in Table 4. 5.

Table 4. 5: Reaction conditions of ethylene experiments (feed 1%)

Reactant	Temperature (°C)	Volumetric fraction (%)	W/F (kg·s·m <sup>-3</sup> )
C <sub>2</sub> H <sub>4</sub>	650	1.00	5.393E+01
	675	1.00	5.393E+01
	700	1.04	7.491E+01
	725	1.00	5.396E+01
	750	1.04	5.395E+01

The volumetric fraction of ethylene and the W/F are planned to be the same for these five experiments, and the mass of catalyst used are also 0.5g. But because of the error coming from the catalyst mass variation and the MFC controlling fluctuation, there is acceptable variation of volumetric fraction and W/F as shown in Table 4. 5.

Another series experiments also have been done for control variable method analysis (shown in Table 4. 6). Reaction temperature is fixed with changing inlet volume fraction of ethylene.

Table 4. 6: Reaction conditions for fixed temperature experiments

Reactant	Temperature (°C)	Volumetric fraction (%)	W/F (kg·s·m <sup>-3</sup> )
C <sub>2</sub> H <sub>4</sub>	700	0.50	5.964E+01
	700	1.00	7.491E+01
	700	2.49	1.497E+02
	700	27.31	4.541E+02

➤ Stepwise temperature rising

After two series experiments for control variable method analysis finished, another kind of experiment for stepwise temperature rising analysis (always the same catalyst, overlap of deactivation catalyst) is conducted (with the same operating error). The reaction temperature is rising for 650 °C to 750 °C step by step with W/F equals to 53.95 kg·s·m<sup>-3</sup> and inlet ethylene volumetric fraction of 1%.

### 4.3.2 Experimental procedures: characterizing mass transfer parameters

Since the carbon membrane used in this work is a porous membrane and is supposed to be hydrogen selective, various gas permeation tests have to be done to quantify the mass transfer of the carbon membrane. Three kinds of permeation tests were carried out, which are single gas, binary and ternary gas mixture permeation. The membrane No. 1 was damaged after some gas tests. So membrane No. 2 was used for MDA reaction in MR. Theoretically, membrane No. 1 and No. 2 should be exactly the same. However, according to the results of gas tests, they are totally different.

#### 4.3.2.1 Single gas permeation

In order to quantify the mass transfer of the carbon membrane, single gas permeation under different temperatures were tested. The operating process are shown in Figure 4. 6 and the experimental conditions are shown in Table 4. 7. For He, CH<sub>4</sub> and H<sub>2</sub>, single gas permeation were tested at 25 °C, 80 °C, 150 °C and 250 °C. For N<sub>2</sub>, only at 25 °C and 80 °C were tested. And no sweep gas is used.

Table 4. 7: Experiments for single gas permeation

Gas Name	25°C	80°C	150°C	250°C
He	✓	✓	✓	✓
CH <sub>4</sub>	✓	✓	✓	✓
H <sub>2</sub>	✓	✓	✓	✓
N <sub>2</sub>	✓	✓		

#### 4.3.2.2 Binary gas mixture permeation

The experimental procedure for binary gas mixture permeation is that 50ml/min or 100ml/min of sweep gas at atmospheric pressure and constant concentration flows from ts while the ss is closed. Before starting a binary gas mixture permeation test, the ts is completely equilibrated with gas 1. At the beginning of the test, gas 1 is replaced by gas 2 (gas 1 → gas 2) by switching the four way valve as shown in Figure 4. 7. The total pressure difference between closed annulus and the open inner chamber is recorded as a function of time. Whether the pressure difference will increase or decrease depends on the velocity of the gases which are passing the membrane. E.g. if gas 1 goes faster than gas 2, the pressure difference will increase and vice versa. The pressure differences are following a step change in the gas composition passing the membrane. Therefore, this arrangement of Wicke-Kallenbach cell is very convenient to measure binary gas mixture diffusion without using composition measuring unit. The experiments for binary gas mixture permeation are shown in Table 4. 8.

Table 4. 8: Experimental plan for binary gas mixture permeation

Gas Name	25°C	80°C	250°C
N <sub>2</sub> ↔ He	✓		
N <sub>2</sub> ↔ CH <sub>4</sub>	✓		
N <sub>2</sub> ↔ H <sub>2</sub>	✓	✓	✓
He ↔ CH <sub>4</sub>	✓		
CH <sub>4</sub> ↔ H <sub>2</sub>	✓		✓

#### 4.3.2.3 Ternary gas mixture permeation

Ternary gas mixture permeation is aimed to test the influence of different sweep gases to different gas mixtures. This means keeping ts and ss both open with feeding ts gas 1 or mixture 1 and feeding ss gas 2 or mixture 2. The volumetric flow at inlet and outlet are measured by FFM and the composition at inlet and outlet of ts and ss can be analyzed by GC. Then the impact of sweep gas can be tested under realistic condition. In this thesis, one case of ternary gas mixture permeation was tested. At 25°C under atmospheric pressure, mixture of He and N<sub>2</sub> (composition 50% He and 50% N<sub>2</sub>) was fed into ts and N<sub>2</sub> was flowed into ss as the sweep gas.

### 4.3.3 Experimental procedures: coupling reaction and hydrogen removal by MR

In order to test the availability of this carbon membrane to MDA system, 5 experiments (No. 1- No. 5) for coupling MDA reaction and hydrogen removal by carbon membrane No. 2 were carried out

with different operating conditions as shown in Table 4. 9. The catalyst used for MR tests is also Mo/MCM-22, the same as for FBR. But in MR, in order to keep the comparable W/F as in FBR ( $2160 \text{ kg}\cdot\text{s}\cdot\text{m}^{-3}$ ), 0.5g of Mo/MCM-22 was mixed with 20g  $\text{Al}_2\text{O}_3$  powder. The mixture of 0.5g Mo/MCM-22 and 20g  $\text{Al}_2\text{O}_3$  was packed in the tube side of the membrane as the catalyst bed. The effective  $\text{H}_2$  separation layer (carbon layer) is in the tube side of the membrane, which is very easy to be scarified during packing catalyst. For this reason, a glass fabric is used between carbon membrane layer and catalyst bed (as shown in Figure 7. 5) to prevent carbon layer from scarification. The whole system was fed with  $\text{N}_2$  from the very beginning with temperature increasing. Until the temperature is reached to and stable at the aim value ( $700^\circ\text{C}$  or  $650^\circ\text{C}$ ), switch from pure  $\text{N}_2$  to the mixture of  $\text{N}_2$  and  $\text{CH}_4$  with the aimed concentration (30% or 90%) and W/F ( $2160 \text{ kg}\cdot\text{s}\cdot\text{m}^{-3}$  or  $576 \text{ kg}\cdot\text{s}\cdot\text{m}^{-3}$ ).

Table 4. 9: Experimental plan for studying MDA in a MR

Number of run	Temperature ( $^\circ\text{C}$ )	$\text{CH}_4$ Volume fraction (%)	W/F ( $\text{kg}\cdot\text{s}\cdot\text{m}^{-3}$ )	$\text{N}_2$ Sweep ratio (-)
No. 1	700	30	2160	1
No. 2	700	30	2160	1
No. 3	700	90	576	1
No. 4	700	30	2160	3
No. 5	650	30	2160	1



## 5. Investigations in a fixed bed reactor (FBR)

### 5.1 General observation

A key result of the experimental observation made in the FBR is the fact, that there is no clear steady state could be achieved. Typical trends are illustrated in the left on Figure 5. 1 for 4 temperatures under standard conditions (inlet  $\text{CH}_4$  vol%=90%,  $W/F=2167\text{kgs/m}^3$ ). In the right of Figure 5. 1, this is illustrated schematically in agreement with others [91, 104, 105]. The process courses can be splitted into 3 parts: (I) induction state, (II) pseudo steady state and (III) deactivation state. The average value in (II) can be seen as a pseudo steady state. The performance corresponding to this pseudo steady state is calculated for each run and used for parameter estimation. The data from the deactivation state (III) are used to parameterize the deactivation function.

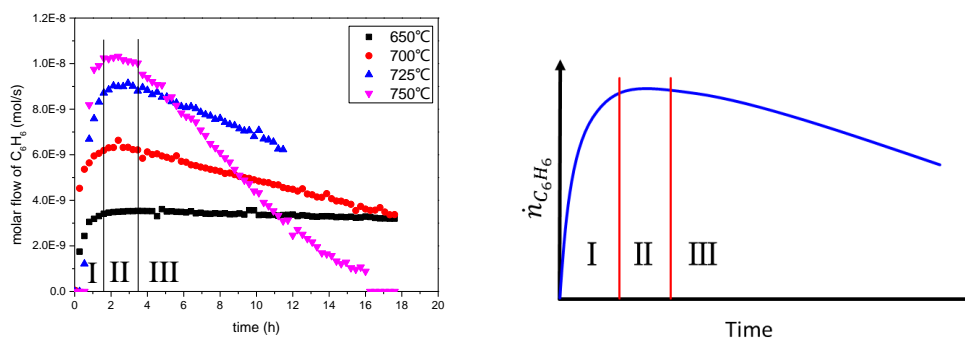


Figure 5. 1: Left: Benzene molar flow at different reaction temperatures (group A experiments, methane feed); Right: Schematic trend of three stages of produced benzene over reaction time following a proposal in the literature [91, 104, 105]

### 5.2 Kinetic measurements

The results of the investigations performed in the FBR are presented in this chapter. It contains results of an experimental study and simulations. The experimental results are given in Section 5.2, which contains the results for methane feed in Section 5.2.1 for the whole reaction network investigation and of ethylene feed in Section 5.2.2 for sub network investigation (see Figure 5. 2). The tendency of MDA performance as a function of different operating parameters are discussed. This is followed by a section about the kinetic investigation of MDA in FBR (Section 5.3). For that, 3 reaction networks with different complexity and 1 sub-network are proposed and parameters in these models are estimated. The investigation of the sub-network is to simplify of the whole network. The simulation results for these 3 reaction networks are finally compared with the experimental results.

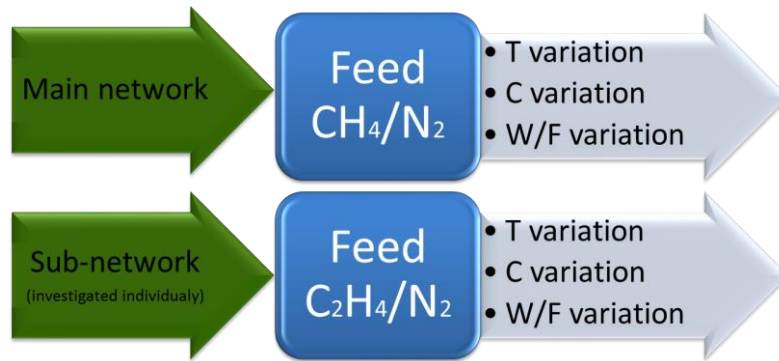


Figure 5. 2: Schematic diagram of experiments in FBR

As already introduced in Section 4.3.1, both methane and ethylene are used as reactants in MDA reaction kinetic investigations. Nitrogen is used to dilute the feed into different fractions and test the influence. Generally, the measurements can be separated into 2 kinds:

- 1). Single experiments for kinetic measurements: for each experiment fresh catalyst was introduced and used;
- 2). Step-wise measurements: one catalyst load was used with step-wise variable changing (e.g. temperature rising or W/F changing), which means catalyst is once loaded and longer used (thus, there is a superposition of deactivation);

Original data obtained from gas chromatograph analysis and mass flow controller are volume fractions in the product steam and volumetric flow rates, from which molar flow rates as well as selectivities of products and reactant conversion can be calculated.

### 5.2.1 Methane feed (total network)

According to the reaction rate laws introduced in section 5.3.1.2, the process parameters which are temperature and concentration dependent of the experiments should be varied accordingly. In addition, residence time is also a very important operating parameter for MDA process. It do not only influence the MDA performance at steady state, but also vary the carbon deposit behavior at deactivation state. Therefore temperature, concentration and W/F series in several experiments as well as individual dynamic experiments were carried out as shown in Table 5. 1.

Table 5. 1: Different process parameters studied with  $\text{CH}_4/\text{N}_2$  feed mixtures in experiments

W/F (kgs/m <sup>3</sup> )	$x_{\text{CH}_4}^0$ (%)	650 (°C)	675 (°C)	700 (°C)	725 (°C)	750 (°C)	SW
720	30	✓	✓	✓	✓	✓	✓
	90			✓			
1200	50			✓			
1680	70			✓			
	30	✓		✓		✓	✓
2160	50			✓			
	70			✓			
	90	✓	✓	✓	✓	✓	✓



Temperatures were varied from 650°C to 750°C with a step of 25°C, which are the common used reacting temperatures for MDA in FBR. Methane feed volumetric fraction and W/F were chosen 30%-90% and 720 kgs/m<sup>3</sup> -2160 kgs/m<sup>3</sup>. Three stepwise experiments were performed at the condition of low methane feed fraction (30%) with low W/F (720 kgs/m<sup>3</sup>), low methane feed fraction (30%) with high W/F (2160 kgs/m<sup>3</sup>) and high methane feed fraction (90%) with high W/F (2160 kgs/m<sup>3</sup>). Due to the subsequent reaction of ethylene to benzene and methane, ethylene feed investigations have been also carried out and will be presented later in Section 5.2.2.

In order to clearly discuss the experimental results, experiments are separated into different groups as shown in Figure 5. 3. The influence of temperature is discussed in group A, group C and group E (see section 5.2.1.1). Methane feed volumetric fraction influence is discussed in group B and group D. The influence of W/F is presented in group H, group F, group G and group I. And the performance of stepwise experiments are compared in group K and group J.

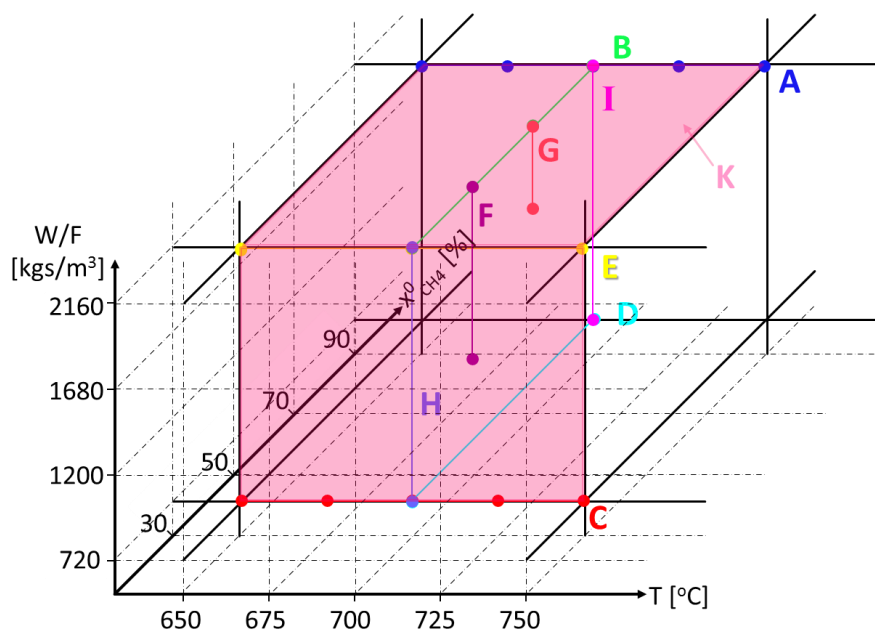


Figure 5. 3: Illustration of all groups (A,...,K) of experiments in FBR

### 5.2.1.1 Influence of temperature on MDA

Most reported MDA reaction temperature is 700°C, in addition to that, experiments to evaluate the influence of temperature on MDA performance were also carried out at temperatures of 650°C, 675°C, 725°C and 750°C. Three groups of experiments (group A, group C and group E) were selected to show the tendency of temperature influence. No pentene was observed, and no naphthalene was found in the GC analysis of the effluents.

- Group A:  $x_{0,CH_4} = 90\%$ ,  $\frac{W}{F} = 2160 \text{ kgs/m}^3$

Figure 5. 4 and Figure 5. 5 show the course of methane conversion, benzene, ethylene and ethane selectivity of Group A single experiments at different temperatures.

It is clear that methane conversions at all reaction temperatures decrease along with reaction time, and the higher the temperature, the sharper the decreasing curve. This is caused by the deactivation

of the catalyst due to the heavier and faster carbon deposit at higher temperature. The highest methane conversion stays at about 16.4% at temperature of 750°C. This phenomenon demonstrates that despite of the high reaction temperature leads to high conversion of methane, it also would result in higher and faster carbon deposit rate bringing catalyst deactivation.

The curves of benzene selectivity tendencies are generally the same with a sharply increase at the beginning and then following a relatively flat curve. There is no big difference between reaction temperature higher than 675°C. Reaction temperature of 650°C shows a relatively high benzene selectivity around 9% at steady state. On the whole, catalyst is quite stable at 700°C and is strong deactivated by CH<sub>4</sub> at 750°C, but has a relatively long induction period at 650°C.

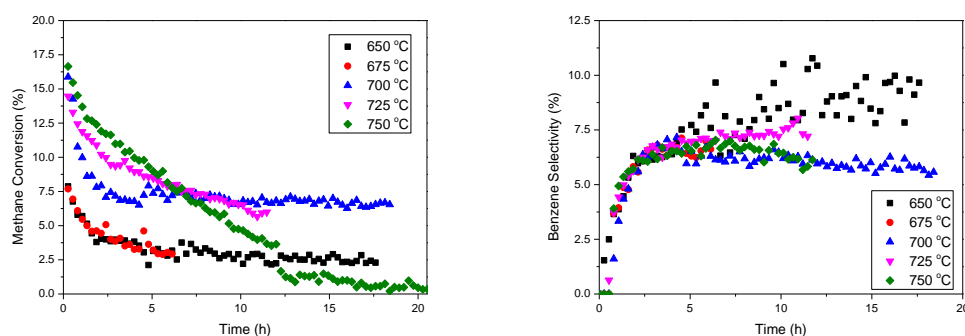


Figure 5. 4: Methane conversion and benzene selectivity according to different temperature with  $x_{0,CH_4}=90\%$ ,  $W/F=2160\text{kg}/\text{m}^3$  (group A)

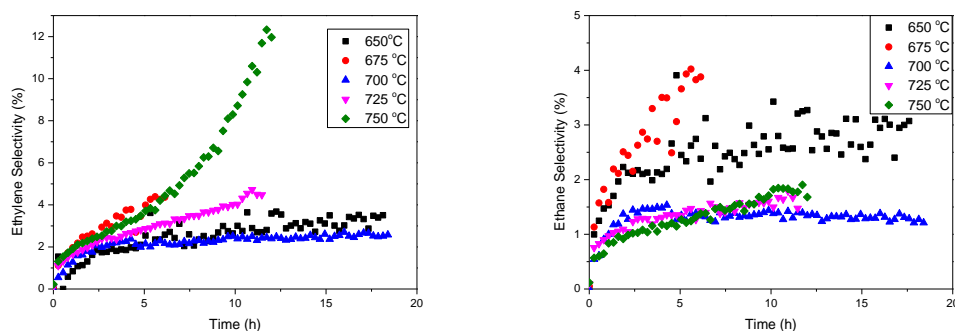


Figure 5. 5: Ethylene selectivity and ethane selectivity according to different temperature with  $x_{0,CH_4}=90\%$ ,  $W/F=2160\text{kg}/\text{m}^3$  (group A)

Ethylene selectivity slightly increase and then stay at a relatively stable range as experiment proceeds at all reaction temperatures except for 750°C. At temperature of 750°C, ethylene selectivity performs an eruption from the fourth hour until the end of the experiment. With higher reaction temperature, the ethylene selectivity increases. The degree of the increase is not so obvious until the temperature rises up to 750°C. Ethane can be detected immediately after the reaction started with all reaction temperatures. No obvious difference exists between reaction temperature 700°C, 725°C and 750°C. They all exhibit a relatively flat curve and are almost at the same range fluctuating from 6% to 8%. Ethane selectivity at 650°C is relatively higher and not very stable compared with other

reaction temperatures. The highest ethane selectivity is at 675 °C, at which ethane selectivity keeps on increasing from the very beginning until the end of reaction. As ethane is not the target product of MDA, it is not favorable to have high ethane selectivity. The performance of each experiment can be seen from Figure A. 1 to Figure A. 5 in appendix.

The stepwise temperature rising experiment without changing the catalyst of Group A was also done for the same reaction condition as shown in Figure 5. 6 and Figure 5. 7. At every temperature jump, the conversion and selectivity jump as well. The tendency is more clearly that, higher temperature results in higher methane conversion and faster catalyst deactivation, which is exactly the same tendency as single experiment results. After the induction period, benzene selectivity slightly decreases with increasing temperature, which also generally fits the results of single experiment results. But ethylene selectivity shows somehow different, that ethylene selectivity decreases from 650 °C to 700 °C, and stays the same as 725 °C then slightly increases at 750 °C, like parabolic tendency. The highest ethylene is at 650 °C, which is completely different from single experiment at 750 °C. The tendency of ethane selectivity is decreasing with increasing temperature, that is also different from single experiment results which has the highest ethane selectivity at 675 °C. The performance of Group A stepwise experiment can be also seen in Figure A. 23.

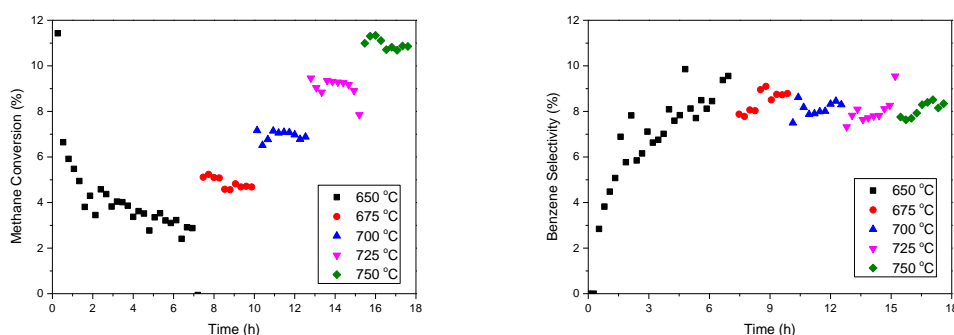


Figure 5. 6: Methane conversion and benzene selectivity according to stepwise temperature rising experiments with  $x_{0,CH_4}=90\%$ ,  $W/F=2160\text{kg}/\text{m}^3$  (group A)

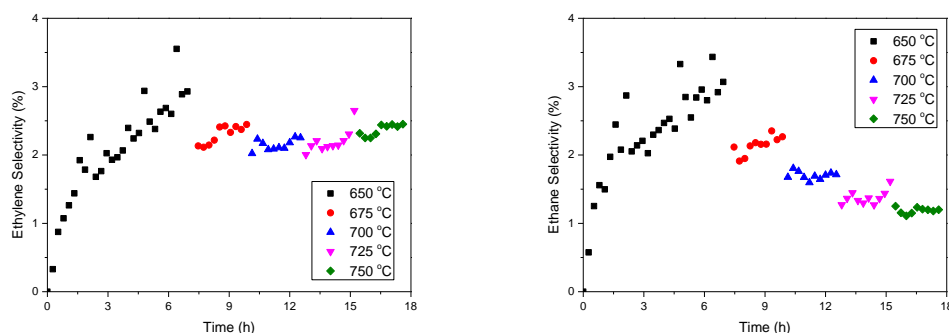


Figure 5. 7: Ethylene selectivity and ethane selectivity according to stepwise temperature rising experiments with  $x_{0,CH_4}=90\%$ ,  $W/F=2160\text{kg}/\text{m}^3$  (group A)

The average methane conversion and benzene selectivity at steady state of single and stepwise experiment are plotted in Figure 5. 8, from which absolute values can be easily compared. Methane

conversion of single experiment from 650 °C to 725 °C are lower than stepwise experiment but at 750 °C is higher than stepwise one, which is because of single experiment reduces the effect of deactivation and stepwise experiment is overlay of deactivation. Benzene selectivity at all temperature of single experiment is lower than stepwise experiment, but with different extent. But both are decreasing with rising temperature. This implies that catalyst with carbon deposit depresses benzene production.

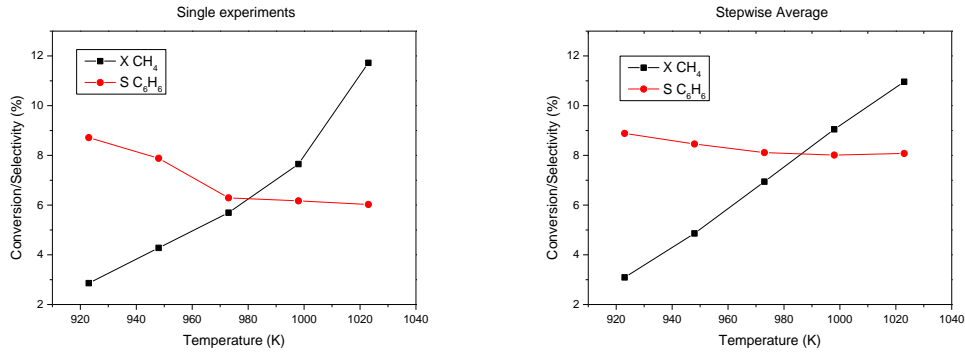


Figure 5. 8: Average methane conversion and benzene selectivity comparison of single and stepwise experiment with  $x_{0,CH_4}=90\%$ ,  $W/F=2160\text{kgs/m}^3$  (group A)

➤ Group C:  $x_{0,CH_4} = 30\%$ ,  $\frac{W}{F} = 720\text{kgs/m}^3$

Figure 5. 9 and Figure 5. 10 show the instant methane conversion, benzene, ethylene and ethane selectivity of Group C single experiments at different temperatures. Methane conversion tendency behaves exactly the same as in Group A single experiment part. The curves of benzene selectivity tendencies are generally the same with a sharply increase at the beginning and then following a relatively flat curve for 650 °C, 675 °C and 700 °C. There is no big difference between reaction temperature lower than 700 °C. Reaction temperature of 725 °C shows a slightly decreasing trend along time and 750 °C shows the same but more sharply decreasing.

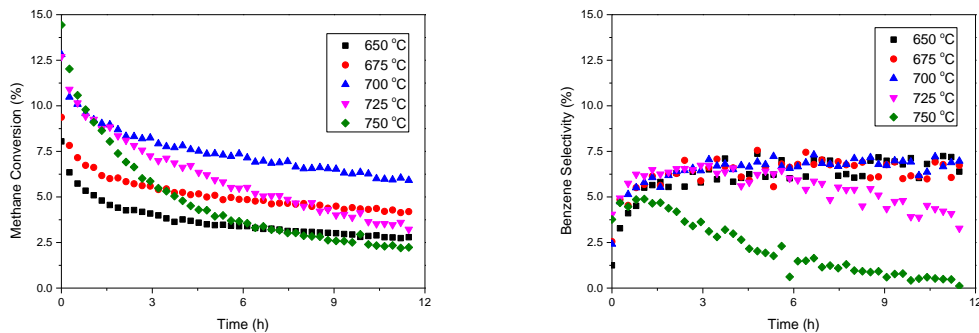


Figure 5. 9: Methane conversion and benzene selectivity according to different temperature with  $x_{0,CH_4}=30\%$ ,  $W/F=720\text{kgs/m}^3$  (group C)

Ethylene selectivity slightly or strongly increase along with reaction time for all the reaction temperature. The curves for 650 °C, 675 °C and 700 °C are more or less overlapped. The increasing slope of 725 °C is larger than the overlapped curves and 750 °C is the largest one. The experimental

dots of ethane selectivity is somehow a puzzle, the only clearly clue is that the dots for 650 °C stays at the top from a statistic point of view. When methane conversion is low, the concentration of ethane in the system is very low. In this condition, significant analysis via gas chromatography is very difficult. Figure 5. 10 right implies that significant failure exists for the ethane selectivity. The performance of each experiment can be seen in Figure A. 14, Figure A. 15, Figure A. 10, Figure A. 20 and Figure A. 18 in appendix.

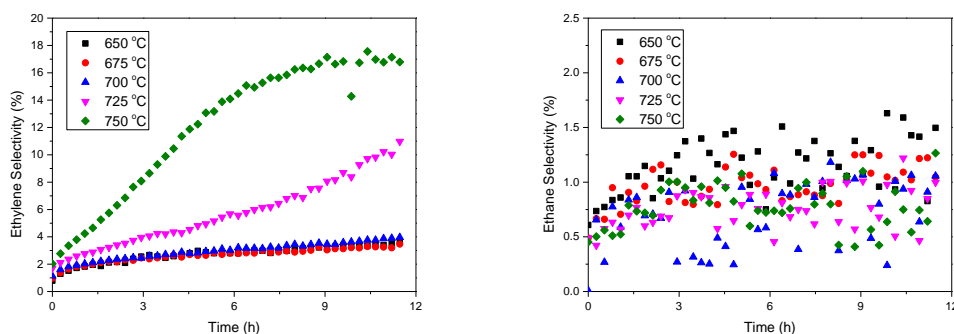


Figure 5. 10: Ethylene selectivity and ethane selectivity according to different temperature with  $x_{0,CH_4}=30\%$ ,  $W/F=720\text{kgs/m}^3$  (group C)

The stepwise temperature rising experiment results of Group C for the same reaction condition are shown in Figure 5. 11 and Figure 5. 12. The tendency of methane conversion is exactly the same as single experiment results, which is that higher temperature results in higher methane conversion and faster catalyst deactivation. Benzene selectivity slightly increase with increasing temperature statistically and 750 °C possess the highest benzene selectivity, which is completely different from the results of single experiment that 750 °C has the lowest one. While ethylene selectivity decreases from 650 °C to 700 °C, and then slightly increases from 725 °C to 750 °C, which is similar as results from Group A stepwise result (in Figure 5. 7). In each temperature step, ethylene selectivity increases along with reaction time, which is the same as single experiment results. The tendency of ethane selectivity is statistically decrease with increasing temperature, which is similar as the single experiment results as shown in Figure 5. 10. The performance of Group C stepwise experiment can be also seen in Figure A. 22.

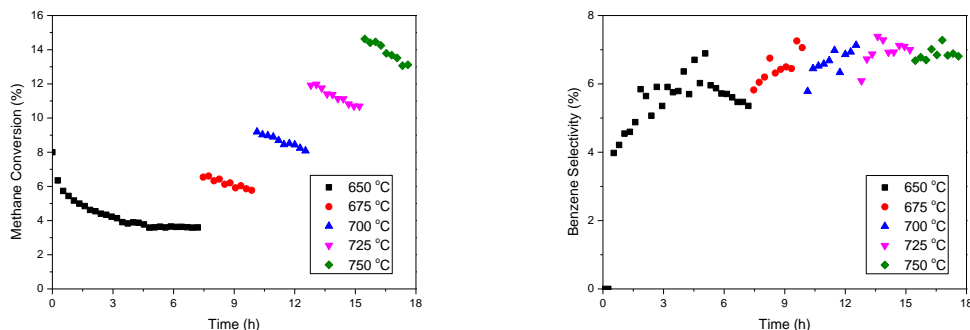


Figure 5. 11: Methane conversion and benzene selectivity according to stepwise temperature rising experiments with  $x_{0,CH_4}=30\%$ ,  $W/F=720\text{kgs/m}^3$  (group C)

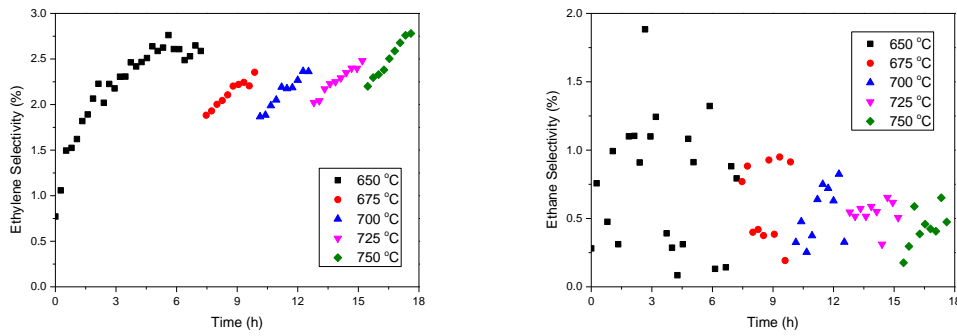


Figure 5. 12: Ethylene selectivity and ethane selectivity according to stepwise temperature rising experiments with  $x_{0,CH_4}=30\%$ ,  $W/F=720\text{kgs/m}^3$  (group C)

The average methane conversion and benzene selectivity at steady state of single and stepwise experiment are plotted in Figure 5. 13, from which absolute values can be easily compared as Group C. Methane conversion of single experiment from 650 °C to 750 °C are lower than stepwise experiment and the increasing slope is also lower. Benzene selectivity at all temperature of single experiment is lower than stepwise experiment especially at 750 °C. The deviation is significantly the biggest operation error of single experiments than stepwise ones.

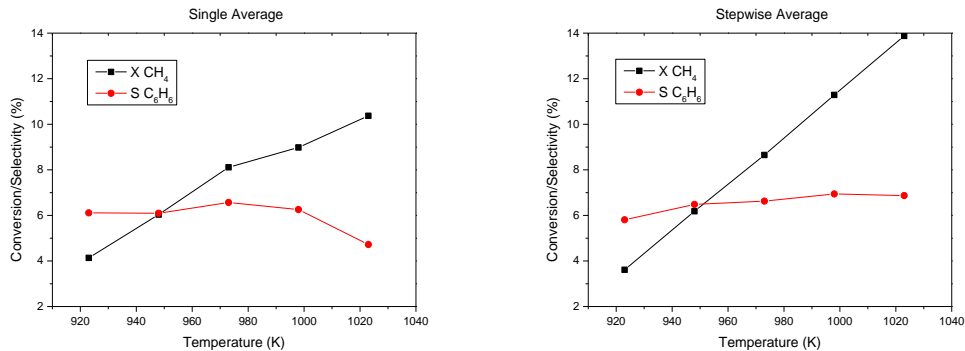


Figure 5. 13: Average methane conversion and benzene selectivity comparison of single and stepwise experiment with  $x_{0,CH_4}=30\%$ ,  $W/F=720\text{kgs/m}^3$  (group C)

➤ Group E:  $x_{0,CH_4} = 30\%$ ,  $\frac{W}{F} = 2160\text{kgs/m}^3$

Figure 5. 14 and Figure 5. 15 show the instant methane conversion, benzene, ethylene and ethane selectivity of Group E single experiments at different temperatures. Methane conversion behaves the same as in Group A and Group C single experiment part, which are methane conversion increases with increasing temperature but faster catalyst deactivation and methane conversion decreases along with on-stream time. All the benzene selectivity sharply increase during induction period. Within our reaction time (18h), benzene selectivity of 650 °C continuously gradually increases and have not reach the steady state; 700 °C curve stays around 6% after induction period, which means until 18h the catalyst can steady selectively produce benzene; while 750 °C shows a parabolic curve, which strongly decrease after 5h.

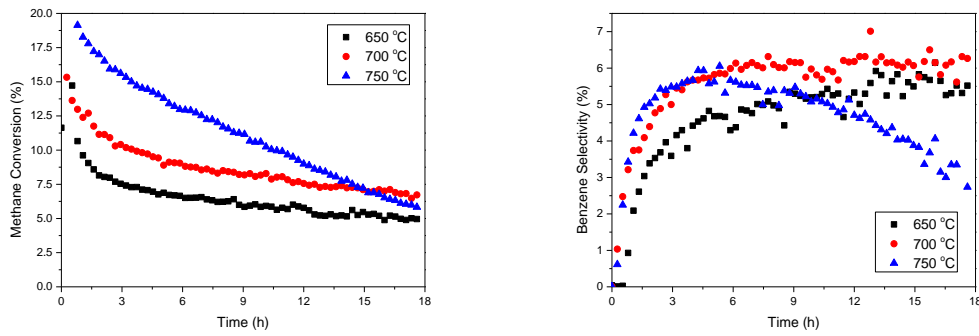


Figure 5. 14: Methane conversion and benzene selectivity for different temperature with  $x_{0,CH_4}=30\%$ ,  $W/F=2160\text{kgs/m}^3$  (group E)

Ethylene selectivity increases with higher temperature. The curves for  $650^\circ\text{C}$  and  $700^\circ\text{C}$  are nearly parallel, slightly increase along reaction time. But  $750^\circ\text{C}$  curve shows a steep increase along reaction time, which is exactly the same as the results of Group A and Group C. The curves for ethane selectivity are still somehow puzzle, which is because of the significant failure from GC analysis as explained in Figure 5. 10. But we can say that, the tendency is sharply increase at the beginning and then steady increase afterwards. The increase slope of  $750^\circ\text{C}$  curve is higher than the ones of  $650^\circ\text{C}$  and  $700^\circ\text{C}$ . The performance of each experiment can be seen in Figure A. 16, Figure A. 6 and Figure A. 17.

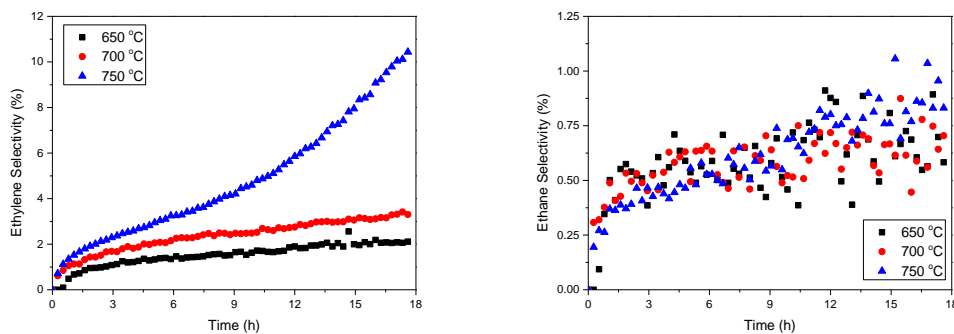


Figure 5. 15: Ethylene selectivity and ethane selectivity for different temperature with  $x_{0,CH_4}=30\%$ ,  $W/F=2160\text{kgs/m}^3$  (group E)

The stepwise temperature rising experiment results for Group E under the same reaction condition are plotted in Figure 5. 16 and Figure 5. 17. The tendency of methane conversion is the same as single experimental results of Group E as well as the stepwise results of Group A and C. Benzene selectivity slightly increase with increasing temperature, the same as Group C. While ethylene selectivity decreases from  $650^\circ\text{C}$  to  $700^\circ\text{C}$ , and then slightly increases from  $725^\circ\text{C}$  to  $750^\circ\text{C}$ , which is the same as results from Group C (in Figure 5. 11). The tendency of ethane selectivity is also somehow puzzle within each temperature step but statistically decrease with increasing temperature, which is similar as Group A and Group C. The performance of Group E stepwise experiment can be also seen in Figure A. 21.

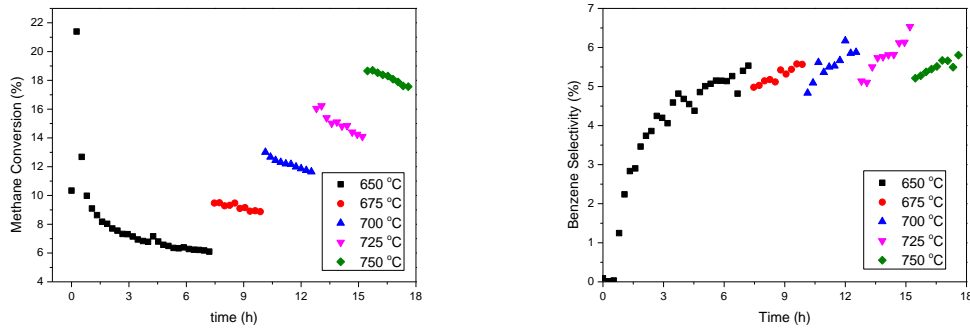


Figure 5.16: Methane conversion and benzene selectivity for stepwise temperature rising experiments with  $x_{0,CH_4}=30\%$ ,  $W/F=2160\text{kg}/\text{m}^3$  (group E)

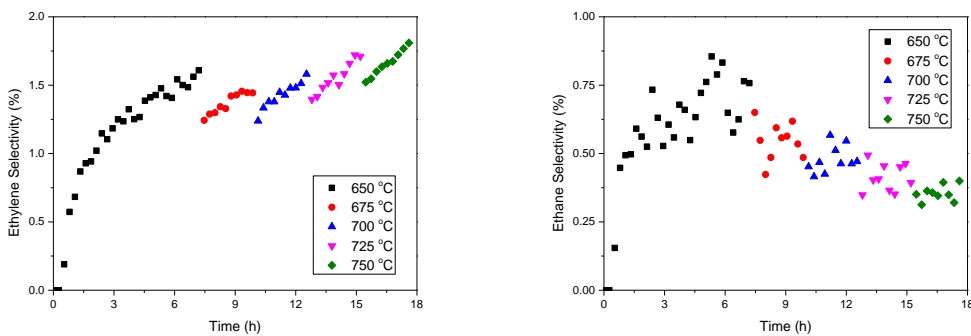


Figure 5.17: Ethylene selectivity and ethane selectivity for stepwise temperature rising experiments with  $x_{0,CH_4}=30\%$ ,  $W/F=2160\text{kg}/\text{m}^3$  (group E)

The average methane conversion and benzene selectivity at steady state of single and stepwise experiment are plotted in Figure 5.18, from which the absolute values as well as tendency of single and stepwise experiments for Group E can be seen. Methane conversion of stepwise at  $700^\circ\text{C}$  and  $750^\circ\text{C}$  are higher than single one, while at  $650^\circ\text{C}$  is lower than single one. Benzene selectivity of stepwise experiment at  $650^\circ\text{C}$  is slightly larger than the one of single experiment.

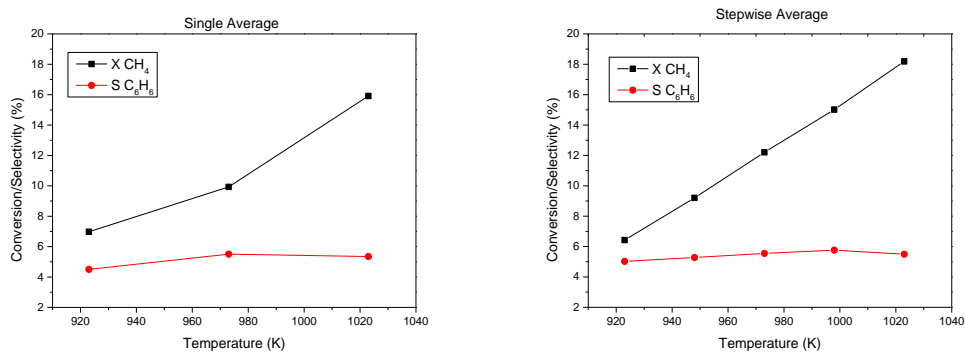


Figure 5.18: Average methane conversion and benzene selectivity comparison of single and stepwise experiment with  $x_{0,CH_4}=30\%$ ,  $W/F=2160\text{kg}/\text{m}^3$  (group E)

As a short conclusion of temperature influence here (as shown in Table 5.2), methane conversion



increases with temperature increasing, but decreases with reaction time and decrease faster at high temperature, which implies that higher temperature results in faster and heavier catalyst deactivation. Benzene selectivity slightly increases for lower inlet concentration (30%) and slightly decreases for higher inlet concentration (90%), with increasing temperature. Ethylene selectivity goes up with reaction time in each temperature, and generally decreases from 650°C to 700°C but increases from 700°C to 750°C. While ethane selectivity decreases with rising temperature.

Table 5. 2: Influence of temperature and reaction time on conversion and selectivity

Performance	Tendency on temperature	Tendency on time
Methane conversion (Eq. (2. 31))	↑	↓
Benzene selectivity (Eq. (2. 32))	90% ↓	Parabolic
	30% ↑	
Ethylene selectivity	Parabolic	↑
Ethane selectivity	↓	Not clear

### 5.2.1.2 Influence of methane feed volumetric fraction on MDA

➤ Group B:  $T = 700^{\circ}\text{C}$ ,  $\frac{W}{F} = 2160\text{kgs/m}^3$

Figure 5. 19 and Figure 5. 20 show the instant methane conversion, benzene selectivity, ethylene selectivity and ethane selectivity of Group B at different inlet methane volumetric fraction. It is clear that methane conversions at all inlet volumetric fraction decrease along with reaction time, just the same tendency and reason (heavier and faster carbon deposit) as all the experimental results in Section 5.2.1.1.

Methane conversion decreases with increasing inlet volumetric fraction, but the decrease from 30% to 50% is relatively big and there is small differences between 50%, 70% and 90%. The curves of benzene selectivity tendencies are similar with a sharply increase at the beginning and then following a relatively flat curve, which is quite flat for 30% and 50%, and slightly rising up for 70% but slightly decreasing for 90%. While 90% shows a relatively high benzene selectivity around 7% at steady state.

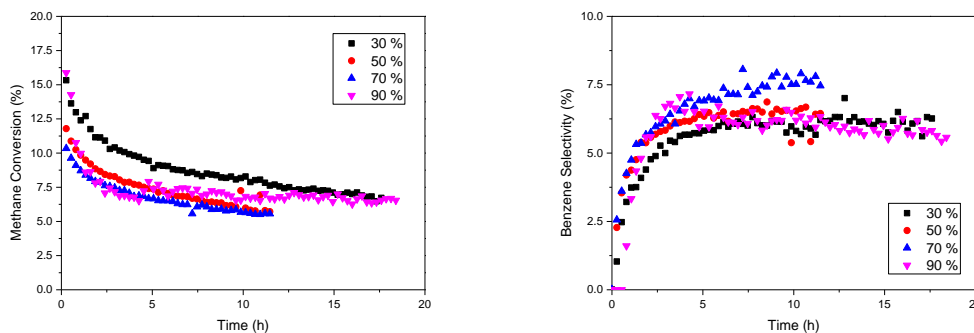


Figure 5. 19: Methane conversion and benzene selectivity for different feed methane fraction with  $T=700^{\circ}\text{C}$ ,  $W/F=2160\text{kgs/m}^3$  (group B)

Ethylene selectivity increase along reaction time and slightly increase with feed fraction. The

increase slop of 50% and 70% is the biggest, then is 30% and 90% is the smallest. Ethane selectivity increase with increasing feed fraction as well but do not change too much along time. The curves tendency for 90% of ethylene and ethane selectivity are the same, which is steeply increase at the beginning and then drops a little bit and afterwards stays nearly at the same value. The performance of each experiment can be seen in Figure A. 6 to Figure A. 9.

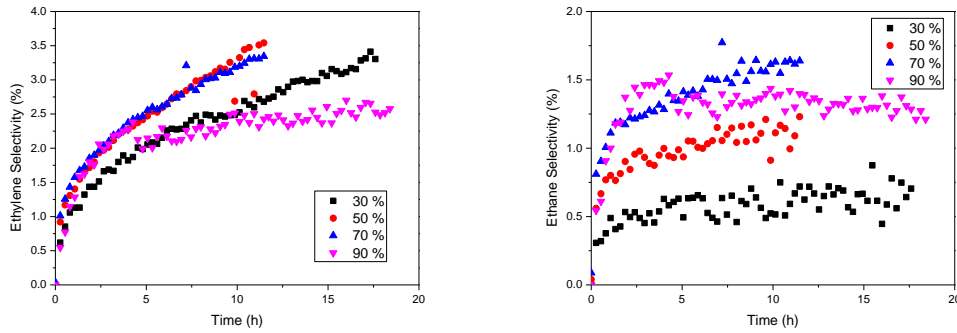


Figure 5. 20: Ethylene selectivity and ethane selectivity for different feed methane fraction with  $T=700^{\circ}\text{C}$ ,  $W/F=2160\text{kgs}/\text{m}^3$  (group B)

The steady state values are plotted in Figure 5. 21. It is very clear that, with increasing methane feed fraction, methane conversion decreases while benzene, ethylene and ethane selectivity slightly increase.

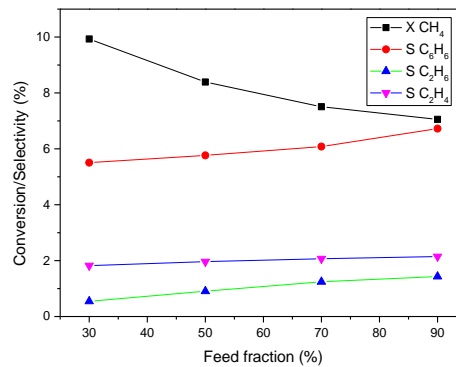


Figure 5. 21: Average conversion and selectivity comparison of single experiments with  $T=700^{\circ}\text{C}$ ,  $W/F=2160\text{kgs}/\text{m}^3$  (group B)

➤ Group D:  $T = 700^{\circ}\text{C}$ ,  $\frac{W}{F} = 720\text{kgs}/\text{m}^3$

The performance of group is plotted in Figure 5. 22 and Figure 5. 23. The tendency of methane conversion over time is the same as Group B but over feed conversion is just the opposite of Group B. The higher the feed fraction, the higher the methane conversion. Benzene selectivity of 30% increases along time but of 90% decrease, while ethylene selectivity of both feed fraction increase but 30% curve has higher slop than 90%. Ethane selectivity of 30% contains significant GC analysis failure which is not suitable for analysis.

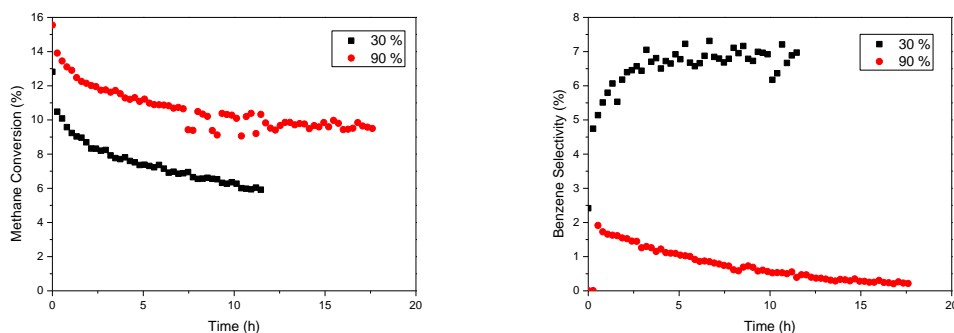


Figure 5. 22: Methane conversion and benzene selectivity for different feed methane fraction with  $T=700^{\circ}\text{C}$ ,  $W/F=720\text{kgs/m}^3$  (group D)

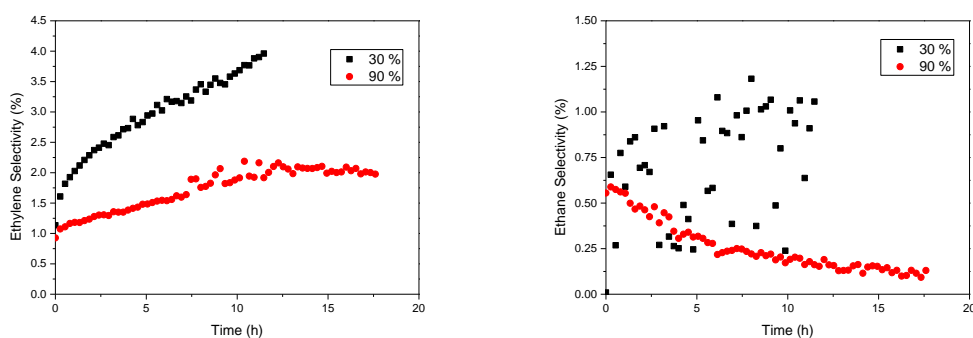


Figure 5. 23: Ethylene selectivity and ethane selectivity for different feed methane fraction with  $T=700^{\circ}\text{C}$ ,  $W/F=720\text{kgs/m}^3$  (group D)

From Figure 5. 24 we can see that, methane conversion increases with increasing feed fraction, but benzene, ethylene and ethane selectivity decrease. This result is just the opposite of Group B, which could be because of different  $W/F$ . Higher  $W/F$  and feed methane fraction favors the selectivity of benzene, ethylene and ethane; lower  $W/F$  but higher feed methane fraction results in high methane conversion but low aimed product selectivity. The performance of each experiment can be seen in Figure A. 10 and Figure A. 19.

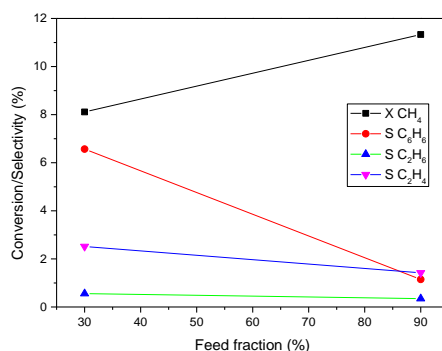


Figure 5. 24: Average conversion and selectivity comparison of single experiments with  $T=700^{\circ}\text{C}$ ,  $W/F=720\text{kgs/m}^3$  (group D)

As short conclusion for the influence of feed fraction influence here: for high  $W/F$  ( $2160 \text{ kgs/m}^3$ ),

higher methane feed fraction results in lower methane conversion but higher aimed product selectivity; while for low W/F ( $720 \text{ kgs/m}^3$ ), higher methane feed fraction results in higher methane conversion and lower product selectivity.

### 5.2.1.3 Influence of W/F on MDA

At  $700^\circ\text{C}$  and each methane feed fraction (30%, 50%, 70% and 90%), there are two comparable experiments with different W/F. These four feed fractions experiments are named as Group H (30%), Group F (50%), Group G (70%) and Group I (90%).

➤ Group H:  $x_{0,\text{CH}_4} = 30\%$ ,  $T = 700^\circ\text{C}$

Higher W/F ( $2163.62 \text{ kgs/m}^3$ ) possesses higher methane conversion and lower benzene, ethylene and ethane selectivity compared to lower W/F ( $719.81 \text{ kgs/m}^3$ ), which can be seen from Figure 5. 25 and Figure 5. 26. Methane conversion decreases along reaction time, just as all the experiments mentioned above. Benzene, ethylene and ethane selectivity increase on the contrary. The performance of each experiment can be seen in Figure A. 10 and Figure A. 6.

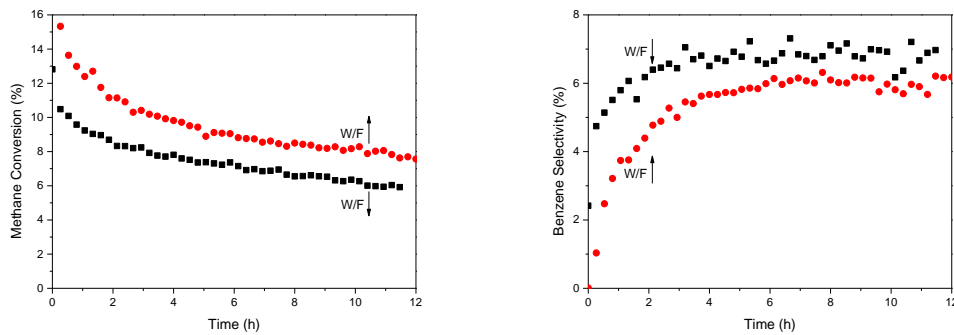


Figure 5. 25: Methane conversion and benzene selectivity for different W/F with  $x_{0,\text{CH}_4}=30\%$ ,  $T=700^\circ\text{C}$ : ■ for  $719.81 \text{ kgs/m}^3$  and ● for  $2163.62 \text{ kgs/m}^3$  (group H)

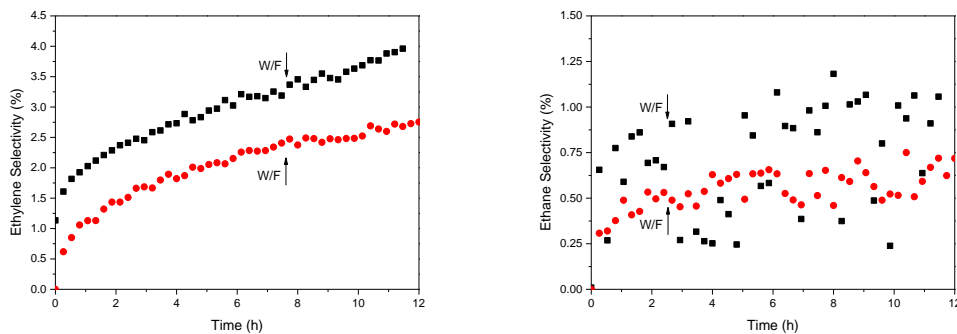


Figure 5. 26: Ethylene and ethane selectivity for different W/F with  $x_{0,\text{CH}_4}=30\%$ ,  $T=700^\circ\text{C}$ : ■ for  $719.81 \text{ kgs/m}^3$  and ● for  $2163.62 \text{ kgs/m}^3$  (group H)

➤ Group F:  $x_{0,CH_4} = 50\%$ ,  $T = 700^\circ C$

The results of Group F are shown in Figure 5. 27 and Figure 5. 28. The tendency to W/F and along with reaction time are the same as Group H. Only the gaps between the two lines are smaller than Group H, which should be caused by the higher methane feed fraction (50%) and also could be caused by a smaller W/F difference (1201.63 kgs/m<sup>3</sup> and 2163.62 kgs/m<sup>3</sup>). The performance of each experiment can be seen in Figure A. 11 and Figure A. 7.

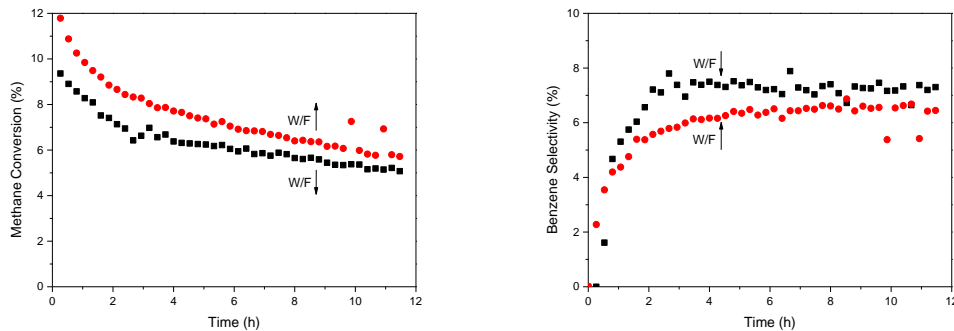


Figure 5. 27: Methane conversion and benzene selectivity for different W/F with  $x_{0,CH_4}=50\%$ ,  $T=700^\circ C$ : ■ for 1201.63 kgs/m<sup>3</sup> and ● for 2163.62 kgs/m<sup>3</sup> (group F)

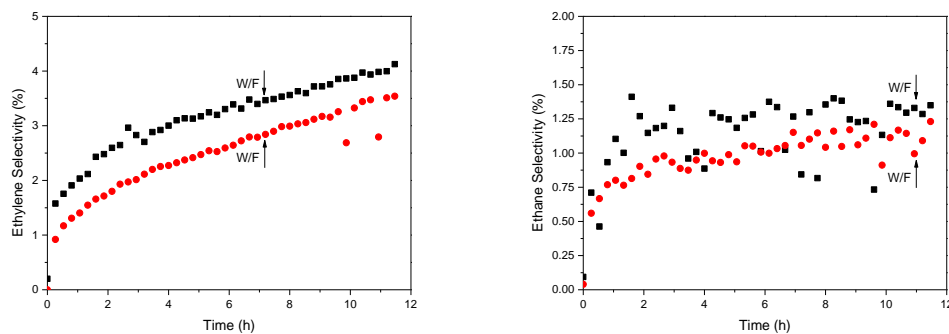


Figure 5. 28: Ethylene and ethane selectivity for different W/F with  $x_{0,CH_4}=50\%$ ,  $T=700^\circ C$ : ■ for 1201.63 kgs/m<sup>3</sup> and ● for 2163.62 kgs/m<sup>3</sup> (group F)

➤ Group G:  $x_{0,CH_4} = 70\%$ ,  $T = 700^\circ C$

From Figure 5. 29 and Figure 5. 30 we can see that, methane conversion and ethane selectivity of Group G are nearly the same. The curves of higher W/F (2163.62 kgs/m<sup>3</sup>) are only a little bit higher than the one of lower W/F (1680.32 kgs/m<sup>3</sup>). The reason can be this lower W/F is already enough to reach enough methane conversion. The difference of benzene and ethylene selectivity are more obvious, but the tendency is still the same as Group H and F. The performance of each experiment can be seen in Figure A. 12 and Figure A. 8.

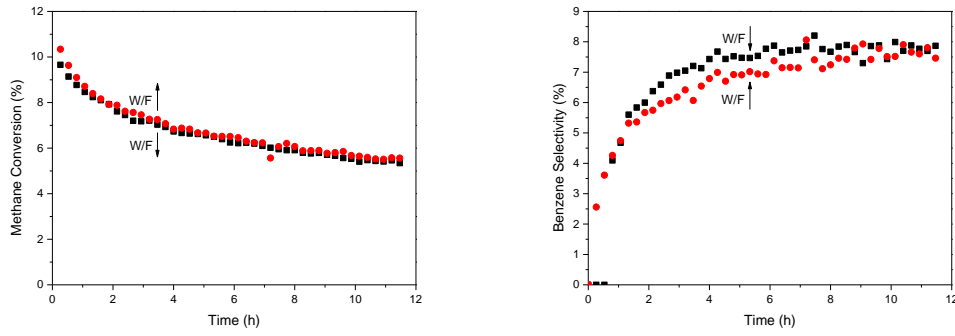


Figure 5. 29: Methane conversion and benzene selectivity for different W/F with  $x_{0,CH_4}=70\%$ ,  $T=700^\circ C$ : ■ for  $1680.32 \text{ kg/m}^3$  and ● for  $2163.62 \text{ kg/m}^3$  (group G)

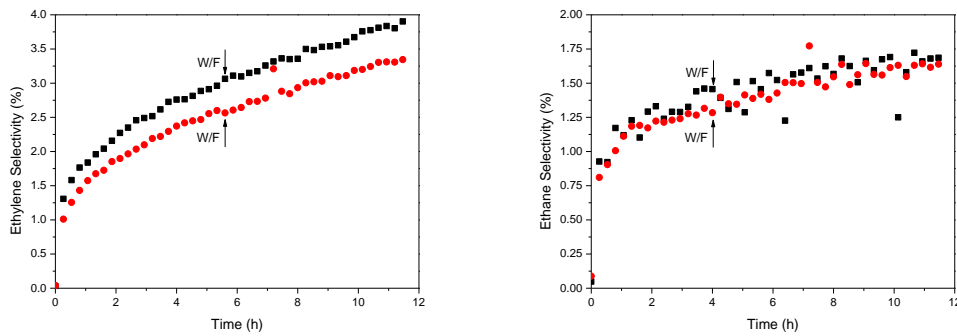


Figure 5. 30: Ethylene and ethane selectivity for different W/F with  $x_{0,CH_4}=70\%$ ,  $T=700^\circ C$ : ■ for  $1680.32 \text{ kg/m}^3$  and ● for  $2163.62 \text{ kg/m}^3$  (group G)

➤ Group I:  $x_{0,CH_4} = 90\%$ ,  $T = 700^\circ C$

The results of Group I is somehow just the opposite as can be seen from Figure 5. 31 and Figure 5. 32. Methane conversion decreases but benzene, ethylene and ethane selectivity increase with increasing W/F. Another aspect is the tendency of benzene and ethane selectivity for low W/F ( $720.52 \text{ kg/m}^3$ ) is decreasing along with reaction time. The performance of each experiment can be seen in Figure A. 19 and Figure A. 3.

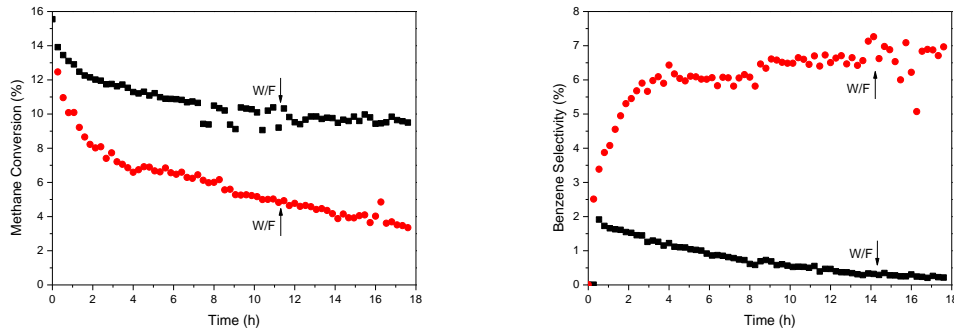


Figure 5. 31: Methane conversion and benzene selectivity for different W/F with  $x_{0,CH_4}=90\%$ ,  $T=700^\circ C$ : ■ for  $720.52 \text{ kg/m}^3$  and ● for  $2163.62 \text{ kg/m}^3$  (group I)

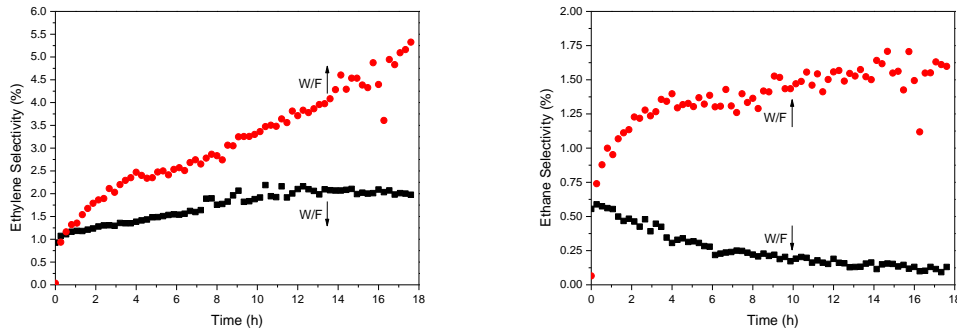


Figure 5. 32: Ethylene and ethane selectivity for different W/F with  $x_{0,CH_4}=90\%$ ,  $T=700^\circ C$ : ■ for  $720.52 \text{ kgs/m}^3$  and ● for  $2163.62 \text{ kgs/m}^3$  (group I)

The conclusion of this section is easier to present in Table 5. 3. Generally speaking then trend of 30%, 50% and 70% are same. However 90% is somehow just the opposite.

Table 5. 3: Influence of W/F and reaction time on conversion and selectivity

	$X_{CH_4}$ (Eq. (2. 31))		$S_{C_6H_6}$ (Eq. (2. 32))		$S_{C_2H_4}$		$S_{C_2H_6}$	
	W/F	Time	W/F	Time	W/F	Time	W/F	Time
30%	↑	↓	↓	↑	↓	↑	↓	↑
50%	↑	↓	↓	↑	↓	↑	↓	↑
70%	↑	↓	↓	↑	↓	↑	↓	↑
90%	↓	↓	↑	High W/F ↑ Low W/F ↓	↑	↑	↑	High W/F ↑ Low W/F ↓

#### 5.2.1.4 Effect of stepwise temperature rise on MDA

➤ Group K: stepwise comparison for:

$$x_{0,CH_4} = 30\% \frac{W}{F} = 720 \text{ kgs/m}^3$$

$$x_{0,CH_4} = 30\% \frac{W}{F} = 2160 \text{ kgs/m}^3$$

$$x_{0,CH_4} = 90\% \frac{W}{F} = 2160 \text{ kgs/m}^3$$

The tendency of methane conversion are the same to temperature and time, which is increasing with high temperature and decreasing along with time. Increasing W/F (from  $720 \text{ kgs/m}^3$  to  $2160 \text{ kgs/m}^3$ ) results in higher  $X_{CH_4}$  but increasing feed fraction (from 30% to 90%) results in lower  $X_{CH_4}$ . Benzene selectivity in each temperature step increases with time. Lower W/F and higher feed fraction favors higher benzene selectivity, as shown in Figure 5. 33.

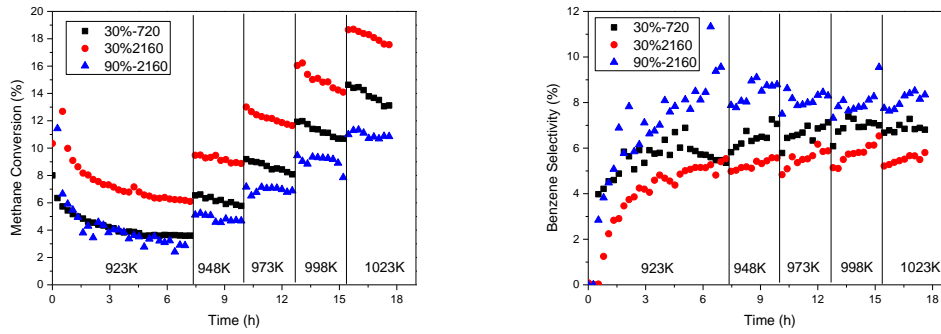


Figure 5. 33: Methane conversion and benzene selectivity of stepwise experiments (group K)

The tendency of ethylene and ethane selectivity is similar, as shown in Figure 5. 34. They are parabolic to temperature and strongly or slightly increasing in each temperature step. They favors for low W/F and high methane feed fraction, but with different increase extent. Ethane selectivity is more sensitive to feed fraction, since there is a big jump from 30% to 90%. The performance of each experiment can be seen from Figure A. 21 to Figure A. 23.

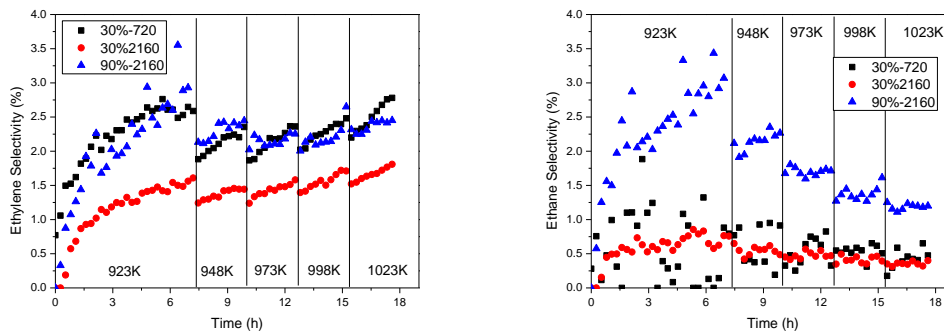


Figure 5. 34: Ethylene and ethane selectivity of stepwise experiments (group K)

The average values at each temperature step for all the stepwise experiments of most interested variables (methane conversion and benzene selectivity) are plotted in Figure 5. 35. It's obvious that the slopes of the two 30% feed fraction experiments are nearly the same, and the slop of the 90% feed is smaller. This implies that the feed fraction affects the methane conversion increasing rate to temperature, which is higher feed fraction results in slower increasing rate. The W/F has an influence on the absolute values of methane conversion, which is higher W/F result in higher methane conversion. High W/F means low space velocity and long residence time, which is reason for the higher methane conversion. While the feed fraction changes the tendency and the shape of benzene selectivity curve. For 30%, the curve is parabolic, which is slightly increasing first and decreasing after 1023K; but for 90%, the curve is continuously gradually decreasing with increasing temperature. The curves for 30% are both parabolic and the maximums are both at 1023K. But lower W/F (shorter residence time) results in higher benzene selectivity, which implies that benzene is not the first choice product of methane conversion. The first choice one should be different carbon deposit. Higher W/F (longer residence time) favors the selectivity of coke more than benzene. It



seems we have to compromise between methane conversion and benzene selectivity when optimizing reaction condition (temperature, feed fraction and W/F).

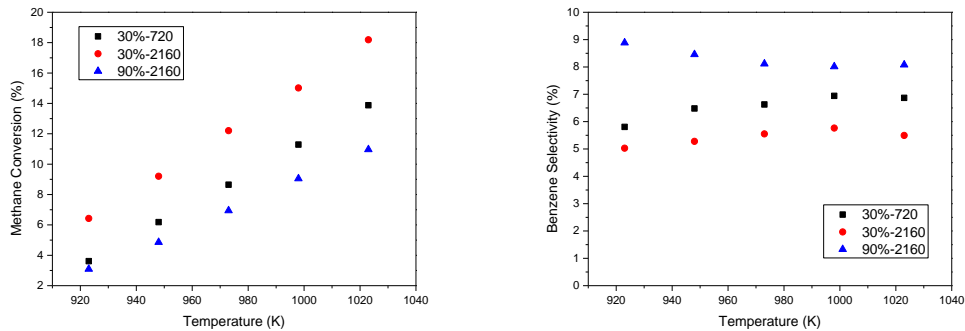


Figure 5.35: Average methane conversion and benzene selectivity of stepwise experiments (group K)

### 5.2.1.5 Stepwise W/F changing on MDA

➤ Group J: W/F switching for  $x_{0,CH_4} = 90\%$ ,  $T = 700^\circ C$

Experimental results of Group J are shown in Figure 5.36 and Figure 5.37. Methane conversion increases with reaction time in each W/F step as well as the same W/F but different time range. Lower W/F ( $1080 \text{ kgs/m}^3$ ) results in higher methane conversion, which is identical with the result of Group I (Figure 5.32).

Benzene selectivity decreases a lot along with time. Ethane selectivity also decreases along with time, but slightly, not as strong as benzene selectivity. While ethylene selectivity does not change with time after induction period. Higher W/F gives higher benzene, ethylene and ethane selectivity, which is also consistent with the results from Group I. The performance of Group I stepwise experiment can be also seen in Figure A.24.

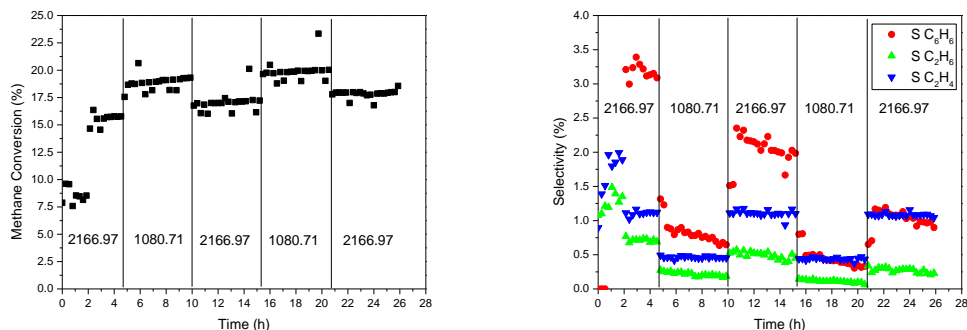


Figure 5.36: Conversion and selectivity of W/F switching experiments (group J)

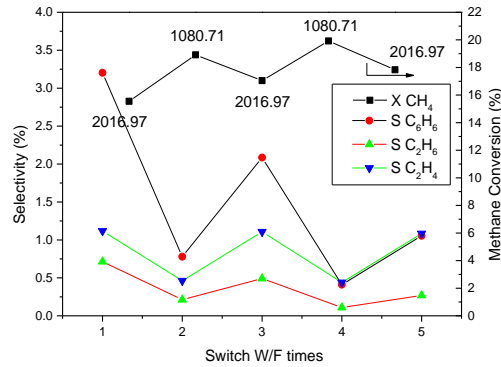


Figure 5.37: Average conversion and selectivity of W/F switching experiments (group J)

## 5.2.2 Ethylene feed (sub-network)

Since ethylene is the most important intermediate, experiments fed with ethylene and nitrogen mixture were carried out for the sub- reaction network exploration. Just as kinetic experiments in Section 5.2.1, process parameters as temperature and concentration series in several experiments as well as individual dynamic experiments were varied accordingly as shown in Table 5. 4. While, because the catalyst can only be activated by methane (introduced in Section 1.2.1.3), most of the experiments here were carried out with activated catalyst, which is detailed introduced in Section 4.3.1. But the performance of not activated catalyst are also compared in this section.

Table 5. 4: Different process parameters with C<sub>2</sub>H<sub>4</sub>/N<sub>2</sub> feed mixtures series experiments

W/F (kgs/m <sup>3</sup> )	x <sub>0</sub> (%)	N. Aact. Cat.	650 (°C)	675 (°C)	700 (°C)	725 (°C)	750 (°C)	SW
54	0.5				✓			
	1	✓	✓	✓	✓	✓	✓	✓
150	2.5				✓			
450	21				✓			
2160	40	✓	✓		✓		✓	

### 5.2.2.1 Influence of temperature on sub-network

➤ Group A:  $x_{0,C_2H_4} = 1\%$ ,  $\frac{W}{F} = 54 \text{ kgs/m}^3$

Figure 5. 38 and Figure 5. 39 show the instant ethylene conversion, benzene, ethane and methane selectivity of Group A single experiments at different temperatures. It is clear that ethylene conversions at all reaction temperatures decrease along with reaction time, and the higher the temperature, the sharper the decreasing curve. This is caused by the heavier and faster catalyst deactivation at higher temperature. When reaction temperature is 650 °C, ethylene conversion decreases sharply along with reaction time contrast to other higher temperature showing flat curves which means the value of ethylene conversion is constant in that time range.

With the increasing of temperature from 650 °C to 700 °C, the curve length of the flat parts also increasing, but decreasing contrarily from 700 °C to 750 °C. The relatively stable ethylene conversion stays at 700 °C, which illustrate the latest starting of catalyst deactivation. The curves of

benzene selectivity tendencies are generally the same with a mild smoothly increase at the beginning and then following a slightly decreasing curve. The tendency respect to temperature is parabolic and the highest benzene selectivity (4.5%) is found at 675°C. Benzene selectivity drop a lot from 675°C to 750°C, which is caused by carbon deposit in catalyst which forms preferentially at high temperature.

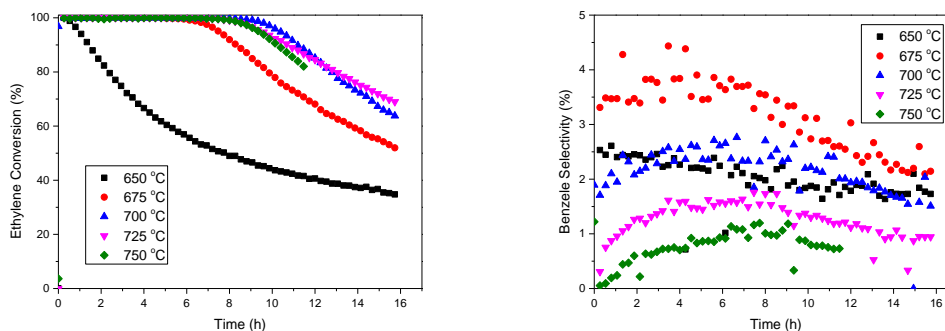


Figure 5.38: Ethylene conversion and benzene selectivity for different temperature with  $x_{0,C_2H_4}=1\%$ ,  $W/F=54\text{kgs/m}^3$  (group A)

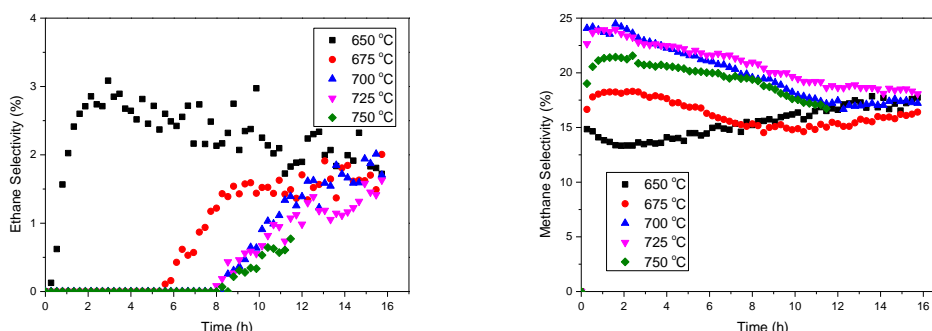


Figure 5.39: Ethane selectivity and methane selectivity for different temperature with  $x_{0,C_2H_4}=1\%$ ,  $W/F=54\text{kgs/m}^3$  (group A)

Ethane selectivity increases sharply at induction period and slightly decreases afterwards at 650°C, which is totally different from the other temperatures. Ethane cannot be detected as a product during steady state at the temperature from 675°C to 750°C. However, as experiment goes on, ethane appears at the end of steady state and increases significantly during deactivation state for 675°C, 700°C and 725°C. A hypothesis can be proposed that ethylene is able to produced ethane at low temperature with less or no presence of hydrogen that comes from cracking reactions (formation of radicals), however at relatively high temperatures (675°C to 750°C) ethane can be only produced when the catalyst is already partial deactivated. The curve of 750°C decreases after 10.5h and drops back to zero at 12h, which might be caused by the ethylene homogeneous pyrolysis as explained for the increase of ethylene conversion. Methane selectivity slightly decrease as reaction proceeding at all reaction temperatures except at 650°C. In correspond to ethane selectivity, ethylene preferentially produces ethane at 650°C, therefore methane selectivity slightly decreases in the same time range. At the time range of deactivation state, methane

selectivity increase at 650 °C as ethane selectivity decrease, but the other four temperatures curves slightly decrease due to the formation of ethane at the end of steady state and in deactivation state. The performance of each experiment can be seen from Figure A. 25 to Figure A. 29.

The stepwise temperature rising experiment of Group A was also conducted for the same reaction condition, the results of which are shown in Figure 5. 40 and Figure 5. 41. At every temperature jump, the conversion and selectivity jump as well. Higher temperature results in higher ethylene conversion until 100%. Each temperature range performs a deactivation stage except 725 °C and 750 °C. The tendency of ethylene conversion is exactly the same as single experimental tendency. However, with the continued rising temperature, the selectivity of benzene is decreasing and shows a jumpy dip when temperature raises from 700 °C to 725 °C and from 725 °C to 750 °C. This is caused by the continued deactivation of the catalyst.

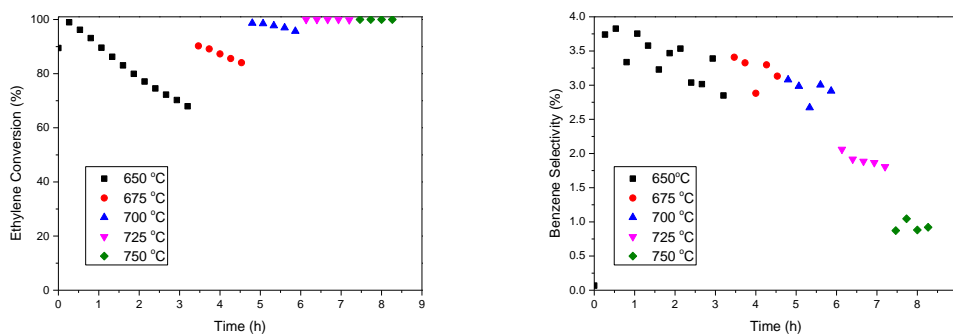


Figure 5. 40: Ethylene conversion and benzene selectivity for stepwise temperature rising experiments with  $x_{0,C_2H_4}=1\%$ ,  $W/F=54\text{kg}/\text{m}^3$  (group A)

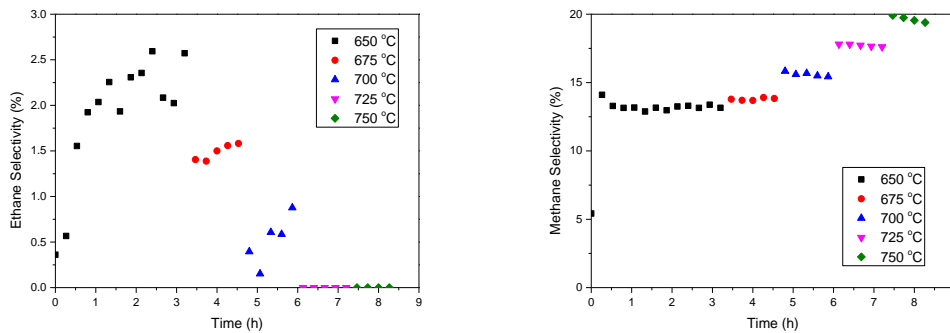


Figure 5. 41: Ethane selectivity and methane selectivity for stepwise temperature rising experiments with  $x_{0,C_2H_4}=1\%$ ,  $W/F=54\text{kg}/\text{m}^3$  (group A)

Ethane selectivity sharply increases at the beginning time of the experiment. As experiment proceed, there is a dip at every temperature change point until 725 °C, after where ethane selectivity becomes zero. This behavior is similar with the trend in single experiments. While methane selectivity remains relatively stable during every temperature range, and only a little bit decrease at the last one hour, which also generally fits the results of single experiment results. The rinsing extent of methane selectivity with the rising temperature is not as much as ethane selectivity. The performance of Group A stepwise experiment can be seen in Figure A. 40.

The average conversion and selectivity at steady state of single and stepwise experiment are plotted in Figure 5. 42, from which absolute values can be easily compared. Obviously the curves belonging to the stepwise experiment are smoother than the ones belonging to the single ones. This is because of stepwise experiments do not have operation error but non-fresh catalyst after 650 °C (or superposition of catalyst deactivation).

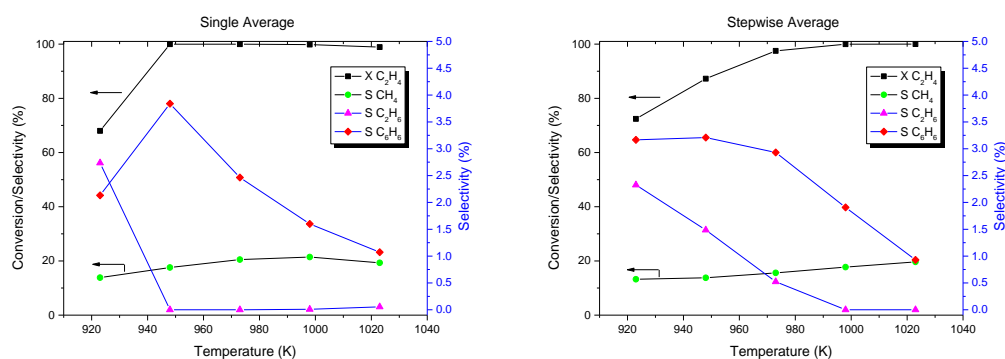


Figure 5. 42: Average conversion and selectivity comparison of single and stepwise experiment with  $x_{0,C_2H_4}=1\%$ ,  $W/F=54\text{kgs/m}^3$  (group A)

Ethylene conversion of single experiment at 675 °C and 700 °C are higher than stepwise experiment, which can attribute to the fresh catalyst used in single experiments. No deviation at higher temperatures (725 °C and 750 °C) is because homogeneous ethylene pyrolysis dominates. So whether the catalyst is deactivated or not do not affect ethylene conversion since it's not involved. Benzene and ethane selectivity at all temperature of single experiment show the same trend as stepwise experiment but stronger extent, especially at 675 °C. Methane selectivity increases with temperature for both set of experiments but different slop trend. Single experiments increases faster from 650 °C to 700 °C and slower from 700 °C to 750, while stepwise result is just the opposite. As introduced in Section 4.3.1, the catalyst used for ethylene feed experiments are activated by methane firstly. While, the influence of catalyst activation is also tested and the result can be seen from Figure 5. 43. Ethylene conversion of non-activated catalyst remains around 100% during the whole reacting time. Methane selectivity of non-activated catalyst is lower than the one of activated catalyst at the beginning time (0-4.2h), but higher after 4.5h. And there is nearly no benzene before 5h and no ethane before 15h. After 5h when there is already certain amount of methane in the system and the catalyst is activated by the produced methane, benzene selectivity continuously increases until the end of experiment. There is only a little bit amount of ethane which can be detect at the last hour. It seems at the beginning 5h, ethylene is homogeneous reacted to methane and carbon. After 5h, there is already considerable amount of methane in the system, which can activated the catalyst to the same one which is used in methane feed experiments. Then the performance of non-activated catalyst starts to go to MDA direction. However, the roughly time-shift observed from ethane and benzene selectivity (since the reaction time for non-activated experiment is not long enough to observe the precise time-shift) is around 7 to 8 hours. This result shows really the influence of a catalyst pre-treatment (or pre-activation) to form reproducible the active  $\text{Mo}_2\text{C}$  species, which has great importance for kinetic modelling. The performance of each experiment can be seen from Figure A. 27 and Figure A. 31.

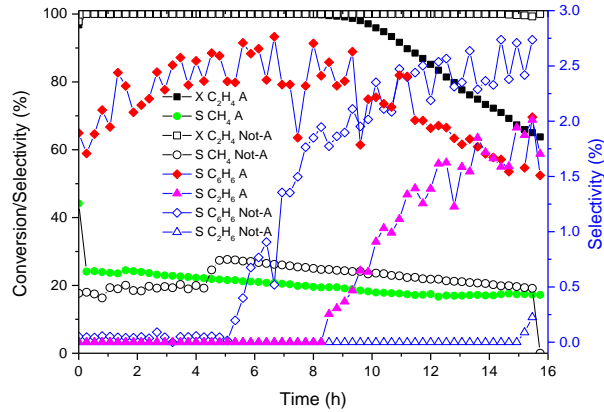


Figure 5.43: Conversion and selectivity comparison of activated and non-activated catalyst experiment with  $x_{0,C_2H_4}=1\%$ ,  $W/F=54\text{kgs/m}^3$  (group A)

➤ Group B:  $x_{0,C_2H_4} = 40\%$ ,  $\frac{W}{F} = 2160\text{kgs/m}^3$

Another set of experiment to investigate the influence of temperature is conducted with higher ethylene feed fraction and  $W/F$ . The resulted tendency of each variable in each experiment is totally different from Group A, as shown in Figure 5.44 and Figure 5.45. Ethylene conversion tendency for all temperature are similar, which is sharply decreasing from 100% at the beginning to a certain value and stays at that small range afterwards. The higher the temperature, the steeper the drop, the faster to reach the stable range, and the higher that steady state value.

Benzene selectivity is zero at the first two hours, and jumps up and then sharply goes down to a stable value. Higher temperature results in higher stable value of benzene selectivity and a higher decrease slope. There is a slightly climbing up during steady state of  $750^\circ\text{C}$ . Ethane selectivity goes up at the beginning and then stays at a stable value, which is just the opposite of ethylene conversion tendency. Methane selectivity goes down from the very beginning and stays relatively stable after a U-turn. Higher temperature results in higher steady value and faster steady state. The second part of the U-turn of  $650^\circ\text{C}$  is very mild and gradual compared with  $700^\circ\text{C}$  and  $750^\circ\text{C}$ . The performance of each experiment can be seen from Figure A.37 to Figure A.39.

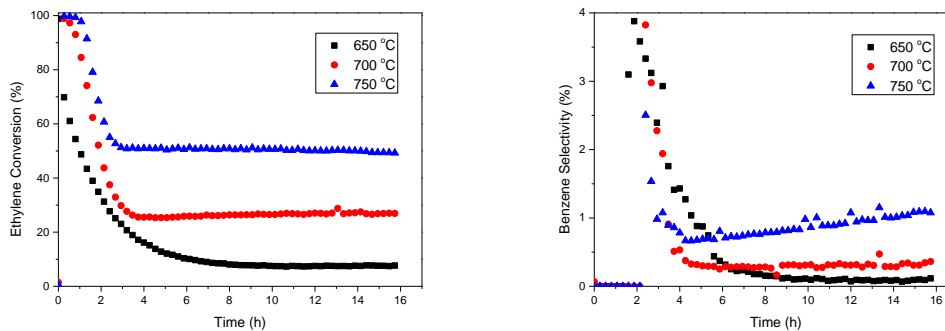


Figure 5.44: Ethylene conversion and benzene selectivity for different temperature with  $x_{0,C_2H_4}=40\%$ ,  $W/F=2160\text{kgs/m}^3$  (group B)

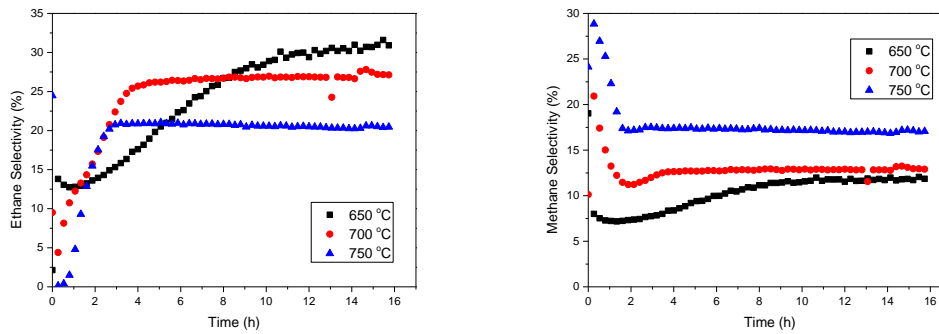


Figure 5. 45: Ethane selectivity and methane selectivity for different temperature with  $x_{0,C_2H_4}=40\%$ ,  $W/F=2160\text{kg}/\text{m}^3$  (group B)

As a short conclusion here compared with Group A: during the first induction period, ethylene conversion decreases from 100% to steady state value, and methane, ethane as well as coke are the main products; when it comes to the second induction period, benzene is produced but decreases fast to the steady value. There is no visible deactivation state in this group of experiments.

The influence of catalyst activation is also tested for Group B and the results are presented in Figure 5. 46. The tendencies of the four variables (ethylene conversion, benzene, ethane and methane selectivity) for activated and non-activated catalyst are exactly the same. Even the steady state value of methane and benzene selectivity are identical. The time shift of Group B is around 1.5h, which is much shorter than the one of Group A. Methane selectivity at the very beginning of non-activated catalyst is around 10% higher than the one of activated catalyst. This means that at the beginning 1.5h (first induction period), ethylene is converted to methane and coke only. After this first induction period, the produced methane activates the catalyst as the induction period of methane feed experiments, and afterward everything is the same as the activated catalyst experiment. This is the reason why there is a 1.5h-shift between the non-activated catalyst results and the activated ones. The performance of each experiment can be seen from Figure A. 39 and Figure A. 30.

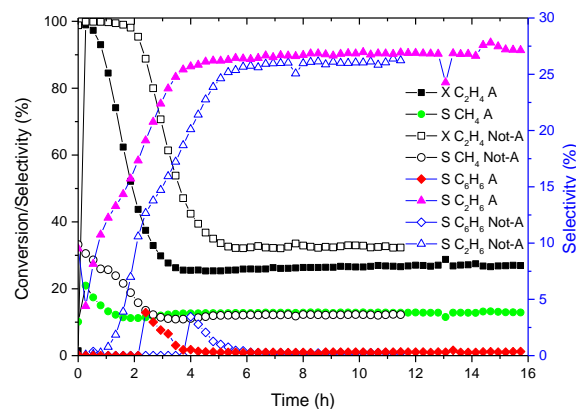


Figure 5. 46: Conversion and selectivity comparison of activated and non-activated catalyst experiment with  $x_{0,C_2H_4}=40\%$ ,  $W/F=2160\text{kg}/\text{m}^3$  (group B)

### 5.2.2.2 Influence of ethylene feed volumetric fraction on sub-network

➤ Group C:  $T = 700^{\circ}\text{C}$ ,  $\frac{W}{F} = 54\text{kgs/m}^3$

Ethylene is the most important intermediate and one of the products of MDA system. In a real MDA reaction system, the concentration of ethylene would not be very high since the low methane conversion and other products production. In this group of experiments, ethylene feed volumetric fraction of 0.5% and 1% are selected in order to simulate the really MDA system.

From Figure 5. 47 we can see the influence of ethylene feed fraction. Ethylene conversion decreases earlier and faster for 1%, but has the same steady state conversion of 100%. Benzene selectivity of 1% is higher during induction and steady state, and slightly decreases to the same value as 0.5% in the last hour. Ethane selectivity of 1% is zero until 8.2h, and starts to increase slightly, while the one of 0.5% is zero all the time. Methane selectivity of 1% is around 5% lower than the one of 0.5% in the whole time range. The performance of each experiment can be seen from Figure A. 27 and Figure A. 33.

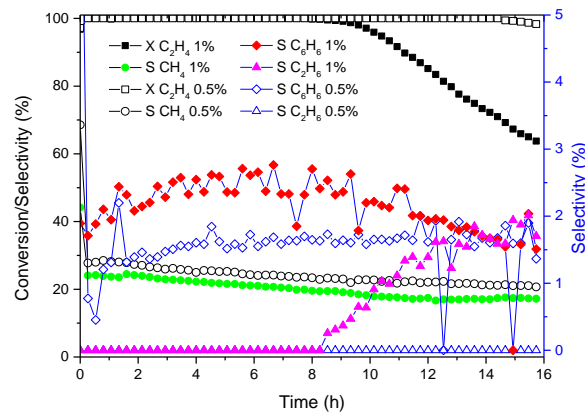


Figure 5. 47: Conversion and selectivity comparison of different ethylene feed volumetric fraction with  $T=700^{\circ}\text{C}$ ,  $W/F=54\text{kgs/m}^3$  (group C)

➤ Group D:  $T = 700^{\circ}\text{C}$

In order to better investigate the influence of ethylene feed volumetric fraction, more different feed fractions are compared in Figure 5. 48 and Figure 5. 49. It seems then tendency and steady state range are more comparable for lower sub-group (0.5%, 1% and 2.5%) and higher sub-group (21% and 40%). The tendency of higher sub-group is the same as Group B (see Figure 5. 44 and Figure 5. 45) and not explained again here.

For the lower sub-group, ethylene conversion decreases earlier and faster with higher feed fraction. Benzene selectivity mild decrease after some time, and the higher the feed fraction, the earlier and faster decrease. Ethane selectivity stays at zero at the induction and steady state, after that increases slightly; and higher feed fraction results in higher increase extent. Methane selectivity gradually decrease along with reaction time, and the higher the feed fraction, the lower the methane selectivity. The average value at steady of all feed fraction are plotted in Figure 5. 50. Generally speaking, ethylene conversion and ethane selectivity increase but benzene and methane selectivity decrease with increasing ethylene feed volumetric fraction. The performance of each experiment can be seen in Figure A. 33, Figure A. 27, Figure A. 34, Figure A. 35 and Figure A. 39.



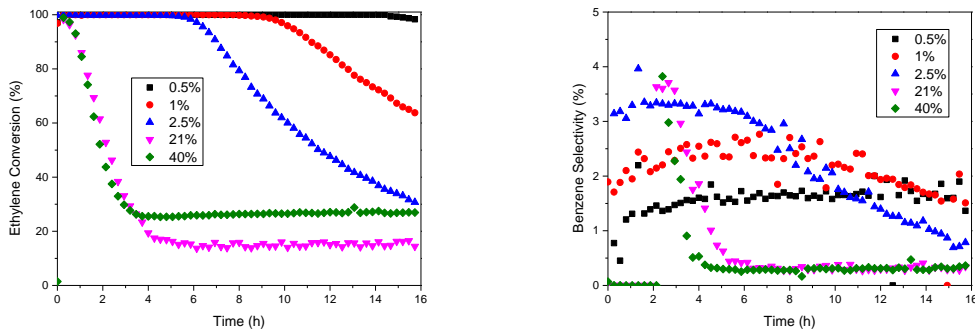


Figure 5. 48: Ethylene conversion and benzene selectivity for different ethylene feed volumetric fraction with  $T=700^{\circ}\text{C}$  (group D)

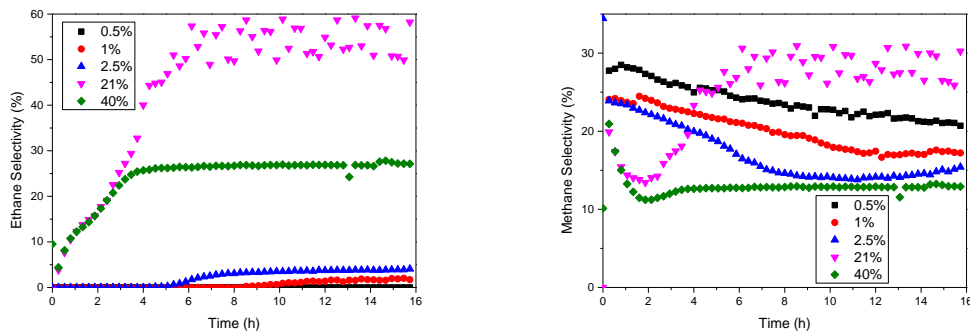


Figure 5. 49: Ethane selectivity and methane selectivity for different ethylene feed volumetric fraction with  $T=700^{\circ}\text{C}$  (group D)

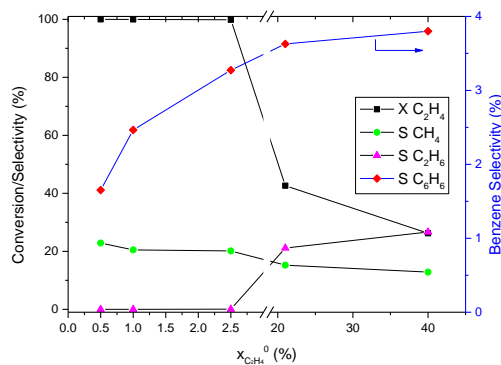


Figure 5. 50: Average conversion and selectivity comparison of different ethylene feed volumetric fraction with  $T=700^{\circ}\text{C}$  (group D)

Figure 5. 51 shows the carbon balance of all methane feed experiments. As can be seen from the figure that carbon balance is bigger than 80% for most of the reacting time. But at the very beginning of each experiment, carbon balance is at low range from 25% to 75%. This is because of the activation of catalyst, during which methane is reacting with the molybdenum sites on the catalyst

to molybdenum carbide. The carbon species in molybdenum carbide is not included in carbon balance as shown in eq. (5. 21). This also verify the assumption of catalyst activation in section 1.2.2. At the same feed volumetric fraction and W/F, higher temperature holds lower carbon balance. This implies that higher temperature has more carbon deposit on the catalyst, which cannot be detected from the product analysis. If we zoom in and only see the selected data, we can see that higher methane feed volumetric fraction results in higher carbon balance, and higher W/F leads to lower carbon balance. This implies that lower methane feed volumetric fraction and higher residence time favors the formation of carbon deposit.

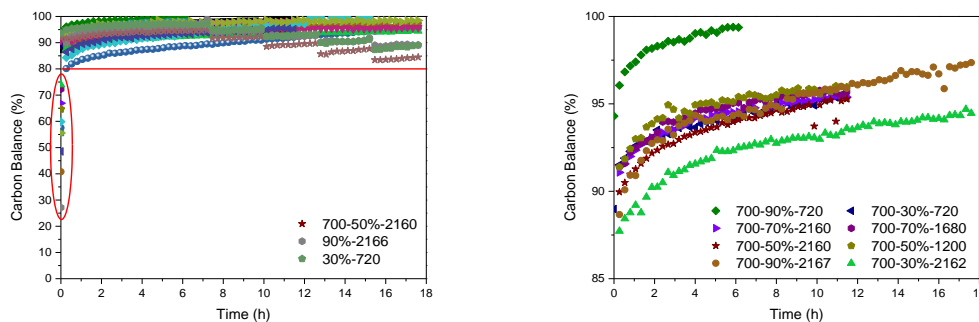


Figure 5. 51: Carbon Balance of all the experiments

### 5.2.3 Summary regarding kinetic measurements

In this section, experimental results in FBR for both methane and ethylene feed were presented and discussed. For all the experiments, there was no clear steady state established. A pseudo steady state was extracted from results corresponding to zone (II) in Figure 5. 1.

For methane feed experiments, with increasing temperature, the pseudo steady state methane conversion increased but benzene selectivity slightly decreased. For low methane feed fraction ( $\leq 70\%$ ), methane conversion increased but benzene selectivity decreased with increasing W/F. For high methane feed fraction ( $=90\%$ ), higher W/F led to lower methane conversion and higher benzene selectivity. This implies methane conversion and benzene selectivity are in conflict. A compromise has to be made in selecting the operating conditions (temperature, methane feed volumetric fraction and W/F).

For the ethylene feed experiments with an ethylene feed fraction of 1%, increasing temperature led to increased ethylene conversion and methane selectivity, but decreasing benzene selectivity. Higher ethylene feed fractions led to lower ethylene conversion and methane selectivity, but higher benzene selectivity. Ethylene conversion and methane selectivity were always synchronized influenced. This means methane is the premier product in the ethylene feed system. As in the methane feed experiments, ethylene conversion and benzene selectivity are in an opposite way influenced.

The operating conditions also strongly influence the catalyst deactivation. In the methane feed system, the sum of benzene, ethylene and ethane selectivities is less than 20%. In ethylene feed system, the sum of benzene, methane and ethane selectivities is around 50%. This means carbon deposition is much stronger in the methane feed system than in the ethylene feed system.

## 5.3 Simplified models to quantify reaction kinetics

### 5.3.1 Reactor modelling and reaction kinetics

Reaction kinetics provide information about the rate with which a reaction system will approach equilibrium. Chemical kinetics is concerned with quantifying these rates and identifying factors affecting them [162]. In contrast to thermodynamics the rates can be often determined only experimentally. Typically, a laboratory scale reactor is used to carry out the reaction to quantify the dependences of rates on various factors, such as concentrations of species and temperature. The primary foal of chemical kinetics is the development and validation of a rate law (for a single system) or a set of rate laws (for complex reaction system). Approaches to study a reaction are normally based on the following aspects: 1. Choice of type of reactor to be used and certain features relating to its mode of operation (e.g. a batch reactor operated at constant volume); 2. Choice of species (reactant or product) to follow during the experiments (e.g. by chemical analysis); 3. Choice of method to determine numerically the values of the parameters, and hence to establish the form of the rate law.

For a simple reaction system, it is only necessary to follow the extent of reaction by means of a suitable measurement. This may be the concentration of one species. Batch reactors are traditionally used. The measurement of the relevant concentration time courses is often time consuming and tedious. A standard operation mode and widely used took of reversible reactions is fixed bed reactor.

#### 5.3.1.1 Reactor modelling

In this section, main theoretical aspects of relevance for the present work has been discussed. For simplifying the modelling work of FBR and MR, some assumptions are made:

- i. Isothermal plug flow in both tube and shell sides; no radial concentration or temperature gradients.
- ii. Negligible pressure drop on both tube and shell side.
- iii. No boundary layer concentration gradients near the membrane surface.
- iv. Membrane permeability is independent of mixture composition.
- v. Exudates concentration on the permeate side is much lower than on the reaction side.

Some of the above assumptions may be invalid in some case, e.g. sometimes the radial temperature gradients may exist and pressure drop may be significant and the reduction potential of the gas may affect the permeability of the membrane, but they seem reasonable for many designs and they have been used in previous MDA studies [111, 136].

One of the simplest models used to describe the performance of tubular reactor is the well-known isothermal one-dimensional plug flow tubular reactor (PFTR) model as shown in Figure 5. 52.

The mass balance of this model is for steady-state conditions with a network of  $N_R$  simultaneously proceeding reactions:

$$\frac{d\dot{n}_i}{dz} = A_R \sum_{j=1}^{N_R} \nu_{ij} r_j \quad i=1, \dots, N_C \quad (5.1)$$

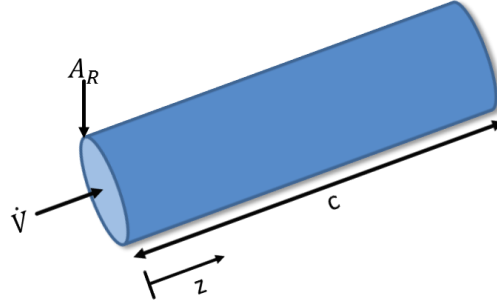


Figure 5. 52: Schematic illustration of PFTR

When the volumetric flow rate  $\dot{V}$  is constant, eq. (5. 1) can be rewrite as:

$$\frac{dc_i}{dz} = \frac{A_R}{\dot{V}} \sum_{j=1}^{N_R} \nu_{ij} r_j \quad i=1, \dots, N_C \quad (5. 2)$$

The  $\nu_{ij}$  are the elements of stoichiometric matrix,  $A_R$  stands for the cross-sectional area of the tube and  $z$  is the axial coordinate. With the residence time  $\tau$  in a reactor section of length  $z$ :

$$\tau = \frac{A_R}{\dot{V}} z \quad (5. 3)$$

The mass balance of the PFTR can be expressed also in the following manner:

$$\frac{dc_i}{d\tau} = \sum_{j=1}^{N_R} \nu_{ij} r_j \quad i=1, \dots, N_C \quad (5. 4)$$

The systems of ordinary differential eq. (5. 2) or (5. 4) can be integrated numerically with the initial conditions  $c_i^0 = c_i(z = 0 \text{ or } \tau = 0)$  and the specific rate laws. If only one reaction needs to be considered and the conversion of component A is chosen to be the state variable of interest, the mass balance of the PFTR can be also expressed as follows:

$$\frac{dX_A}{d\tau} = \frac{(-\nu_A) r^0 f(X_A)}{c_A^0} \quad (5. 5)$$

For the tubular membrane reactor (MR) modelling, the mass balance of this model is for steady-state conditions and a network of  $N_R$  simultaneously reactions with  $N_C$  species:

Tube side (abbreviated as “ts”)/react side:

$$\frac{d\dot{n}_i^{ts}}{dz} = \pi \cdot r_{\text{tube}}^2 \cdot \sum_{j=1}^{N_R} \nu_{ij} r_j - 2\pi \cdot r_{\text{tube}} \cdot J_i \quad i=1, \dots, N_C \quad (5. 6)$$

$$\frac{d\dot{n}_{\text{tot}}^{ts}}{dz} = \sum_{i=1}^{N_C} \frac{d\dot{n}_i^{ts}}{dz} = \pi \cdot r_{\text{tube}}^2 \cdot \sum_{i=1}^{N_C} \sum_{j=1}^{N_R} \nu_{ij} r_j - 2\pi \cdot r_{\text{tube}} \cdot \sum_{i=1}^{N_C} J_i \quad (5. 7)$$

$$\frac{dP_i^{ts}}{dz} = \frac{P_{\text{tot}}^{ts}}{n_{\text{tot}}^{ts}} \left[ \pi \cdot r_{\text{tube}}^2 \cdot \sum_{j=1}^{N_R} \nu_{ij} r_j - 2\pi \cdot r_{\text{tube}} \cdot J_i \right] - \frac{P_i^{ts}}{n_{\text{tot}}^{ts}} \left[ \pi \cdot r_{\text{tube}}^2 \cdot \sum_{i=1}^{N_C} \sum_{j=1}^{N_R} \nu_{ij} r_j - 2\pi \cdot r_{\text{tube}} \cdot \sum_{i=1}^{N_C} J_i \right] \quad i=1, \dots, N_C \quad (5. 8)$$

Shell side (abbreviated as “ss”)/permeate side:

$$\frac{d\dot{n}_i^{ss}}{dz} = 2\pi \cdot r_{\text{tube}} \cdot J_i \quad i=1, \dots, N_C \quad (5.9)$$

$$\frac{d\dot{n}_{\text{tot}}^{ss}}{dz} = \sum_{i=1}^{N_C} \frac{d\dot{n}_i^{ss}}{dz} = 2\pi \cdot r_{\text{tube}} \cdot \sum_{i=1}^{N_C} J_i \quad (5.10)$$

$$\frac{dP_i^{ss}}{dz} = 2\pi \cdot r_{\text{tube}} \cdot J_i \cdot \frac{P_{\text{tot}}^{ss}}{n_{\text{tot}}^{ss}} - 2\pi \cdot r_{\text{tube}} \cdot \sum_{i=1}^{N_C} J_i \cdot \frac{P_i^{ss}}{n_{\text{tot}}^{ss}} \quad i=1, \dots, N_C \quad (5.11)$$

In the above equations,  $i$  stands for the number of species,  $j$  is the number of reactions,  $\nu_{ij}$  is the stoichiometric coefficient of specie  $i$  in reaction  $j$ ,  $n_i$  is the molar flow rate of  $i$ ,  $P_i$  is the partial pressure of  $i$ ,  $z$  is the axial coordinate of reactor and  $r_{\text{tube}}$  is the inner radius of reactor.  $J_i$  is the permeation flux of component  $i$ , which is already introduced in the previous section.

### 5.3.1.2 Reaction kinetics

As mentioned above, the reaction rates are the key information required to quantify chemical reactions and to describe the performance of chemical reactors. Broad knowledge regarding the kinetics of chemical reactions can be found in the literature. In this section, a short empirical macroscopic description of the rates of chemical reactions is given. The description concentrates on the definition of reaction rates and on the development of a quantitative analysis of the dependence of the reaction rates on the reaction conditions, including concentration of involved components and temperature.

When the system is at steady state, all the steps in the sequence take place at the same rate. However, the overall rate is often controlled by one step, which is the slowest one.

The reaction rate is defined either as the amount of product produced or the amount of reactant consumed per unit volume or per mass of catalyst of the reaction phase per unit time.

The rate of a single reaction in which  $N_C$  components are involved is defined as:

$$r_{\text{Scale}} = \frac{1}{\text{Scale}} \frac{1}{\nu_i} \frac{dn_i}{dt} \Big|_{\text{Reaction}} \quad i=1, \dots, N_C \quad (5.12)$$

The stoichiometric coefficient  $\nu_i$  guarantees that the reaction rate does not depend on the component  $i$  considered. Regarding the selection of Scale, reaction volume  $V_R$  is normally used for homogeneous reaction leading to a reaction rate with the dimension of  $[\text{mol}/\text{m}^3\text{s}]$ ; and the mass or surface area of catalyst  $m_{\text{Cat}}$  or  $A_{\text{Cat}}$  are more useful for heterogeneous reaction leading to reaction rates with the unit of  $[\text{mol}/\text{kgs}]$  or  $[\text{mol}/\text{m}^2\text{s}]$ .  $n_i$  is the number of moles of component  $i$ ; and  $N_C$  is the number of components. For a reaction system with  $N_R$  reactions, the rate of transformation of component  $i$ ,  $r_i^{\text{overall}}$ , can be written as:

$$r_i^{\text{overall}} = \sum_{j=1}^{N_R} \nu_{ij} r_j \quad i=1, \dots, N_C \quad (5.13)$$

where  $\nu_{ij}$  is the stoichiometric coefficient of component  $i$  in reaction  $j$ , and  $r_j$  is the rate of reaction  $j$ . If reactor volume  $V_R$  is chosen as the scale and is assumed to be constant, the reaction rate can be expressed as:

$$r = \frac{1}{\nu_i} \frac{dc_i}{dt} \quad i=1, \dots, N_C \quad (5.14)$$

where  $c_i$  is the molar concentration of component  $i$  and has the relation with the specific numbers of moles of component  $i$ :

$$n_i = V_R c_i \quad i=1, \dots, N_C \quad (5.15)$$

or has the relation with molar flow rate  $\dot{n}_i$  and volumetric flow rate  $\dot{V}$  for an open system:

$$\dot{n}_i = \dot{V} c_i \quad i=1, \dots, N_C \quad (5.16)$$

Postulating that the rate controlling mechanism involves the collision or interaction of a single molecule of a reactant with a single molecule of the other reactants, than the number of collision of those molecules is proportional to the rate of reaction. However, in the case of ideal system, at a given temperature the number of collisions is proportional to the concentration of reactants in the mixture [163]. Thus, for an irreversible reaction the rate of reaction can be described by the famous power law, which is defined as:

$$r = k(T) \prod_{i=1}^{N_{\text{react}}} (c_i)^{\alpha_i} \quad (5.17)$$

where  $N_{\text{react}}$  is the number of reactant;  $\alpha_i$  is the order of the reaction with respect to the component  $i$ . the rate constant  $k(T)$  is found empirically to be dependent on temperature as shown in the following Arrhenius equation.

$$k(T) = k_{\infty} \exp\left(-\frac{E_A}{RT}\right) \quad (5.18)$$

where  $E_A$  is called the activation energy for the reaction and  $k_{\infty}$  is called the pre-exponential factor. If the reaction is reversible, the rate can be written as a difference between the rate of the forward reaction  $r_f$  and the rate of the backward reaction  $r_b$ :

$$r = r_f - r_b = k_f(T) \prod_{i=1}^{N_{\text{react},f}} (c_i)^{\alpha_{i,f}} - k_b(T) \prod_{i=1}^{N_{\text{react},b}} (c_i)^{\alpha_{i,b}} \quad (5.19)$$

or

$$r = k_f(T) \left( \prod_{i=1}^{N_{\text{react},f}} (c_i)^{\alpha_{i,f}} - \frac{1}{K_P} \prod_{i=1}^{N_{\text{react},b}} (c_i)^{\alpha_{i,b}} \right) \quad (5.20)$$

where  $k_f$  and  $k_b$  are the rate constants for the forward and backward reactions, respectively.  $K_P$  is the equilibrium constant ( $K_P = k_f(T)/k_b(T)$ , see Eq. (2. 18) in chapter 2).

### 5.3.2 Methodology for kinetic investigations

A conventional approach to the quantification of reaction rates is to measure reactant or product concentrations as functions of time in a batch reactor or the outlet of PFTR. To verify the reaction rate constants quantified from measured results, in the present work the kinetic experiments were performed in a PFTR reactor for steady state conditions as described in section 4.3.1. Based on literature data and steady state experimental data, 3 different reaction networks for MDA are proposed and all the estimated parameters for the reaction networks are presented and discussed in this chapter. At the same time, the model and the parameters are validated as well. This is followed by the chapter about simulation of deactivation state (Chapter 5).

After the analysis of original experimental data, the kinetic parameters are in a first step preliminarily estimated by differential method and then in a second step optimized by MATLAB

(with the solver of “lsqnonlin”). As for the analysis of the experimental data described before, simulation of the kinetic parameters can be (but not compulsively) divide into two steps: feed with ethylene and feed with methane. The reason to do so is that ethylene is the primary intermediate in MDA process and ethylene converting to benzene is an easier sub-network of the MDA system. Part of the simulation results of feed with ethylene can be used in the simulation of methane so that can decrease the number of parameters which should be optimized with the feed of methane. After this part, we can represent and optimized the MDA system in the computer with the help of kinetic parameters.

### 5.3.2.1 Parameter estimation

Parameter estimation in this chapter is based on analyzing steady state experimental data of both ethylene and methane feed (Figure 5. 53). So the parameter estimation also separate into two steps: ethylene experiments estimation (sub-network estimation) and methane experiments estimation (whole network estimation). The aim of steady state sub-network analysis is to decouple the complexity of steady state whole network estimation. Each step goes through the preliminary estimation (analytical/graphical analysis to find suitable start values for numerical optimization by differential method) and optimized estimation (based on least square method numerically).

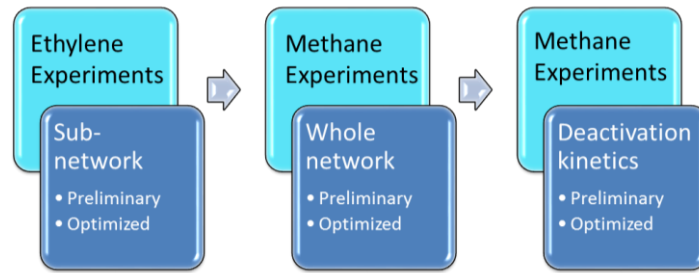


Figure 5. 53: Schematic diagram of steps of data analysis

With the estimated parameters of steady state, the parameters of deactivation kinetics can be also estimated follow the same procedure (preliminary and optimized estimation), which will be detailed introduce in Chapter 5.

### 5.3.2.2 Preliminary estimation

In the experiments, no naphthalene or higher carbon chain could be detected by GC. Carbon deposits on the catalyst are numerous. This affects the evaluation of the course of the reaction and the following calculations greatly. The carbonaceous deposits are considered in this thesis as an average component with the composition  $C_xH_y$ . First of all, the value of  $x$  and  $y$  were quantified using the following carbon and hydrogen balances (eq. (5. 21) and (5. 22)).

$$\dot{n}_{CH_4}^{in} = \dot{n}_{CH_4}^{out} + 6 \times \dot{n}_{C_6H_6}^{out} + 2 \times \dot{n}_{C_2H_4}^{out} + 2 \times \dot{n}_{C_2H_6}^{out} + x \times \dot{n}_{C_xH_y}^{out} \quad (5. 21)$$

$$4 \times \dot{n}_{CH_4}^{in} = 4 \times \dot{n}_{CH_4}^{out} + 6 \times \dot{n}_{C_6H_6}^{out} + 4 \times \dot{n}_{C_2H_4}^{out} + 6 \times \dot{n}_{C_2H_6}^{out} + 2 \times \dot{n}_{H_2}^{out} + y \times \dot{n}_{C_xH_y}^{out} \quad (5. 22)$$

During preliminary evaluation of pseudo steady states, the differential method is applied and all the reactions are considered as irreversible although some of them are reversible for the reaction order

estimation.

For the differential method, normally the concentration-time course of one component is measured as shown in Figure 5. 54. For a reaction rate described by a power law holds:

$$r = \frac{dC_i}{dt} = \vartheta_i k C_i^\alpha \quad (5. 23)$$

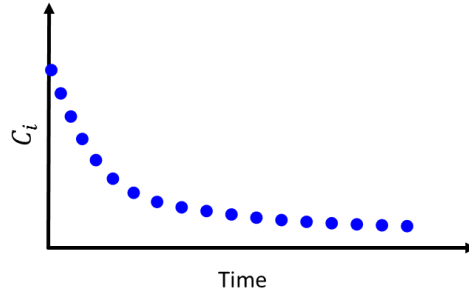


Figure 5. 54: Experimental concentration time course

By means of numerical and/or graphic differentiation of measured concentration data  $C_i(t)$ , the derivative  $\frac{dC_i}{dt}$  (i.e. the rate) can be determined. Plotting the logarithm of reaction rate as a function of logarithm of reactant concentration, the results can be approximated as a straight line (by linear regression), the slop of which is the reaction order as shown in Figure 5. 55.

$$\ln r = \ln \vartheta_i k + \alpha \ln C_i \quad (5. 24)$$

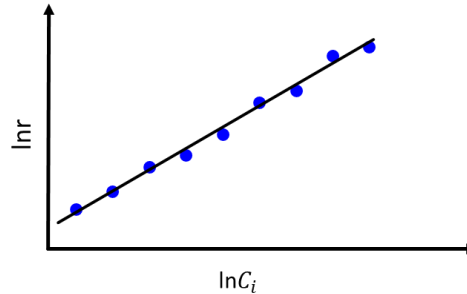


Figure 5. 55: Determination of the reaction order using differential method

With the estimated reaction order, the reaction rate constant  $k$  can be estimated numerically. Assuming the reaction rate constant  $k$  follows the Arrhenius law, which is as:

$$k(T) = k_\infty \exp\left(-\frac{E_A}{RT}\right) \quad (5. 25)$$

$$\ln k(T) = \ln k_\infty - \frac{E_A}{R} \cdot \frac{1}{T} \quad (5. 26)$$

Taking logarithms of both sides of eq. (5. 25) gives the napierian logarithm of reaction rate constant as shown in eq. (5. 26), which provides the pre-exponential factor ( $k_\infty = e^{\text{intercept}}$ ) and the activation energy ( $E_A = -T \cdot \text{slop}$ ) from the slopes and intercepts.



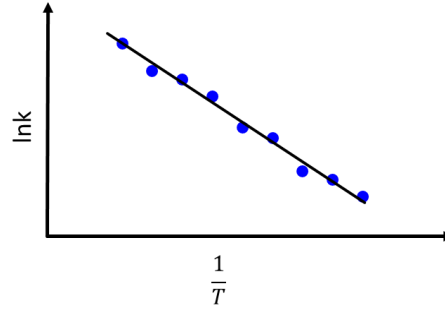


Figure 5.56: Determination of pre-exponential factor and activation energy by differential method

### 5.3.2.3 Objective function and final optimization

Kinetic parameters obtained from preliminary estimation are substitute into MATLAB program as initial values to get more precise and realistic ones. The optimized estimation of kinetic parameters was performed by analytical regression and minimizing the objective function (OF) with MATLAB®. The objective function OF(k) is the residual sum of squares of the component molar flow rates, with respect to the model parameter vector k.

$$\text{OF}(k) = \sum_{j=1}^{n_{\text{resp}}} \omega_j \sum_{p=1}^{n_{\text{exp}}} (F_{p,j}^{\text{cal}} - F_{p,j}^{\text{exp}})^2 \xrightarrow{k} \text{test} \quad (5.27)$$

Where  $F_{p,j}^{\text{exp}}$  is the j-th experimental response in the p-th experiment and  $F_{p,j}^{\text{cal}}$  is the j-th response value calculated for the p-th experiment and are the weights for each response, which are calculated from:

$$\omega_j = \frac{\left( \sum_{i=1}^{n_{\text{exp}}} F_{j,i}^{\text{exp}} \right)^{-1}}{\sum_{j=1}^{n_{\text{resp}}} \left( \sum_{i=1}^{n_{\text{exp}}} F_{j,i}^{\text{exp}} \right)^{-1}} \quad (5.28)$$

During MATLAB optimization, “lsqnonlin” method is used for optimization. “lsqnonlin” solves nonlinear least-squares problems, including nonlinear data-fitting problems. Rather than compute the value  $\|f(x)\|_2^2$  (the sum of squares), lsqnonlin requires the user-defined function to compute the vector-valued function

$$f(x) = \begin{bmatrix} f_1(x) \\ \vdots \\ f_n(x) \end{bmatrix} \quad (5.29)$$

Then, in vector terms, you can restate this optimization problem as

$$\min_x \|f(x)\|_2^2 = \min_x (f_1(x)^2 + f_2(x)^2 + \dots + f_n(x)^2) \quad (5.30)$$

where x is a vector and f(x) is a function that returns a vector value.

## 5.3.3 Postulated reaction network 1

In the next three sections, three reaction networks of increasing complexity are suggested. Temperature profile along with the reactor length is considered as isothermal condition, because the length of catalyst bed is only 50mm (in the middle of a 250mm length quartz reactor) and the

temperature gradient is negligible.

Initially, a simplified reaction network (designated as network 1) with 3 reactions (Figure 5. 57) was studied. In this case, starting both with methane feed experimental data or ethylene feed ones, there are three reactions needed to be investigated. So for reaction network 1, all the parameters are estimated based on methane feed experimental data.

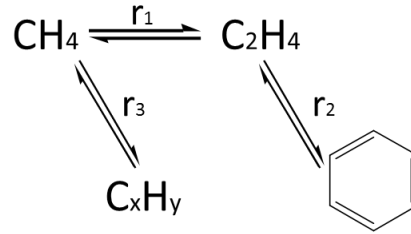
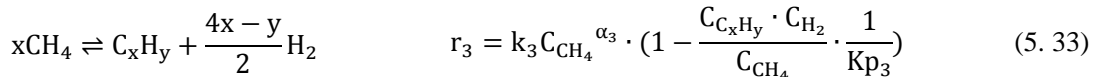
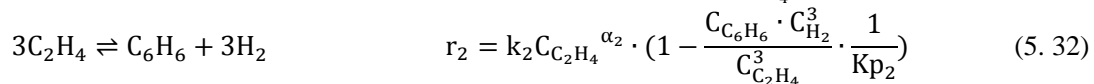
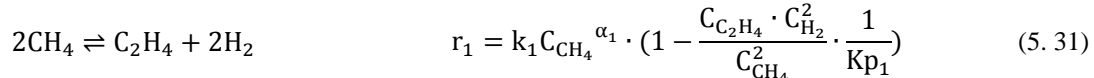


Figure 5. 57: Reaction network 1 with 3 reactions

The following reactions are considered in the postulated reaction network 1 and rate expressions are shown as follow:



While the reaction rates of reaction network 1 have to be calculated from experimental data, which are show as follow:

$$R_{\text{CH}_4} = \frac{\dot{n}_{0,\text{CH}_4} \cdot X_{\text{CH}_4}}{V_R} \quad (5.34)$$

$$r_1 = R_{\text{CH}_4} \cdot S_{\text{C}_2\text{H}_4} \cdot \frac{1}{2} + 3r_2 \quad (5.35)$$

$$r_2 = R_{\text{CH}_4} \cdot S_{\text{C}_6\text{H}_6} \cdot \frac{1}{6} \quad (5.36)$$

$$r_3 = \frac{1}{x}(R_{\text{CH}_4} - 2r_1) \quad (5.37)$$

With the experimental data, estimation of kinetic parameters is conduct by preliminary estimation (differential method) and optimized estimation (least square method).

### 5.3.3.1 Preliminary estimation of reaction network 1

All the simulations are based on the experimental data, therefore preliminary estimation of MDA in FBR includes 3 parts: (1) carbon and hydrogen balance calculation for all experimental data, based on which the composition of C<sub>x</sub>H<sub>y</sub> can be estimated (or the value of x and y); (2) fixed reaction temperature with changing inlet volumetric fraction, based on which reaction order can be estimated; (3) fixed inlet volumetric fraction with changing reaction temperature, based on which pre-exponential factor and activation energy can be calculated. As introduced in section 5.3.2.2, the value of x and y can be calculated since the carbon and hydrogen balance need to be fulfilled at the same time. And the value for network 1 is 10 and 8 respectively. So the coke for network 1 is in the

form of  $C_{10}H_8$ , but nothing to do with naphthalene. Firstly, experimental data of fixed reaction temperature with changing inlet methane volume fraction is simulated to get the reaction order of each reaction equations. Plotting napierian logarithm of reaction rate as a function of napierian logarithm of reactant concentration, the resulted slop of the linear regression is the reaction order. Figure 5. 58 shows one example of reaction number 1 at  $700^\circ\text{C}$ .

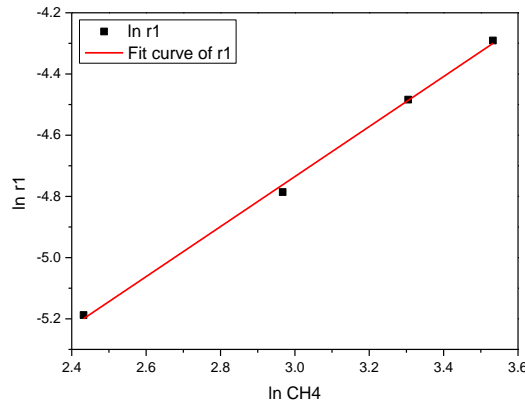


Figure 5. 58: Simulation of reaction order of reaction network 1

Table 5. 5: Reaction orders for all the temperature for network 1

Temperature ( $^\circ\text{C}$ )	$\alpha_1$	$\alpha_2$	$\alpha_3$
650	0.9204	1.0183	0.6641
675	0.8335	0.9505	0.6685
700	0.8173	0.9646	0.6494
725	0.8033	1.0001	0.6490
750	0.8394	1.0330	0.6042
Average	0.8408	0.9933	0.6470

Plotting napierian logarithm of reaction rate as a function of napierian logarithm of reactant concentration was made to each temperature and the final reaction order of each reaction is taken as the average of all the temperatures, as shown in Table 5. 5. The results shows that reaction No. 2 is nearly a first order reaction and reaction No. 3 has the lowest order which means the concentration of methane contributes the least to the rate of reaction No. 3.

After the simulation of reaction order, the pre-exponential factor and the activation energy of each reaction is estimated based on the experimental data of fixed inlet concentration at different temperatures. Plotting napierian logarithm of reaction rate constant as a function of reaction temperature reciprocal, the resulted slop and intercept of the linear regression is the napierian logarithm of pre-exponential factor and activation energy divided by minus gas constant, as shown in Figure 5. 59. The points of reaction 2 at  $725^\circ\text{C}$  and  $750^\circ\text{C}$  are deviated from the tendency, so this two points are excluded from the linear fit. From the fitting report we know that the residual sum of squares and the Pearson's  $r$  for all reactions are all smaller than 0.02 and -0.95 respectively, which indicates that the linear fits are pretty reliable. The slopes and intercepts of each fitting line can be got from the fitting report, with which the pre-exponential factors and activation energy can be calculated as can be seen from Table 5. 6. The value of  $E_{a1}$  is 92.25, which is 6.4 times bigger

than the value of  $E_{a2}$  (14.83). This means reaction No.1 needs high temperature to reach reasonable conversion, but reaction No. 2 favors low temperature.

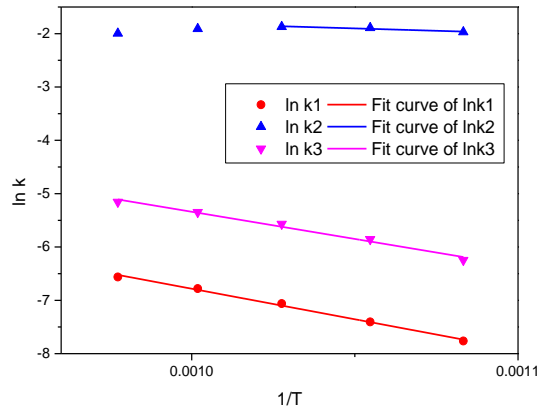


Figure 5. 59: Simulation of pre-exponential factor and the activation energy of network 1

Table 5. 6: Pre-exponential factor and the activation energy of network 1

Reaction	Slope	Intercept	$k_{\infty,i} \left( \frac{\text{m}^{3\alpha-3}}{\text{s}\cdot\text{mol}^{\alpha-1}} \right)$	$E_{A,i} \left( \frac{\text{kJ}}{\text{mol}\cdot\text{K}} \right)$
$r_1$	-11457	4.6743	107.16	95.25
$r_2$	-1783.4	-0.0286	0.9718	14.83
$r_3$	-10193	4.8542	128.28	84.74

### 5.3.3.2 Final optimize of reaction network 1

Kinetic parameters obtained from preliminary estimation are used as the initial values of optimized estimation to get more precise and realistic ones by the method of weighted least square method as introduced in section 5.3.2.3. The results are listed in Table 5. 7, from which we can see that the final results are quite similar as the results from preliminary estimation. Only  $k_{0,3}$  has a relatively big deviation, which confirms the availability of the preliminary estimation. The ratio of  $E_{A,1}/E_{A,2}$  is 6.6 now, which still indicates the contradicted temperature choice problem.

Table 5. 7: Optimized estimation of parameters in reaction network 1 (eq. (5. 31)-(5. 33))

Reaction	Activation Energy	Pre-factor	Reaction Order
	$(E_A \frac{\text{kJ}}{\text{mol}\cdot\text{K}})$	$(k_{\infty} \frac{\text{m}^{3\alpha-3}}{\text{s}\cdot\text{mol}^{\alpha-1}})$	$(\alpha)$
$r_1$	95.25	107.16	0.84
$r_2$	14.83	1.20	0.99
$r_3$	84.75	88.28	0.65

The estimated parameters in Table 5. 7 are checked with methane feed fraction of 30% and 90% from stepwise experiment for a smaller operation error. From Figure 5. 60 we can see that the experiment data and the simulate data are at the same degree and similar tendency. There is a relative big deviation of benzene molar flow rate at 750°C, which can be caused by the deactivated catalyst at 750°C in stepwise experiment. Maybe there is no real steady state for 750°C in stepwise experiment, so the experimental data at 750°C is already the value at deactivation state, which

should be lower than the value at steady state.

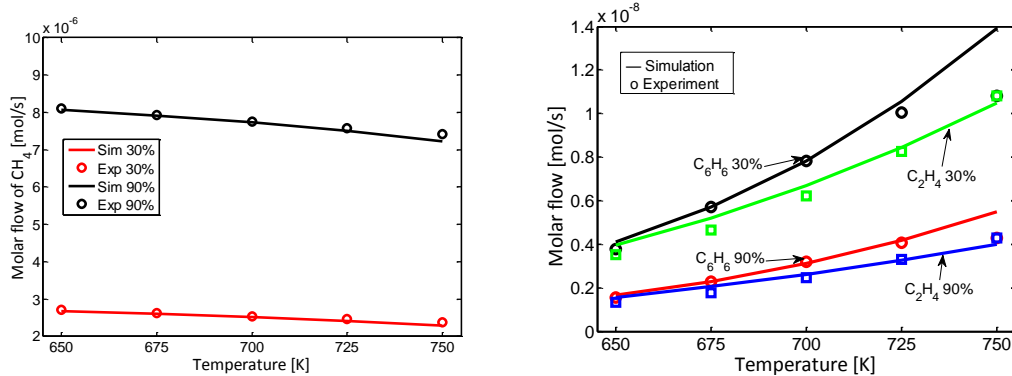


Figure 5.60: Comparison of simulated and stepwise experimental component molar flow rate

The estimated parameters are also used to compare with single experimental data, as shown in Figure 5.61. It is clear that, the simulation generally fits the experimental data. Again the biggest deviation appears to benzene molar flow rate, however not only at  $750^\circ\text{C}$  but also the other temperatures.

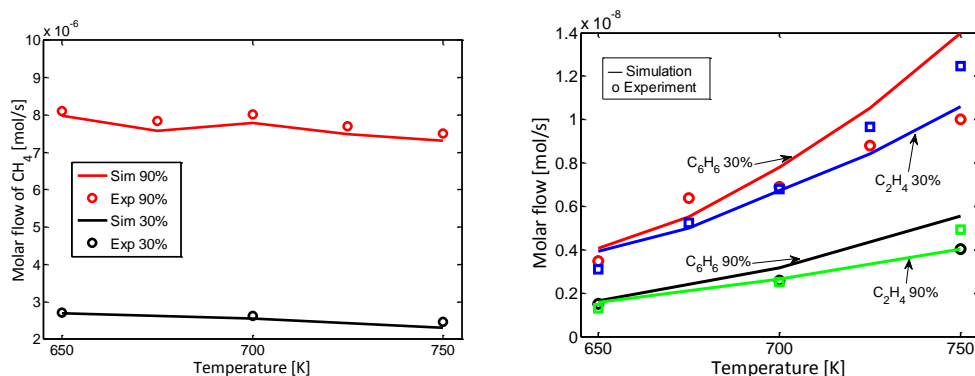


Figure 5.61: Comparison of simulated and single experimental component molar flow rate

### 5.3.4 Postulated reaction network 2

The simulation of reaction network 1 can perfectly represent the experiments below  $700^\circ\text{C}$ , and generally represent the ones at  $725^\circ\text{C}$  and  $750^\circ\text{C}$ . However, one weakness of reaction network 1 is ethane is not included in it. But actually ethane does exist in the product with a considerable amount. From the thermodynamic point of view, ethylene is much more reactive than methane, especially for the formation of carbon deposit. So, in the reaction network 2 (shown in Figure 5.62), the production from ethylene to ethane and coke are under more detailed consideration. For this case, there are five reversible reactions present in reaction network 2. The parameter estimation work should start from ethylene feed experiments, mainly consider 3 reactions which are  $r_2$ ,  $r_3$  and  $r_5$ . After that, the parameter estimation of the whole network could be done accordantly with sub network.

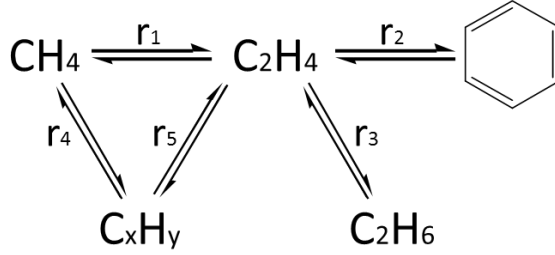
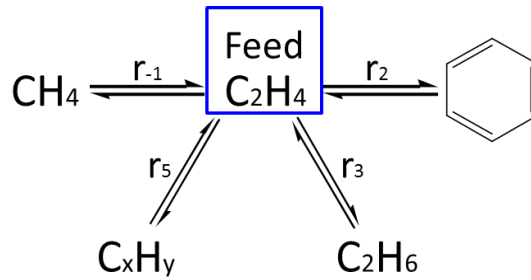


Figure 5. 62: Illustration of reaction network 2 with 5 reactions

### 5.3.4.1 Parameter estimation of sub-network 2

From the experimental result of ethylene feed, we know that the main products are benzene, methane and ethane. All the other hydrocarbons which cannot be detected by our GC is considered as coke with the homogeneous composition of C<sub>x</sub>H<sub>y</sub>. The sub-network of reaction network 2 are shown as Figure 5. 63. Within the sub-network 2, in total 4 reactions are studied, which are r<sub>2</sub>, r<sub>3</sub>, r<sub>5</sub> and the reverse reaction of r<sub>1</sub> in the whole network, which is represented as r<sub>-1</sub> here.

Figure 5. 63: Illustration of sub-network 2 with 4 reactions (C<sub>2</sub>H<sub>4</sub> feed)

The reactions and rate expressions of r<sub>2</sub> is eq. (5. 32), the rest are as follow:

$$\text{C}_2\text{H}_4 + 2\text{H}_2 \rightleftharpoons 2\text{CH}_4 \quad r_{-1} = k_{-1} \text{C}_{\text{C}_2\text{H}_4}^{\alpha_{-1}} \cdot \left(1 - \frac{\text{C}_{\text{CH}_4}^2}{\text{C}_{\text{C}_2\text{H}_4} \cdot \text{C}_{\text{H}_2}^2} \cdot \frac{1}{\text{Kp}_{-1}}\right) \quad (5. 38)$$

$$\text{C}_2\text{H}_4 + \text{H}_2 \rightleftharpoons \text{C}_2\text{H}_6 \quad r_3 = k_3 \text{C}_{\text{C}_2\text{H}_4}^{\alpha_3} \cdot \left(1 - \frac{\text{C}_{\text{C}_2\text{H}_6}}{\text{C}_{\text{C}_2\text{H}_4} \cdot \text{C}_{\text{H}_2}} \cdot \frac{1}{\text{Kp}_3}\right) \quad (5. 39)$$

$$x\text{C}_2\text{H}_4 \rightleftharpoons 2\text{C}_x\text{H}_y + (2x - y)\text{H}_2 \quad r_5 = k_5 \text{C}_{\text{C}_2\text{H}_4}^{\alpha_5} \cdot \left(1 - \frac{\text{C}_{\text{C}_x\text{H}_y}^2 \cdot \text{C}_{\text{H}_2}}{\text{C}_{\text{C}_2\text{H}_4}} \cdot \frac{1}{\text{Kp}_5}\right) \quad (5. 40)$$

While the reaction rates of sub-network 2 have to be calculated from experimental data, which are show as follow:

$$R_{\text{C}_2\text{H}_4} = \frac{\dot{n}_{0,\text{C}_2\text{H}_4} \cdot X_{\text{C}_2\text{H}_4}}{V_R} \quad (5. 41)$$

$$r_2 = R_{\text{C}_2\text{H}_4} \cdot S_{\text{C}_6\text{H}_6} \cdot \frac{1}{3} \quad (5. 42)$$

$$r_{-1} = R_{\text{C}_2\text{H}_4} \cdot S_{\text{CH}_4} \quad (5. 43)$$

$$r_3 = R_{\text{C}_2\text{H}_4} \cdot S_{\text{C}_2\text{H}_6} \quad (5. 44)$$

$$r_5 = \frac{1}{x}(R_{C_2H_4} - 3r_2 - r_{-1} - r_3) \quad (5.45)$$

With the experimental data, estimation of kinetic parameters is done with the same procedure introduced in section 5.3.2.2 and 5.3.2.3.

#### 5.3.4.1.1 Preliminary estimation of sub-network 2

The preliminary estimation for sub-network 2 also includes three parts: (1) estimation based on all ethylene feed experimental data for the  $C_xH_y$  composition calculation; (2) estimation based on fixed reaction temperature with changing inlet volumetric fraction experimental data for reaction order assessment; (3) estimation based on fixed inlet volumetric fraction with changing reaction temperature experimental data for pre-exponential factor and activation energy estimation.

The calculated values of  $x$  and  $y$  for sub-network 2 is 15.46 and 14.99 respectively with the lowest carbon and hydrogen balance variance of 4.7364E-43, which is acceptable. With that, reaction orders estimation from isothermal experimental data are plotted in Figure 5. 64. Since there are not so many available data for ethylene feed experiments, only 700°C data are used for reaction order calculation. From the linear fitting reports we can know that the slopes represent for reaction order for each reaction are 0.7877, 0.3012, 3.2343 and 0.3907 for  $r_2$ ,  $r_{-1}$ ,  $r_3$  and  $r_5$  respectively. The Pearson's  $r$  for all reactions are larger than 0.9 and the residual sub of squares are smaller than 0.061, which reveals reliable linear fittings. The fitted order of reaction No.3 (3.2343) is much higher than the stoichiometric coefficient (1). This may be caused by only ethylene concentration is considered for  $r_3$ . When hydrogen concentration is also considered as part of contribution to  $r_3$  and the same order as ethylene concentration, then the reaction order becomes to 0.5905 with the Pearson's  $r$  of 0.992.

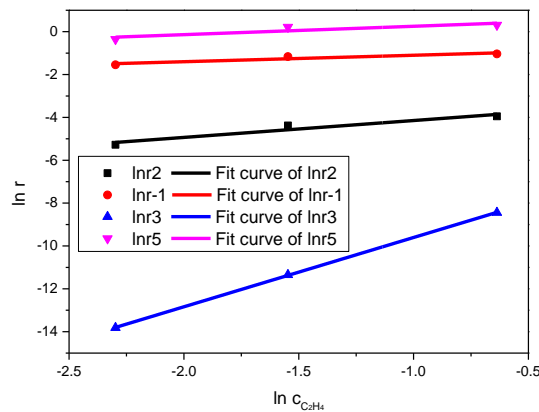


Figure 5. 64: Estimation of reaction order of sub-network 2

After the estimation of reaction order, the pre-exponential factor and the activation energy of each reaction is estimated based on the constant inlet fraction experimental data. Plotting napierian logarithm of reaction rate constant as a function of reaction temperature reciprocal for ethylene feed experimental data, the results are shown in Figure 5. 65. The points of reaction -1 at 700°C and 750°C as well as the points of reaction 2 at 700°C and 725°C are deviated from the tendency, so this four points are excluded from the linear fit. Tm the fitting report tell us that the residual sum of squares for all reactions and the Pearson's  $r$  for  $r_2$  and  $r_5$  are all smaller than 0.09 and -0.97 respectively, which indicates that the linear fits are pretty reliable. But the the Pearson's  $r$  for  $r_{-1}$  and  $r_3$  are 0.76 and 0.66, which are acceptable but not strongly reliable. The slopes and intercepts

are written in the fitting report, with which the pre-exponential factors and activation energy can be calculated as can be seen from Table 5. 8. From the values of activation energies ( $E_{a_{-1}} < E_{a_3} < E_{a_2} < E_{a_5}$ ) we know that, ethylene preferentially reacts to methane and ethane than benzene and carbon under low temperature condition, and vice versa.

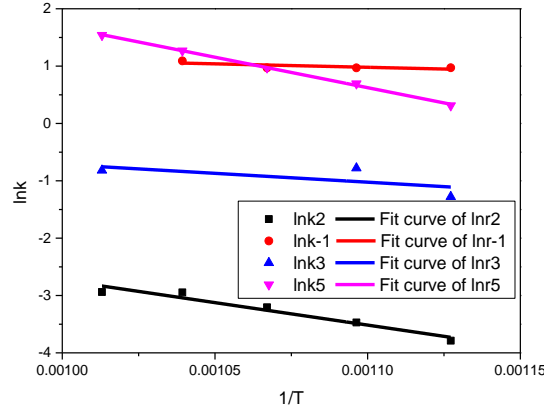


Figure 5. 65: Estimation of pre-exponential factor and the activation energy of sub-network 2

Table 5. 8: Pre-exponential factor and the activation energy of network 2

Reaction	Slope	Intercept	$k_{\infty,i} \left( \frac{\text{m}^{3\alpha-3}}{\text{s}\cdot\text{mol}^{\alpha-1}} \right)$	$E_{A,i} \left( \frac{\text{kJ}}{\text{mol}\cdot\text{K}} \right)$
$r_2$	-7833.0	5.1004	1.6409E+2	65.12
$r_{-1}$	-1206.5	2.3065	1.0039E+1	10.03
$r_3$	-3090.9	2.3759	1.0761E+1	25.70
$r_5$	-10624.4	12.3108	2.2213E+5	88.33

#### 5.3.4.1.2 Final optimization of sub-network 2

Kinetic parameters obtained from preliminary estimation are used as the initial values of optimized estimation, the same way as in section 5.3.3.2. The optimized estimation results of sub-network 2 is listed in Table 5. 9. The activation energy of  $r_2$ ,  $r_{-1}$  and  $r_5$  are more or less the same as preliminary results, which indicate similar product priority from ethylene feed. The reaction order of  $r_{-1}$  is higher than preliminary one. All the other parameters are lower than the one from preliminary estimation. The highest extent of declines is the pre-exponential factor of  $r_5$ , which decreases from  $2.22\text{E}+5$  to 17.77. The activation energy of  $r_{-1}$  and  $r_3$  are much smaller than  $r_2$  and  $r_5$ , which implies that  $r_2$  and  $r_5$  are the limitation of net reaction rate by thermodynamics in sub-network 2.

The optimized estimated parameters are checked with stepwise and single experimental results with 1% ethylene feed fraction at all temperatures. It can be seen from Figure 5. 66 that the simulation result of methane and ethylene molar flow rates are comparable to both experimental results. However, the simulation of benzene and ethane molar flow rates are deviated from experimental points, especially for benzene molar flow rate, even the opposite tendency to temperature. For ethane production, there is nearly no ethane except at  $650^\circ\text{C}$  for experiments. The simulation of ethane molar flow rate fit the point of single experimental results at  $650^\circ\text{C}$  and the tendency which is decrease with increasing temperature.



Table 5. 9: Optimized estimation of parameters in reaction network 2

Reaction	Activation Energy	Pre-factor	Reaction Order
	$(E_A \frac{\text{kJ}}{\text{mol}\cdot\text{K}})$	$(k_\infty \frac{\text{m}^{3\alpha-3}}{\text{s}\cdot\text{mol}^{\alpha-1}})$	$(\alpha)$
$r_2$	65.12	54.70	0.15
$r_{-1}$	10.03	2.01	1.00
$r_3$	25.70	1.08	0.94
$r_5$	58.33	17.77	0.05

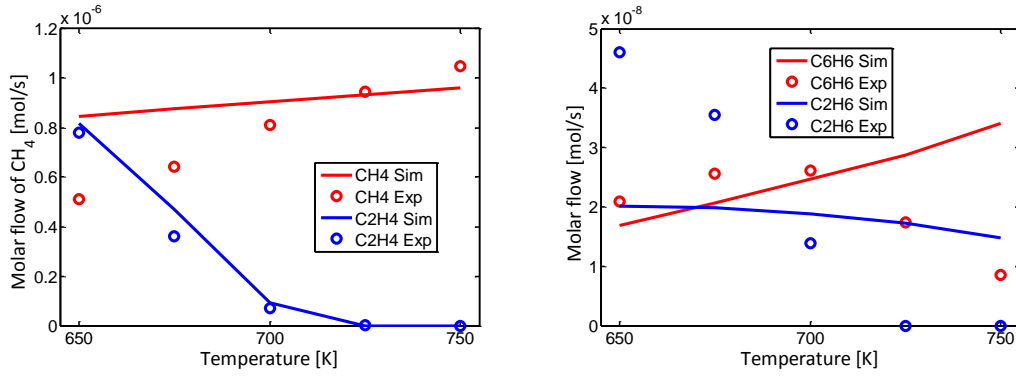
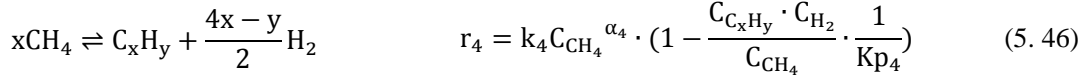


Figure 5. 66: Comparison of simulated and experimental component molar flow rate

### 5.3.4.2 Parameter estimation of reaction network 2

The reaction network 2 is shown in Figure 5. 62. The reactions and rate expressions of  $r_1$ ,  $r_2$ ,  $r_3$  and  $r_5$  are eq. (5. 31), (5. 32), (5. 39) and (5. 40), and the ones of  $r_4$  are shown below:



While the reaction rates of network 2 have to be calculated from experimental data, which are show as follow:

$$R_{\text{CH}_4} = \frac{\dot{n}_{0,\text{CH}_4} \cdot X_{\text{CH}_4}}{V_R} \quad (5. 47)$$

$$r_1 = R_{\text{CH}_4} \cdot S_{\text{C}_2\text{H}_4} \cdot \frac{1}{2} + 3r_2 + r_3 + x \cdot r_5 \quad (5. 48)$$

$$r_2 = R_{\text{CH}_4} \cdot S_{\text{C}_6\text{H}_6} \cdot \frac{1}{6} \quad (5. 49)$$

$$r_3 = R_{\text{CH}_4} \cdot S_{\text{C}_2\text{H}_6} \cdot \frac{1}{2} \quad (5. 50)$$

$$r_4 = R_{\text{CH}_4} \cdot S_{\text{C}_x\text{H}_y} \cdot \frac{1}{x} - 2 \cdot r_5 \quad (5. 51)$$

$$r_5 = k_5 \text{C}_{\text{C}_2\text{H}_4}^{\alpha_5} \cdot \left(1 - \frac{\text{C}_{\text{C}_x\text{H}_y}^2 \cdot \text{C}_{\text{H}_2}}{\text{C}_{\text{C}_2\text{H}_4}} \cdot \frac{1}{Kp_5}\right) \quad (5. 52)$$

One different aspect is  $r_5$  is not calculated from methane feed experimental data but from the theoretical equation with the parameters estimated from section 5.3.4.1. So the parameters from  $r_5$  are not estimated again in section 5.2.4.2.1, but are optimized in section 5.2.4.2.2.

### 5.3.4.2.1 Preliminary estimation of reaction network 2

The preliminary followed the same procedure as introduced in section 5.3.2.2. Since the rate of reaction No. 5 is calculated from the estimation results of sub-network 2, the value of  $x$  and  $y$  is also taken from the result of sub-network 2 which is 15.46 and 14.99 respectively. However, the carbon and hydrogen balances for methane feed experimental data are checked and fulfilled by this pair of values. The reaction orders of  $r_1$  to  $r_4$  are estimated in the same way as in section 5.3.2.2, which means the reaction orders are estimated at each temperature and then the average value of all temperatures are taken as the final result.

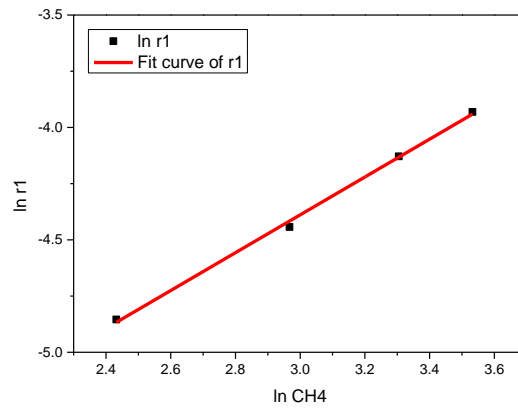


Figure 5. 67: Estimation of reaction order of reaction network 2

One example of reaction order estimation at 700°C is shown in Figure 5. 67 and all the estimation results are listed in Table 5. 10.  $\alpha_1$  is 0.8563 which is little bit bigger than the one from network 1 (0.8408), while  $\alpha_4$  is 0.6145 which is little lower than the one from network 1 (0.6470).  $\alpha_2$  is 0.9385 which is larger than the one from sub-network 2 (0.7877), and  $\alpha_3$  is 2.4517 which is lower than the one of preliminary estimation (3.2343) but higher than the one of optimized estimation (0.94) of sub-network 2. Generally speaking, the reaction orders are comparable to the ones estimated in the previous sections.

Table 5. 10: Reaction orders for all the temperature for network 2

Temperature (°C)	$\alpha_1$	$\alpha_2$	$\alpha_3$	$\alpha_4$
650	0.9120	1.0606	2.6431	0.6123
675	0.9012	0.9581	2.1968	0.6576
700	0.8299	0.8973	2.4212	0.5650
725	0.8058	0.8077	2.3711	0.5630
750	0.8327	0.9686	2.6261	0.6746
Average	0.8563	0.9385	2.4517	0.6145

After the simulation of reaction order, the pre-exponential factor and the activation energy of each reaction is estimated based on the constant concentration experimental data. Figure 5. 68 shows the plot of napierian logarithm of reaction rate constant as a function of reaction temperature reciprocal and the linear fitting report. The points of  $r_2$  and  $r_3$  at 725°C and 750°C are out of the tendency, so these points are not fitted by the linear regression. From the fitting report in Figure 5. 68 we can

read the residual sum of squares and Pearson's  $r$  of the regression are lower than 0.01 and -0.97. The slopes and intercepts are used to calculate the pre-exponential factors and activation energy as shown in Table 5. 11. The ratio of  $E_{a1}/E_{a2}$  is 5.9 now, which is comparable to the result in section 5.3.3.1.

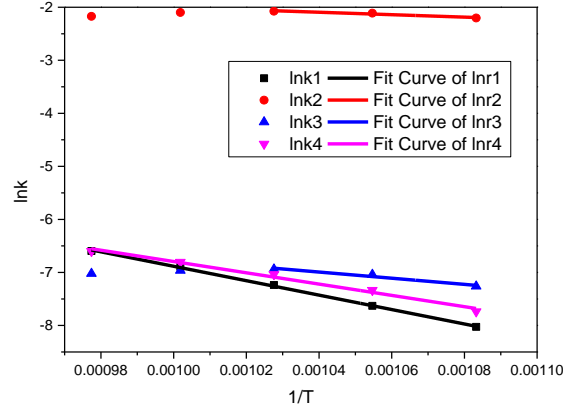


Figure 5. 68: Estimation of pre-exponential factor and the activation energy of reaction network 2

Table 5. 11: Pre-exponential factor and the activation energy of network 2

Reaction	Slope	Intercept	$k_{\infty,i} \left( \frac{\text{m}^{3\alpha-3}}{\text{s}\cdot\text{mol}^{\alpha-1}} \right)$	$E_{A,i} \left( \frac{\text{kJ}}{\text{mol}\cdot\text{K}} \right)$
$r_1$	-13602	6.7182	827.33	113.1
$r_2$	-2304.0	0.3020	1.3526	19.16
$r_3$	-5807.5	-0.9530	0.3856	48.28
$r_4$	-10642	3.8476	46.880	88.48

#### 5.3.4.2.2 Final optimization of reaction network 2

The kinetic parameters of  $r_1$  to  $r_4$  from preliminary estimation of network 2 and the parameters of  $r_5$  from sub-network 2 are used as the initial values of optimized estimation to get more precise and realistic ones by the method of weighted least square method as the same in the previous sections. The results are listed in Table 5. 12, which can be compared with the results in Table 5. 9, Table 5. 10 and Table 5. 11. It is clear that the value of  $E_{a1}$ ,  $E_{a3}$ ,  $k_{0,1}$  and  $\alpha_3$  are smaller, but the value of  $k_{0,2}$ ,  $k_{0,3}$  and  $k_{0,4}$  are larger than the ones from previous estimation. The ratio of  $E_{a1}/E_{a2}$  is 5.6 here, which indicates the same contradicted temperature choice problem as mentioned in section 5.3.3.1.

The estimated parameters in Table 5. 12 are also checked by the stepwise experimental results of 30% and 90% methane inlet volumetric fraction. The comparison of benzene, methane, ethylene, ethane, hydrogen as well as coke species molar flow rates are shown from Figure 5. 69 to Figure 5. 71. We can see that the simulation of methane and ethylene molar flow rate fit all the experimental points perfectly. For the molar flow rate of  $C_xH_y$  and  $H_2$ , simulation fits 30% feed experimental points very good, but is generally lower than the experimental points of 90% feed. While the simulation of  $C_6H_6$  molar flow rate is higher than the experimental points at high temperatures (725°C

and 750°C). The biggest deviation is the simulation of  $C_2H_6$  molar flow rate, which is higher than the 30% feed and crosses the 90% experimental points.

Table 5. 12: Optimized estimation of parameters in reaction network 2  
(eq. (5. 31), eq. (5. 32), eq. (5. 39), eq. (5. 46) and eq. (5. 40))

Reaction	Activation Energy	Pre-factor	Reaction Order
	$(E_A \frac{\text{kJ}}{\text{mol}\cdot\text{K}})$	$(k_\infty \frac{\text{m}^{3\alpha-3}}{\text{s}\cdot\text{mol}^{\alpha-1}})$	$(\alpha)$
$r_1$	108.1	627.3	0.85
$r_2$	19.16	1.653	0.94
$r_3$	23.28	1.928	0.90
$r_4$	88.48	136.9	0.61
$r_5$	58.33	17.77	0.05

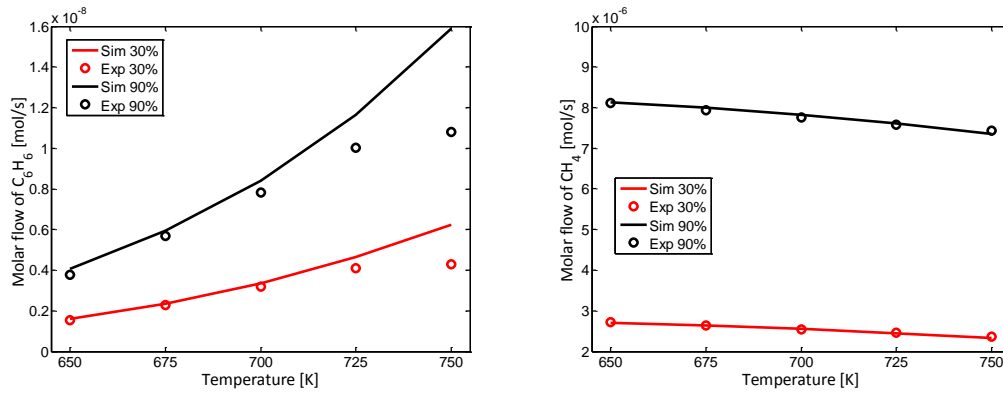


Figure 5. 69: Simulated and stepwise experimental benzene and methane molar flow rate

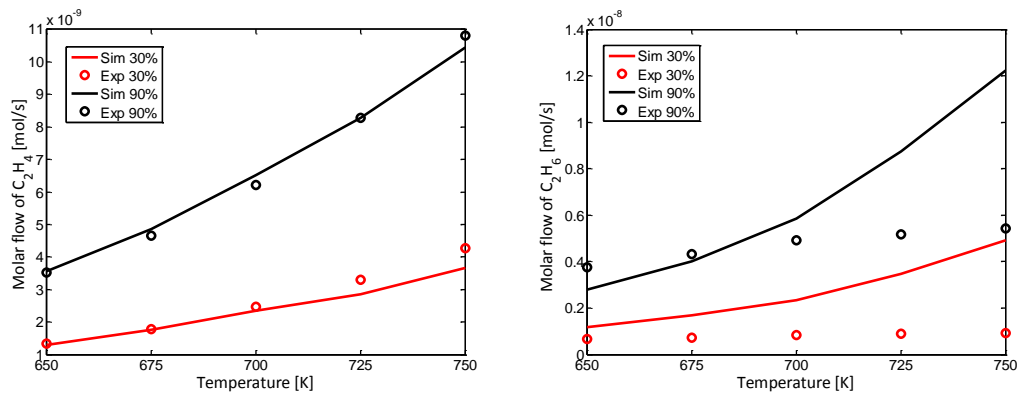


Figure 5. 70: Simulated and stepwise experimental ethylene and ethane molar flow rate

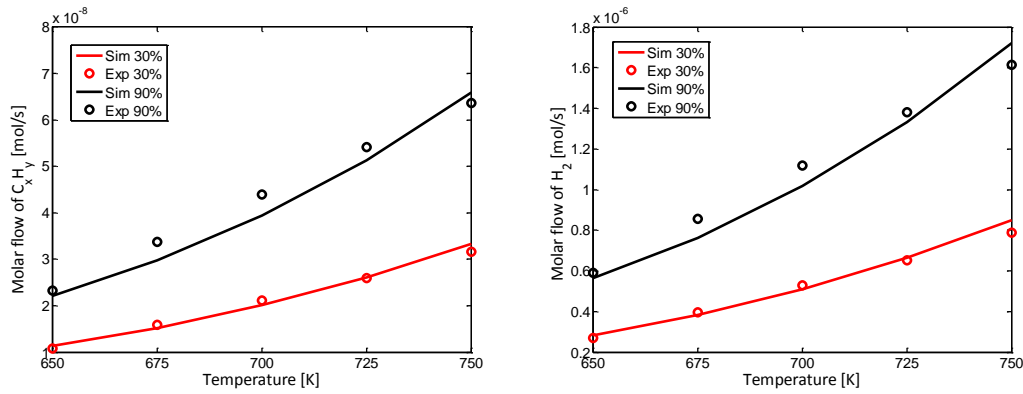


Figure 5.71: Simulated and stepwise experimental coke molar formation rate and hydrogen molar flow rate

The comparison of simulation to single experimental results are carried out as well and result can be seen from Figure 5.72 to Figure 5.74. The consistency is similar as the one of stepwise comparison, which is perfectly fitted to methane and ethylene, well fitted to  $C_xH_y$  and hydrogen and generally fitted to benzene and ethane molar flow rates.

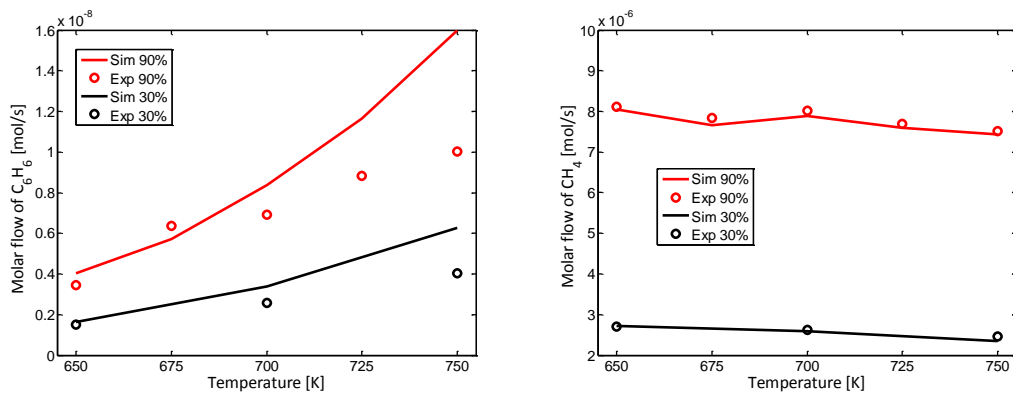


Figure 5.72: Simulated and single experimental benzene and methane molar flow rate

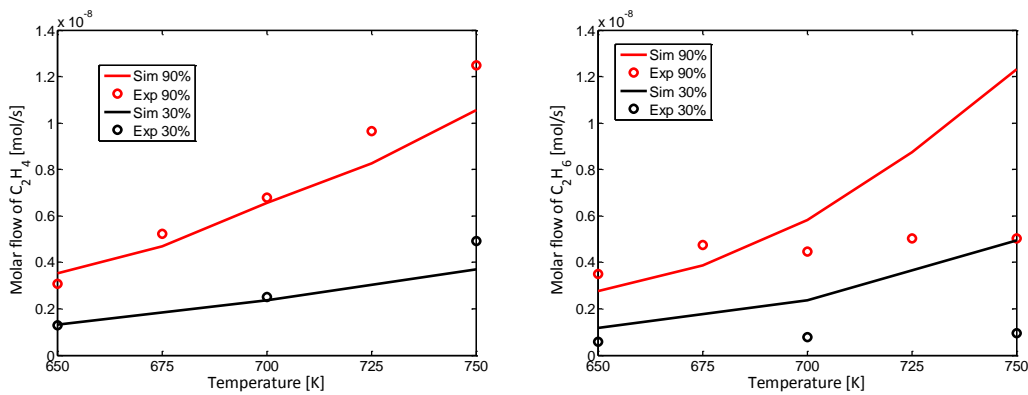


Figure 5.73: Simulated and single experimental ethylene and ethane molar flow rate

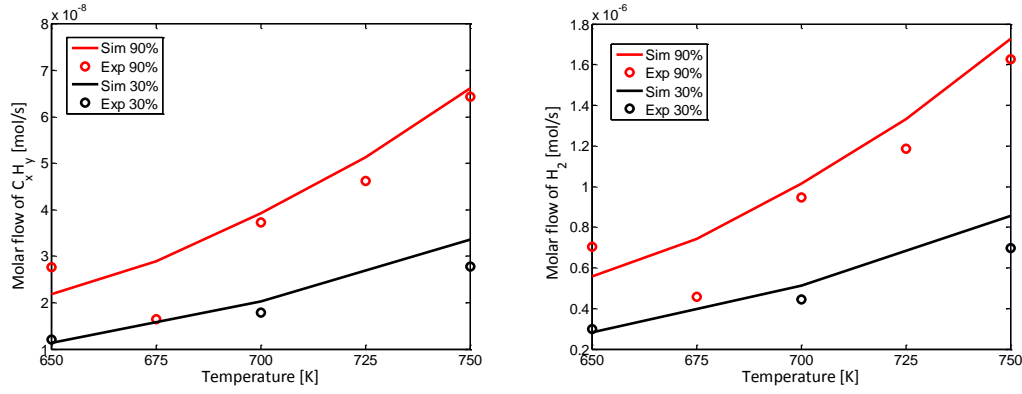


Figure 5.74: Simulated and single experimental coke molar formation rate and hydrogen molar flow rate

### 5.3.5 Postulate reaction network 3

The simulation of reaction network 2 can represent well the experimental results of methane and ethylene molar flow rate, and generally represent the others. However, there is another possibility for the production of ethane, which is methane dimerized to ethane. From the thermodynamic point of view, methane reacting to ethane ( $K_p(T = 700^\circ\text{C}) = 1.5221\text{E} - 04$ ) is much easier than to ethylene ( $K_p(T = 700^\circ\text{C}) = 3.3092\text{E} - 05$ ). So in the reaction network 3 (shown in Figure 5.75), the production from methane to ethane is also under consideration. For this case, there are six reversible reactions present in reaction network 3. The parameter estimation work should also start from ethylene feed experiments, mainly consider 4 reactions which are  $r_{-1}$ ,  $r_2$ ,  $r_3$  and  $r_5$ , which is exactly the same as sub-network 2. With the estimation results of sub-network 2, the parameter estimation of the whole network 3 could be done accordantly.

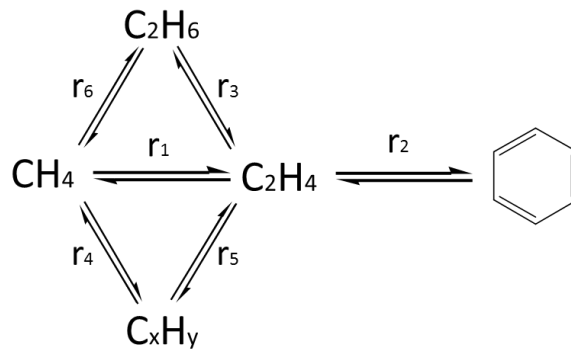
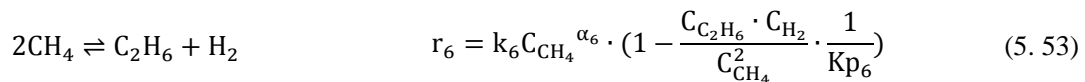


Figure 5.75: Illustration of reaction network 3 with 6 reactions

The reaction network 3 is shown in Figure 5.75 and the reactions and rate expressions of  $r_1$  to  $r_5$  are shown in the previous section (see eq. (5.31), (5.32), (5.39), (5.46) and (5.40)), the ones for  $r_6$  are:



While the reaction rates of network 3 have to be calculated from experimental data, which are show as follow:

$$R_{CH_4} = \frac{\dot{n}_{0,CH_4} \cdot X_{CH_4}}{V_R} \quad (5.54)$$

$$r_1 = R_{CH_4} \cdot S_{C_2H_4} \cdot \frac{1}{2} + 3r_2 + r_3 + x \cdot r_5 \quad (5.55)$$

$$r_2 = R_{CH_4} \cdot S_{C_6H_6} \cdot \frac{1}{6} \quad (5.56)$$

$$r_3 = k_3 C_{C_2H_4}^{\alpha_3} \cdot \left(1 - \frac{C_{C_2H_6}}{C_{C_2H_4} \cdot C_{H_2}} \cdot \frac{1}{Kp_3}\right) \quad (5.57)$$

$$r_4 = R_{CH_4} \cdot S_{C_xH_y} \cdot \frac{1}{x} - 2 * r_5 \quad (5.58)$$

$$r_5 = k_5 C_{C_2H_4}^{\alpha_5} \cdot \left(1 - \frac{C_{C_xH_y}^2 \cdot C_{H_2}}{C_{C_2H_4}} \cdot \frac{1}{Kp_5}\right) \quad (5.59)$$

$$r_6 = R_{CH_4} \cdot S_{C_2H_4} \cdot \frac{1}{2} - r_3 \quad (5.60)$$

The value of  $r_3$  and  $r_5$  is calculated form the sub-network estimated parameters (section 5.3.4.1) and the others are from methane feed experimental data. But the parameters for  $r_3$  and  $r_5$  will be optimized with all the other parameters together in section 5.3.5.2.

### 5.3.5.1 Preliminary estimation of reaction network 3

The preliminary followed the same procedure as introduced in section 5.3.2.2. Since the rate of reaction No. 3 and 5 are calculated from the estimation results of sub-network 2, the value of  $x$  and  $y$  is also taken from the result of sub-network 2 which is 15.46 and 14.99 respectively.

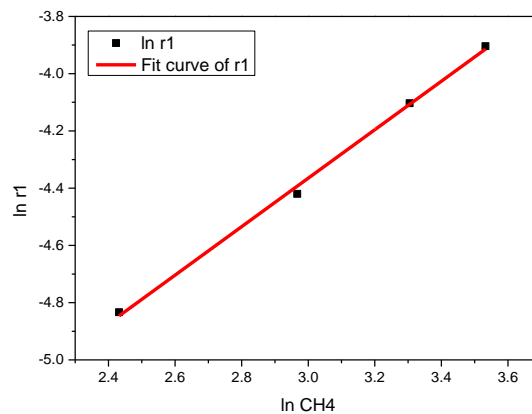


Figure 5. 76: Estimation of reaction order of reaction network 3

However, the carbon and hydrogen balances for methane feed experimental data are checked and fulfilled by this pair of values. The reaction orders of  $r_1$ ,  $r_2$ ,  $r_4$  and  $r_6$  are estimated in the same way as in section 5.3.3.1 and 5.3.4.2, which means the reaction orders are estimated at each temperature and then the trim average value (without the max and min value) are taken as the final result. One example of reaction order estimation at 700°C is shown in Figure 5. 76 and all the estimation results are listed in Table 5. 13.  $\alpha_1$  is 0.8630 which is a bit bigger than the one from

network 1 (0.8408) and the one from network 2 (0.8563), while  $\alpha_4$  is 0.5710 which is little lower than the one from network 1 (0.6470) and the one from network 2 (0.6145).  $\alpha_2$  is 0.9413 which is in between of the one from network 1 (0.9933) and the one from network 2 (0.9385). However,  $\alpha_6$  is 1.8336 which is slightly lower than the stoichiometric coefficient (2). Generally speaking, the reaction orders are comparable to the ones estimated in the previous sections.

Table 5. 13: Reaction orders for all the temperature for network 3

Temperature (°C)	$\alpha_1$	$\alpha_2$	$\alpha_4$	$\alpha_6$
650	0.9138	1.0606	0.6085	1.8016
675	0.9048	0.9581	0.3219	1.8217
700	0.8470	0.8973	0.5572	1.7381
725	0.8117	0.8077	0.5532	1.8775
750	0.8370	0.9686	0.6690	2.4480
Average	0.8630	0.9413	0.5710	1.8336

After the simulation of reaction order, the pre-exponential factor and the activation energy of each reaction is estimated the same way as in the above preliminary estimation sections. Figure 5. 77 shows the linear fitting report of napierian logarithm of reaction rate constant as a function of reaction temperature reciprocal plot. The points of  $r_2$  and  $r_6$  at 725°C and 750°C are out of the tendency, so these four points are not considered in the linear regression. From the fitting report in Figure 5. 77 we can read the residual sum of squares and Pearson's r of the regression are lower than 0.012 and -0.96. The slopes and intercepts are used to calculate the pre-exponential factors and activation energy as shown in Table 5. 14. The ratio of  $E_{a1}/E_{a2}$  is 5.9, which is quite comparable to the value of reaction network 1 and 2.

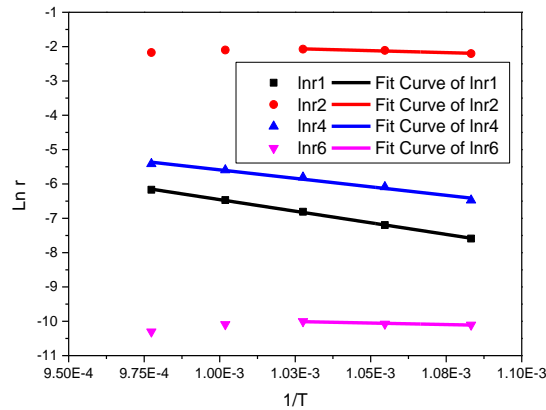


Figure 5. 77: Estimation of pre-exponential factor and the activation energy of reaction network 3

Table 5. 14: Pre-exponential factor and the activation energy of network 3

Reaction	Slope	Intercept	$k_{\infty,i} \left( \frac{\text{m}^3\alpha-3}{\text{s}\cdot\text{mol}^{\alpha-1}} \right)$	$E_{A,i} \left( \frac{\text{kJ}}{\text{mol}\cdot\text{K}} \right)$
$r_1$	-13501	7.0446	1.1467E+03	112.25
$r_2$	-2304.0	0.3020	1.3526E+00	19.156
$r_4$	-9889.0	4.2997	7.3678E+01	82.217
$r_6$	-1769.5	-8.1927	2.7667E-04	14.712



### 5.3.5.2 Final optimization of reaction network 3

The kinetic parameters of  $r_1$ ,  $r_2$ ,  $r_4$  and  $r_6$  from preliminary estimation of network 3 and the parameters of  $r_3$  and  $r_5$  from sub-network 2 are used as the initial values of optimized estimation to get more precise and realistic ones by the method of weighted least square method as the same in the previous sections. The results are listed in Table 5. 15, which can be compared with the results in Table 5. 12. It is clear that the value of  $E_{a1}$ ,  $E_{a3}$ ,  $k_{0,1}$ ,  $\alpha_1$ ,  $\alpha_3$  and  $\alpha_5$  are bigger, but the value of  $E_{a4}$ ,  $k_{0,2}$ ,  $k_{0,3}$ ,  $k_{0,4}$  and  $\alpha_4$  are smaller than the ones from previous estimation. The ratio of  $E_{a1}/E_{a2}$  is the same as in the previous section.  $E_{a4}$  and  $E_{a5}$  are relatively big, which means high temperature operation benefits the coke formation ( $r_4$  and  $r_5$ ). This still implies the contradicted temperature choice problem, which is high temperature benefits methane conversion but also benefits coke formation and loses benzene production, and vice versa.

Table 5. 15: Optimized estimation of parameters in reaction network 3  
(eq. (5. 31), eq. (5. 32), eq. (5. 39), eq. (5. 46), eq. (5. 40) and eq. (5. 53))

Reaction	Activation Energy	Pre-factor	Reaction Order
	$(E_A \frac{\text{kJ}}{\text{mol}\cdot\text{K}})$	$(k_\infty \frac{\text{m}^{3\alpha-3}}{\text{s}\cdot\text{mol}^{\alpha-1}})$	$(\alpha)$
$r_1$	112.2	1147	0.86
$r_2$	19.16	1.550	0.94
$r_3$	25.70	2.160	1.24
$r_4$	82.22	73.68	0.57
$r_5$	58.33	22.78	1.00
$r_6$	14.71	2.8e-4	1.02

The estimated parameters in Table 5. 15 are checked by the stepwise experimental results of 30% and 90% methane inlet volumetric fraction. The comparison of benzene, methane, ethylene, ethane, hydrogen as well as coke specise molar flow rates are shown from Figure 5. 78 to Figure 5. 80. We can see that the simulation of methane molar flow rate fit all the experimental points perfectly. For the molar flow rates of  $C_6H_6$ ,  $C_2H_4$ ,  $C_xH_y$  and  $H_2$ , the simulation fit all the experimental points except at 750°C. At 750°C, the simulated molar flow rates of benzene, hydrogen and carbon deposit are slightly higher than experiments, while the simulated molar flow rates of ethylene are lower than the experimental ones. The biggest diviation is the simulation of  $C_2H_6$  molar flow rate, which is higher than the 30% feed and crosses the 90% experimental points.

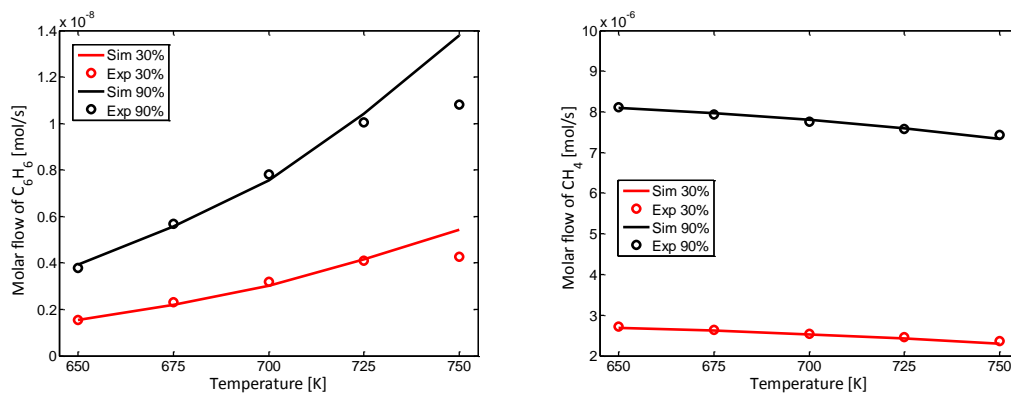


Figure 5. 78: Simulated and stepwise experimental benzene and methane molar flow rate

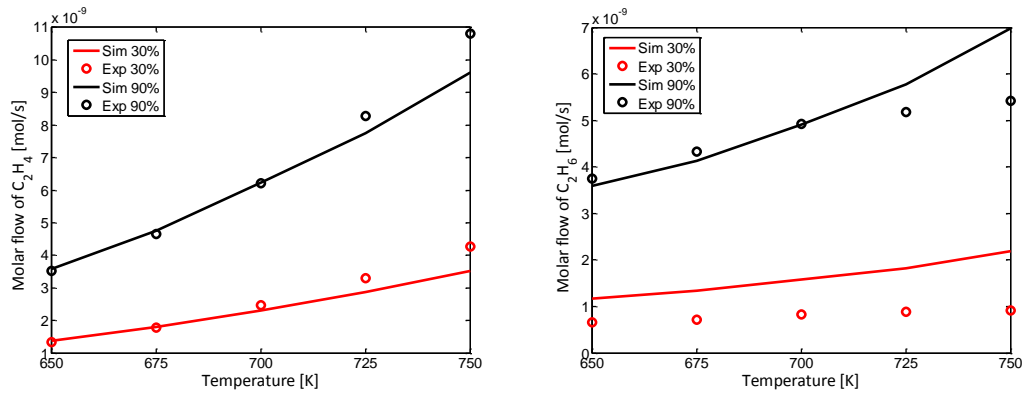


Figure 5.79: Simulated and stepwise experimental ethylene and ethane molar flow rate

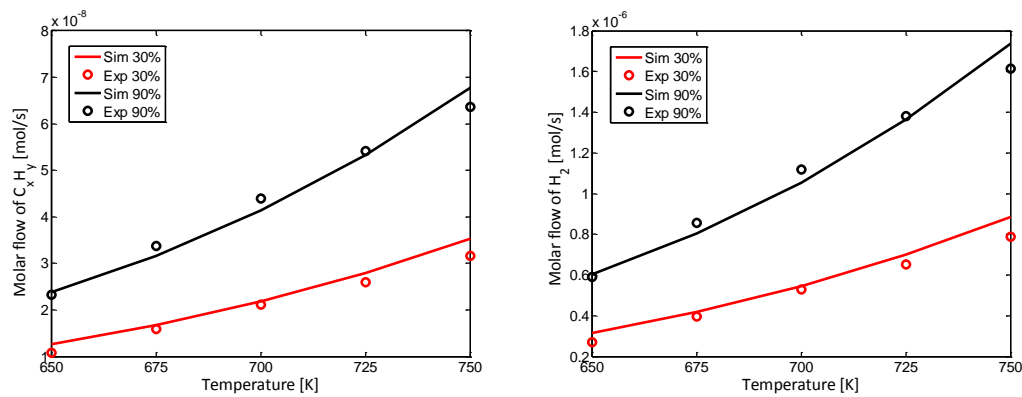


Figure 5.80: Simulated and stepwise experimental coke molar formation rate and hydrogen molar flow rate

The comparison of simulation to single experimental results are carried out as well and result can be seen from Figure 5.81 to Figure 5.83. The consistency is similar as the one of stepwise comparison, which is perfectly fitted to methane, well fitted to benzene, ethylene,  $C_xH_y$  and hydrogen and generally fitted to ethane molar flow rates.

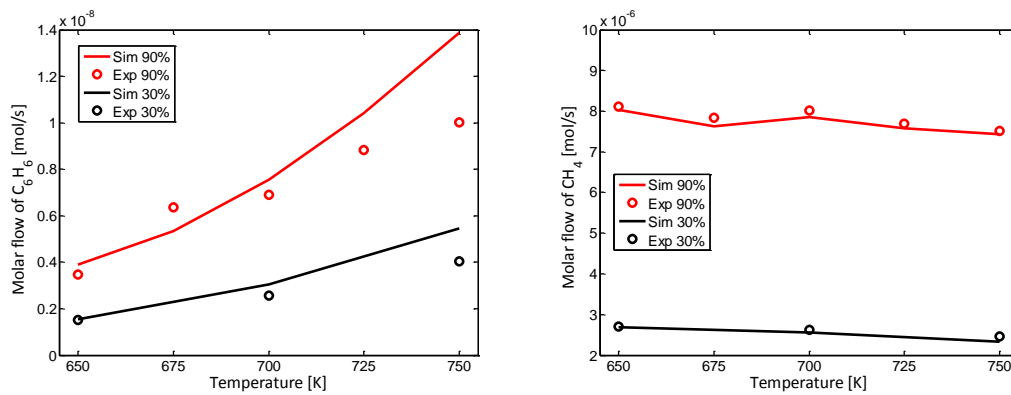


Figure 5.81: Simulated and single experimental benzene and methane molar flow rate

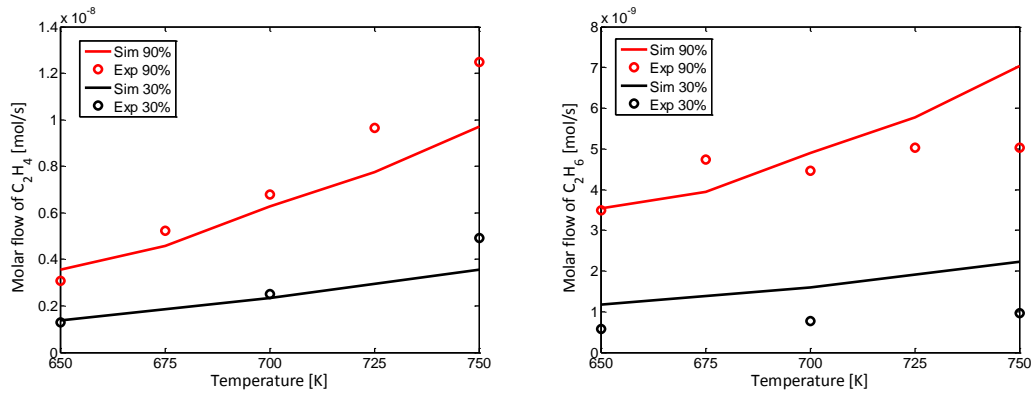


Figure 5.82: Simulated and single experimental ethylene and ethane molar flow rate

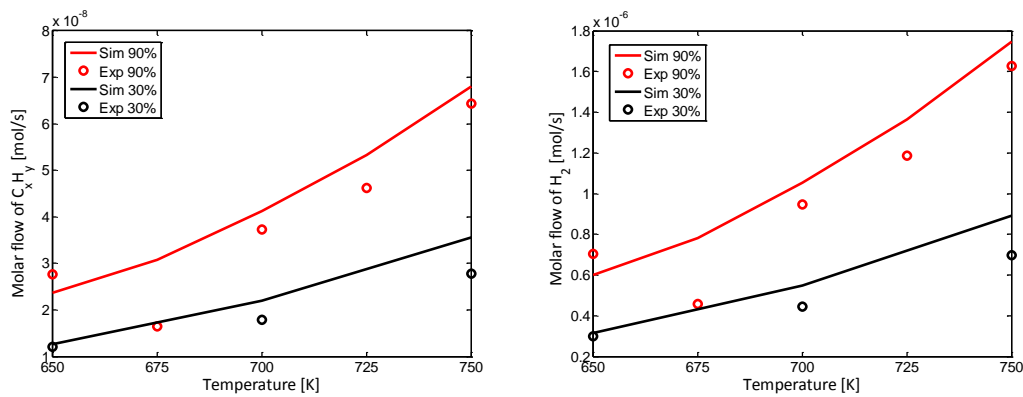


Figure 5.83: Simulated and single experimental coke molar formation rate and hydrogen molar flow rate

The effectiveness of the simulation is evaluated and plotted in Figure 5.84. The solid line in the figure is the symmetry line with the function of  $y=x$ , and the two dash lines are the 10% deviation from the symmetry line with the function of  $y=x \pm 1e-6$ . From the figure we can see that all the points are around the symmetry line and are in the domain of the two dash lines, which refers to a very good simulation performance.

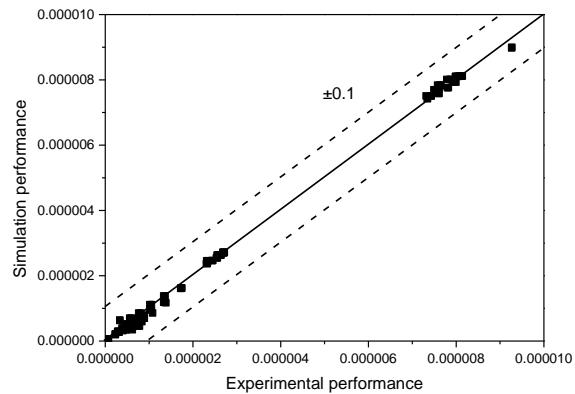


Figure 5.84: Simulation performance evaluation compared with experimental performance

## 5.4 Conclusions

This chapter has presented the analysis of the experimental results of MDA obtained in a FBR for the main reaction network with methane feed and for the sub-network with ethylene feed. The goal was to derive simplified models, which are able to describe the complex reaction kinetics. Different attempts were made in order to determine reliable kinetic data.

Single experiments and stepwise experiments were carried out for the same operating condition to illuminate the operating regime effect, as well as to study the effect of deactivation in long time experiments. For all the experiments, no real steady state was observed. A pseudo steady state was defined based on the benzene molar flow rate in a characteristic time window.

For methane feed experiments, with increasing temperature, the pseudo steady state methane conversion increased but benzene selectivity slightly decreased. W/F and methane feed fraction caused a coupled influence of methane conversion and product (benzene, ethylene and ethane) selectivities. Methane conversion and benzene selectivity were always in opposite direction influenced jointly. Methane conversion for all experiments was generally lower than 10%, which show a great potential for applying membrane reactors.

For ethylene feed experiments, ethylene conversion and methane selectivity are always influenced by temperature and ethylene feed fraction. This means methane is the premier product in ethylene feed system. As in the methane feed experiments, ethylene conversion and benzene selectivity are differently influenced. Operating conditions also strongly influenced the catalyst deactivation state. This implies that a compromised balance has to be made during selecting a suitable operating condition (temperature, methane feed volumetric fraction and W/F).

Based on experimental results, three simplified reaction networks with different complexity were proposed and parameterized. The simplest network is reaction network No. 1 (see Figure 5. 57 with parameters in Table 5. 7) with the most limited accuracy. The most accurate one is reaction network No. 3 (see Figure 5. 75 with parameters in Table 5. 15). The estimated parameters (especially activation energies) imply that high temperature operation of MDA favors methane conversion to ethylene also causes coke formation and reduced benzene production. The choice of temperature is a crucial problem in carrying out MDA.

The experimental results of this chapter provide useful information how temperature, feed concentration and residence time influence MDA performance. This operation performance map allows to choose suitable operating parameters. The simulation results of this chapter will be used below to predict MDA performance for selected conditions.

An important information for the later application of membrane in a membrane reactor is the amount of hydrogen generated by the MDA reaction. In the applied FBR volume of  $1.413\text{E-}6\text{m}^3$ , the molar flow rate of hydrogen produced in the pseudo steady state is approximately  $3.0\text{E-}8\text{ mol/s}$  at  $T = 700^\circ\text{C}$  for  $x_{0,\text{CH}_4} = 30\%$  and  $W/F = 2160\text{ kgs/m}^3$ . This means the space time yield (STY),  $STY_{\text{H}_2} = \frac{\dot{n}_{\text{H}_2}^R}{V_R}$  of hydrogen is approximately  $0.021\text{ mol}/(\text{s}\cdot\text{m}^3)$  also for product benzene  $STY_{\text{C}_6\text{H}_6}$  is

---

approximately  $0.0017 \text{ mol}/(\text{s}\cdot\text{m}^3)$ , which is below the typical “window of reality” of  $\text{STY}=1\text{-}10 \text{ mol}/(\text{s}\cdot\text{m}^3)$  for the operation of catalytic reactors operated in industry [164] (see Figure 6. 27). To be effective in a MR of the extractor type [165], a membrane is needed which matches to the specific amount produced in terms of its area time yield (ATY,  $\text{ATY}_{\text{H}_2} = \frac{\dot{n}_{\text{H}_2}^M}{A_M}$ ).



## 6. Investigation in membrane reactors (MR)

### 6.1 Introduction into membrane reactor and theory of mass transfer

In recent years, several new and more sophisticated reactor types have been suggested and attract interest from researchers all over the world [166]. One of the most promising concepts is membrane reactor, which is based on separating certain reactants or products from each other directly in the reactor by membrane. Thus, the undesired backward reactions or side reactions can be suppressed. From the increasingly stringent environmental regulations as well as the quest for efficient multifunctional process intensification means, the use of membrane separation processes is foreseen to become widespread in industrial practice soon. The application of membrane reactors for dehydrogenation [167] and hydrogenation [168, 169] reactions has been receiving greater attention over the past few years. A membrane reactor is a device that takes advantage of the separation function of a membrane to imbalance selectively the species concentration distribution at specific locations within equilibrium controlled reaction media. Though the principle of such dual process is encountered in many naturally occurring biological functions, it seduced industry in the catalytic membrane reactor technology to find applications in selective recovery and separation of hydrogen that surpass the equilibrium conversion bottleneck.

In order to open more possibilities for enhancing the mature processes, membrane reactors have been intensively studied during the last few decades. The sixties of last century, Michaels [170] gave a definition of membrane reactor. In general, membrane reactor combines a catalyst-filled reaction chamber with a membrane to add reactants or remove products along the reactor length. According to IUPAC, membrane reactor is to integrate catalytic reaction and membrane separation into one operating unit, permeate certain component through selective membrane to verify the local concentration of certain component and then to verify the equilibrium or intermediate selectivity. Membrane reactors have many advantages: breaking the limitation of thermodynamic equilibrium, realizing the integration of reaction, separation and concentration, reducing the side reactions, coupling series or parallel multi-step reactions, alleviating or eliminating catalysts poisoning, controlling the reaction process of complex reaction system, combination of heat exchange and catalytic reaction, effectively increasing the contacts of incompatible reactants, eliminating the diffusion resistance of fast reactions, implement continuous automatic control easily and etc.. The more detailed state of the art and features of membrane reactors has been discussed in several reviews [167, 171-174]. In industry processes, usually the most important and also costly steps are the reactor and the separation of products. The combination of the two steps (catalytic reaction and membrane separation) into a single operating unit can improve both the process economics and the efficient use of resources, furthermore can potentially save energy and reactant consumption and reduce side-products production. For those reasons mentioned above, membrane reactors have long been the focus of interest and intensively studied. Membrane reactor is exactly the combined single unit and that's the reason why it has attracted so much attention. Membrane reactor could lead to potential applications in chemical industry especially in petrochemical industry.

In MDA process, the conversion of methane and selectivity of aromatics are strongly suppressed by

thermodynamics of the reaction as we discussed in the previous section 2.2. Not only the MDA process, but also many other endothermic synthesis reactions are vitally limited by their unfavorable thermodynamics. Consequently, the application of membranes exhibits the potential to improve the performance of MDA process in various ways compared with conventional reactors.

### 6.1.1 Application of membrane reactor in heterogeneous reaction

Tubular reactors, either fixed-bed or packed-bed reactors, combined with membrane are used the most widely when applying membrane reactors in heterogeneous catalysis. The heterogeneous catalysis is defined as catalysis with the catalyst in a different phase from reactants; usually the catalyst is a solid and the reactants and products are in liquid or gaseous phase and the reaction occurs at or near the phase boundary (solid surface). Tubular reactors for heterogeneous catalysis combined with a membrane could be classified by Caro [165] and Seidel-Morgenstern [175] into several types:

#### Type 1: Retainment of homogeneous catalysts

This kind of reactor shown in Figure 6. 1 exhibits the membrane to retain catalyst (homogenous) in the reactor. As this arrangement, continuous operation without separating and recycling the typically valuable catalyst can be achieved.

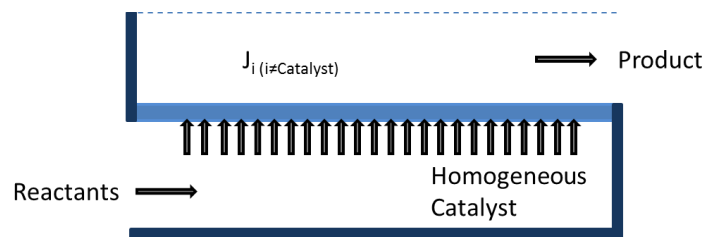


Figure 6. 1: Schematic diagram of retainment of homogeneous catalysts type

#### Type 2: Contactor

This kind of reactor shown in Figure 6. 2 is based on applying the membrane as an active “Contactor”. The reactants are fed into the reactor from different sides and react within the membrane.

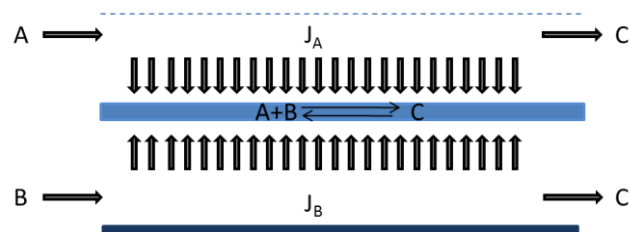


Figure 6. 2: Schematic diagram of “Contactor”

#### Type 3: Extractor

Extractor means it removes selectively certain products from the reaction zone via a membrane, as shown in Figure 6. 3. This concept has been widely studied and rather well understood. It



possesses the potential to enhance the reversible reaction conversion. In order to remove the permeable products and to increase the driving force for the transport, additional sweep gases or solvents are needed to apply the “Extractor” principle.

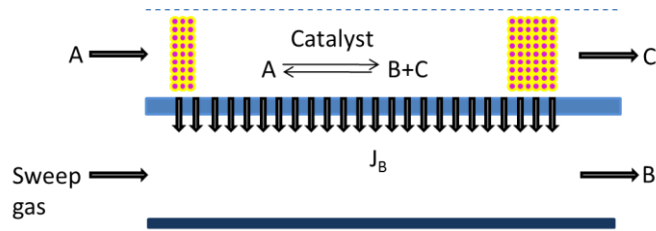


Figure 6. 3: Schematic diagram of extractor-type membrane reactor

#### Type 4: Energetic coupling

This concept shown in Figure 6. 4 can be used when two reactions are endothermic and exothermic and an attractive thermal coupling can be realized. In this situation an additional heat flux over the membrane takes place which offers interesting degrees of freedom to optimize the reactor from an energetic point of view.

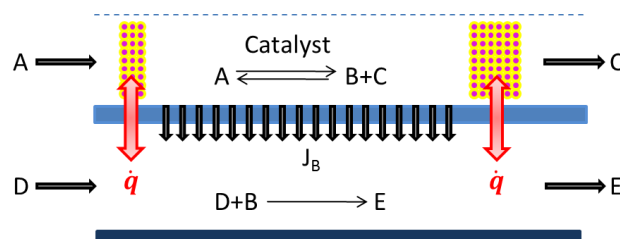


Figure 6. 4: Schematic diagram of energetic coupling membrane reactor

#### Type 5: Selectivity enhancement through withdrawal of a product

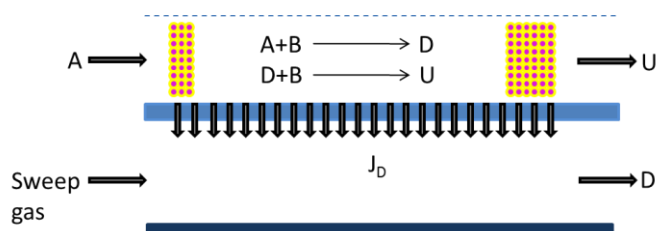


Figure 6. 5: Schematic diagram of selectivity enhancement through withdrawal of a product

Selectivity enhancement through withdrawal of a product: This concept is similar to “Extractor”. The removed component via membrane is an intermediate component generated in a reaction network. This removal can lead to reduce or completely avoid the undesired consecutive reaction or thermodynamic constraints so that further enhance the selectivity of intermediate component, as shown in Figure 6. 5. However the application of this concept requires very selective porous or dense membrane which is often not available for industry.

#### Type 6: Selectivity enhancement through optimized reactant dosing (distributor)

This interesting and attractive approach is using membrane to dose or distribute certain reactants in the reactor in order to achieve higher selectivity and yield, as shown in Figure 6. Different local concentrations and residence time in a reactor can vary the product's selectivity and yield. Distributor can change the selectivity of some certain product in parallel reactions. Distributor could dose one of the reactants through membrane to control the concentration of explosive reactant under the limitation to improve the security of the reaction system. Regarding rapid reaction systems, which demand extreme strict quantitative feed, one can use the large number of meso-scale pore of porous membrane as a special meso-scale membrane reactor. If the rapid reaction rate is controlled by diffusion and reactants diffuse from the two sides of membrane respectively, there will be a stoichiometric reaction surface in the membrane. Distributor could enhance the mass transfer between liquid and gas as well. Although this principle has been known and exploited for a long time, no industrial application of this concept has been reported.

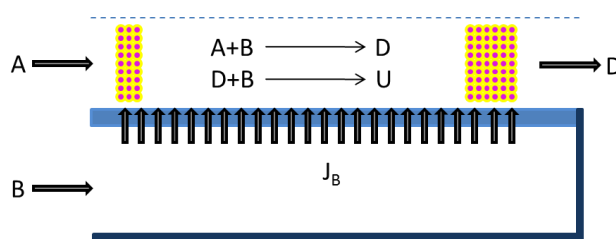


Figure 6. 6: Schematic diagram of distributor-type membrane reactor

### 6.1.2 Application of inorganic membrane reactor in MDA system

MDA process based on Mo catalysts shows relatively low reaction temperature ( $T < 975\text{K}$ ) with low carbon deposit and benzene yields, because active sites activate methane within shape-selectivity which restrict chain growth and produce aromatic polymer. The coupling of hydrogen permeating through the membrane will lead to higher methane conversion as a result of the breaking down of thermodynamic constraints, as discussed in chapter 2. Greater attention has been focused on the inorganic membrane design for membrane reactors because of their thermal stability, chemical resistance and mechanical strength. Such membranes may be either porous materials or dense impervious films. One of the major concerns in both cases is the film thickness. Thin membranes are more desirable because the hydrogen permeation flux is inversely proportional to the film thickness. However, very thin membranes may have the drawback of low mechanical strength and poor hydrogen perm-selectivity at high temperatures. One option to overcome this difficulty is to make composite membranes consisting of a thin impervious film deposited on a porous substrate such as glass, polyimide, ceramics, stainless steel or porous silver disks. In view of the reactor design, porous stainless steel materials seem to be a good choice because of their easiness in fabrication and processing, lack of corrosiveness, resistance to cracking and low cost. Coupling inorganic membrane separation with catalysis by membrane reactor, and extracting hydrogen from the reaction system to improve methane conversion and benzene selectivity has been studied [55, 112, 136, 140, 141, 176]. But the applied membrane are limited into Pd or Pd/Ag ally, which are costly. Preparative techniques of composite membranes include physical and chemical vapor deposition,

electroplating, and electroless plating. Electroless deposition has been widely used for the preparation of Pd-based membrane materials. Pre Pd membranes are prone to hydrogen embrittlement that occurs at temperatures below 523K. Hence, silver is added to prevent embrittlement and to improve the hydrogen permeation flux. The optimal alloy was found to have around 77% Pd and 23% Ag composition. Because of their high permeability and their mechanical strength, such membranes have found wide application in hydrogen recovery or purification and in the broader area of membrane reactor technology.

Palladium membranes have drawn increasing attention in recent years due to their good properties, such as good mechanical stability, thermal stability and only permeable to hydrogen [167]. Therefore, as one kind of membrane reactors, Pd membranes have wide applications in hydrogenation, dehydrogenation, H<sub>2</sub> separation and purification and some hydrogen related reactions. Especially the unique property of Pd membrane was illustrated in MDA, which made the research of Pd membrane more significant in academic and industry. Pd membrane has a special permeability to hydrogen, which means only hydrogen, no other gases, can pass through Pd membrane. The mechanism of hydrogen permeation, is really complex and complicated. There is a general theory named “dissolve -diffuse” [177] mechanism, which divides the permeation process into five reversible steps:

- (1) Hydrogen molecular spread to Pd membrane surface and adsorb chemically and reversibly;
- (2) Adsorbed hydrogen atom dissolve into the Pd lattice;
- (3) Dissolved hydrogen atom diffuse through the bulk of Pd membrane;
- (4) Hydrogen atom come out and adsorb on another surface of membrane;
- (5) Hydrogen atom assemble to hydrogen molecular and desorbed from the membrane surface and then spread to the gas flow.

The reason why hydrogen could permeate through Pd membrane is the formation of Pd-H solid solution in the body of palladium. When the temperature is higher than 573K and Pd/H ratio is low, only the  $\alpha$ -phase Pd-H exists. But when the temperature is below 573K and the pressure is lower than 2.0MPa, with increasing concentration of hydrogen in Pd membrane, there will be two different kinds of Pd-H solid solution exist at the same time,  $\alpha$ -phase (3.89Å) and  $\beta$ -phase (4.10Å). When verify the temperature or hydrogen concentration of palladium membrane,  $\beta$ -phase will nucleate and grow up in  $\alpha$ -phase because of the different lattice sizes of  $\alpha$ - and  $\beta$ -phase, which results the formation of strong stress within Pd membrane and then resulting in distorted and reducing the mechanical strength of palladium membrane. After continuously repeatedly absorbing and releasing hydrogen, it might lead to membrane rupture, which is defined as “hydrogen embrittlement” (HE) phenomenon. In order to avoid the impact of HE, some other metals, such as Ru, Rh, Ni, Cu, Ag, can be introduced to form a palladium alloy membrane. The alloy membrane can reduce the lattice sizes difference of  $\alpha$ - and  $\beta$ -phase, thereby reduce the influence of lattice expansion, which makes alloy membrane have more advantage at lower than 573K. Govind et al [178]. reported that the usage of Pd-Ag alloy membrane could lower down the HE temperature to 473K. Armor et al. [179] found that the use of Ru and Rh alloy membrane can even run stably at room temperature. Although palladium alloy membrane has a high resistance ability to HE, the introduction of alloying elements will reduce the catalytic performance of palladium membrane in reactions. Therefore, the synthesis of high stability pure Pd membrane has become the urgent problem of widely used of Pd membrane reactor.

Pd membrane reactor is a very important type of membrane reactor. Compared with the porous

membrane reactor, Pd membrane reactor has a unique selectivity for hydrogen, so it reflects great advantages at hydrogen related reaction system:

- 1) Breaking the thermodynamic equilibrium limitation;
- 2) Increasing the conversion and changing the selectivity of reactions;
- 3) Can get higher conversion at lower temperature;
- 4) Integrating several operating units such as reactant purification, products separation and chemical reaction;
- 5) Operating simply and saving energy.

With more concerning of Pd membrane reactor, the research about Pd membrane reactor is more in-deep. Research have mainly focused on dehydrogenation, hydrogenation, coupling of de- and hydrogenation, hydrogen purification and separation. Some progress has been made in membrane catalysis field. Dehydrogenation reaction is a kind of endothermic reaction, the equilibrium conversion of which is limited by temperature. Pd membrane reactor can removed the produced hydrogen timely, thus breaking down the thermodynamic limitation and moving the equilibrium to the target product direction. Guo et al. [180] studied Pd-Ag composite membrane reactor in isobutene dehydrogenation reaction and found that the equilibrium conversion of isobutene increased from 19.8% to 50.5% at 723K. She et al. investigated Pd membrane reactor for ethylbenzene dehydrogenation reaction and found that ethylbenzene conversion and styrene selectivity were increased 10% and 15% respectively compared with fixed bed reactor. Ali et al. [181] found that Pd membrane performed significantly higher than fixed bed reactor for methyl cyclohexane dehydrogenation to toluene reaction system. Pd membrane can improve the conversion of methyl cyclohexane to 80%, over the equilibrium conversion by 38%. Itoh et al. [182] studied Pd-Ag membrane reactor for cyclohexane dehydrogenation to benzene and found Pd-Ag membrane reactor could make the cyclohexane conversion reach to 99.7%, which is far exceeding the performance of fixed bed reactor. Sheintuch et al. [183] reported the use of Pd-Ru alloy membrane reactor for dehydrogenation reactions. The results found that isobutene conversion and butane yield can reach 81.2% and 75.9% respectively in isobutene dehydrogenation to butane reaction; propane conversion is up to 70% in propane dehydrogenation to propylene reaction, far higher than the equilibrium conversion of 38%. Kinage et al. [55] applied Pd membrane in MDA reaction system and found benzene yield is as tenfold high as fixed bed reactor at 883K and 3wt% Mo/ZSM-5. Chu [176] conducted MDA reaction in Pd/SAPO-34 composite membrane reactor and found methane conversion rate has more than double at 973K 6wt% Mo/HZSM-5 and purge ratio of 3:1.

Gallucci et al. [184] compared and simulated methanol steam reforming reaction in Pd-Ag membrane reactor and conventional reactor. The results show that methanol conversion was 25% higher in Pd-Ag membrane reactor than in conventional. Sandra et al. [185] compared the performance of methanol steam reforming reaction in Pd and carbon membrane reactor respectively by simulation. The results show that carbon membrane could improve the flux of products, but the selectivity of hydrogen was much lower than Pd membrane. They were studying the combination of carbon and Pd membrane to get a higher hydrogen yield.

Tong [186] investigated the performance of methane steam reforming reaction in Pd membrane reactor. By optimizing the reaction conditions, the maximum of methane conversion and hydrogen yield can reach 96.9% and 90.4% at the same time hydrogen producing capacity can reach 180.8ml/min. Matsumura et al. [187] also improved methane conversion in methane steam

reforming reaction by using Pd/PSS composite membrane reactor. In addition, high pure hydrogen can be get by Pd membrane reactor in water gas reforming reaction. Kikuchi et al. [188] found CO conversion and H<sub>2</sub> yield can both reach 100% by Pd membrane reactor in water gas reforming reaction at 673K. Basile [189] reported that CO conversion can be as high as 99.89% by Pd membrane reactor in water gas reforming reaction at 595K. Similarly, Xu et al. [190] obtained a higher CO conversion using Pd membrane reactor. Zhang et al. [191] reported the use of Pd membrane reactor for ammonia decomposition for high purity hydrogen and found that ammonia conversion, hydrogen recovery rate and purity can be up to 99.80%, 84.00% and 99.98% respectively.

### 6.1.3 Fundamentals of mass transfer

Molecular moves from an area of high concentration to an area of low concentration spontaneously, which is the reason why diffusion happens (into a catalyst particle or through a porous membrane). Diffusion processes occurring in porous media can be classified into various types, which include molecular diffusion, Knudsen diffusion, forced viscous flow, slip flow, configurational diffusion and surface diffusion. According to information by the manufacture, the carbon membranes used in this work consisted of five porous layers (see Table 4. 2). The transport through these layers occurs due to contributions of more than one mechanism. A detailed investigation of mass transfer should be done layer by layer. Since we did not have access to the support and the individual layers, simplified overall mass transfer models are used to describe the gas diffusion through carbon membranes.

In 1833, Graham [158] claimed that the rate of gas exchange is inversely proportional to the square root of their molar masses (6. 1). He did not only perform the first quantitative experiment of diffusion, but also provided the first reliable measurement allowing the determination of a coefficient of diffusion.

$$\frac{J_1}{J_2} = -\sqrt{\frac{M_2}{M_1}} \quad (6. 1)$$

In 1855, Fick [192] proposed the foundations of diffusion theory. According to Fick's law, the flow of a certain species in one dimension is related to the gradient of concentration.

$$J_i = -D_i \cdot \frac{\partial c_i}{\partial z} \quad i=1, \dots, N_C \quad (6. 2)$$

The diffusion coefficient D is defined as proportionality constant between the rate of flow and the concentration gradient.

$$\mu_i = \mu_i^0 + RT \cdot \ln \frac{\gamma_i P_i}{P^0} \quad i=1, \dots, N_C \quad (6. 3)$$

Thus the flux  $J_i$  can be described by a product of concentration  $c_i$ , mobility  $b_i$  and chemical potential driving force  $\frac{\partial \mu_i}{\partial z}$ .

$$J_i = -b_i c_i \cdot \frac{\partial \mu_i}{\partial z} \quad i=1, \dots, N_C \quad (6. 4)$$

With the definition of chemical potential eq. (6. 3), eq. (6. 4) can be transformed into eq. (6. 5) with the driving force of chemical potential gradient.

$$J_i = -b_i \cdot \frac{P_i}{RT} \cdot RT \cdot \frac{\partial \ln(\gamma_i P_i)}{\partial P_i} \cdot \frac{\partial P_i}{\partial z} = -b_i \cdot \frac{\partial \ln(\gamma_i P_i)}{\partial P_i} \cdot \frac{\partial P_i}{\partial z} \quad i=1, \dots, N_C \quad (6.5)$$

Comparing with eq. (6.5), eq. (6.2) can be written as:

$$J_i = -D_i \cdot \frac{\partial c_i}{\partial z} = -\frac{D_i}{RT} \cdot \frac{\partial P_i}{\partial z} \quad i=1, \dots, N_C \quad (6.6)$$

The diffusion related to mobility is defined:

$$D = bRT \cdot \frac{\partial \ln(\gamma_i P_i)}{\partial P_i} = D_c \cdot \Gamma \quad (6.7)$$

where  $D_c = bRT$  is corrected diffusivity and  $\Gamma$  is thermodynamic factor. While more often, the porous structure of real solids contributes a lot to the diffusion as well as the effective diffusivity. One simple way is to include proportional constants into transport coefficients as structural properties, such as porosity  $\varepsilon$  and tortuosity  $\tau$ . Therefore the flux through pore involves solely gas phase is usually defined as eq. (6.8).

$$J_g = -\frac{\varepsilon}{\tau} \cdot \frac{D}{RT} \quad (6.8)$$

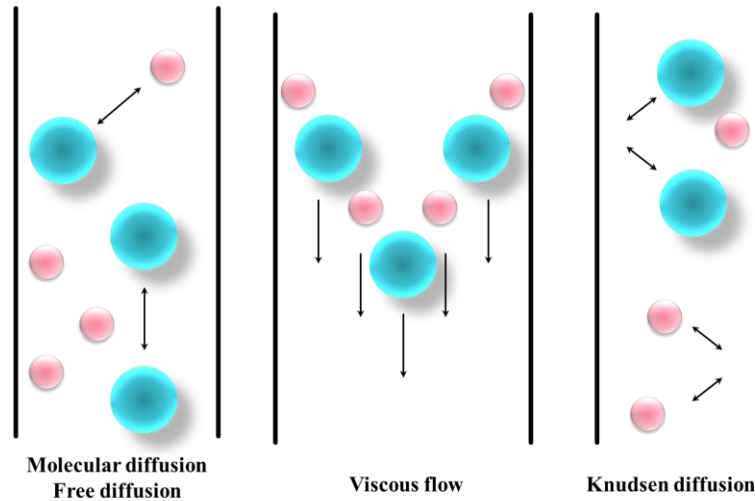


Figure 6.7: Transport mechanisms in porous media

According to IUPAC definition, materials can be classified in terms of pore size to: macroporous (pore diameter  $> 50\text{nm}$ ), mesoporous ( $2\text{nm} < \text{pore diameter} < 50\text{nm}$ ) and microporous (pore diameter  $< 2\text{nm}$ ) [193]. The diffusion of molecules in pores can be classified corresponding to the pore diameter as shown in Figure 6.7:

- Molecular diffusion dominating in macropores (diffusion constants of gases  $\approx 10^{-5}\text{m}^2\text{s}^{-1}$ )  
Molecular diffusion results from the collisions between diffusing molecules, which is dominant whenever the mean free path (average distance traveled between molecular collisions) of gases is relative small to pore diameter. It takes place in systems imposed by convective transport. For single gas or binary gas mixture system, the diffusive flux can be quantified by Fick's law as shown in eq. (6.2). For ternary or multiple systems, the diffusive flux can be expressed by Maxwell-Stefan approach see eq. (6.9).

$$-\frac{1}{P} \cdot \frac{\partial P_i}{\partial z} = \sum_{i=1, j \neq i}^n \left[ \frac{y_i J_{g,j} - y_j J_{g,i}}{c \cdot D_{ij}} \right] \quad (6.9)$$

where the Maxwell-Stefan diffusivity  $D_{ij}$  can be estimated as:

$$D_{ij} = \frac{\varepsilon}{\tau} \cdot \frac{0.00158 \cdot T^{\frac{3}{2}} \cdot \left(\frac{1}{M_i} + \frac{1}{M_j}\right)^{\frac{1}{2}}}{P \cdot \sigma_{ij}^2 \cdot \Omega\left(\frac{e}{kT}\right)} \quad (6.10)$$

In eq. (6.10),  $M_i$  and  $M_j$  are molecular weights,  $\sigma_{ij}$  is collision diameter and  $\Omega$  is a function of  $\frac{e}{kT}$ .

b. Knudsen diffusion for mesopores

Knudsen diffusion is induced by collision of gaseous molecules with the pore walls when the mean free path is larger than the pore diameter. Knudsen diffusion flux is:

$$J_k = -D_k \cdot \frac{\partial P}{\partial z} \quad (6.11)$$

$D_k$  is Knudsen diffusivity, the mostly common used of which in porous materials can be expressed as:

$$D_k = \frac{\varepsilon}{\tau} \cdot D_{k0} \quad \text{with } D_{k0} = \frac{1}{3} \cdot d_p \cdot \sqrt{\frac{8RT}{\pi M}} \quad (6.12)$$

c. Viscous flow for mesopores

When a total pressure gradient gives rise to mass transport by convective, there will be a contribution of viscous flow from the laminar flow through the mesopores. It can occur in the bigger pores in defects and cracks in the porous materials where interaction between molecules are so strong that the fluid can be considered to be flowing. Though viscous flow does not contribute to the separation of different species, its role may be very important in membrane reactors. For a single capillary, viscous flow can be calculated according to Hagen and Poiseuille. Due to laminar conditions, average velocity is directly proportional to the pressure gradient. A modified version of the Hagen-Poiseuille law that goes back to Darcy can be used for porous media, leading to a flux of:

$$J_v = -\frac{B_0}{RT} \cdot \frac{P}{\eta} \cdot \frac{\partial P}{\partial z} \quad \text{with } B_0 = \frac{\varepsilon}{\tau} \cdot \frac{d_p^2}{32} \quad (6.13)$$

d. Configurational diffusion for micropores

Configurational diffusion is reached when the molecular diameter is comparable to the pore diameter. The values of configurational diffusion coefficients span an enormous range from  $10^{-20}$  to  $10^{-8} \text{m}^2 \text{s}^{-1}$ . The configurational flux in the expression of pressure gradient is:

$$J_c = -D_c \cdot \frac{\partial P}{\partial z} \quad \text{with } D_c = \frac{1}{3} \cdot \frac{\varepsilon}{RT\tau} \cdot d_p \cdot \sqrt{\frac{8RT}{\pi M}} \cdot \exp\left(-\frac{\Delta E_g}{RT}\right) \quad (6.14)$$

There is possible an addition contribution to the flux through physically adsorbed layers on the surface of the macropores, which is called surface diffusion. Surface diffusion might be relatively very high due to larger molecular densities in adsorbed phase, especially at low temperature. The flux of surface diffusion can be written as:

$$J_s = -(1 - \varepsilon) \cdot D_s \cdot \frac{\partial q}{\partial z} \quad q \text{ is adsorbed concentration per unit of membrane volume} \quad (6.15)$$

The surface diffusion coefficient  $D_s$  is typically concentration dependent and follows:

$$D_s = RT\hat{b} \cdot \frac{\partial \ln P}{\partial \ln q} \quad (6.16)$$

where  $\hat{b}$  is the mobility on the surface.

## 6.2 Results for dense membrane (Palladium)

According to the analysis in section 2.2 and 2.3, we know that reactions in MDA are reversible reactions and the removal of hydrogen can be a solution to improve the performance. For that reason, membrane reactor can be applied to MDA system to remove the hydrogen from reaction zone. In order to investigate the potential of hydrogen selective membrane, palladium membrane model is used here since palladium membrane is dense with 100% selectivity to hydrogen. The model for hydrogen permeation through Pd membrane used here as shown in eq. (6.17) is from Gallucci [194].

$$J_{H_2} = A_0 \cdot e^{-\frac{E_a}{RT}} \cdot \left( \sqrt{p_{H_2}^{tube}} - \sqrt{p_{H_2}^{shell}} \right) \quad (6.17)$$

with  $A_0 = 7.06 \times 10^{-4} \text{ mol}/(\text{m}^2 \cdot \text{s} \cdot \text{Pa}^{0.5})$  and  $E_a = 29.16 \text{ kJ/mol}$ . Kinetic of reaction network 1 is applied as shown in Table 5.7. Equations for reactor modelling are shown from eq. (5.6) to (5.11). Figure 6.8 shows each component molar flow rate over dimensionless reactor axial coordinate in FBR and MR. Methane molar flow rate decreases and products ( $C_6H_6$ ,  $C_2H_4$ ,  $H_2$  and  $C_xH_y$ ) molar flow rates increase along with reactor length for both reactors but with different extent. The total molar flow of FBR increases but of MR decreases, which is because a certain amount of hydrogen is permeated through the Pd membrane.

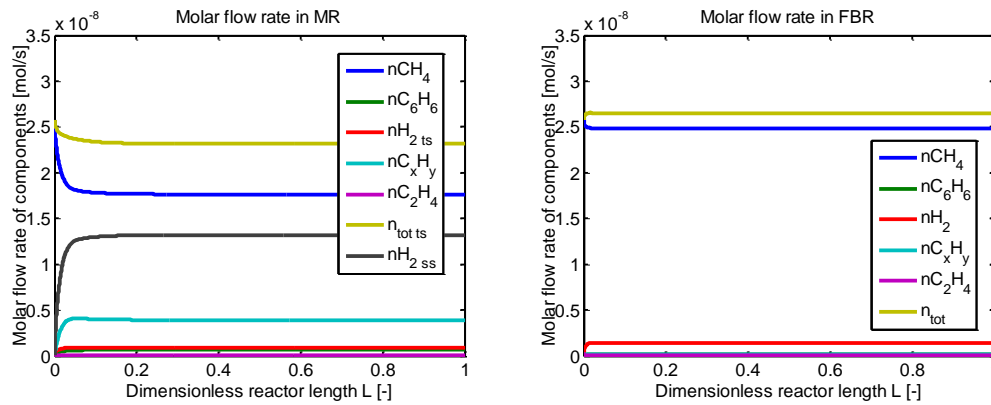


Figure 6.8: Components molar flow rates in FBR and “Pd MR”

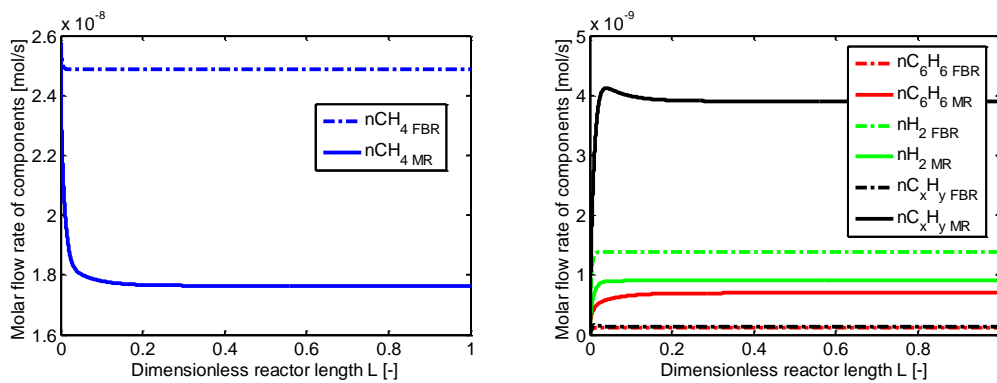


Figure 6.9: Comparison of component molar flow rates in FBR and “Pd MR”



It can be seen more clearly from Figure 6. 9 that,  $\text{CH}_4$  and  $\text{H}_2$  molar flow rate in MR tube side are lower than FBR, but  $\text{C}_6\text{H}_6$  and  $\text{C}_x\text{H}_y$  molar flow rate in MR tube side are higher than FBR. This implies that the removal of  $\text{H}_2$  caused more  $\text{CH}_4$  is reacted and produced more  $\text{C}_6\text{H}_6$  and  $\text{C}_x\text{H}_y$  at the same time. This is consisted with Figure 6. 10 that MR has higher methane conversion of 31.50% than FBR of 3.44%. But the benzene selectivity for MR, which is 5.15%, is lower than the one for FBR, which is 8.19%. Which from the benzene yield comparison, we can see that benzene yield in MR (1.62%) is much higher than in FBR (0.28%). In this condition, the flux of  $\text{H}_2$  through Pd membrane is  $4.73 \times 10^{-4} \text{ mol}/(\text{m}^2 \cdot \text{s})$ .

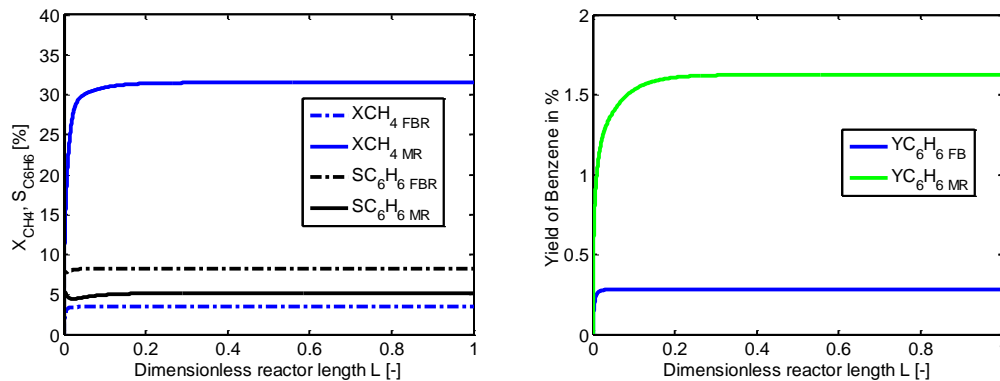


Figure 6. 10: Comparison of methane conversion, benzene selectivity and yield in FBR and “Pd MR”

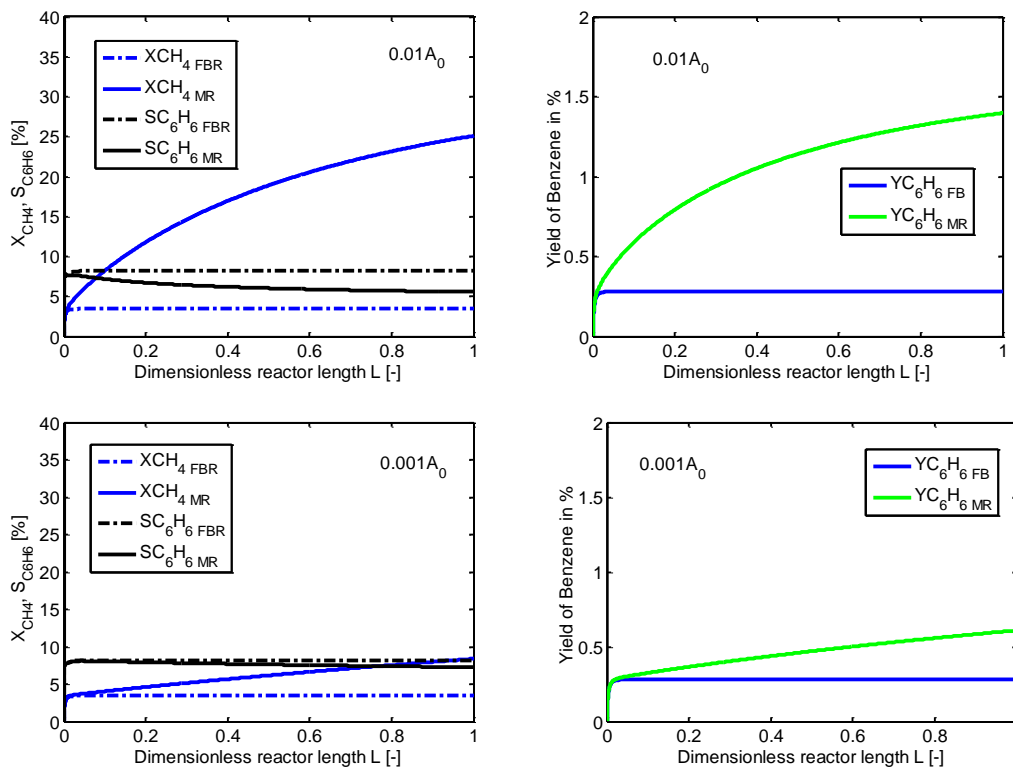


Figure 6. 11: Comparison of methane conversion, benzene selectivity and yield in FBR and “Pd MR” by varying  $A_0$

In order to investigate the influence of removed hydrogen amount to MDA performance, the flux of hydrogen through Pd membrane is manually varied by enlarge or reduce  $A_0$ . When there is a factor larger than 0.05 multiplied to  $A_0$ , there is no difference of  $J_{H_2}$ .

When the factor is 0.01, the  $J_{H_2}$  reduced to  $1.05 \times 10^{-5} \text{ mol}/(\text{m}^2 \cdot \text{s})$  with methane conversion of 25.10% and benzene selectivity of 5.57%. While the factor is relegated to 0.001, the  $J_{H_2}$  decreased to  $1.20 \times 10^{-6} \text{ mol}/(\text{m}^2 \cdot \text{s})$  with methane conversion of 8.40% and benzene selectivity of 7.26% (as shown in Figure 6. 11).

A short conclusion can be made here that hydrogen selective membrane reactor can increase methane conversion and benzene yield with relatively low benzene selectivity. And the more hydrogen is removed, the higher the methane conversion. For the realistic limitation that there is no Pd available, the hydrogen selective carbon membranes are tested and applied.

### 6.3 Results of gas permeation for carbon membranes

The carbon membranes used in this work were prepared by Fraunhofer Institute (IKTS) Hermsdorf with the properties listed in Table 4. 2. According to the thermodynamic and kinetic studies above, we know that a membrane with hydrogen permeating flow of  $1.5\text{E-}8 \text{ mol/s}$  is necessary to reach 20% of methane conversion at the condition of  $T = 700^\circ\text{C}$ ,  $x_{0,\text{CH}_4} = 30\%$  and  $W/F = 2160 \text{ kgs/m}^3$ . As already introduced in section 4.2.2 and 4.3.2, the membrane (No. 1) characterization experiments are single gas, binary and multiple gas mixture permeation. The results are presented in the same order.

#### 6.3.1 Single gas permeation

Single gas permeation experiments were first carried out for the gases  $H_2$ , He,  $CH_4$  and  $N_2$  from tube side to shell side at the conditions listed in Table 4. 7. Based on these results, permeation model parameters can be calculated for each gas. In addition, single gas permeation experiments with He,  $N_2$  and  $H_2$  were also conducted from the shell side to tube side with the purpose of evaluating the symmetry of the membrane.

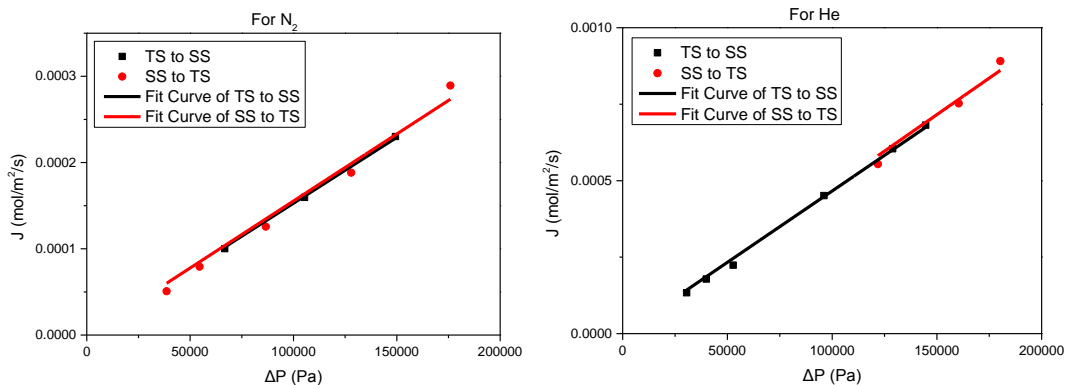


Figure 6. 12: Single gas permeation results for  $N_2$  and He for each direction of flow

As can be seen in Figure 6. 12, for  $N_2$  and He, the fluxes (flux from tube side to shell side and flux from shell side to tube side) are generally the same. While more precisely, the flux from shell side to tube side is slightly higher than the one from tube side to shell.

However, from Figure 6. 13 we can see that the behavior of the flux was different in the case of H<sub>2</sub>, showing an obviously higher flux for H<sub>2</sub> from shell side to tube side. This behavior is commonly observed in membranes that have a set of layers with different pore diameters.

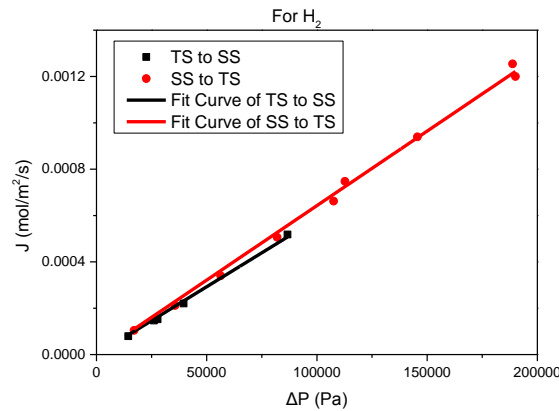


Figure 6. 13: Single gas permeation results for H<sub>2</sub> for each direction of flow

### 6.3.2 Binary gas mixture permeation

Binary gas mixture diffusion experiments have been carried out for different gas pairs at the experimental condition as shown in Table 4. 8. The observed pressure profiles for different gases and conditions are shown in Figure 6. 14 to Figure 6. 18.

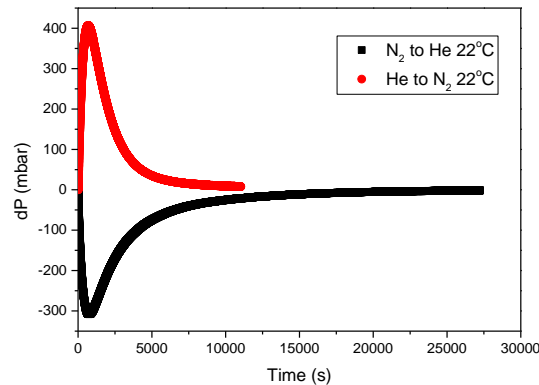


Figure 6. 14: Binary gas mixture diffusion experiment results for the pair He-N<sub>2</sub>

For the combination of inert gas (He and N<sub>2</sub>), there is an asymmetry (about 100 mbar) of the pressure profile (Figure 6. 14). Due to different molecular weights of gases, the transmembrane fluxes caused pressure change over time. The positive total pressure over time was obtained when He substitutes N<sub>2</sub>, since He is diffusing faster through the membrane than N<sub>2</sub>. Thus, He consequently increased the total pressure in the closed chamber and created overpressure in comparison with atmospheric pressure on the sweep gas side. And vice versa. The membrane used in this work contains porous and relatively dense layer, which is the reason why mass transfer is asymmetric. This means He and N<sub>2</sub> permeate from shell side to tube side faster than from tube side to shell side. When the system is changing from He to N<sub>2</sub>, He goes out of the shell side very fast and N<sub>2</sub> goes into the shell side slowly, which results in a higher pressure difference between tube side and shell side. When the system is

changing from  $N_2$  to He,  $N_2$  goes out of the shell side relatively fast and He goes into the shell side relatively slow (comparing with He goes out of shell side) but still faster than the rate of  $N_2$  permeating from shell side to tube side.

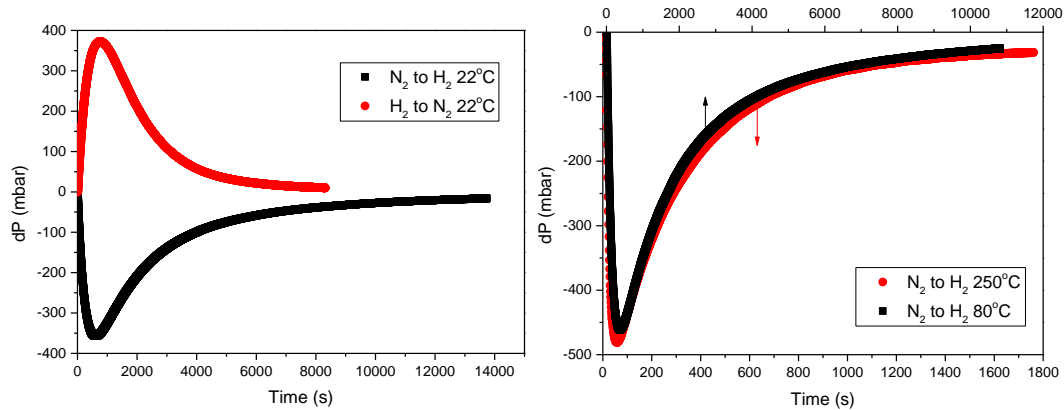


Figure 6. 15: Binary gas mixture diffusion experiment results for the pair  $H_2-N_2$

From Figure 6. 15 it can be seen that the increase in temperature produced a bigger and faster pressure difference change response. This is in accordance with the change of the permeability of  $H_2$  and  $N_2$  with temperature, which means that the  $H_2$  at higher temperature ( $80^\circ C$  and  $250^\circ C$ ) will permeates to the shell side faster than at lower temperature ( $22^\circ C$ ). For this combination of gases, the asymmetry of the membrane cannot be obviously observed, probably due to the fact that the flow of  $N_2$  from shell side to tube side is higher than from tube side to shell side, but for  $H_2$  the behavior is the opposite (flow from tube side to shell side is higher than from shell side to tube side), which neutralize the effect of the change in flow of each gas.

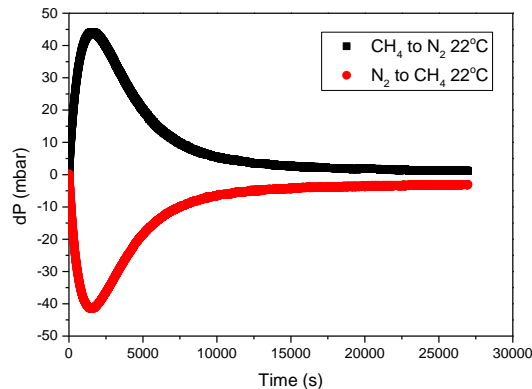


Figure 6. 16: Binary gas mixture diffusion experiment results for the pair  $CH_4-N_2$

For the combination of  $N_2$  and  $CH_4$  (Figure 6. 16), the pressure difference (45 mbar) is much smaller than  $N_2$  with He and  $H_2$  (around 400 mbar), which implies that the permeating rate of  $CH_4$  is much smaller than He and  $H_2$ . While methane permeating rate is faster than nitrogen, because the pressure difference of  $CH_4$  to  $N_2$  is positive.

Figure 6. 17 shows the pressure profile of  $CH_4$  and He pair. The pressure differences are generally symmetry, which confirms the conclusion of Figure 6. 14 and Figure 6. 15 that He permeates faster from shell side to tube side while  $CH_4$  permeates faster from tube side to shell side.

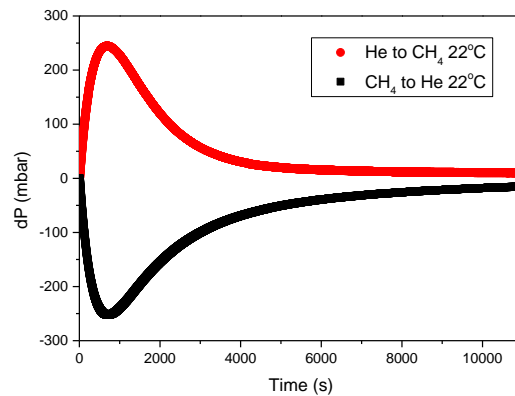


Figure 6. 17: Binary gas mixture diffusion experiment results for the pair CH<sub>4</sub>-He

For the system H<sub>2</sub>-CH<sub>4</sub> (see Figure 6. 18), the effect of the asymmetry of the membrane can be easily observed, presenting a difference of around 50 mbar simply due to the different direction of the flow. For higher temperature (250°C) and higher hydrogen volumetric flow rate (100 ml/min), the time to reach the maximum pressure difference and equilibrium are shorter.

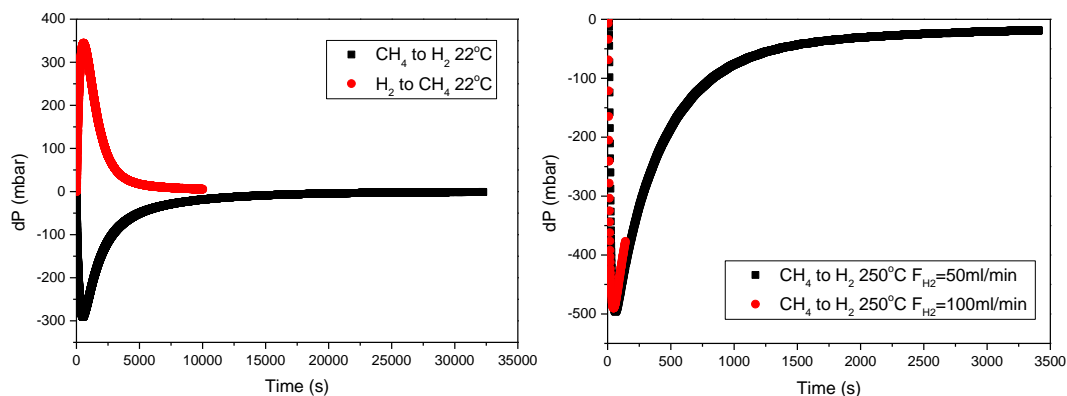


Figure 6. 18: Binary gas mixture diffusion experiment results for the pair H<sub>2</sub>-CH<sub>4</sub>

### 6.3.3 Ternary gas mixture permeation

In order to investigate the influence of gas mixture to the membrane permeability, ternary gas mixture permeation test (50% He + 50% N<sub>2</sub> to N<sub>2</sub>) was also carried out. Comparing with binary gas mixture diffusion results, the maximum pressure difference of ternary permeation (~170 mbar) is smaller than half of the binary permeation one (~420 mbar). And the time to reach equilibrium of ternary test (~6250s) is longer than half of the binary one (~10250s). This means the presence of N<sub>2</sub> in the system at the very beginning does influence the gas permeation through the carbon membrane.

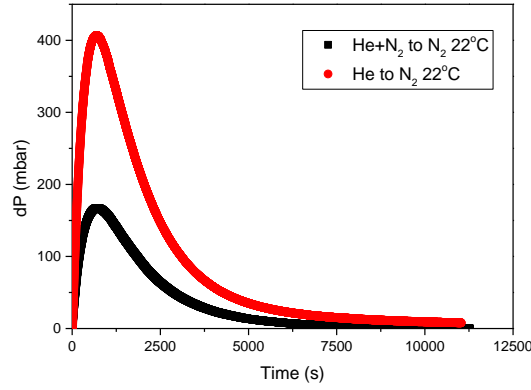


Figure 6. 19: Ternary gas mixture diffusion experiment results for the pair He + N<sub>2</sub>-N<sub>2</sub>

In summary, the characterized carbon membrane behaves asymmetrically even for pairs of inert gases (He and N<sub>2</sub> in Figure 6. 14). Higher temperature resulted in higher fluxes (larger dP in Figure 6. 15). Faster sweep gas flow rate accelerated the approach to equilibrium (see Figure 6. 18). The specific composition of gases mixture in the system strongly influence the permeation behavior (see Figure 6. 19). The permeation rate of different gases followed generally the order of molecular weights. The main diffusion mechanisms are Knudsen or configurational diffusion, separately or combined.

#### 6.4 Quantification of permeability of carbon membranes

The model chosen for membrane No. 1 was the configurational diffusion (eq. (6. 14)). In order to simplify the parameter estimation process, eq. (6. 14) is rewritten as follow:

$$J = -\frac{A_1}{\delta} \cdot \exp\left(-\frac{B_1}{T}\right) \cdot \frac{1}{\sqrt{T}} \cdot \Delta p \quad (6. 18)$$

Accordingly, the permeability and selectivity can be calculated:

$$P = A_1 \cdot \exp\left(-\frac{B_1}{T}\right) \cdot \frac{1}{\sqrt{T}} \quad (6. 19)$$

$$S_{i/j} = P_i/P_j \quad (6. 20)$$

The modelling of membrane No. 2 is little bit unusual, which means none of the diffusion models (as introduced in section 6.1.3) can fit for the gas permeation data. The real permeation mechanism of membrane No. 2 can be a combination of the diffusion models or has different mechanism in different layers. From a macro point of view, the best fitting form the experimental data of membrane No.2 is polynomial of temperature. For He, H<sub>2</sub> and CH<sub>4</sub>, the diffusion flux as a function of pressure difference is eq. (6. 21).

$$J = -(A \cdot T^2 + B \cdot T + C) \cdot \Delta p \quad (6. 21)$$

Accordingly, the permeability can be calculated:

$$P = A\delta \cdot T^2 + B\delta \cdot T + C\delta \quad (6. 22)$$

While for N<sub>2</sub> permeation, the diffusion flux can be calculated as eq. (6. 23).

$$J = -\left(\frac{1}{D \cdot T^2 + E \cdot T + F}\right) \cdot \Delta p \quad (6. 23)$$

Accordingly, the permeability can be calculated:

$$P = \frac{1}{\frac{D}{\delta} \cdot T^2 + \frac{E}{\delta} \cdot T + \frac{F}{\delta}} \quad (6.24)$$

### 6.4.1 Carbon membrane No. 1

In order to investigate the permeation flux, single gas permeation under different pressures and temperatures are carried out. According to eq. (6. 18), the permeation flux as a function of pressure difference for different temperatures and gases are plotted as Figure 6. 20. And the results of linear regression are listed in Table 6. 1.

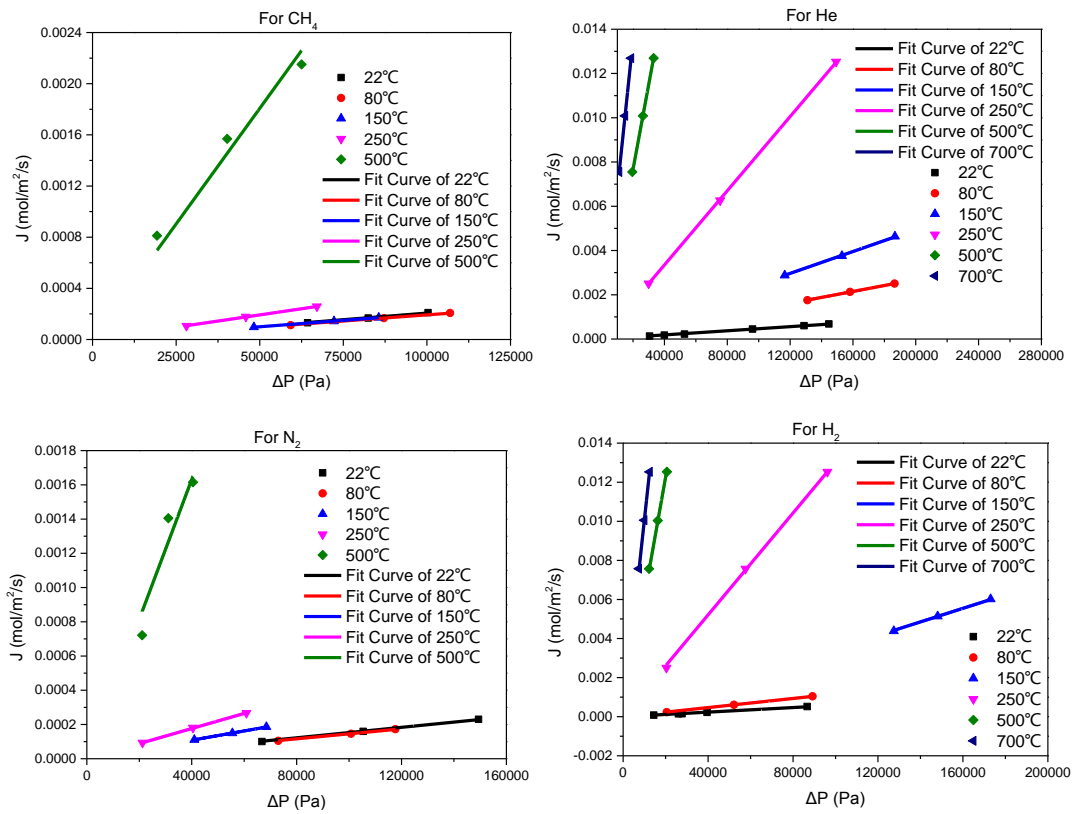


Figure 6. 20: Single gas permeation results at different temperatures for membrane No. 1

Table 6. 1: Linear regression of diffusivities for membrane No. 1

Gas	22°C	80°C	150°C	250°C	500°C	700°C
CH <sub>4</sub>	2.0651E-9	1.9250E-9	1.9934E-9	3.8458E-9	3.6138E-8	
He	4.6625E-9	1.3436E-8	2.4716E-8	8.3770E-8	3.8397E-7	6.7690E-7
N <sub>2</sub>	1.5284E-9	1.4538E-9	2.7050E-9	4.4105E-9	4.0775E-8	
H <sub>2</sub>	5.8553E-9	1.1666E-8	3.4658E-8	1.3030E-7	6.1305E-7	1.0072E-6

While according to eq. (6. 18), the diffusivities parameters  $A_1$  and  $B_1$  have to be estimated from the linear regression slope as a function of temperature. Since the relationship of slope and temperature is the combination of exponential and root reciprocal,  $A_1$  and  $B_1$  have to be estimated numerically instead of graphically. And the estimated results are listed in Table 6. 2.

Table 6. 2: Diffusivities parameters for membrane No. 1

Gas	$A_1$ (molK <sup>0.5</sup> s/Kg)	$B_1$ (K)
CH <sub>4</sub>	2.75E-7	4.00E+3
He	4.94E-7	2.64E+3
N <sub>2</sub>	2.95E-7	3.98E+3
H <sub>2</sub>	6.57E-7	2.52E+3

In order to validate the estimated diffusivities parameters, calculated permeating flux with parameters in Table 6. 2 compared with experimental results are plotted in Figure 6. 21. We can see that the calculation of He and H<sub>2</sub> fluxes fit the experimental data best, only a little bit deviation at 150°C. For CH<sub>4</sub> and N<sub>2</sub>, the best fits are at high temperature (250°C and 500°C).

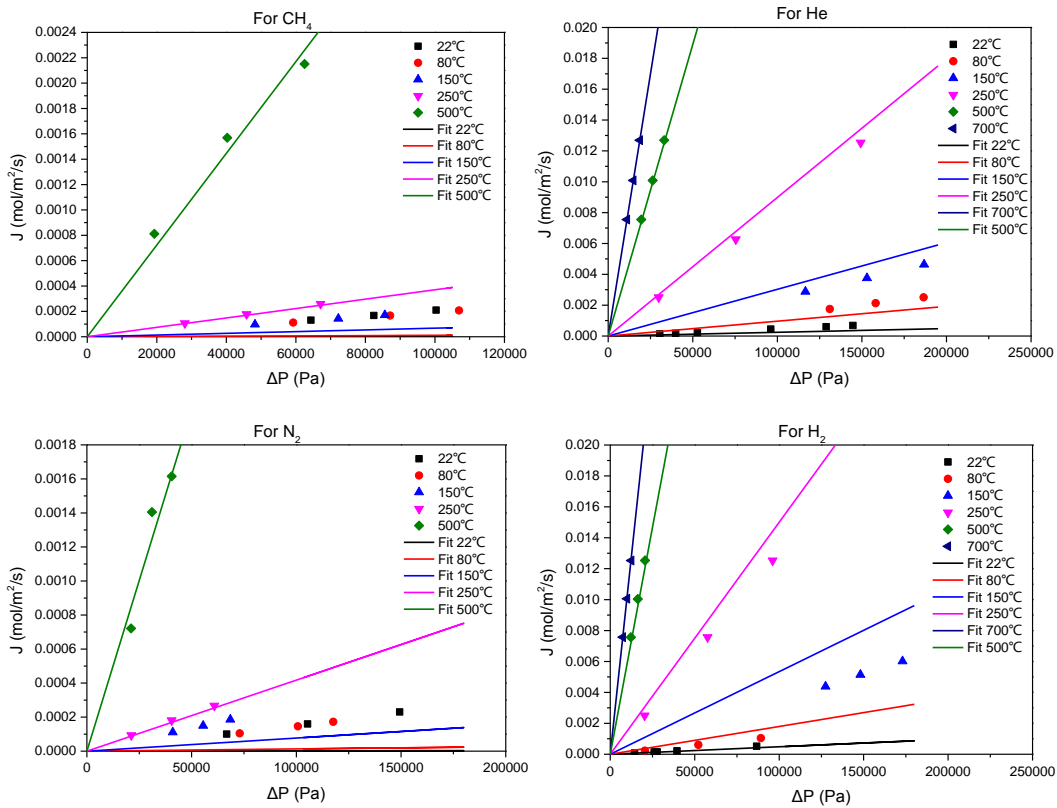


Figure 6. 21: Validation of diffusivities parameters at different temperatures for membrane No. 1

According to eq. (6. 19) and (6. 20) and the parameters in Table 6. 2, permeability and selectivity of all gases at different temperatures can be calculated and are compared with the experimental data as shown in Figure 6. 22. It's clear that the calculated permeability fit the experimental results perfectly for all the gases under all temperatures. While for selectivity, generally speaking, the calculation can represent the experimental data only under high temperature conditions (250°C and 500°C), which is the same as for permeation flux of CH<sub>4</sub> and N<sub>2</sub> (Figure 6. 21). The deviation of permeability at low temperature can be also notable, but they are not that obvious in the plot scale of Figure 6. 22.

Shortly conclude for membrane No. 1 here, the permeation model and estimated parameters can be used for high temperature with enough accuracy to calculate the permeation flux, permeability and selectivity for all the gases. For the application of low temperature, this model and parameters can



be only used for He and H<sub>2</sub>. For the permeability of He and H<sub>2</sub>, a continuous and rapid increase in the permeability with respect to temperature was observed, similar to an exponential behavior; for the case of CH<sub>4</sub> and N<sub>2</sub>, first a minimum was observed followed by an increase in permeability. This type of behavior with respect to temperature can be observed in configurational diffusion but not in Knudsen diffusion (where the permeability would decrease with respect to temperature).

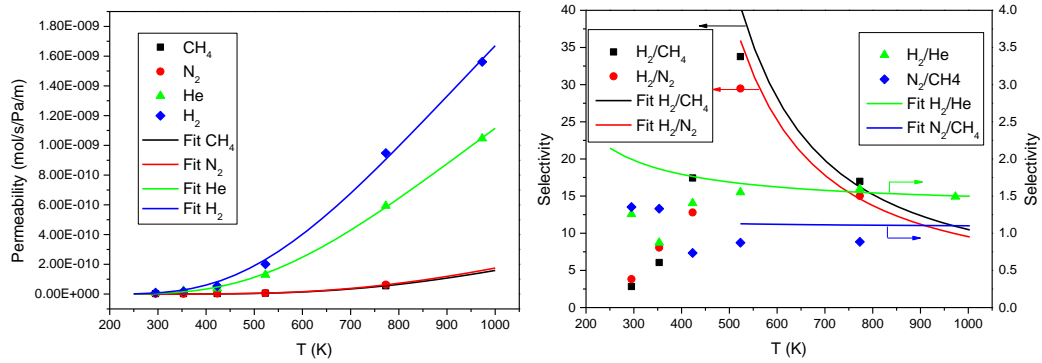


Figure 6. 22: Permeability and selectivity at different temperatures for membrane No. 1

## 6.4.2 Carbon membrane No. 2

For the investigation of carbon membrane No. 2, similar process was carried out as for membrane No. 1. According to eq. (6. 21) and (6. 23), the permeation flux as a function of pressure difference are plotted in Figure 6. 23. And the results of linear regression are listed in Table 6. 3.

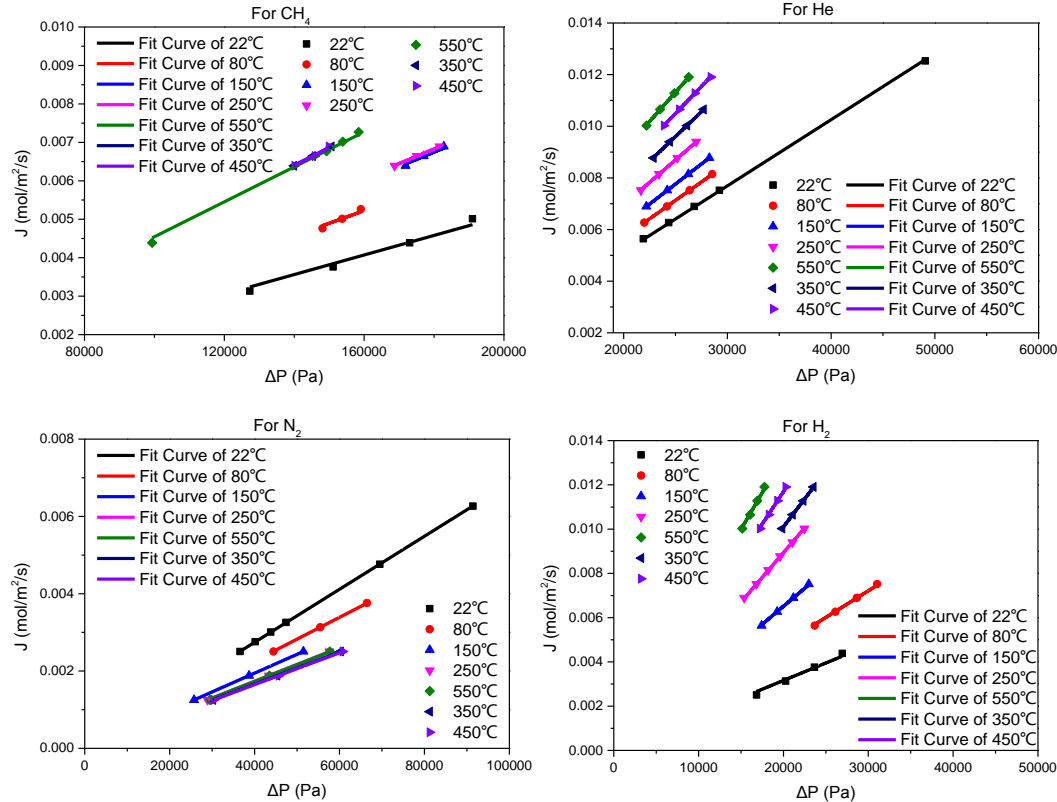


Figure 6. 23: Single gas permeation results at different temperatures for membrane No. 2

While according to eq. (6. 21) and (6. 23), the diffusivities parameters A to F have to be estimated from the linear regression slope as a function of temperature. Since the relationship of slope and temperature for  $N_2$  is the polynomic reciprocal, D, E and F have to be estimated from the slope reciprocal as a function of temperature. And the estimated results are shown in Figure 6. 24 and the values are listed in Table 6. 4.

Table 6. 3: Linear regression of diffusivities for membrane No. 2

Gas	22°C	80°C	150°C	250°C	350°C	450°C	550°C
CH <sub>4</sub>	2.5443E-8	3.2642E-8	3.7479E-8	3.7931E-8	4.5714E-8	4.5721E-8	4.5444E-8
He	2.5639E-7	2.8520E-7	3.1056E-7	3.4798E-7	3.8413E-7	4.1990E-7	4.5283E-7
N <sub>2</sub>	6.8586E-8	5.6495E-8	4.8644E-8	4.3432E-8	4.1533E-8	4.1217E-8	4.3227E-8
H <sub>2</sub>	1.5804E-7	2.4047E-7	3.2567E-7	4.4699E-7	5.0517E-7	5.8472E-7	6.6592E-7

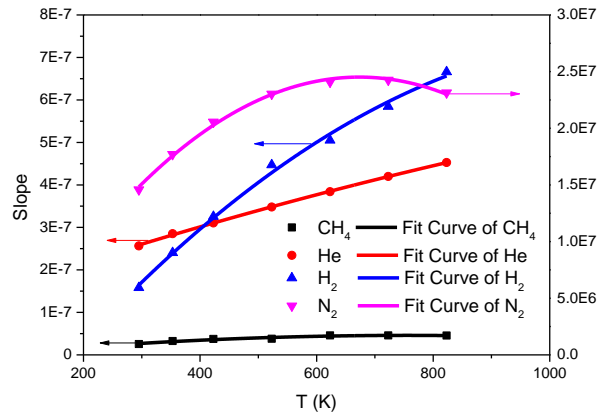


Figure 6. 24: Diffusivities parameter estimation at different temperatures for membrane No. 2

Table 6. 4: Diffusivities parameters for membrane No. 2

Gas	A (mol/(sm <sup>2</sup> PaK <sup>2</sup> ))	B (mol/(sm <sup>2</sup> PaK <sup>2</sup> ))	C (mol/(sm <sup>2</sup> PaK <sup>2</sup> ))	D ((sm <sup>2</sup> PaK <sup>2</sup> )/mol)	E ((sm <sup>2</sup> PaK <sup>2</sup> )/mol)	F ((sm <sup>2</sup> PaK <sup>2</sup> )/mol)
CH <sub>4</sub>	-9.055E-14	1.368E-10	-5.787E-09			
He	-9.176E-14	4.700E-10	1.278E-07			
N <sub>2</sub>				-6.768E+01	9.116E+04	-6.178E+06
H <sub>2</sub>	-7.597E-13	1.782E-9	-2.952E-07			

In order to validate the estimated diffusivities parameters for membrane No. 2, calculated permeating flux with parameters in Table 6. 4 compared with experimental results are plotted in Figure 6. 25. We can see that the calculation of He, N<sub>2</sub> and H<sub>2</sub> fluxes fit the experimental data very well at all temperatures. For CH<sub>4</sub>, the best fits are at high temperature (350°C to 550°C). The calculated methane flux at 22°C is also good, but for 80°C to 250°C, the discrepancy is obvious.

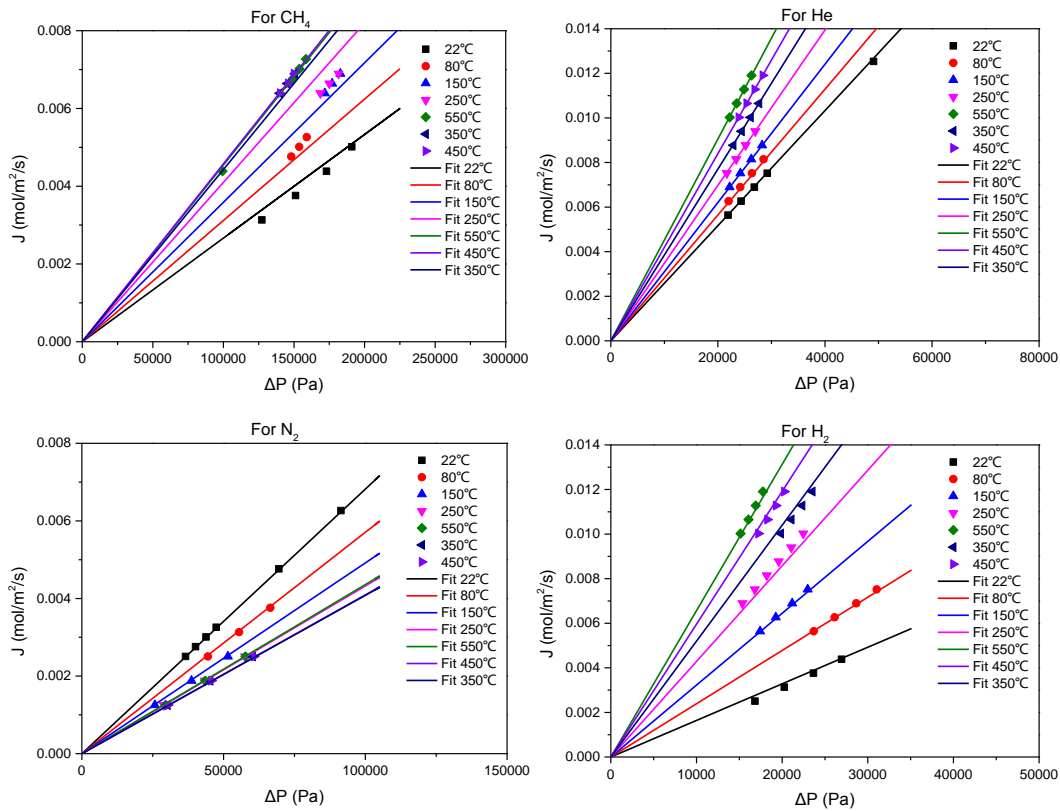


Figure 6. 25: Validation of diffusivities parameters at different temperatures for membrane No. 2

According to eq. (6. 22), (6. 24) and (6. 20), and the parameters in Table 6. 4, permeability and selectivity of all gases at different temperatures can be calculated and are compared with the experimental data as shown in Figure 6. 26. It's clear that the calculated permeability and selectivity fit the experimental results very good for all the gases under all temperatures. For the permeability of CH<sub>4</sub>, He and H<sub>2</sub>, a continuous increase in the permeability with respect to temperature was observed; for the case of N<sub>2</sub>, a decreased permeability to reach a minimum was observed.

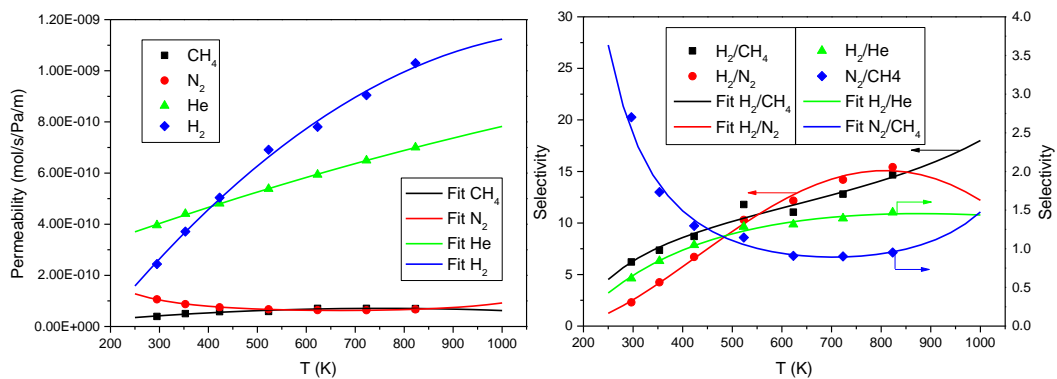


Figure 6. 26: Permeability and selectivity at different temperatures for membrane No. 2

## 6.5 Feasibility of membrane reactor (carbon membrane)

Based on the calculations in the previous sections, we know that at  $T=700^{\circ}\text{C}$  the hydrogen area time yield (ATY,  $ATY = \frac{\dot{n}_{H_2}^M}{A_M}$ ) of membrane No. 1 with an area of  $4.8\text{E-}3\text{ m}^2$  is  $0.01\text{ mol}/(\text{s}\cdot\text{m}^2)$  and the ATY of membrane No. 2 is  $0.018\text{ mol}/(\text{s}\cdot\text{m}^2)$ . According to the above estimated STY of a FBR  $0.021\text{ mol}/(\text{s}\cdot\text{m}^3)$  (in section 5.4), to match the hydrogen fluxes of reaction and separation (“kinetic compatibility” [195]), the required ratios of membrane area to reactor volume ( $\frac{A_M}{V_R}$  for  $\frac{\dot{n}_{H_2}^M}{\dot{n}_{H_2}^R} = 1$ ) are  $2.12\text{ m}^{-1}$  for membrane No. 1 and  $1.18\text{ m}^{-1}$  for membrane No. 2. These relative low values indicate that an accommodation of a sufficiently large membrane area in a considered reactor volume is easily feasible (see Figure 6. 27). In van de Graaf et al. [195], examples are given that  $\frac{A_M}{V_R}$  ratios of up to 100 can be nowadays achieved.

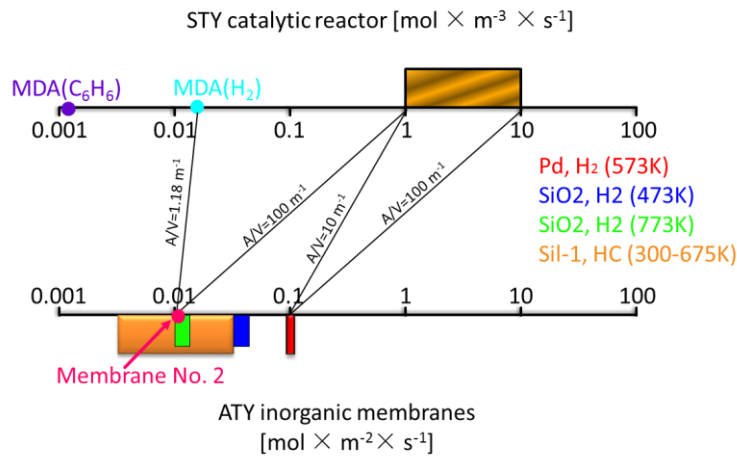


Figure 6. 27: Comparison of the space time yield (STY) of typical large scale catalytic reactors (box) with area time yield (ATY) of several inorganic membranes [195]

To illustrate the effect of the characterized membrane, MDA reaction is simulated in a MR using the model described in section 6.4.2 and the reaction rates described in sections 5.3.3 and the characterized carbon membrane (section 6.3). The models for gas permeation through carbon membrane used here are shown in eq. (6. 21) and (6. 23) with the value of parameters as shown in Table 6. 4. Equations for reactor modelling are again shown from eq. (5. 6) to (5. 11). Figure 6. 28 shows each component molar flow rate over dimensionless reactor axial coordinate in FBR and MR. Methane molar flow rate in MR tube side is much lower than in FBR, which is because this carbon membrane permeates methane to the shell side. The nitrogen molar flow rate in tube side increases and the one in shell side decreases, which is because the carbon membrane permeates nitrogen as well. The total molar flow rate of tube side increases and the one of shell side decreases, which means there are more nitrogen permeated from shell side to tube side than the gases ( $\text{CH}_4$ ,  $\text{H}_2$ ) permeated from tube side to shell side.

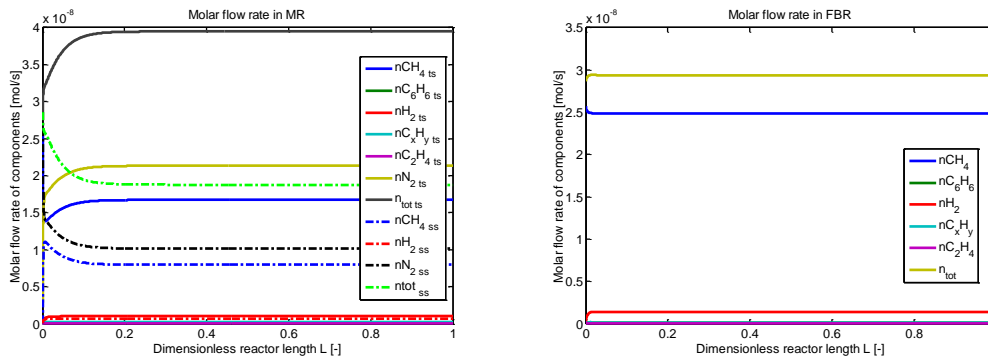


Figure 6. 28: Predicted components molar flow rates in FBR and “carbon MR”

It can be seen more clearly from Figure 6. 29 that,  $\text{CH}_4$  and  $\text{H}_2$  molar flow rate in MR tube side are lower than FBR, but  $\text{C}_6\text{H}_6$  and  $\text{C}_x\text{H}_y$  molar flow rate in MR tube side are higher than FBR. This implies that the removal of  $\text{H}_2$  and  $\text{CH}_4$  caused more  $\text{CH}_4$  is reacted and produced more  $\text{C}_6\text{H}_6$  and  $\text{C}_x\text{H}_y$  at the same time.

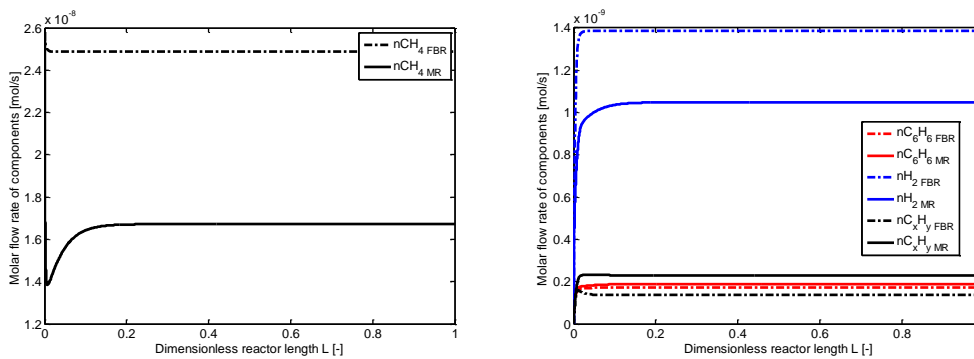


Figure 6. 29: Comparison of predicted component molar flow rates in FBR and “carbon MR”

While from Figure 6. 30 we can see that “carbon MR” has higher methane conversion of 4.19% than FBR of 3.44%. But the benzene selectivity for MR, which is 7.71%, is lower than the one for FBR, which is 8.19%. Which from the benzene yield comparison, we can see that benzene yield in MR (0.32%) is little bit higher than in FBR (0.28%). This result is similar as Pd membrane, which is the membrane increases the methane conversion and benzene yield but decreases the benzene selectivity.

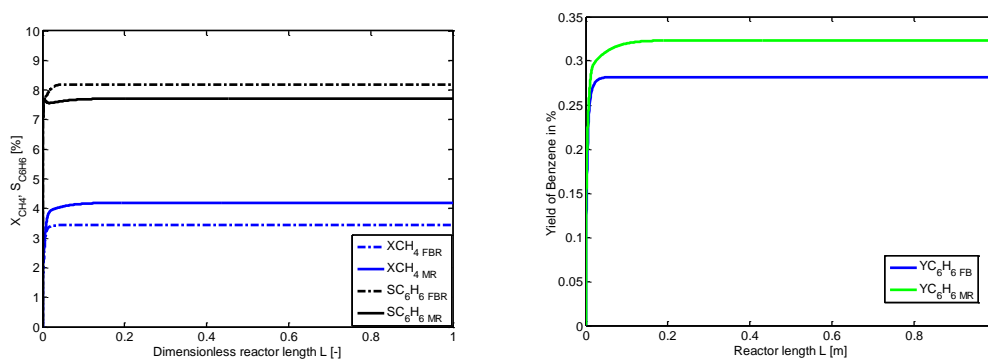


Figure 6. 30: Comparison of predicted methane conversion, benzene selectivity and yield in FBR and “carbon MR”

## 6.6 Experiments in MDA-MR using a carbon membrane

Carbon membrane No. 2 is used here for MR because membrane No. 1 was damaged after gas tests. As already introduced in section 4.3.3, five experiments (in the name of experiment No. 1-No. 5) in “carbon MR” were carried out at different conditions as listed in Table 4. 9, and all the experimental results are shown in this section.

Figure 6. 31 shows the methane conversion and benzene selectivity in “carbon MR”. Experiment No. 2 is the repeat of No.1. But No. 2 possesses lower methane conversion and higher benzene selectivity, which may be because of the property changes of the carbon membrane. While experiment No. 3 has lower methane conversion and higher benzene selectivity than No. 2, which consists with the results in FBR for the same situation. For experiment No. 4, it has slightly higher methane conversion and lower benzene selectivity than No. 2, which means high sweep gas flow ratio (3 for No. 4) favors the conversion of methane but not the selectivity of benzene in this “carbon MR”. For the case of lower temperature influence (experiment No. 5), the result show a lower methane conversion and benzene selectivity. While it’s obvious that No. 5 has a relatively long induction state and a later time range of steady state and deactivation, which also consists with the FBR results.

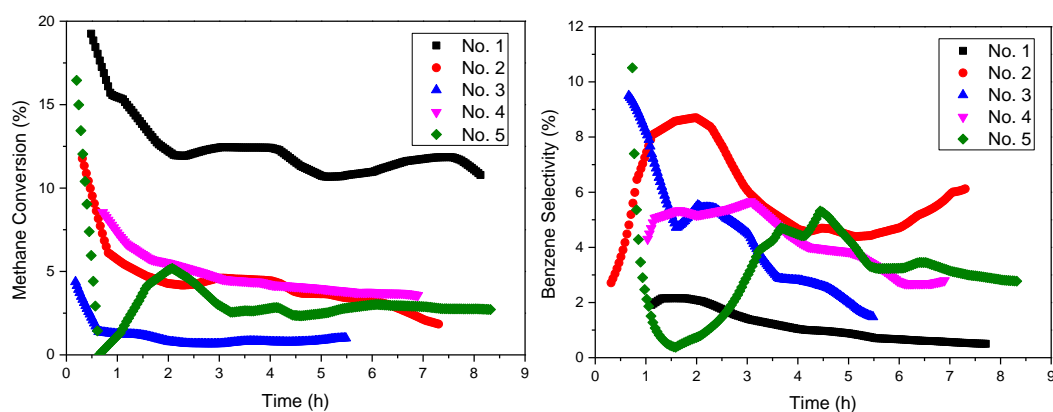


Figure 6. 31: Methane conversion and benzene selectivity in “carbon MR”

The ethylene and ethane selectivity are shown in Figure 6. 32. Experiment No. 3 shows high ethylene and ethane selectivity, which is the same as in FBR experiments. Experiment No. 5 shows the long induction state more obvious here, and lower ethylene selectivity than in FBR.

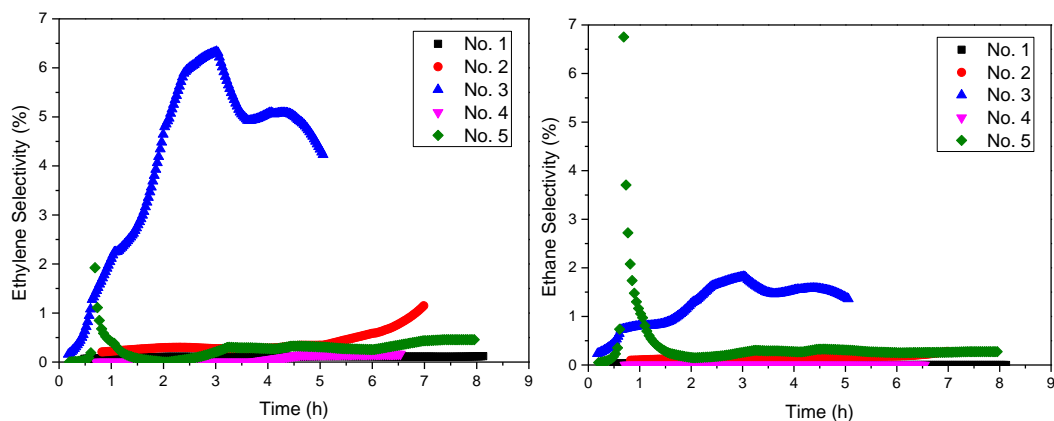


Figure 6.32: Ethylene and ethane selectivity in “carbon MR”

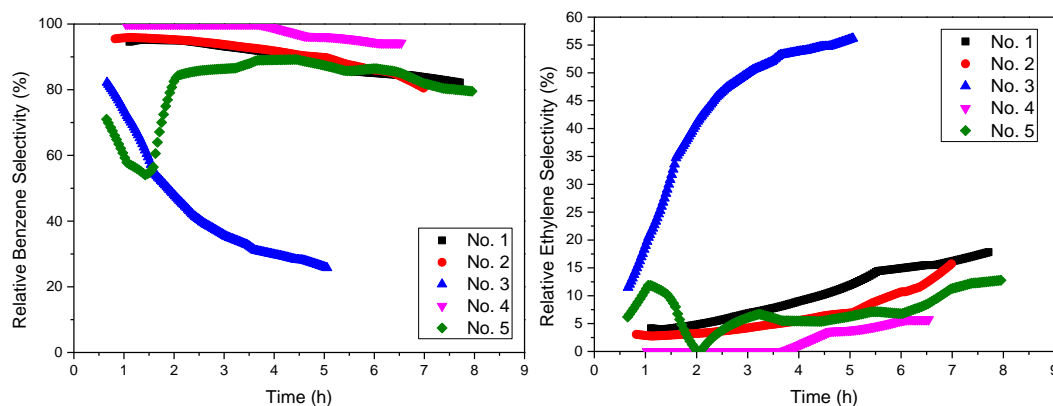


Figure 6.33: Relative benzene and ethylene selectivity in “carbon MR”

While the relative product selectivity (see eq. (2.33)) are also calculated and the results are shown in Figure 6.33 and Figure 6.34. For relative benzene selectivity, No. 2 shows good consistency with No. 1. And comparing with experiment No. 2, No. 3 shows lower relative benzene selectivity because of high methane feed volumetric fraction (90%); No. 4 gives higher one because of high sweep gas flow ratio (3); and No. 5 has lower one because of low temperature (650°C).

For ethylene and ethane relative selectivity, experiment No. 3 shows high ethylene and ethane relative selectivity than all others, which is because of higher methane feed volumetric fraction. No. 5 gives higher ethane relative selectivity in “steady state” than other 30% methane feed volumetric fraction experiments (No. 1, 2 and 4), which may be because of low reaction temperature. But this phenomena has not been observed in FBR experiments.

The experimental results in MR cannot be fairly compared with the results in FBR. Because this carbon membrane permeates around 50% of the methane feed to the shell side, which does not pass through the catalyst bed and goes out of the reactor as unreacted methane. This lower down the methane feed concentration and of course lower down the methane conversion in MR at the same time. However, macroscopic speaking, this “carbon MR” decreased methane conversion from 9% in FBR to 4%, but increased benzene selectivity from 6% in FBR to 9% under the condition of  $T = 700^{\circ}\text{C}$ ,  $x_{0,\text{CH}_4} = 30\%$  and  $W/F = 2160 \text{ kgs/m}^3$ .

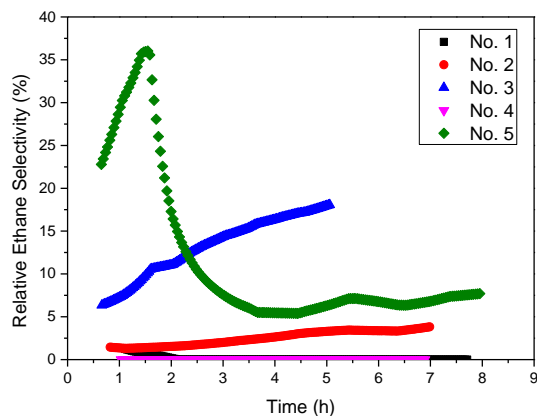


Figure 6. 34: Relative ethane selectivity in “carbon MR”

As introduced at the beginning of chapter 5, three states (induction, steady and deactivation state) can be distinguished in MDA process according to the outlet molar flow of benzene. The experimental benzene molar flow rate as a function of time of all the experiments in “carbon MR” are plotted in Figure 6. 35. Comparing with Figure 5. 1, the tendency of benzene molar flow rate in “carbon MR” are not as similar as the one illustrated in Figure 5. 1 and the one in FBR. This is because of we cannot continuously record benzene molar flow rate data from the very beginning intensively, due to the limitation of experimental apparatus. So reasonable regression has been done between two experimental points. In this condition, it’s very hard to distinguish the steady state. For simplification, the time moment with maximum benzene molar flow rate is chosen as for steady state data.

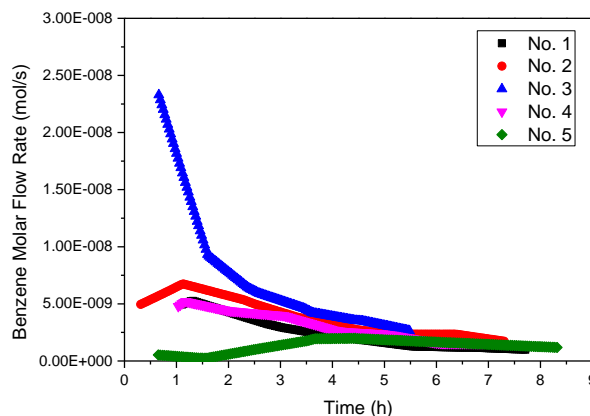


Figure 6. 35: Benzene molar flow rate along with reaction time in “carbon MR”

The estimated parameters in Table 6. 4 for carbon membrane permeation are checked with all experimental data of MDA reaction in “carbon MR”. From Figure 6. 36 and Figure 6. 37 we can see that the experimental data and the simulation data are at the same degree and similar tendency. The simulated methane molar flow rates in shell side are smoother than the real ones; while the simulated benzene molar flow rates are bigger than the experiments. There are relatively big deviation of reaction No. 3 that nearly all the simulation data are under-estimated (lower than the real ones).



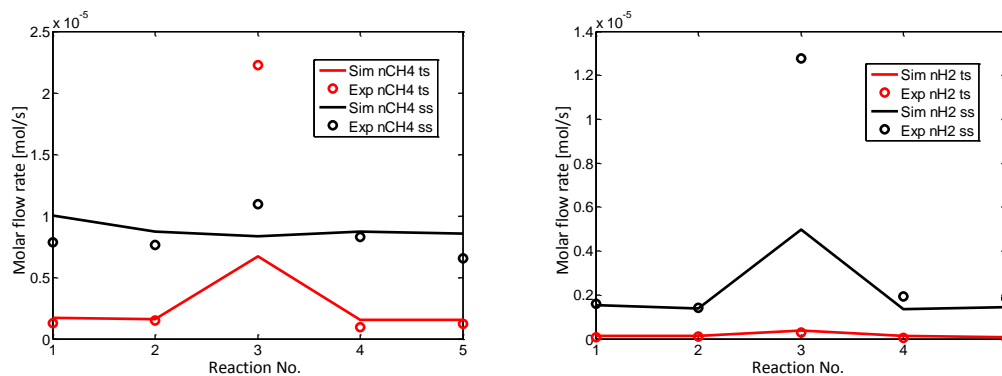


Figure 6.36: Comparison of methane and hydrogen molar flow rates in “carbon MR” at steady state

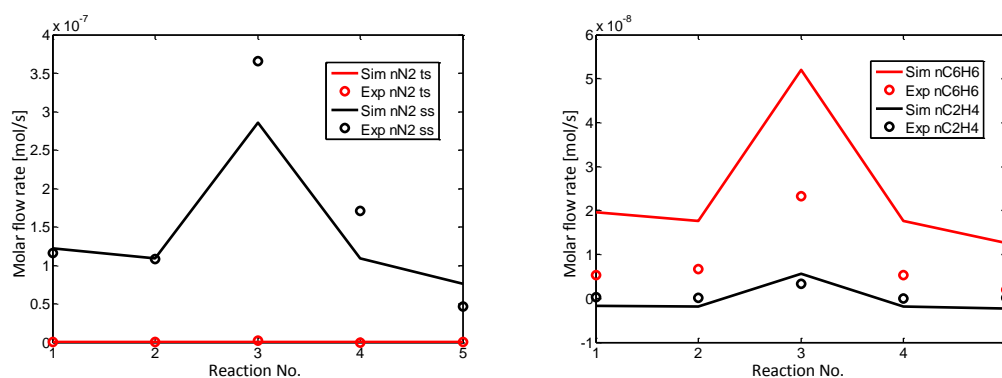


Figure 6.37: Comparison of benzene, ethylene and nitrogen molar flow rates in “carbon MR” at steady state

## 6.7 Conclusions

In this chapter, a feasibility study using a Pd membrane and carbon membranes in a MDA MR is described. The experimental results of testing the carbon membrane as well as corresponding “carbon MR” experiments were presented. Simulations of gas permeation were also provided.

In order to investigate the feasibility of MR application to MDA system, a Pd membrane model was selected to simulate the hydrogen extraction from the reacting chamber. The simulation results show that a “Pd MR” can deliver higher methane conversion and benzene yield compared to FBR.

The experimental results of gas tests show that for the applied asymmetric carbon membrane the selectivity to hydrogen is not as high as expected. There is a strong influence of gas mixture composition on the permeation behavior. According to the experimental data, two permeating models were derived for the two membranes (No. 1 and No. 2), respectively. The model for membrane No. 1 is configurational diffusion, and the simulation with estimated parameters show good consistency for He and H<sub>2</sub> at all tested temperatures, and for CH<sub>4</sub> and N<sub>2</sub> at 250°C and 500°C. However, the model for membrane No. 2 had to be modified as a second order polynomial function, which gives very good consistency for all the gases at all temperatures tested.

With the developed permeation model and the estimated parameters for the carbon membrane, the compatibility of the transport through this membrane with the MDA reaction was estimated. The results show that this membrane is compatible with the productivity of the MDA using the Mo/MCM-22 catalyst. However, altogether the STY of MDA with this catalyst is still very small compared with the “window of reality” of large scale reactions carried out in industry.

MDA performance in the corresponding “carbon MR” was simulated and compared with experimental data. The simulations could represent the experiments good for 30% of methane feed. The simulation results of the “carbon MR” are similar as for the “Pd MR”, which means higher methane conversion and benzene yield were predicted. The experimental results of MDA in this “carbon MR” shows however that, there around 50% of methane also permeated through the membrane from tube side to shell side. This caused a low methane conversion. Unfortunately, the removal of hydrogen intensifies the carbon deposit, which is a serious problem for continuous operation. The catalyst deactivation rate in FBR and MR is investigated in the next chapter.

## 7. Deactivation investigation

### 7.1 Introduction

Mo/zeolite (Mo/ZSM-5 or Mo/MCM-22) catalysts are considered as the best catalyst for MDA for their high activity and aromatic selectivity, but the stability problem (catalyst deactivation) is fatal especially under high temperature conditions. In MDA system, the deactivation of catalyst is generally accepted to be caused by three types of surface carbon deposit. They include 1). adventitious or graphite-like carbon, present mainly in the zeolite channels; 2). carbidic carbon as a component of  $\text{Mo}_2\text{C}$ , predominantly located on the external zeolite surfaces of the zeolite; 3). hydrogen-poor sp-type (heavier aromatic-type) or pre-graphitic type carbon [78, 89-91, 105, 117, 196, 197]. The accumulation of the third type of carbon increases with both time-on-stream [198] and reaction temperature at the early stage of MDA until this type of carbon gradually covers the whole zeolite surface and  $\text{Mo}_2\text{C}$  species, which is considered responsible for the catalyst deactivation [59, 74, 142, 199].

Catalyst regeneration in hydrogen atmosphere was tested in this study. When aromatics yield reduce to 80% of the last stage, switching from methane to hydrogen for 30-60 min to regenerate the catalyst and the regeneration ends while aromatics yield is lower than 5%. The results are shown in Figure 7. 1. During stage I , MDA was carried out with fresh catalyst and performed very good. After 48h aromatics yield is lower than 8%, and hydrogen is switched as the feed. After 30 min, methane is switched back and MDA continue. During stage II , methane conversion and aromatics yield are recovered to 85% of stage I and last for 48h, which means catalysts are effectively regenerated. But the more times catalyst is regenerated, the less time is can last. The regenerated catalyst last 24h for stage III, and 20h for stage IV and V . The whole regeneration-reaction operated for 160h, which is the longest life time so far for now. This also implied the superior catalytic stability of hierarchical Mo/MCM-22-HA catalyst.

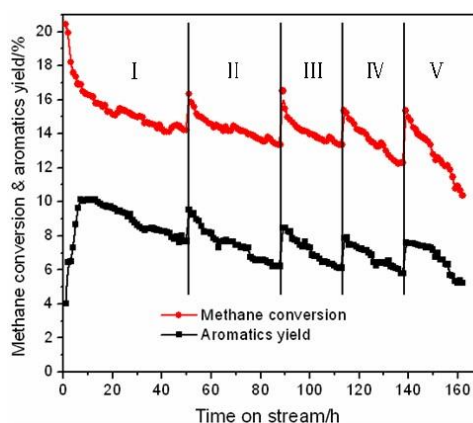


Figure 7. 1: Continued manufacture of MDA reaction over the Mo/MCM-22-HA catalyst [200]

### 7.2 Modelling of catalyst deactivation

Catalyst deactivation, the loss of catalytic activity or selectivity with time-on-stream, is one of the major problems related to the operation of heterogeneous catalysis and is of great economical

concern. It's both of chemical and physical nature and occurs simultaneously with the main reaction. Any chemical or physical interaction that reduces catalyst activity or selectivity is classified as catalyst deactivation phenomena. In general, deactivation leads to a shortened catalyst lifetime, and improved catalyst lifetime is of great commercial value to the process economics. In practical, catalyst deactivation is inevitable, but the lifetime can range from some seconds to several years. The knowledge of catalyst deactivation is of great importance for the operation of industrial chemical reactors and the study of specific reaction procedure. The mechanisms of catalyst deactivation can be commonly grouped into: poisoning, leaching, coking and sintering [201-203] (see Figure 7. 2).

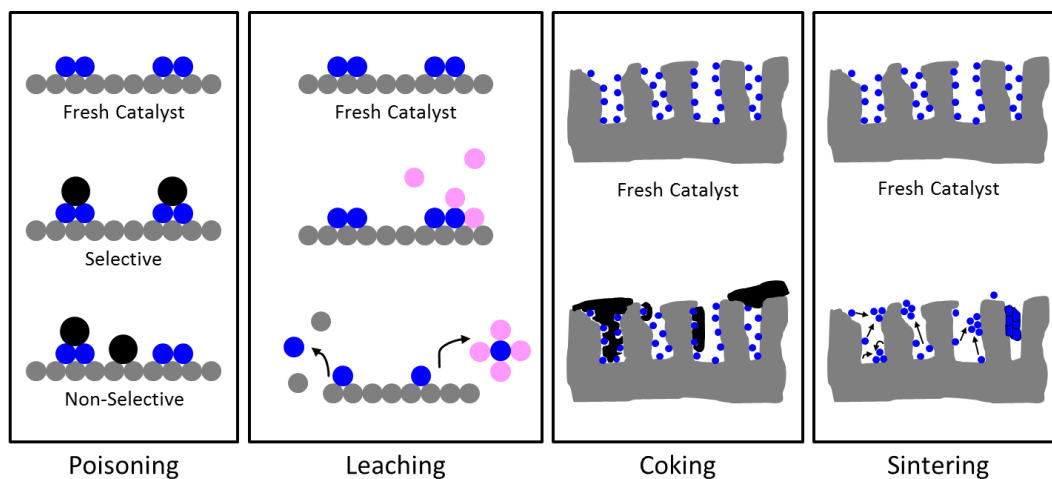


Figure 7. 2: Mechanisms of catalyst deactivation

Poisoning is the loss of activity due to the strong chemisorption on the active sites of impurities present in the stream [204]. Poisoning can be classified as “selective” and “non-selective”. A selective poisoning may act simply by blocking an active site or may alter the absorptivity of other species. In this case, the strongest active sites will be poisoned first, which may lead to curious relationships between catalyst activity and amount of poison chemisorbed. A non-selective one is poisoning the catalyst surface uniformly. Accordingly, the net activity of the catalyst is a linear function of the amount of poison chemisorbed.

Leaching is the loss of active species because of either attrition or volatilization. Attrition occurs mainly in moving or fluidized beds, since the catalyst is continuously abraded away. In this case accordingly, the availability of attrition resistant catalysts for fluid bed catalytic reaction is extremely important since the process operates with regeneration and catalyst recycle. Volatilization means that the active metal on the catalyst is easily reactive with one of the components (reactants, products or intermediates) in the reaction atmosphere.

Coking can be formed in catalytic reactions involving hydrocarbons when side reactions occur on the catalyst surface [201]. It may deactivate the catalyst either by covering of the active sites or by pore blocking. Most of the time, a distinction between coke and carbon is made: usually carbon is considered as the product of carbon monoxide disproportionation; whereas coke is referred to some arbitrary hydrocarbons or a mixture of them, which are originated by decomposition (cracking) or condensation (polymerization) of hydrocarbons.

Sintering normally refers to the loss of active surface through dispersive (for supported metal

catalyst) or structural (for unsupported catalyst) modification of the catalyst, which is generally a thermally activated process [201]. The dispersive modification reduces the active surface area through agglomeration and coalescence of small metal crystallites into larger ones with lower effective surface. Most of the case, sintering occurs through escape of metal atoms from a crystallite, transport of these atoms on the surface of the support, and subsequent capture of the migrating atoms on collision with another metal crystallite. The structural modification occurs at extremely high temperatures and leads to the transformation of one crystalline phase into a different one, which may involves both metal supported catalysts and metal oxide catalysts as well.

A quantitative description of a deactivating system is essential in order to optimize the operation of catalytic process, especially for fast deactivating systems. The activity of a deactivating catalyst [205] is expressed as:

$$a(t) = r(t)/r_0 \quad (7.1)$$

where  $r_0$  is the rate of reaction of a fresh catalyst and  $r(t)$  is the reaction rate at time-on-stream  $t$ . The kinetic of deactivation can be expressed as a function of temperature and concentration [206]:

$$\frac{da(t)}{dt} = -R(T) \cdot f(a(t), c_{de}) \quad (7.2)$$

where  $R(T)$  is a temperature related factor, which can be expressed in the form of Arrhenius equation:

$$R(T) = -k_{de} \cdot \exp\left(-\frac{E_{A\ de}}{RT}\right) \quad (7.3)$$

For simplification,  $f(a(t), c_{de})$  can be written in the form of power law:

$$\frac{da(t)}{dt} = -R(T) \cdot (a(t))^n \cdot c_{de}^m \quad (7.4)$$

When there is no poisoning in the deactivation,  $m=0$ . And if  $n=1$ , eq. (7.4) can be rewrite as:

$$\frac{da(t)}{dt} = -R(T) \cdot a(t) \quad (7.5)$$

The integration form of eq. (7.5) is:

$$a(t) = e^{-k_{de} \cdot \exp\left(-\frac{E_{A\ de}}{RT}\right) \cdot t} \quad (7.6)$$

In MDA reaction system, the deactivation of Mo/zeolite catalyst is mainly caused by severe carbon deposition. There are many kinds of coke formation, e.g. methane pyrolysis ( $\text{CH}_4 \rightarrow \text{C} + 2\text{H}_2$ ), Mo-species related carbon and large hydrocarbons formation. The deactivation of catalysts will directly affect the performance of MDA reaction. So we will try to investigate the mechanism and kinetic of carbon deposit. A deactivation function  $a_j$  is defined as the ratio of reaction rate at time  $t$   $r_j(t)$  divided by the reaction rate at steady state  $r_j(\text{steady state})$  to describe the deactivation kinetic with the expression:

$$a_j = \frac{r_j(t)}{r_j(\text{steady state})} \quad (7.7)$$

and it is quantified by an Arrhenius function:

$$a_j(t) = e^{-k_{de,j} \cdot \exp\left(-\frac{E_{A\ de,j}}{RT}\right) \cdot t} \quad (7.8)$$

with the differential form of:

$$\frac{da_j(t)}{dt} = -k_{de,j} \cdot \exp\left(-\frac{E_{A\ de,j}}{RT}\right) \cdot a_j(t) \quad (7.9)$$

With this deactivation function, the reaction rate at all time range can be expressed as:

$$r_j(t) = a_j(t) * r_j^{SS} = a_j(t) \cdot k_j \cdot \prod (c_{react})^{\alpha_{react}} \left(1 - \frac{1}{K_{p,j}} \prod \frac{(c_{prod})^{\alpha_{prod}}}{(c_{react})^{\alpha_{react}}}\right) \quad (7.10)$$

In MDA reaction system, the deactivation of Mo/zeolite catalyst is mainly caused by severe carbon deposition. There are many kinds of coke formation as introduced above. The deactivation of catalysts will directly affect the performance of MDA reaction. So it is necessary to investigate the kinetic of carbon deposit for full time range of MDA simulation. The deactivation function is already introduced as eq. (7. 8), which can be rewritten as follow:

$$a_i(t) = e^{R_i(T) \cdot t} \quad (7.11)$$

$$R_i(T) = -k_{de,i} \cdot \exp\left(-\frac{E_{A\ de,i}}{R \cdot T}\right) \quad (7.12)$$

During preliminary simulation,  $a_i(t)$  is calculated according to eq. (7. 7), followed by an exponential curve fitting (see Figure 7. 3) to get the value of  $R_i(T)$  in eq. (7. 11).

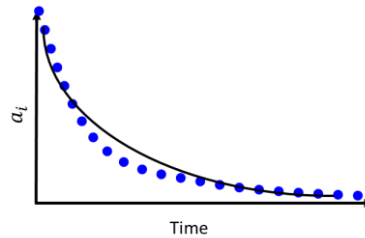


Figure 7. 3: Exponential fitting for  $R_i$  by the plot of  $a_i$  as a function of time

After logarithm on both sides of eq. (7. 12) gives:

$$\ln(R_i(T)) = \ln(-k_{de,i}) - \frac{E_{A\ de,i}}{R} \cdot \frac{1}{T} \quad (7.13)$$

or

$$\ln(-R_i(T)) = \ln(k_{de,i}) - \frac{E_{A\ de,i}}{R} \cdot \frac{1}{T} \quad (7.14)$$

Eq. (7. 13) applies for the case of  $R_i$  is positive, which means  $a_i$  increases along with reaction time, and eq. (7. 14) applies for the case of the opposite. Plotting eq. (7. 13) or (7. 14) with x label of  $\frac{1}{T}$  and y label of  $\ln(\pm R_i(T))$  is shown in Figure 7. 4.

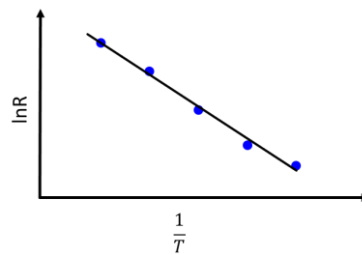


Figure 7. 4 Determination of deactivation pre-exponential factor and deactivation energy

Activation energy of deactivation state can be achieved by the slope of the curve:  $-\frac{E_{Ai}}{R}$  and pre-exponential factor of deactivation state can be read from the intercept of the curve:  $\ln(k_{de,i})$ . The results simulated by differential method are taken into the optimization program to get a better set of results and also to check the consistence of molar flow rate of the feed and the products between the experimental data and the calculated data.

The deactivation function estimation is carried out to reaction network 3 (see Figure 5. 75). The reaction rate of each reaction at time  $t$  is defined as the deactivation function multiply the reaction rate at steady state as follows:

$$a_i(t) = e^{-k_{de,i} \cdot \exp\left(-\frac{E_{Ade,i}}{R \cdot T}\right) \cdot t} \quad r_i(t) = a_i(t) \cdot r_{i,ss} \quad i=1,6 \quad (7. 15)$$

### 7.3 Observed deactivation in FBR and description

As shown in Figure 7. 5, the catalyst has been deactivated. The original white catalyst turned to black due to the heavy carbon deposits on the catalyst. Under this situation, the catalyst should be shifted with a fresh one or refreshed by means of regeneration (introduced in 7.1). The solid carbon deposit on/in the catalyst cannot go into the chromatography column since any solid will block the capillary column. So the composition of the solid coke cannot be precisely analyzed by means of GC. However, the portion or fraction of the solid coke strongly affects the conversion of methane and has to be considered in the carbon and hydrogen balance calculations (the specific equations can be found in section 5.3.2.2).

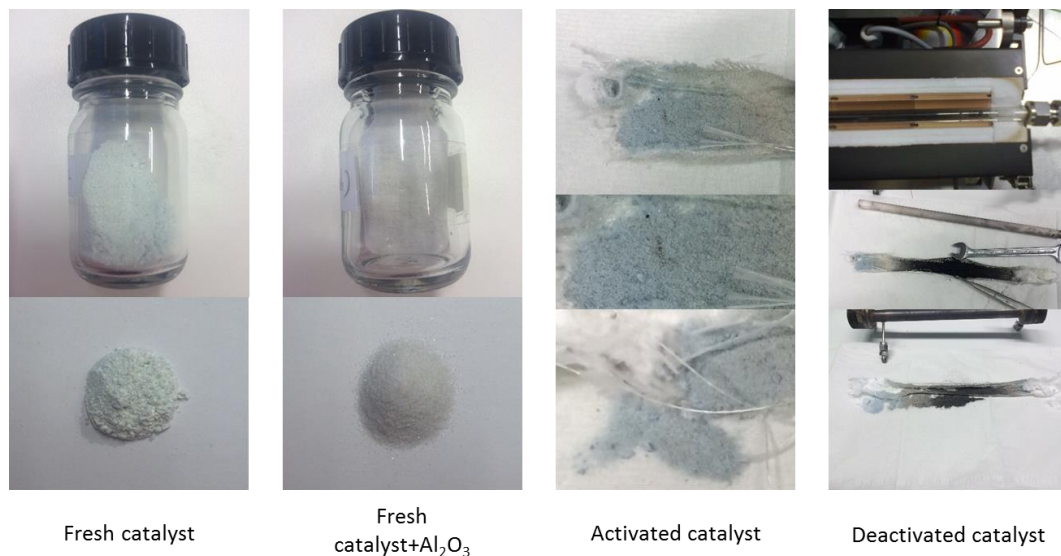


Figure 7. 5: Photograph of deactivated catalyst

#### 7.3.1 Experimental tendency of deactivation of FBR

The experimental appearance of deactivation should be decreasing methane conversion (catalyst are not as active as fresh one) and may be also decreasing aimed products selectivity (preferentially selectively produced undesired coke). Both phenomena can be observed in my experimental result

as shown in Figure A. 17- Figure A. 21, Figure A. 39 ( $x_{\text{CH}_4}^{\text{feed}} = 90\%$ ,  $\frac{W}{F} = 2165.67$ , single and stepwise experiments), Figure A. 30, Figure A. 31, Figure A. 26, Figure A. 36, Figure A. 34, Figure A. 38 ( $x_{\text{CH}_4}^{\text{feed}} = 30\%$ ,  $\frac{W}{F} = 720.26$ , single and stepwise experiments), Figure A. 32, Figure A. 22, Figure A. 33 and Figure A. 37 ( $x_{\text{CH}_4}^{\text{feed}} = 30\%$ ,  $\frac{W}{F} = 2165.67$ , single and stepwise experiments).

The methane conversion decreasing can be clearly seen from all the figures mentioned above, and the higher the temperature, the sharper the decreasing curve (as discussed in 5.2). The decreasing tendency of benzene can be easier observed from Figure A. 33- Figure A. 36.

### 7.3.2 Preliminary estimation of FBR

At the beginning of the investigation of deactivation stage, all the reaction rates are calculated as well as the average reaction rates of the steady state. Then the value of deactivation function at each experimental time point  $a_i(t)$  can be calculated by eq. (7. 7). Then plots can be made according to eq. (7. 11) of  $a_i$  as a function of  $t$ . Then an exponential fitting can be made as shown in Figure 7. 6 to Figure 7. 8. It is clear that  $a_3$  and  $a_5$  increase with time, which refers to a positive value of  $R_3$  and  $R_5$ , and the rest decrease along with time that refers to a negative value of  $R_i$ . According to Figure 5. 75, reaction number 3 and 5 present for ethylene reacts to ethane and  $\text{C}_x\text{H}_y$  respectively. So that means the coked catalyst can accelerate the reaction rate of ethylene reacts to ethane and benzene.

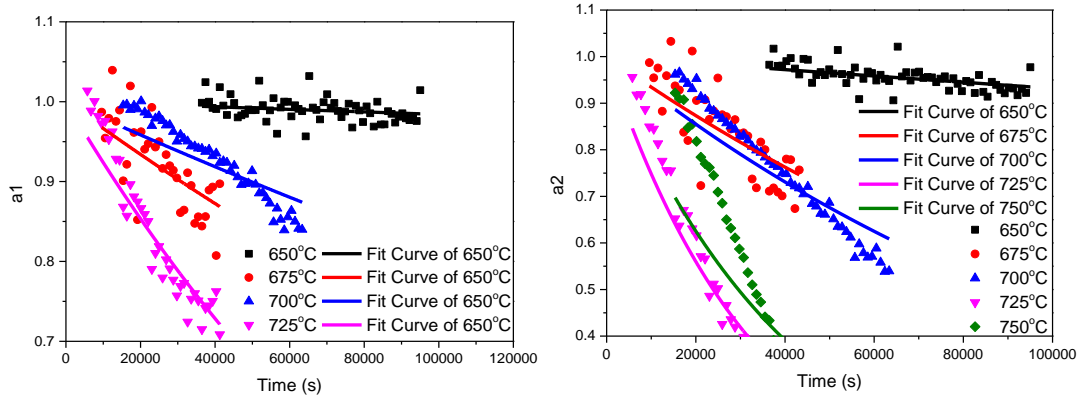


Figure 7. 6: Exponential fitting for  $a_1$  and  $a_2$

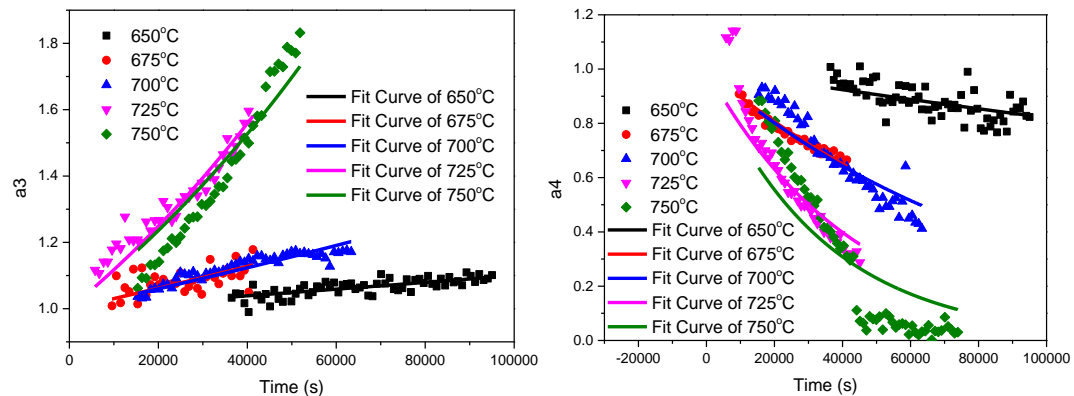
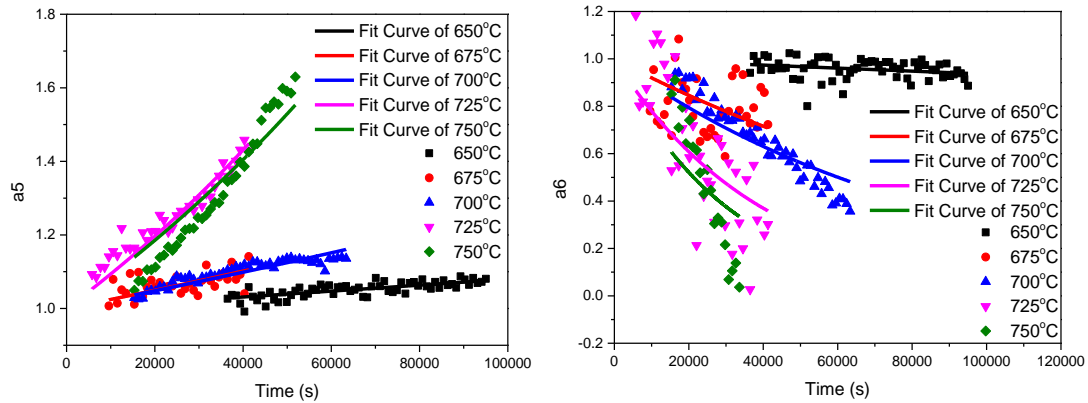


Figure 7. 7: Exponential fitting for  $a_3$  and  $a_4$



Figure 7. 8: Exponential fitting for  $a_5$  and  $a_6$ 

After exponential curve fitting, we can get the indexes (equaling to  $-k_{de,i} \cdot \exp(-\frac{E_{A\ de,i}}{RT})$  as shown in eq. (7. 11)) of the fitted equations for all reactions at all temperatures. And the results are shown in Table 7. 1. The general tendency is the absolute value of  $R_i$  increases with temperature.

Table 7. 1: Exponential estimation results for deactivation

Reaction	650°C	675°C	700°C	725°C	750°C
$R_1$	-1.6067E-07	-3.4107E-06	-2.1227E-06	-7.9206E-06	-3.1516E-06
$R_2$	-7.0695E-07	-6.7707E-06	-7.8353E-05	-2.8999E-05	-2.3468E-05
$R_3$	+9.5313E-07	+2.9944E-06	+2.9070E-06	+1.1095E-05	+1.0581E-05
$R_4$	-1.9745E-06	-1.0763E-05	-1.1027E-05	-2.3013E-05	-2.9405E-05
$R_5$	+7.6896E-07	+2.4184E-06	+2.3495E-06	+8.9617E-06	+8.4944E-06
$R_6$	-6.6353E-07	-8.3546E-06	-1.1527E-05	-2.4873E-05	-3.2578E-05

Afterwards, the deactivation kinetic parameters  $k_{de,i}$  and  $E_{A\ de,i}$  can be calculated by another curve fitting of logarithm on both sides of eq. (7. 12), which is eq. (7. 13) for  $a_3$  and  $a_5$  and eq. (7. 14) for  $a_1$ ,  $a_2$ ,  $a_4$  and  $a_6$ . The plots of  $\ln(\pm R_i(T))$  as a function of  $\frac{1}{T}$  are shown in Figure 7. 9.

Table 7. 2: Preliminary estimation results for deactivation

Reaction	Slope	Intercept	$k_{de,i}$ ( $\frac{1}{s}$ )	$E_{A\ de,i}$ ( $\frac{kJ}{mol \cdot K}$ )
$r_1$	-26817.66	14.51	+2.00E+06	222.97
$r_2$	-34209.73	23.48	+1.57E+10	284.42
$r_3$	-15287.11	3.091	-2.20E+01	127.10
$r_4$	-28567.75	18.10	+7.27E+07	237.51
$r_5$	-15901.92	3.439	-3.11E+01	132.21
$r_6$	-37522.77	27.06	+5.66E+11	311.96

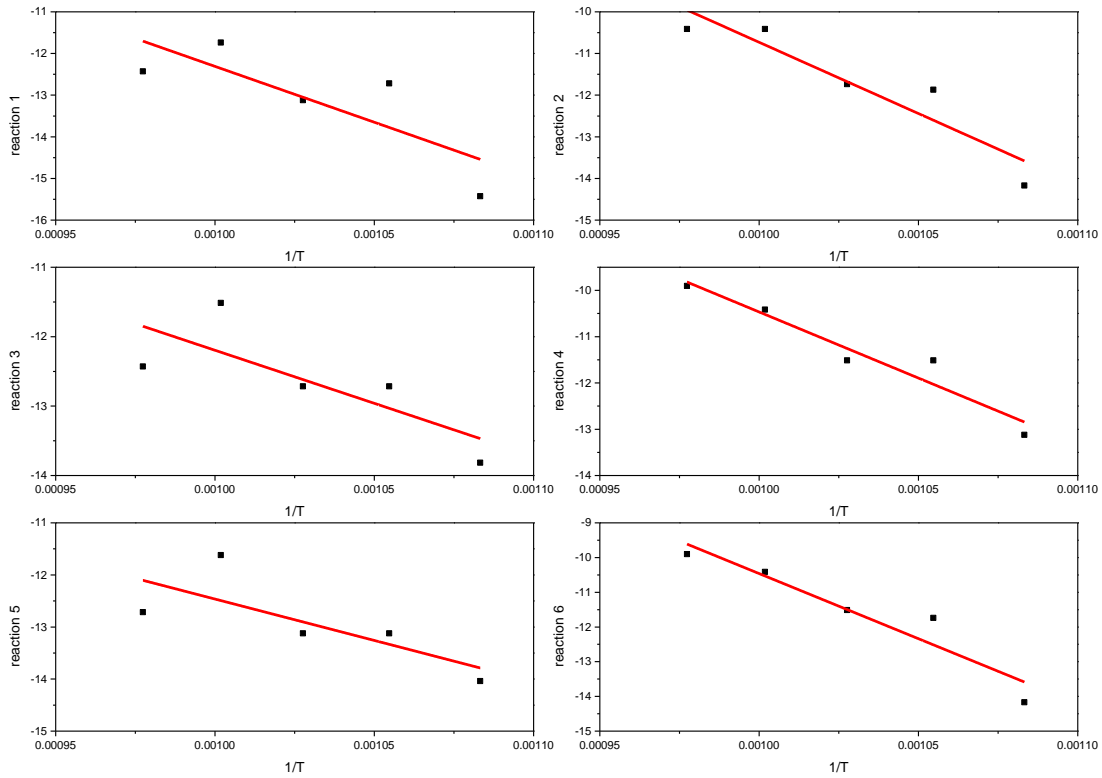


Figure 7. 9: Preliminary estimation for deactivation function parameters

The slope and intercept can be read from the fitting report directly, and the relative  $k_{de,i}$  and  $E_{A\ de,i}$  are calculated as in Table 7. 2. It is clear that the  $k_{de,3}$  and  $k_{de,5}$  are negative, and  $E_{A\ de,3}$  and  $E_{A\ de,5}$  are relative small, which imply a steady increase of  $r_3$  and  $r_5$  instead of decrease. For the rest reactions,  $r_6$  possesses the highest deactivation pre-exponential factor and energy; while  $r_1$  possesses the lowest ones.

### 7.3.3 Deactivation parameters (FBR)

The same like parameter estimation in steady state, the preliminary results are optimized by MATLAB, and the optimized results are shown in Table 7. 3. Compared with Table 7. 2,  $k_{de,6}$ ,  $E_{A\ de,2}$ ,  $E_{A\ de,3}$ ,  $E_{A\ de,4}$  and  $E_{A\ de,5}$  are higher and the rest are lower than the preliminary results. The biggest variation is  $E_{A\ de,3}$ , which increases 43.31% to the preliminary one.

Table 7. 3: Optimized estimation results for deactivation

Reaction	$k_{0,i} \left(\frac{1}{s}\right)$	$E_{a_i} \left(\frac{kJ}{mol \cdot K}\right)$
$r_1$	2.0028E+06	215.59
$r_2$	1.5545E+10	382.12
$r_3$	2.1371E+01	182.15
$r_4$	7.2642E+07	244.30
$r_5$	3.0578E+01	168.11
$r_6$	5.6657E+11	300.85

The optimized results are also validated by MATLAB to check the consistence of experimental and calculated components molar flow rates as shown in Figure 7. 10. As we can see that the deviation between the calculated data and the experimental data is acceptable. However, the differences between the outlet molar flow of carbon deposit with the experimental data is relatively obvious than that of other species, because there is no direct experimental data of carbon deposits and the so called experimental data in Figure 7. 10 is calculated according to the simulated  $x$  and  $y$  due to hydrogen and carbon balances. Therefore, the considerably big difference of carbon deposit molar flow rate is also acceptable. While the simulation performance is also checked and the all the simulated molar flow rates vary less than 10% to the experimental ones, which confirms the availability of the deactivation parameters.

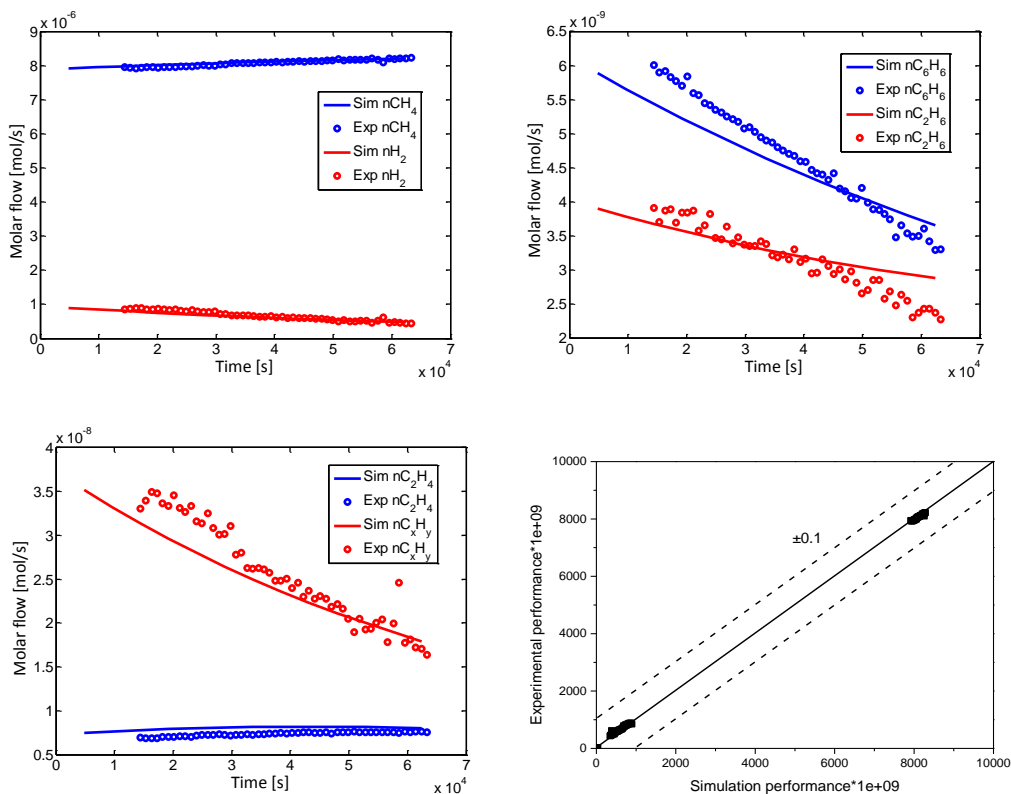


Figure 7. 10: Component molar flow rate at FBR outlet comparison

With the estimated deactivation parameters, the calculated concentration of all components in the reaction system are leaving in a full experimental time and reactor length range (of  $0-7E+04s$  and  $0-0.065m$ ) are summarized graphically in 3-D illustrations as shown in Figure 7. 11. Methane concentration decreases along with reactor length but increases with time, which is because methane is reacted and converted to products along with reactor length but increases with time due to the catalyst deactivation and then lower methane conversion then. For benzene, ethane, hydrogen and  $C_xH_y$ , the concentrations increase along with reactor length but decrease with time, which are just the opposite of methane concentration changing tendency. It is also reasonable since these components are produced from zero (so they increase with reactor length) and affected by the deactivated catalyst (so decrease with time). The profile of ethylene concentration is somehow beyond our expectation, which increases both along with reactor length and time. This can be

explained by that the coked catalyst affects the reactions of ethylene to others ( $r_2$ ,  $r_3$  and  $r_5$ ) more than the one of ethylene production ( $r_1$ ).

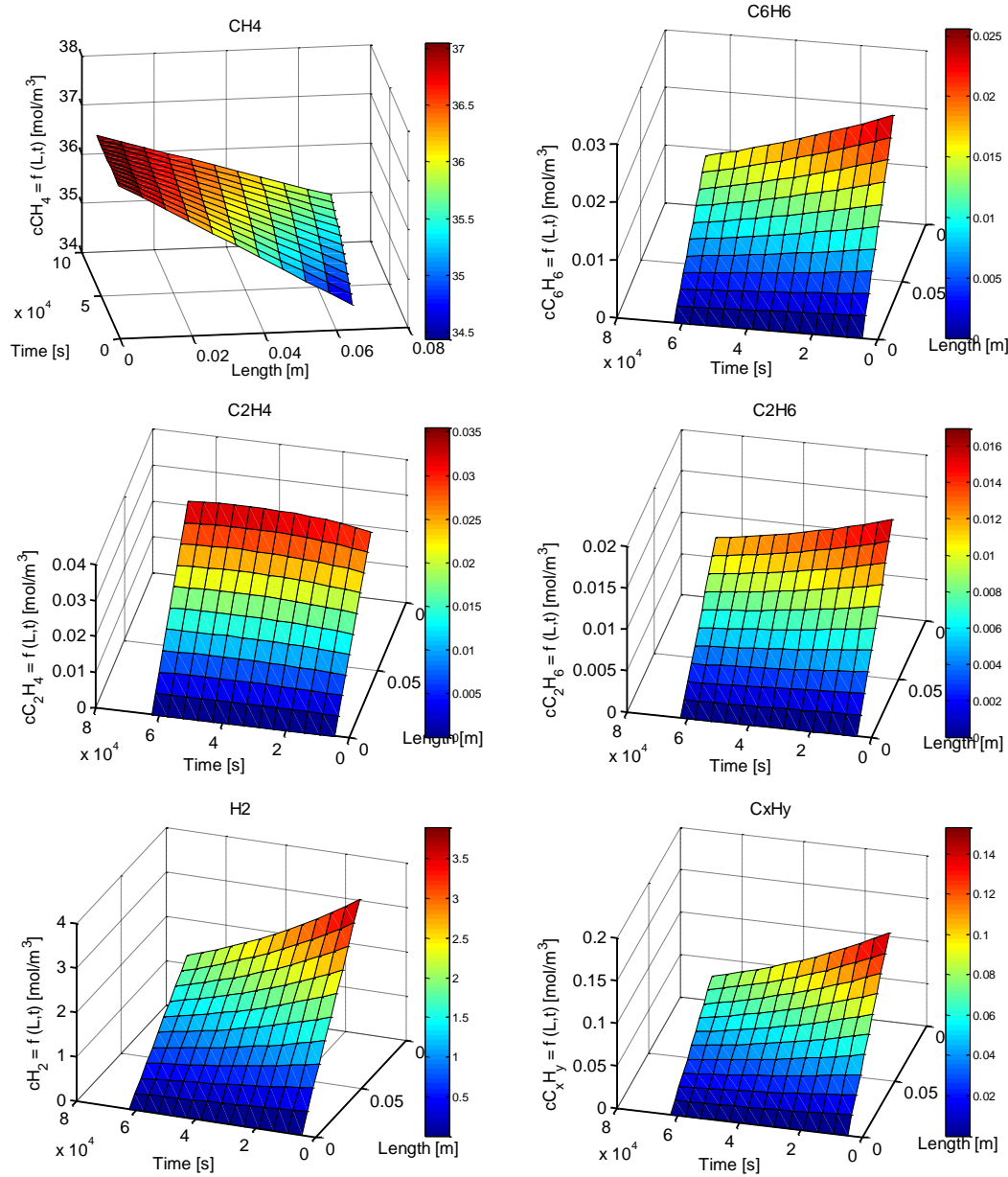


Figure 7. 11: 3D illustration of components molar flow rates in FBR

The kinetic parameters for deactivation stage shown in Table 7. 3 are validated. In addition, the rapid increasing molar flow of either products or methane in the induction period is not simulated according to the kinetic parameters of the induction period, but simulated due to convention. The detected molar flow is at the end of FBR, therefore all components molar flow rates at  $t=0$  are also zero. We can see from the results that reaction number 2 (ethylene to benzene) can deactivate relatively faster than the other reactions because of the larger resulted  $R_3$  at  $700\text{ }^\circ\text{C}$ . This phenomenon illustrates that the reaction number 2 relies on the catalytic sites more than the other reactions. When the catalyst deactivates, it will predominately decrease the production of benzene. However, anyway the deactivation of catalysts is one of the most urgent problems to be solved in order to realize MDA process industrialization.

## 7.4 Observed deactivation in MR and description

As already shown in Figure 7. 5, the catalyst after reaction has been deactivated. The original white catalyst turned to black due to the heavy carbon deposits on the catalyst both in FBR and in MR. Under this situation, the catalyst should be shifted with a fresh one or refreshed by means of regeneration (introduced in 7.1). The solid carbon deposit on/in the catalyst cannot go into the chromatography column since any solid will block the capillary column. So the composition of the solid coke cannot be precisely analyzed by means of GC. However, the portion or fraction of the solid coke strongly affects the conversion of methane and has to be considered in the carbon and hydrogen balance calculations (the specific equations can be found in section 5.3.2.2).

### 7.4.1 Experimental tendency of deactivation of MR

The experimental appearance of deactivation should be decreasing methane conversion (catalyst are not as active as fresh one) and may be also decreasing aimed products selectivity (preferentially selectively produced undesired coke). Both phenomena can be observed in my “carbon MR” experimental result as shown in Figure A. 41- Figure A. 44. The methane conversion decreasing can be clearly seen from all the figures mentioned, and the higher the temperature, the sharper the decreasing curve (as discussed in 5.2). In Figure A. 42 ( $x_{\text{CH}_4}^{\text{feed}} = 90\%$ ,  $SW = 1$ ,  $T = 700^\circ\text{C}$ ), we can clearly see the relatively high ethylene selectivity and generally increases along with time.

### 7.4.2 Preliminary estimation of MR

As similar as the deactivation investigation in FBR, deactivation in MR also consists of preliminary and optimized estimation. All the reaction rates are calculated as well as the average reaction rates of steady state. Then the value of deactivation function at each experimental time point  $a_i(t)$  can be calculated by eq. (7. 7). Then plots can be made according to eq. (7. 11) of  $a_i$  as a function of  $t$ . Then an exponential fitting can be made as shown in Figure 7. 12.

For “carbon MR” case, only two different temperatures ( $700^\circ\text{C}$  and  $650^\circ\text{C}$ ) experiments were carried out. It's clear that  $a_3$ ,  $a_5$  and  $a_6$  increase with time, which refers to a positive value of  $R_3$ ,  $R_5$  and  $R_6$ . Different from the results of FBR (see Figure 7. 8),  $R_6$  for FBR is negative but for MR is positive. According to Figure 5. 75, reaction number 3 and 5 present for ethylene reacts to ethane and  $\text{C}_x\text{H}_y$  respectively. And reaction number 6 is methane reacts to ethane. In this “carbon MR”, methane and hydrogen are mainly permeated from tube side to shell side, and nitrogen is mainly permeated from shell side to tube side. This leads to less methane concentration in the tube side of “carbon MR” compared with FBR. So we may say that deactivated catalyst favors the reaction from methane to ethane in this “carbon MR”.

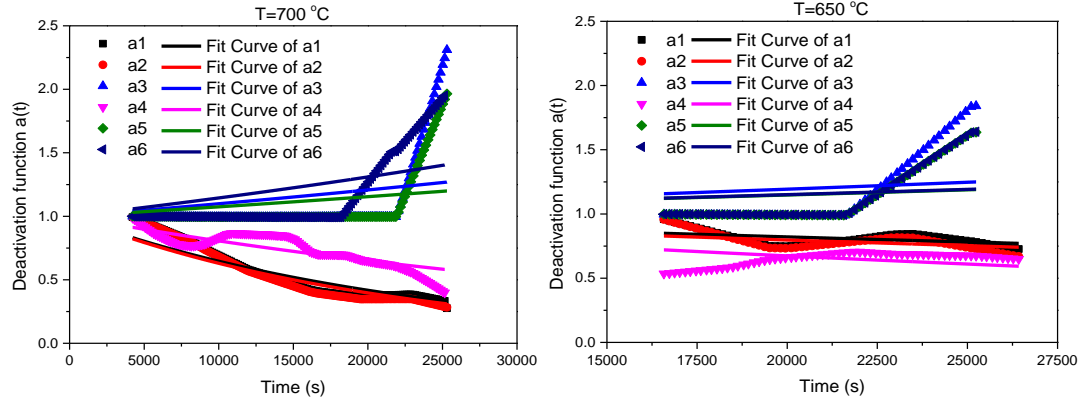


Figure 7. 12: Exponential fitting for 700°C and 650°C in “carbon MR”

After exponential curve fitting, we can get the indexes (equaling to  $-k_{de,i} \cdot \exp(-\frac{E_{A\ de,i}}{RT})$ ) as shown in eq. (7. 11) of the fitted equations for all reactions at 700°C and 650°C. And the results are shown in Table 7. 4. Compared with Table 7. 1, we know that the deactivation of  $r_1$  and  $r_4$ , the acceleration of  $r_3$ ,  $r_5$  and  $r_6$  in MR are much faster than in FBR. While for  $r_2$ , at 650°C, the deactivation in MR is faster; at 700°C, the deactivation in FBR is faster.

Table 7. 4: Exponential estimation results for deactivation in “carbon MR”

Reaction	$R_1$	$R_2$	$R_3$	$R_4$	$R_5$	$R_6$
700°C	-4.3684E-5	-4.6233E-5	9.4266E-6	-2.1542E-5	7.1839E-6	1.3495E-5
650°C	-9.8375E-6	-1.1343E-5	8.8261E-6	-1.9763E-5	6.8925E-6	7.0081E-6

Afterwards, the deactivation kinetic parameters  $k_{de,i}$  and  $E_{A\ de,i}$  can be calculated by another curve fitting of logarithm on both sides of eq. (7. 12), which is eq. (7. 13) for  $a_3$ ,  $a_5$  and  $a_6$  and eq. (7. 14) for  $a_1$ ,  $a_2$  and  $a_4$ . The plots of  $\ln(\pm R_i(T))$  as a function of  $\frac{1}{T}$  are shown in Figure 7. 13. The slopes and intercepts can be read from the fitting report directly, and the relative  $k_{de,i}$  and  $E_{A\ de,i}$  are calculated as in Table 7. 5.

Table 7. 5: Preliminary estimation results for deactivation in “carbon MR”

Reaction	Slope	Intercept	$k_{de,i}$ ( $\frac{1}{s}$ )	$E_{A\ de,i}$ ( $\frac{kJ}{mol \cdot K}$ )
$r_1$	-26785.16	17.49	+3.93E+07	222.69
$r_2$	-25245.48	15.96	+8.54E+06	209.89
$r_3$	-1182.70	-10.36	-3.51E-05	9.83
$r_4$	-1548.23	9.15	+1.06E-04	12.87
$r_5$	-734.95	-11.08	-1.54E-05	6.19
$r_6$	-11773.16	-0.88	-2.42E+00	97.88

It is clear that the  $k_{de,3}$ ,  $k_{de,5}$  and  $k_{de,6}$  are negative, and  $E_{A\ de,3}$  and  $E_{A\ de,5}$  are relative small, which imply a steady increase of  $r_3$ ,  $r_5$  and  $r_6$  instead of decrease. For the rest reactions,  $r_1$

possesses the highest deactivation pre-exponential factor and energy; while  $r_4$  possesses the lowest ones, which is completely different from the results in FBR.

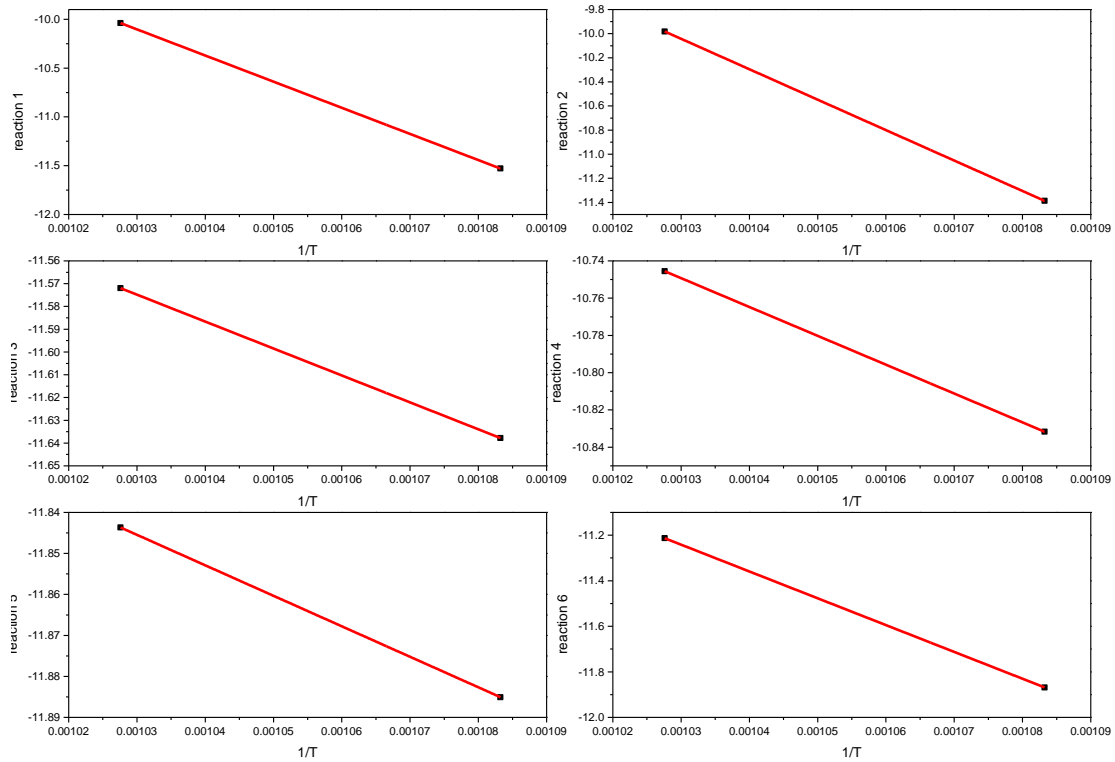


Figure 7. 13: Preliminary estimation for deactivation function parameters in “carbon MR”

### 7.4.3 Deactivation parameters (MR)

The same like parameter estimation in steady state, the preliminary results are optimized by MATLAB, and the optimized results are shown in Table 7. 6. Compared with Table 7. 5,  $k_{de,1}$ ,  $k_{de,2}$ ,  $k_{de,4}$ , and  $E_{A\ de,6}$  are higher and the  $E_{A\ de,1}$ ,  $E_{A\ de,2}$ ,  $E_{A\ de,4}$  and  $k_{de,6}$  are lower than the preliminary results. The parameters for reaction No. 3 and 5 are not changed. The biggest variation is  $E_{A\ de,1}$ , which decreases 61.19% to the preliminary one.

Table 7. 6: Optimized estimation results for deactivation in “carbon MR”

Reaction	$k_{de,i}$ ( $\frac{1}{s}$ )	$E_{A\ de,i}$ ( $\frac{kJ}{mol \cdot K}$ )
$r_1$	+4.0129E+07	86.43
$r_2$	+8.5626E+06	178.93
$r_3$	-3.5125E-05	9.83
$r_4$	+1.7877E-04	3.94
$r_5$	-1.5430E-05	6.19
$r_6$	-2.4199E+00	99.13

The optimized results are also validated by MATLAB to check the consistence of experimental and calculated components molar flow rates as shown in Figure 7. 14 and Figure 7. 15. As we can see

that the deviation between the calculated data and the experimental data for MR is much bigger than for FBR. The differences between the outlet molar flow of hydrogen (shell side) with the experimental data is relatively obvious than that of other species, because there is no direct experimental data of carbon deposits and the simulation data in Figure 7. 14 and Figure 7. 15 is calculated according to the simulated  $x$  and  $y$  (which is 4 and 9 here) due to hydrogen and carbon balances. While comparing Figure 7. 14 and Figure 7. 15 with Figure 7. 10, it's clear that the deactivation in “carbon MR” is heavier than in FBR because the steeper methane molar flow increase and benzene molar flow decrease. Another point is, ethylene molar flow rate in “carbon MR” ( $1.93\text{E}-10$  mol/s) is lower than in FBR ( $7.52\text{E}-09$  mol/s).

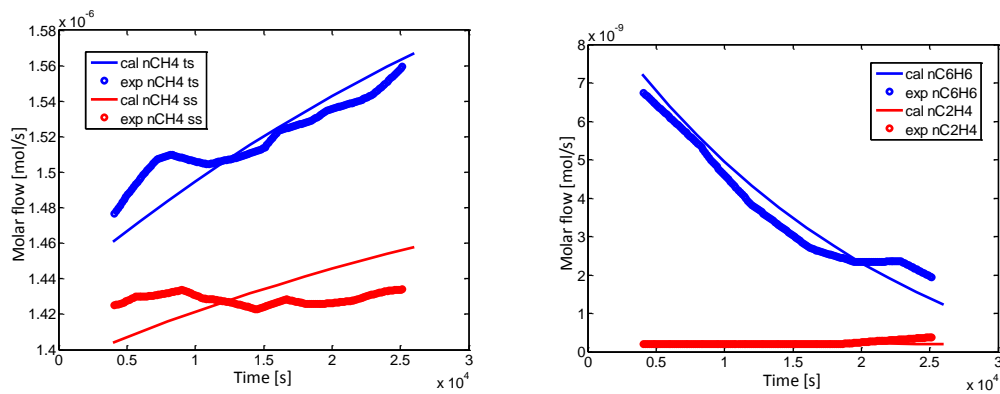


Figure 7. 14: Component molar flow rate at MR outlet comparison

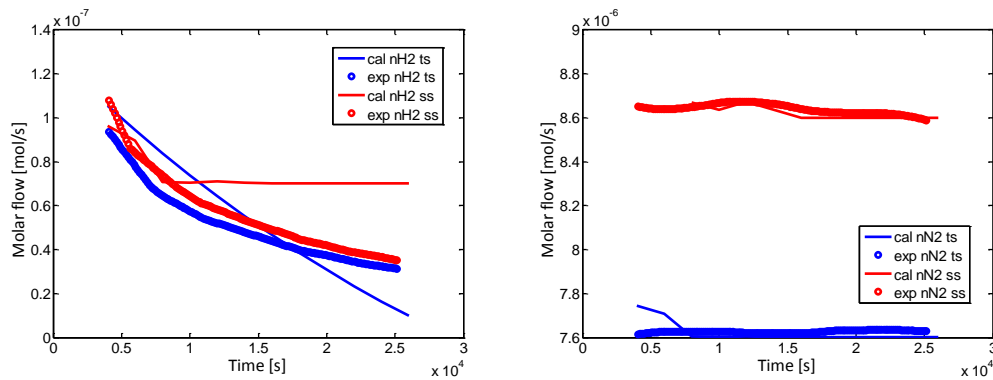


Figure 7. 15: Component molar flow rate at MR outlet comparison

With the estimated deactivation parameters for “carbon MR”, the calculated concentration of all components in the reaction system are leaving in a full experimental time and reactor length range (of 0-2.6E+04s and 0-0.22m) are summarized graphically in 3-D illustrations as shown in Figure 7. 16. Methane concentration in tube side decreases along with reactor length but increases with time, which is because methane is reacted and converted to products along with reactor length but increases with time due to the catalyst deactivation and then lower methane conversion then. Methane concentration in shell side stays nearly unchanged. For benzene, hydrogen in tube side and C<sub>x</sub>H<sub>y</sub>, the concentrations increase along with reactor length but decrease with time, which are just the opposite of methane concentration changing tendency. It is also reasonable since these components are produced from zero (so they increase with reactor length) and affected by the



deactivated catalyst (so decrease with time). The profile of ethylene concentration is somehow beyond our expectation, which increases along with reactor length and is parabolic with time. Ethylene concentration is affected by the reaction rates of  $r_1$ ,  $r_2$ ,  $r_3$  and  $r_5$ . The deactivated catalyst couple influence these reaction rates, which results in the profile of ethylene concentration. Ethane concentration increases along with reactor length and time, which is consisted with the conclusion in Chapter 5 that deactivated catalyst can produce more ethane.

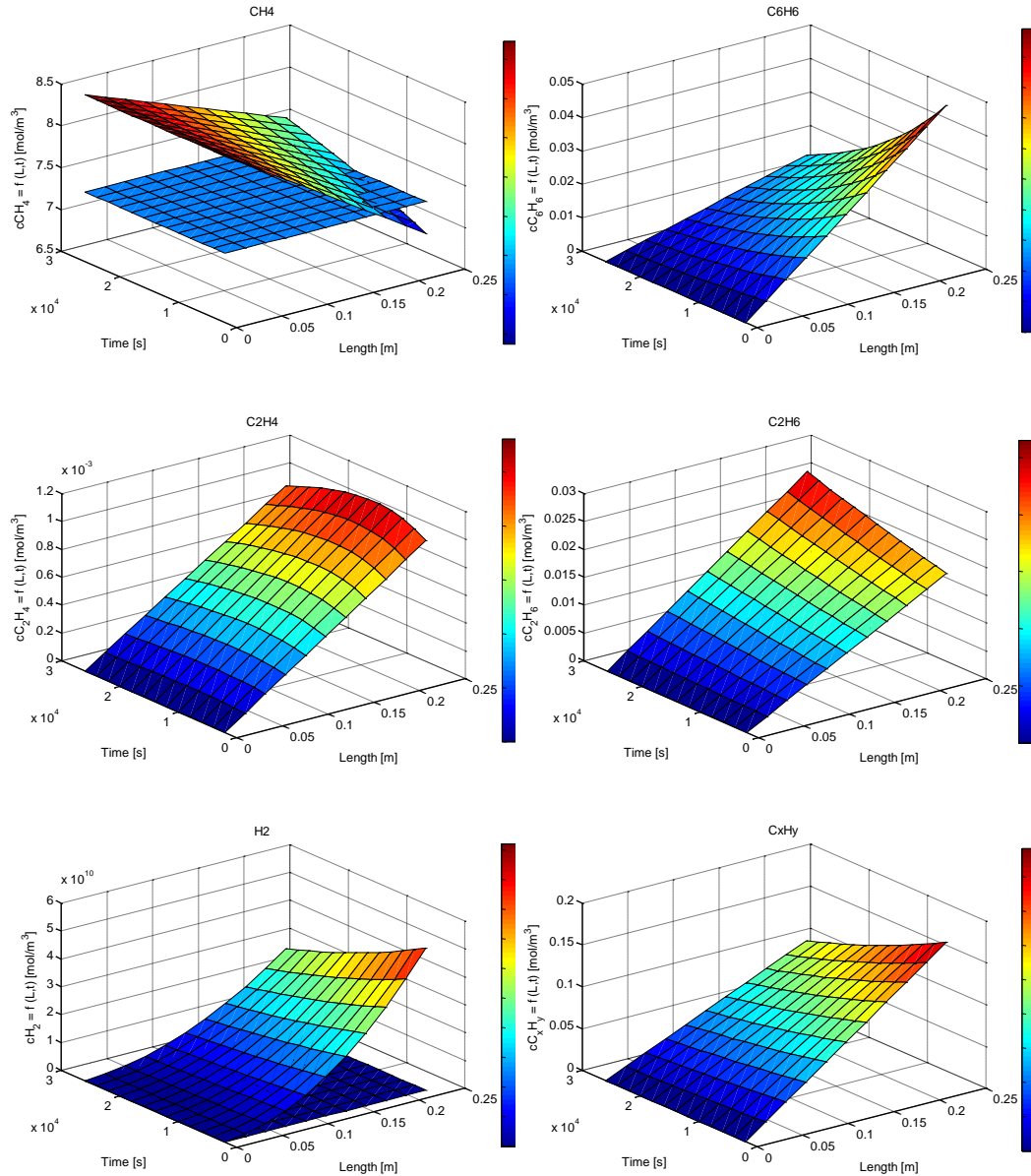


Figure 7. 16: 3D illustration of components molar flow rates in “carbon MR”

The kinetic parameters for deactivation stage shown in Table 7. 6 are validated. The detected molar flow is at the end of “carbon MR”, therefore all components molar flow rates at  $t=0$  are missing. We can see from the results that reaction number 1 (methane to ethylene) and 2 (ethylene to benzene) can deactivate relatively faster than the other reactions because of the larger resulted  $R_3$  at  $700^\circ\text{C}$ , which is the same as in FBR. This phenomenon illustrates that the reaction number 1 and 2 relies

on the catalytic sites more than the other reactions. When the catalyst deactivates, it will predominately decrease the production of benzene. Comparing with the deactivation in FBR, it's clear that deactivation in MR is much faster and stronger, which can be seen from the total reaction time and slope of benzene molar flow rate decreasing curve. However, anyway the deactivation of catalysts is one of the most urgent problems to be solved in order to realize MDA process industrialization.

## 7.5 Conclusions

Catalyst deactivation is a very serious problem for continuous operation in industry. Also MDA suffers from fast catalyst deactivation. The experimental results of this work show that the hierarchical Mo/MCM-22 has a relative good tolerance against coke formation at 700°C.

When the catalyst deactivates, the molar flow rates of benzene, ethylene and ethane decrease while the molar flow rate of methane increases. Catalyst deactivation in “carbon MR” is stronger than in FBR, which can be concluded from the decrease of benzene molar flow rates in both reactors.

A deactivation function (eq. (7. 8)) is used to describe the catalyst deactivation. All parameters in this deactivation model are estimated. The simulation results for FBR show good consistency to the experimental result except for the molar flow rate of  $C_xH_y$ . This is because the calculated molar flow rate of  $C_xH_y$  contains bigger error than the molar flow rates directly measured from experiments. The simulation results for deactivation in the “carbon MR” also show good consistency to the experiments, except for the molar flow rate of  $H_2$  in shell side. A further problem was, that the permeating behavior of the carbon membranes changed with time, which was not included in the model. This catalyst deactivation model can be used to estimate the deactivation performance and the catalyst lifetime.

---

## Summary and conclusions

The topics of this work were a) to enlarge the database regarding the heterogeneously catalyzed methane dehydro-aromatization (MDA) reaction, b) to study MDA thermodynamics, c) to estimate kinetic parameters for a specific catalyst belonging to proposed networks and d) to investigate the potential of membrane reactors (MR).

An alternative way to produce benzene instead of applying traditional catalytic reforming and steam cracking possesses a large relevance. For a comprehensive investigation, an analysis of thermodynamics and kinetics of MDA was done with a Mo/MCM-22 catalyst using both fixed-bed reactor (FBR) and MR. The reaction performances of MDA under various reacting conditions were studied experimentally for methane and ethylene feeds. Reaction rates depend on operation conditions, in particular temperature. The influence of temperature, feed composition and residence times (W/F) in FBR was quantified. With simultaneous composition measurements, it was possible to identify kinetic parameters of reaction rates. A difficulty in the model development was the proposition of possibly reactions and reasonable reaction network. Regarding the experimental investigation of the reaction kinetics of MDA, three reaction networks with different complexity were proposed. Pre-exponential factors of the rate constants, reaction orders and activation energies were quantified for each network. Besides, the parameters estimated were also evaluated by comparing with the experimental results.

Chapter 2 presents the results of the thermodynamic study of MDA including the effect of hydrogen removal. These results show that under realistic experimental conditions, the MDA equilibrium composition is characterized by very low of methane conversion and benzene yield. The removal of hydrogen offers the possibility to shift the equilibrium to the product side, which means first of all to increase the methane conversion.

The catalyst used in this thesis is hierarchically structured Mo/MCM-22, which was synthesized at the Dalian University of Technology in China. This hierarchical Mo/MCM-22 gives better MDA performance than alternative catalysts and shows better tolerance against carbon deposition.

Experimental results and kinetic investigations using a FBR are discussed in chapter 5. Results of MDA for the main reaction network with methane as feed and for the instructive sub-network with ethylene as feed are given. Different attempts were made in order to determine reliable kinetic data. Following the goal to describe the MDA performance quantitatively, a controlled variable method was used to evaluate the influence of a single reaction condition (temperature, feed composition and W/F). For comparison, single experiments and stepwise experiments were carried out for the same operating condition, as well as studies of deactivation in long time experiments. Furthermore, dynamic experiments were performed by changing feed concentrations periodically. Practically, the experimental results of this chapter provides a performance map and guidelines how temperature, feed concentration and residence time influence the MDA performance. However, critical inspection show that the MDA performance achieved in this work is still rather small compared to the “window of reality” in industry. The simulation results of chapter 5 can be used to predict MDA performance under certain conditions within the range of the experiments. Furthermore, the methodological

---

aspects regarding the analysis of the kinetics provide procedures to investigate other complex reaction systems.

Results of a feasibility study and experimental investigations of MR in conjunction with MDA are presented in chapter 6. Firstly, a Pd membrane model is used to study the feasibility theoretically. Simulation results of a “Pd MR” show that this can be in principle very promising for MDA system. However, since there is no temperature resistant Pd membrane available, two carbon membranes were used in an experimental study for hydrogen removal. The obtained results regarding characterization and reactions in a MR were presented, followed by simulation results. The results show that the selectivity to hydrogen of this asymmetric carbon membrane is not as high as expected. Two permeating models were derived. The performance of these two membranes was unfortunately found to be different. The results of MDA in this “carbon MR” shows that around 45-50% of methane also permeated to the shell side, which results in reduced methane conversion. The theoretical and practical results of MDA using this “carbon MR” are not comparable with the result of FBR due to the insufficient hydrogen selectivity. The simulation results for the carbon membrane in the MR are similar as the results of the “Pd MR”. The carbon membrane applied in the experimental study was found to be compatible with the relative low productivity of the MDA reaction.

Chapter 7 is dedicated to deactivation of the catalyst in both FBR and MR. Catalyst deactivation was found to be a very serious problem of MDA. Nevertheless, the experimental results show that this hierarchical Mo/MCM-22 has a rather good tolerance against coke formation at 700°C, which means a longer life time (up to 48h) in FBR. A simple deactivation function is used to describe the catalyst deactivation and all corresponding parameters are estimated. This deactivation model can be used to predict the deactivation performance and the catalyst lifetime (48h in FBR and 4h in “carbon MR”) under certain reaction conditions in both FBR and MR.

The potential of membrane reactor is promising to increase the methane conversion and benzene yield in MDA. However, currently no suitable membranes are available and the catalysts are not sufficient selective, active and stable. For further investigation of non-oxidative MDA, both better catalysts and suitable membranes need to be developed.

# Nomenclature

## Latin Symbols

A	Reactor Cross-section Area	$m^2$
A, B, C	Gibbs Enthalpy Parameters	
$a_i$	Deactivation Function	
$c_i$	Concentration	$mol/m^3$
$B_0$	Permeability Parameter	$m^2$
$\hat{b}$	Mobility of the Surface Molecules	$mol \cdot m^2/J/s$
$b_i$	Mobility of the Gas Molecules	$mol \cdot m^2/J/s$
Da	Damkohler Number	
$D_i$	Diffusion Coefficient	$m^2/s$
$D_{k0}$	Knudsen Diffusion coefficient	$m^2/s$
$D_k$	Knudsen Diffusivity	$m^2/s$
$D_C$	Maxwell-Stefan Diffusivity	$m^2/s$
$E_{Ai}$	Activation Energy	J/mol
F/W	Flow Weight Ratio	mL/gh
$G_R$	Reaction Gibbs Enthalpy	J
$J_i$	Permeation Flux	$mol/m^2/s$
$K_P$	Equilibrium Constant	
$k_i$	Reaction rate constant	$m^{3\alpha-3}/s/mol^{1-\alpha}$
$k_{\infty i}$	Pre-exponential Factor	$m^{3\alpha-3}/s/mol^{1-\alpha}$
$M_i$	Molecular Weight	g/mol
$N_C$	Number of Components	
$N_R$	Number of Reactions	
$n_i$	Mole Number	mol
$n_i^0$	Initial Mole Number	mol
$\dot{n}_i$	Mole Flow	mol/s
P	Pressure	Pa or bar
$p^0$	Standard Pressure	Pa or bar
$p_i$	Partial Pressure	Pa or bar
R	Universal Gas Constant	J/mol/K
$R_i$	Concentration Changing Rate of Component i	$mol/m^3/s$
r	Reactor Radius	m
$r_i$	Reaction Rate	$mol/m^3/s$
$r_{tube}$	Tube Side Diameter in Membrane Reactor	m
$S_R$	Reaction Entropy	J/K
$S_i$	Selectivity	%
$T^0$	Standard Temperature	K
T	Temperature	K or °C
t	Time	s
V	Volume	$m^3$
$\dot{V}$	Volumetric Flow	$m^3/s$

---

$V_R$	Reactor Volume	
W/F	Weight Flow Ratio	kgs/m <sup>3</sup>
$X_i$	Conversion	%
$x_i, y_i$	Mole Fraction	
$Y_i$	Yield	%
$z$	Reactor Length Coordinate	m
$\Delta_r H^0$	Standard Reaction Enthalpy	kJ/mol
$\Delta_r G^0$	Standard Reaction Gibbs Enthalpy	kJ/mol
$\Delta H_{298.15}^0$	Enthalpy under standard pressure at 298.15K	kJ/mol
$\Delta_r S^0$	Standard Reaction Entropy	kJ/molK

### Greek Symbols

$\alpha$	Reaction Order	
$\varepsilon$	Porosity	
$\tau$	Tortuosity	
$\gamma_i$	Activity Coefficient	
$\Gamma$	Matrix of Thermodynamic Correction Factors	
$\omega_i$	Weights for Responses	
$\eta$	Dynamic Viscosity	Pas
$\mu_i$	Chemical Potential	J/mol
$\nu_{ij}$	Stoichiometric Number	
$\xi$	Reaction Extend	mol

### Superscript

cal, exp	Calculation, Experiment
in, out	Inlet, Outlet
$\Phi$	Standard Pressure Condition
0	Standard Condition or Initial Condition
SS	Steady State
ts, ss	Tube Side, Shell Side

### Subscript

de	Deactivation
exp	Experiment
f	Formation
f, b	Forward and Backward
i	Component i
j	Reaction j
prod	Product
r	Reaction
resp	Response
react	Reactant
S	Surface
tot	Total

---

**Abbreviation**

AAS	Atomic Absorption Spectroscopy
ASS	Atomic Absorption Spectroscopy
BET	Brunauer Emmett Teller theory
CC	Cross Channel
CO <sub>2</sub> R	Carbon Dioxide Reforming
Conv.	Conversion
CS	Cage Structure
CuC	Curved Channel
EDX	Energy Dispersive X-ray detector
EPR	Electron Paramagnetic Resonance
EXAFS	Extended X-ray Absorption Fine Structure
FBR	Fixed Bed Reactor
FFM	Film Flow Meter
FT	Fischer-Tropsche Process
FTIR	Fourier Transform Infrared Radiation
GC	Gas Chromatography
IR	Infrared Radiation
ISS	Ion Scattering Spectroscopy
IUPAC	International Union of Pure and Applied Chemistry
MAS-NMR	Magic Angle Spinning Nuclear Magnetic Resonance
MDA	Methane Dehydro-Aromatization
MFC	Mass Flow Controller
MR	Membrane Reactor
M-R	Molecular-Ring
MSD	Mass Selective Detector
NMR	Nuclear Magnetic Resonance
OCM	Oxidative Coupling of Methane
OD	Oxidative Dimerization
OM	Oxidative Methylation
PFTR	Plug Flow Tubular Reactor
POM	Partial Oxidation of Methane
RC	Ring Channel
SC	Straight Channel
SCS	Super Cage Structure
Select.	Selectivity
StR	Steam Reforming
SV	Space Velocity
TCD	Thermal Conduction Detector
TCP	Thermal Catalytic Pyrolysis
TEM	Transmission Electron Microscopy
TG	Thermogravimetry

---

TGA	Thermal Gravimetric Analysis
TPCO <sub>2</sub>	Temperature Programmed CO <sub>2</sub> reaction
TPD	Temperature Programmed Desorption
TPH	Temperature Programmed Hydrogenation
TPO	Temperature Programmed Oxidation
TPR	Temperature Programmed Reduction
TPSR	Temperature Programmed Surface Reaction
UV	Ultra Violet
XPS	X-ray Photoelectron Spectroscopy
XRD	X-Ray Diffraction



## Appendix

This appendix describes: A) FBR results with methane feed in section 5.2.1; B) FBR results with ethylene feed in section 5.2.2; and C) MR results with methane feed in section 6.6.

### A) FBR results with methane feed (detailed discussed in section 5.2.1):

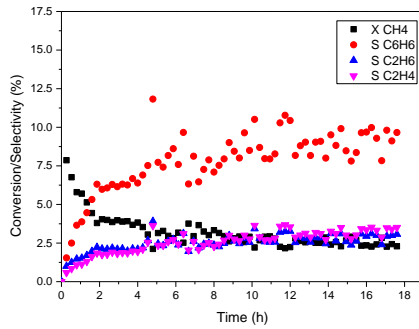


Figure A. 1: Feed=CH<sub>4</sub>, T=650°C, feed volumetric fraction=90%, W/F=2166.91kg/m<sup>3</sup>

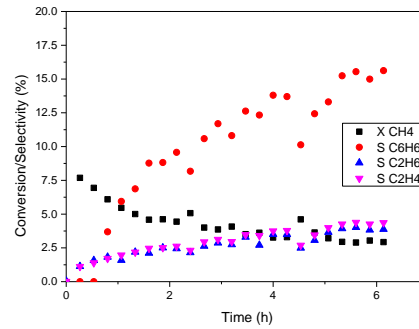


Figure A. 2: Feed=CH<sub>4</sub>, T=675°C, feed volumetric fraction=90%, W/F=2165.67kg/m<sup>3</sup>

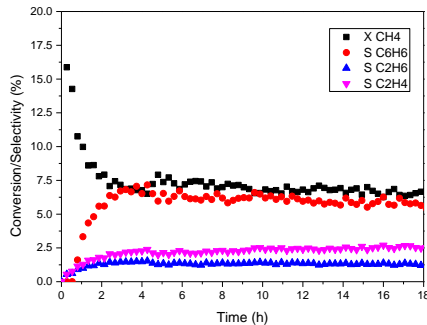


Figure A. 3: Feed=CH<sub>4</sub>, T=700°C, feed volumetric fraction=90%, W/F=2207.86kg/m<sup>3</sup>

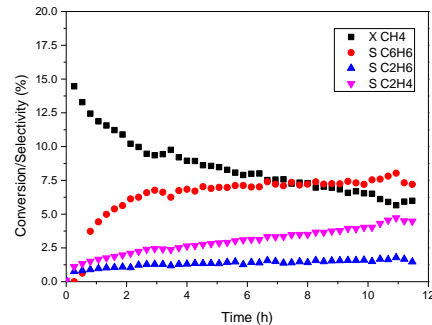


Figure A. 4: Feed=CH<sub>4</sub>, T=725°C, feed volumetric fraction=90%, W/F=2166.53kg/m<sup>3</sup>

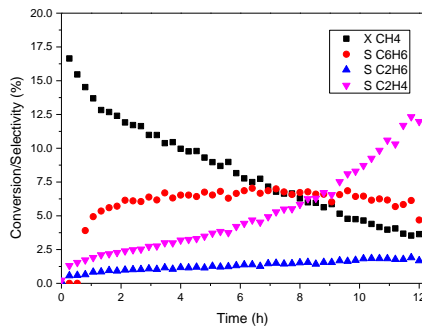


Figure A. 5: Feed=CH<sub>4</sub>, T=750°C, feed volumetric fraction=90%, W/F=2166.49kgs/m<sup>3</sup>

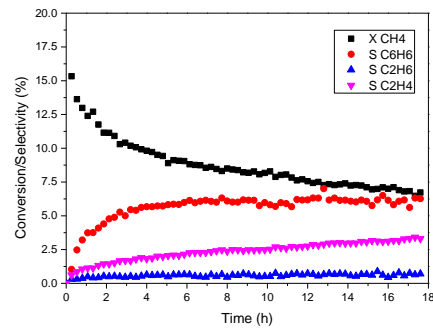


Figure A. 6: Feed=CH<sub>4</sub>, T=700°C, feed volumetric fraction=30%, W/F=2162.28kgs/m<sup>3</sup>

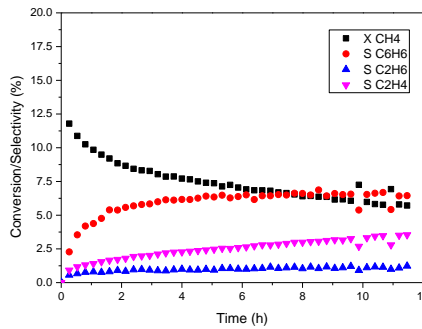


Figure A. 7: Feed=CH<sub>4</sub>, T=700°C, feed volumetric fraction=50%, W/F=2163.62kgs/m<sup>3</sup>

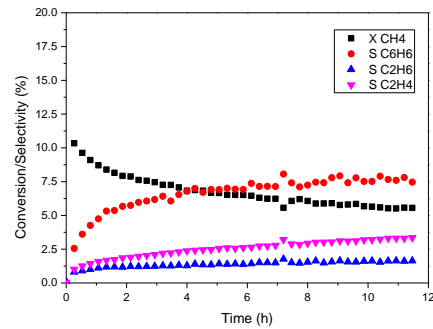


Figure A. 8: Feed=CH<sub>4</sub>, T=700°C, feed volumetric fraction=70%, W/F=2163.74kgs/m<sup>3</sup>

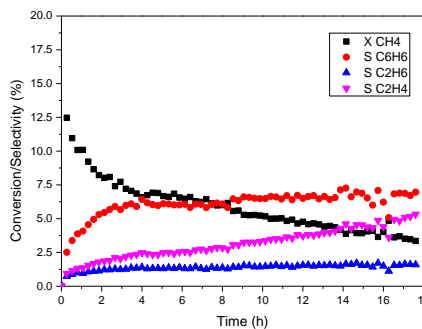


Figure A. 9: Feed=CH<sub>4</sub>, T=700°C, feed volumetric fraction=90%, W/F=2167.24kgs/m<sup>3</sup>

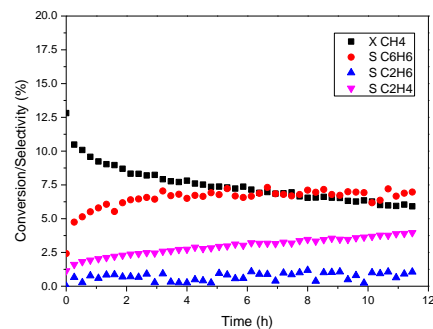


Figure A. 10: Feed=CH<sub>4</sub>, T=700°C, feed volumetric fraction=30%, W/F=719.81kgs/m<sup>3</sup>

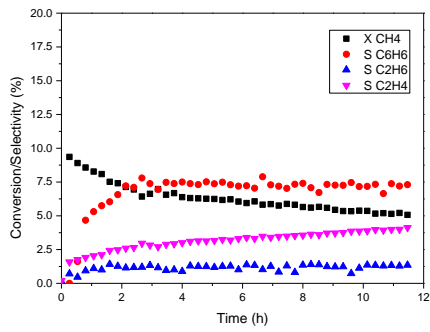


Figure A. 11: Feed=CH<sub>4</sub>, T=700°C, feed volumetric fraction=50%, W/F=1201.63kgs/m<sup>3</sup>

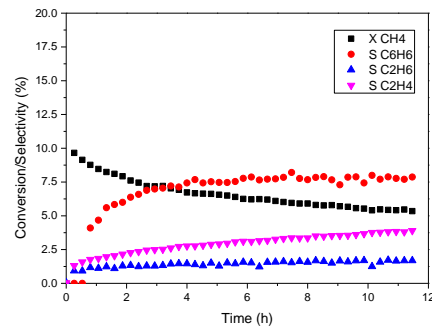


Figure A. 12: Feed=CH<sub>4</sub>, T=700°C, feed volumetric fraction=70%, W/F=1680.32kgs/m<sup>3</sup>

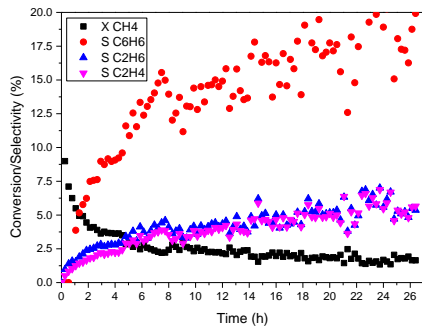


Figure A. 13: Feed=CH<sub>4</sub>, T=650°C, feed volumetric fraction=90%, W/F=2178.12kgs/m<sup>3</sup>

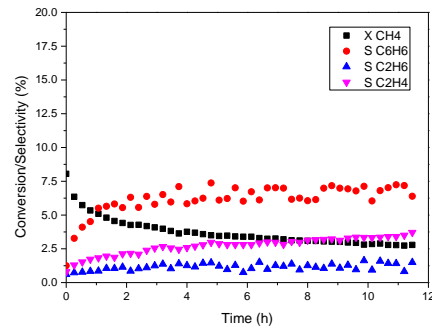


Figure A. 14: Feed=CH<sub>4</sub>, T=650°C, feed volumetric fraction=30%, W/F=720.26kgs/m<sup>3</sup>

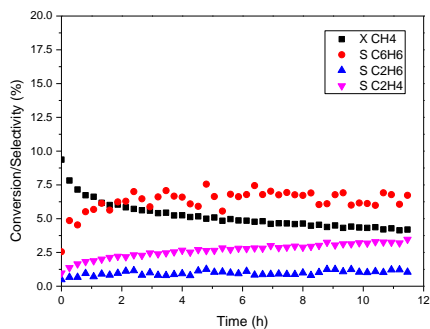


Figure A. 15: Feed=CH<sub>4</sub>, T=675°C, feed volumetric fraction=30%, W/F=720.26kgs/m<sup>3</sup>

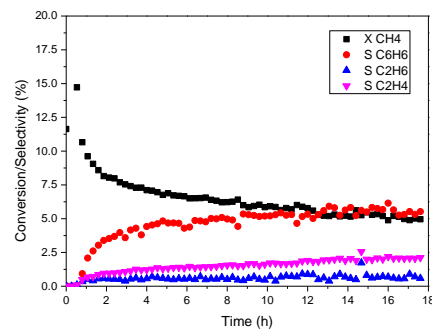


Figure A. 16: Feed=CH<sub>4</sub>, T=650°C, feed volumetric fraction=30%, W/F=2162.68kgs/m<sup>3</sup>

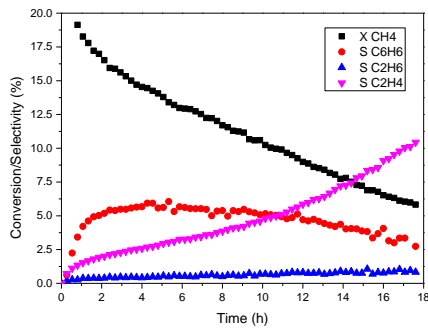


Figure A. 17: Feed=CH<sub>4</sub>, T=750°C, feed volumetric fraction=30%, W/F=2163.48kgs/m<sup>3</sup>

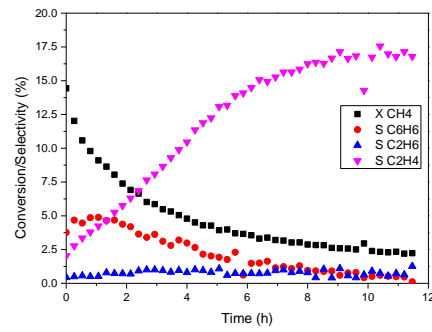


Figure A. 18: Feed=CH<sub>4</sub>, T=750°C, feed volumetric fraction=30%, W/F=720.19kgs/m<sup>3</sup>

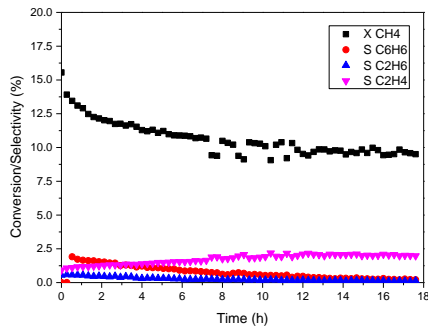


Figure A. 19: Feed=CH<sub>4</sub>, T=700°C, feed volumetric fraction=90%, W/F=720.52kgs/m<sup>3</sup>

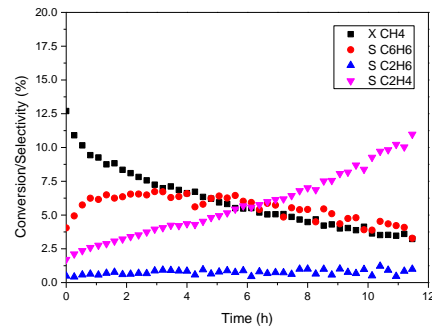


Figure A. 20: Feed=CH<sub>4</sub>, T=725°C, feed volumetric fraction=30%, W/F=720.30kgs/m<sup>3</sup>

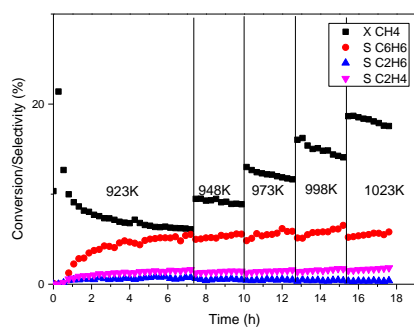


Figure A. 21: Feed=CH<sub>4</sub>, T=650-750°C, feed volumetric fraction=30%, W/F=2162.37kgs/m<sup>3</sup>

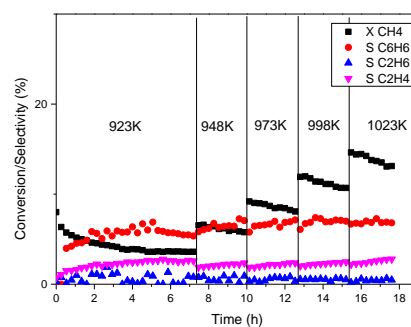


Figure A. 22: Feed=CH<sub>4</sub>, T=650-750°C, feed volumetric fraction=30%, W/F=720.42kgs/m<sup>3</sup>

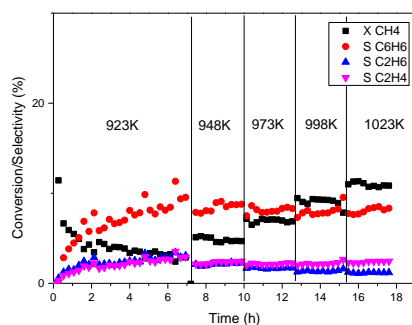


Figure A. 23: Feed= $\text{CH}_4$ ,  $T=650\text{-}750^\circ\text{C}$ , feed volumetric fraction=90%,  $W/F=2166.06\text{kg}/\text{m}^3$

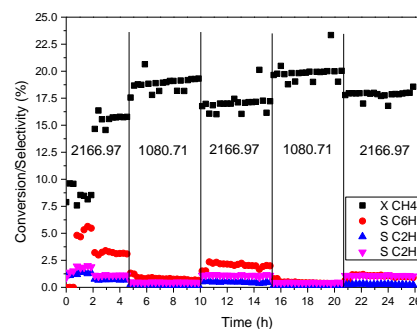


Figure A. 24: Feed= $\text{CH}_4$ ,  $T=700^\circ\text{C}$ , feed volumetric fraction=90%,  $W/F=1080.71\text{-}2166.97\text{kg}/\text{m}^3$

## B) FBR results with ethylene feed (detailed discussed in section 5.2.2):

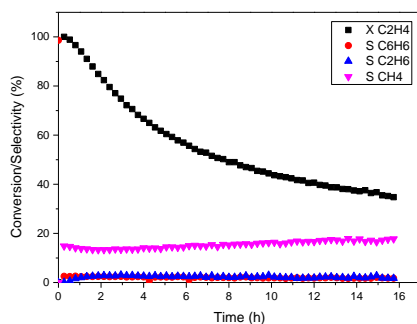


Figure A. 25: Feed= $\text{C}_2\text{H}_4$ ,  $T=650^\circ\text{C}$ , feed volumetric fraction=1%,  $W/F=53.93\text{kg}/\text{m}^3$ , Cat.=activated

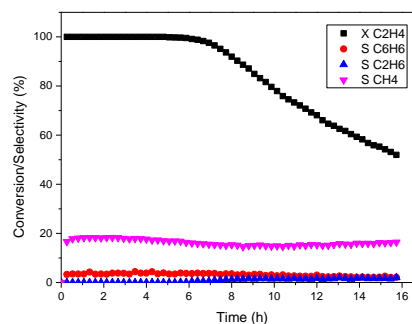


Figure A. 26: Feed= $\text{C}_2\text{H}_4$ ,  $T=675^\circ\text{C}$ , feed volumetric fraction=1%,  $W/F=53.93\text{kg}/\text{m}^3$ , Cat.=activated

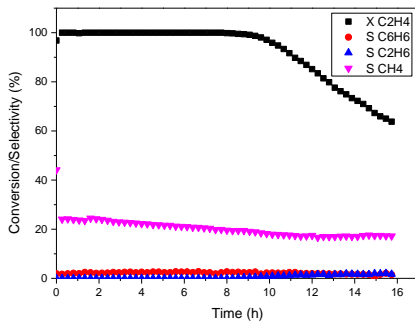


Figure A. 27: Feed= $C_2H_4$ ,  $T=700^\circ C$ , feed volumetric fraction=1%,  $W/F=74.90kgs/m^3$ , Cat.=activated

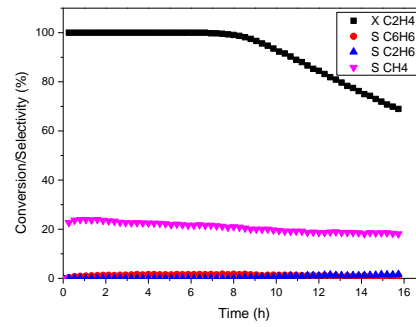


Figure A. 28: Feed= $C_2H_4$ ,  $T=725^\circ C$ , feed volumetric fraction=1%,  $W/F=53.96kgs/m^3$ , Cat.=activated

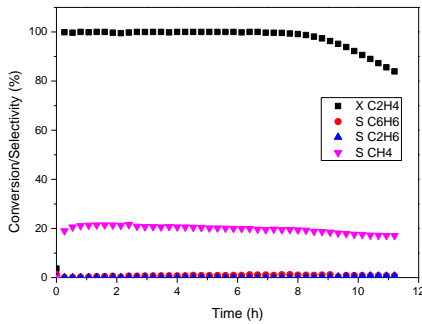


Figure A. 29: Feed= $C_2H_4$ ,  $T=750^\circ C$ , feed volumetric fraction=1%,  $W/F=53.95kgs/m^3$ , Cat.=activated

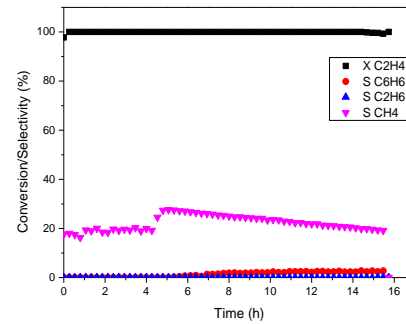


Figure A. 31: Feed= $C_2H_4$ ,  $T=700^\circ C$ , feed volumetric fraction=1%,  $W/F=74.94kgs/m^3$ , Cat.=not activated

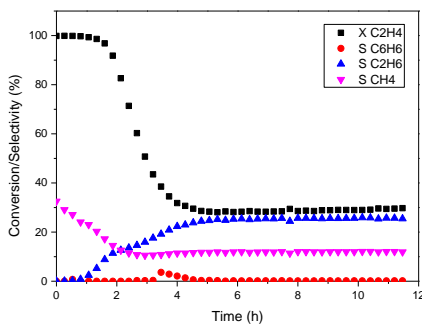


Figure A. 30: Feed= $C_2H_4$ ,  $T=700^\circ C$ , feed volumetric fraction=40%,  $W/F=2161.69kgs/m^3$ , Cat.=not activated

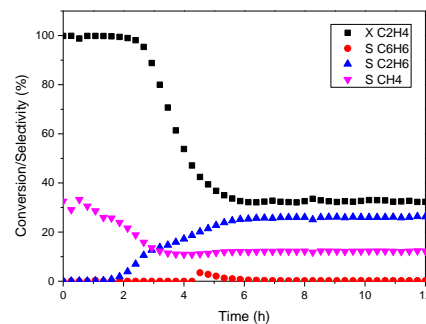


Figure A. 32: Feed= $C_2H_4$ ,  $T=700^\circ C$ , feed volumetric fraction=39.06%,  $W/F=2161.26kgs/m^3$ , Cat.=not activated

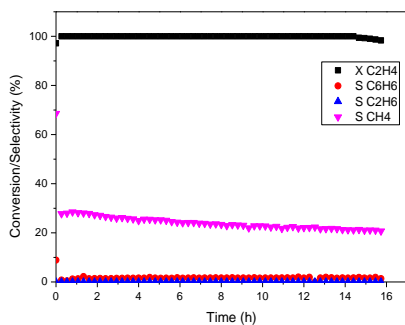


Figure A. 33: Feed= $C_2H_4$ ,  $T=700^\circ C$ , feed volumetric fraction=0.5%,  $W/F=59.64kgs/m^3$ , Cat.=activated

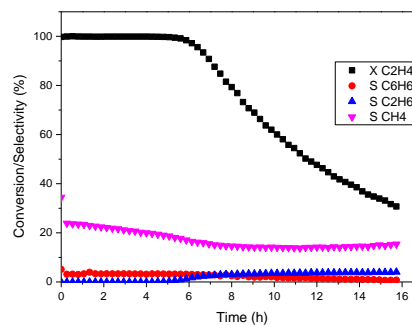


Figure A. 34: Feed= $C_2H_4$ ,  $T=700^\circ C$ , feed volumetric fraction=2.5%,  $W/F=149.74kgs/m^3$ , Cat.=activated

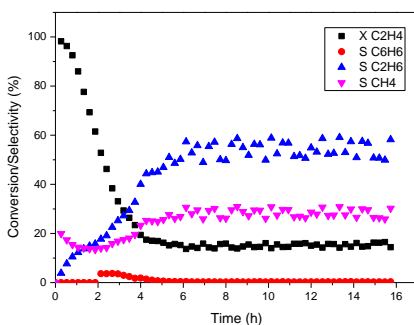


Figure A. 35: Feed= $C_2H_4$ ,  $T=700^\circ C$ , feed volumetric fraction=21%,  $W/F=456.19kgs/m^3$ , Cat.=activated

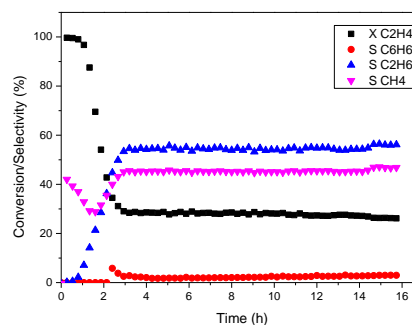


Figure A. 36: Feed= $C_2H_4$ ,  $T=750^\circ C$ , feed volumetric fraction=40%,  $W/F=2167.54kgs/m^3$ , Cat.=activated

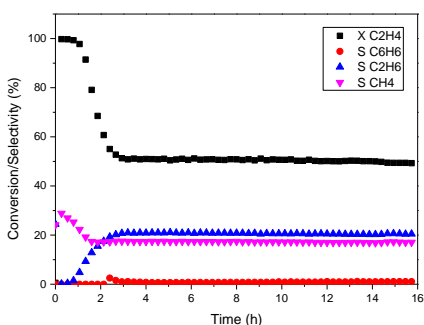


Figure A. 37: Feed= $C_2H_4$ ,  $T=750^\circ C$ , feed volumetric fraction=40%,  $W/F=2167.53kgs/m^3$ , Cat.=activated

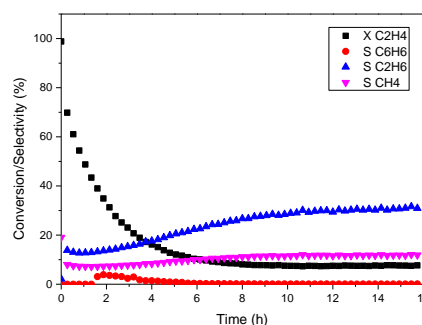


Figure A. 38: Feed= $C_2H_4$ ,  $T=650^\circ C$ , feed volumetric fraction=40%,  $W/F=2166.41kgs/m^3$ , Cat.=activated

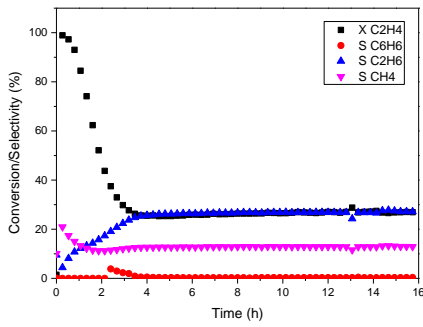


Figure A. 39: Feed= $\text{C}_2\text{H}_4$ ,  $T=700^\circ\text{C}$ , feed volumetric fraction=40%,  $W/F=2167.15\text{kg}/\text{m}^3$ , Cat.=activated

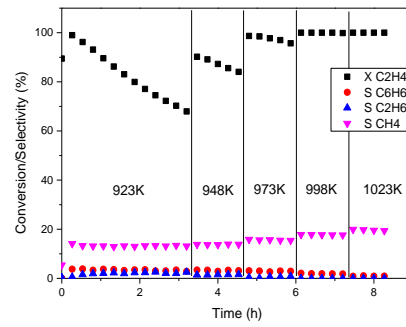


Figure A. 40: Feed= $\text{C}_2\text{H}_4$ ,  $T=650\text{-}750^\circ\text{C}$ , feed volumetric fraction=1%,  $W/F=53.94\text{kg}/\text{m}^3$ , Cat.=activated

### C) MR results with methane feed (detailed discussed in section 6.6):

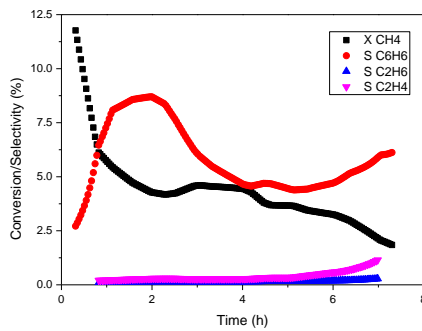


Figure A. 41: Feed= $\text{CH}_4$ ,  $T=700^\circ\text{C}$ , feed volumetric fraction=30%,  $SW=1$

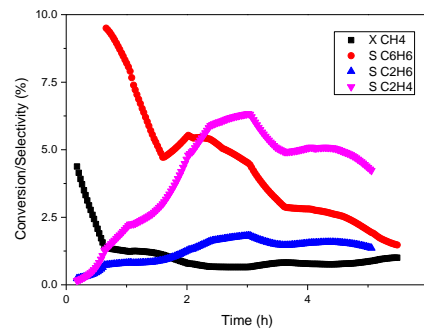


Figure A. 42: Feed= $\text{CH}_4$ ,  $T=700^\circ\text{C}$ , feed volumetric fraction=90%,  $SW=1$

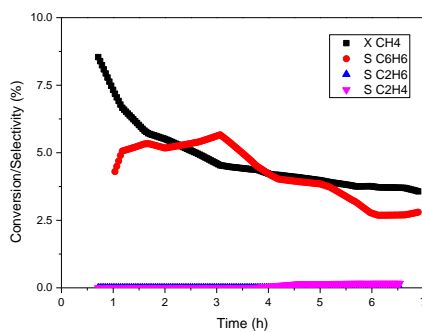


Figure A. 43: Feed= $\text{CH}_4$ ,  $T=700^\circ\text{C}$ , feed volumetric fraction=30%,  $SW=3$

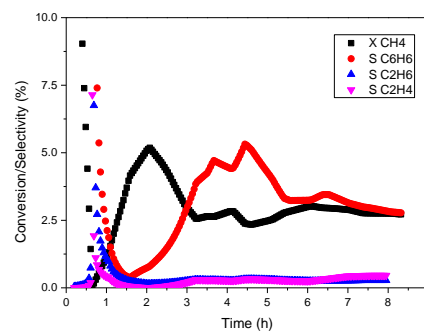


Figure A. 44: Feed= $\text{CH}_4$ ,  $T=650^\circ\text{C}$ , feed volumetric fraction=30%,  $SW=1$



---

## Reference

1. Survey, U.S.G., *Natural gas production in the United States*. USGS Fact Sheet FS-113-01, 2002: p. 2.
2. bp. *Statistical Review of World Energy*. Natural gas reserves 2013; <http://www.bp.com/en/global/corporate/about-bp/energy-economics/statistical-review-of-world-energy-2013/review-by-energy-type/natural-gas/natural-gas-reserves.html>.
3. Bradford, M.C.J. and M.A. Vannice, *CO<sub>2</sub> Reforming of CH<sub>4</sub>*. *Catalysis Reviews*, 1999. **41**(1): p. 1-42.
4. Rostrup-Nielsen, J.R., *Production of synthesis gas*. *Catalysis Today*, 1993. **18**(4): p. 305-324.
5. Vannice M, A., *Catalytic Synthesis of Hydrocarbons from Carbon Monoxide and Hydrogen*, in *Solid State Chemistry of Energy Conversion and Storage*. 1977, AMERICAN CHEMICAL SOCIETY. p. 15-32.
6. Ashcroft, A.T., et al., *Partial oxidation of methane to synthesis gas using carbon dioxide*. *Nature*, 1991. **352**(6332): p. 225-226.
7. Choudhary, V.R., A.M. Rajput, and B. Prabhakar, *NiO/CaO-Catalyzed Formation of Syngas by Coupled Exothermic Oxidative Conversion and Endothermic CO<sub>2</sub> and Steam Reforming of Methane*. *Angewandte Chemie International Edition in English*, 1994. **33**(20): p. 2104-2106.
8. Brown, M.J. and N.D. Parkyns, *Progress in the partial oxidation of methane to methanol and formaldehyde*. *Catalysis Today*, 1991. **8**(3): p. 305-335.
9. Michalkiewicz, B., *Partial oxidation of methane to formaldehyde and methanol using molecular oxygen over Fe-ZSM-5*. *Applied Catalysis A: General*, 2004. **277**(1-2): p. 147-153.
10. Nguyen, L.D., et al., *Study of new catalysts based on vanadium oxide supported on mesoporous silica for the partial oxidation of methane to formaldehyde: Catalytic properties and reaction mechanism*. *Journal of Catalysis*, 2006. **237**(1): p. 38-48.
11. Muradov, N.Z., *How to produce hydrogen from fossil fuels without CO<sub>2</sub> emission*. *International Journal of Hydrogen Energy*, 1993. **18**(3): p. 211-215.
12. Poirier, M.G. and C. Sapundzhiev, *Catalytic decomposition of natural gas to hydrogen for fuel cell applications*. *International Journal of Hydrogen Energy*, 1997. **22**(4): p. 429-433.
13. Bonura, G., et al., *A basic assessment of the reactivity of Ni catalysts in the decomposition of methane for the production of "CO<sub>x</sub>-free" hydrogen for fuel cells application*. *Catalysis Today*, 2006. **116**(3): p. 298-303.
14. Reshetenko, T.V., et al., *Catalytic filamentous carbons-supported Ni for low-temperature methane decomposition*. *Catalysis Today*, 2005. **102-103**(0): p. 115-120.
15. Wang, H., Y. Cong, and W. Yang, *Oxidative coupling of methane in Ba<sub>0.5</sub>Sr<sub>0.5</sub>Co<sub>0.8</sub>Fe<sub>0.2</sub>O<sub>3-δ</sub> tubular membrane reactors*. *Catalysis Today*, 2005. **104**(2-4): p. 160-167.
16. Otsuka, K., M. Hatano, and T. Amaya, *Oxidative cross-coupling of methane and toluene over LiCl-added Co<sub>3</sub>O<sub>4</sub>*. *Journal of Catalysis*, 1992. **137**(2): p. 487-496.
17. Keller, G.E. and M.M. Bhasin, *Synthesis of ethylene via oxidative coupling of methane: I. Determination of active catalysts*. *Journal of Catalysis*, 1982. **73**(1): p. 9-19.
18. Lee, J.S. and S.T. Oyama, *Oxidative Coupling of Methane to Higher Hydrocarbons*. *Catalysis Reviews*, 1988. **30**(2): p. 249-280.
19. Lunsford, J.H., *The catalytic conversion of methane to higher hydrocarbons*. *Catalysis Today*, 1990. **6**(3): p. 235-259.

20. Qiu, X.-q., et al., *Low temperature catalysts for oxidative coupling of methane*. Journal of Chemical Technology & Biotechnology, 1996. **65**(4): p. 303-308.
21. Choudhary, V.R., B.S. Uphade, and S.A.R. Mulla, *Oxidative Coupling of Methane over a Sr-Promoted La<sub>2</sub>O<sub>3</sub> Catalyst Supported on a Low Surface Area Porous Catalyst Carrier*. Industrial & Engineering Chemistry Research, 1997. **36**(9): p. 3594-3601.
22. Platon, C.E. and W.J. Thomson, *A Comparison of LSCF-6428 and Bys for the Oxidative Conversion of Methane and Ethane*. Industrial & Engineering Chemistry Research, 2002. **41**(26): p. 6637-6641.
23. Czuprat, O., et al., *Oxidative Coupling of Methane in a BCFZ Perovskite Hollow Fiber Membrane Reactor*. Industrial & Engineering Chemistry Research, 2010. **49**(21): p. 10230-10236.
24. Tonkovich, A.L., R.W. Carr, and R. Aris, *Enhanced C<sub>2</sub> Yields from Methane Oxidative Coupling by Means of a Separative Chemical Reactor*. Science, 1993. **262**(5131): p. 221-223.
25. Jiang, Y., I.V. Yentekakis, and C.G. Vayenas, *Methane to Ethylene with 85 Percent Yield in a Gas Recycle Electrocatalytic Reactor-Separator*. Science, 1994. **264**(5165): p. 1563-1566.
26. Choudhary, V.R., et al., *Beneficial effect of oxygen distribution on methane conversion and C<sub>2</sub>-selectivity in oxidative coupling of methane to C<sub>2</sub>-hydrocarbons over lanthanum-promoted magnesium oxide*. Journal of the Chemical Society, Chemical Communications, 1989(20): p. 1526-1527.
27. Bjorklund, M.C. and R.W. Carr, *The simulated countercurrent moving bed chromatographic reactor: a catalytic and separative reactor*. Catalysis Today, 1995. **25**(2): p. 159-168.
28. Cordi, E.M., et al., *Steady-state production of olefins in high yields during the oxidative coupling of methane: Utilization of a membrane contactor*. Applied Catalysis A: General, 1997. **155**(1): p. L1-L7.
29. Han, S., et al., *The direct partial oxidation of methane to liquid hydrocarbons over HZSM-5 zeolite catalyst*. Journal of Catalysis, 1992. **136**(2): p. 578-583.
30. Wang, L., et al., *Dehydrogenation and aromatization of methane under non-oxidizing conditions*. Catalysis Letters, 1993. **21**(1): p. 35-41.
31. Ma, S., et al., *Recent progress in methane dehydroaromatization: From laboratory curiosities to promising technology*. Journal of Energy Chemistry. **22**(1): p. 1-20.
32. Nagy, A. and G. Mestl, *High temperature partial oxidation reactions over silver catalysts*. Applied Catalysis A: General, 1999. **188**(1-2): p. 337-353.
33. Wang, D.J., M.P. Rosynek, and J.H. Lunsford, *Oxidative Coupling of Methane over Oxide-Supported Sodium-Manganese Catalysts*. Journal of Catalysis, 1995. **155**(2): p. 390-402.
34. Bao, X., et al., *Oxidative coupling of methane on silver catalysts*. Catalysis Letters, 1995. **32**(1-2): p. 185-194.
35. Nagy, A.J., G. Mestl, and R. Schlögl, *The Role of Subsurface Oxygen in the Silver-Catalyzed, Oxidative Coupling of Methane*. Journal of Catalysis, 1999. **188**(1): p. 58-68.
36. Shepelev, S.S. and K.G. Ione, *Preparation of aromatic hydrocarbons from methane in the presence of O<sub>2</sub>*. Reaction Kinetics and Catalysis Letters, 1983. **23**(3-4): p. 323-325.
37. Guo, X., and Bao, X., *Direct, Nonoxidative Conversion of Methane to Ethylene, Aromatics, and Hydrogen*. Science, 2014. **344**(6184): p. 616-619.
38. Ismagilov, Z.R., E.V. Matus, and L.T. Tsikoza, *Direct conversion of methane on Mo/ZSM-5 catalysts to produce benzene and hydrogen: achievements and perspectives*. Energy & Environmental Science, 2008. **1**(5): p. 526.

39. OTSUKA, et al., *Conversion of methane to aromatic hydrocarbons by combination of catalysts*. 1986, Tokyo, JAPON: Chemical Society of Japan.
40. Claridge, J.B., et al., *Oxidative oligomerisation of methane to aromatics*. Applied Catalysis A: General, 1992. **89**(1): p. 103-116.
41. Yu, Z., et al., *From CH<sub>4</sub> reforming with CO<sub>2</sub> to pyrolysis over a platinum catalyst*. Reaction Kinetics and Catalysis Letters, 1993. **51**(1): p. 143-149.
42. Inui, T., et al., *Pt Loaded HIGH-Ga Silicates for Aromatization of Light Paraffins and Methane*, in *Studies in Surface Science and Catalysis*, P.A. Jacobs and R.A.v. Santen, Editors. 1989, Elsevier. p. 1183-1192.
43. Qiu, P., J.H. Lunsford, and M.P. Rosynek, *Steady-state conversion of methane to aromatics in high yields using an integrated recycle reaction system*. Catalysis Letters, 1997. **48**(1-2): p. 11-15.
44. Weckhuysen, B.M., et al., *Conversion of Methane to Benzene over Transition Metal Ion ZSM-5 Zeolites: I. Catalytic Characterization*. Journal of Catalysis, 1998. **175**(2): p. 338-346.
45. Chu, N., *Studies on Hierarchical Catalysts and Membrane Catalytic Reactor in Methane Dehydroaromatization*. Doctoral Thesis of Dalian University of Technology, 2010.
46. Chu, N., et al., *Nestlike Hollow Hierarchical MCM-22 Microspheres: Synthesis and Exceptional Catalytic Properties*. Chemistry of Materials, 2010. **22**(9): p. 2757-2763.
47. Chu, N., et al., *A feasible way to enhance effectively the catalytic performance of methane dehydroaromatization*. Catalysis Communications, 2010. **11**(6): p. 513-517.
48. Abasov S J, B.F.A., Dadashev B A, *Determination of the activation energy of a surface reaction with a complex thermal desorption spectrum*. Kinetics and Catalysis, 1991. **32**: p. 202-205.
49. Murata, K. and H. Ushijima, *Dehydrogenation-aromatization of methane on amorphous-like carbons*. Journal of the Chemical Society, Chemical Communications, 1994(10): p. 1157-1158.
50. Marczewski, M. and H. Marczevska, *Oxide catalysts for methane transformations in the absence of oxygen*. Reaction Kinetics and Catalysis Letters, 1994. **53**(1): p. 33-38.
51. Marczewski, M., H. Marczevska, and M. Debowski, *Catalysts for methane transformation in the absence of oxygen, II. Nature of active centers*. Reaction Kinetics and Catalysis Letters, 1995. **55**(1): p. 207-212.
52. Marczewski, M., H. Marczevska, and K. Mazowiecka, *Catalysts for methane transformations into aromatics*. Reaction Kinetics and Catalysis Letters, 1995. **54**(1): p. 81-86.
53. Liu, S., et al., *Bifunctional Catalysis of Mo/HZSM-5 in the Dehydroaromatization of Methane to Benzene and Naphthalene XAFS/TG/DTA/MASS/FTIR Characterization and Supporting Effects*. Journal of Catalysis, 1999. **181**(2): p. 175-188.
54. Shu, Y., R. Ohnishi, and M. Ichikawa, *Pressurized Dehydrocondensation of Methane toward Benzene and Naphthalene on Mo/HZSM-5 Catalyst: Optimization of Reaction Parameters and Promotion by CO<sub>2</sub> Addition*. Journal of Catalysis, 2002. **206**(1): p. 134-142.
55. Kinage, A.K., R. Ohnishi, and M. Ichikawa, *Marked Enhancement of the Methane Dehydrocondensation Toward Benzene Using Effective Pd Catalytic Membrane Reactor with Mo/ZSM-5*. Catalysis Letters, 2003. **88**(3-4): p. 199-202.
56. Ma, H., et al., *Efficient regeneration of Mo/HZSM-5 catalyst by using air with NO in methane dehydro-aromatization reaction*. Applied Catalysis A: General, 2004. **275**(1-2): p. 183-187.
57. Liu, H., X. Bao, and Y. Xu, *Methane dehydroaromatization under nonoxidative conditions over Mo/HZSM-5 catalysts: Identification and preparation of the Mo active species*. Journal of

- Catalysis, 2006. **239**(2): p. 441-450.
58. Rodrigues, A.C.C. and J.L.F. Monteiro, *The use of CH<sub>4</sub>/H<sub>2</sub> cycles on dehydroaromatization of methane over Mo/MCM-22*. Catalysis Communications, 2008. **9**(6): p. 1060-1065.
59. Ma, D., et al., *Mo/MCM-22 Catalysts for Methane Dehydroaromatization: A Multinuclear MAS NMR Study*. The Journal of Physical Chemistry B, 2001. **105**(9): p. 1786-1793.
60. Wong, K.S., et al., *Methane aromatisation based upon elementary steps: Kinetic and catalyst descriptors*. Microporous and Mesoporous Materials, 2012. **164**(0): p. 302-312.
61. Cao, Z., et al., *Natural Gas to Fuels and Chemicals: Improved Methane Aromatization in an Oxygen-Permeable Membrane Reactor*. Angewandte Chemie International Edition, 2013. **52**(51): p. 13794-13797.
62. Xu, Y., X. Bao, and L. Lin, *Direct conversion of methane under nonoxidative conditions*. Journal of Catalysis, 2003. **216**(1-2): p. 386-395.
63. Liu, B.S., et al., *Characteristic and Mechanism of Methane Dehydroaromatization over Zn-Based/HZSM-5 Catalysts under Conditions of Atmospheric Pressure and Supersonic Jet Expansion*. The Journal of Physical Chemistry C. **115**(34): p. 16954-16962.
64. Luzgin, M.V., et al., *Understanding Methane Aromatization on a Zn-Modified High-Silica Zeolite*. Angewandte Chemie International Edition, 2008. **47**(24): p. 4559-4562.
65. Kusmiyati and N.A.S. Amin, *Dual effects of supported W catalysts for dehydroaromatization of methane in the absence of oxygen*. Catalysis Letters, 2005. **102**(1-2): p. 69-78.
66. Xiong, Z.-T., et al., *Study of W/HZSM-5-Based Catalysts for Dehydro-aromatization of CH<sub>4</sub> in Absence of O<sub>2</sub>. I. Performance of Catalysts*. Catalysis Letters, 2001. **74**(3-4): p. 227-232.
67. Zeng, J.L., et al., *Nonoxidative dehydrogenation and aromatization of methane over W/HZSM-5-based catalysts*. Catalysis Letters, 1998. **53**(1-2): p. 119-124.
68. Ding, W., et al., *Synthesis, Structural Characterization, and Catalytic Properties of Tungsten-Exchanged H-ZSM5*. The Journal of Physical Chemistry B, 2001. **105**(18): p. 3928-3936.
69. Kozlov, V.V., et al., *Active sites of the methane dehydroaromatization catalyst W-ZSM-5: An HRTEM study*. Kinetics and Catalysis, 2008. **49**(1): p. 110-114.
70. Shu, Y., R. Ohnishi, and M. Ichikawa, *Improved methane dehydrocondensation reaction on MCM-22 and HZSM-5 supported rhenium and molybdenum catalysts*. Applied Catalysis A: General, 2003. **252**(2): p. 315-329.
71. Tan, P.L., C.T. Au, and S.Y. Lai, *Methane dehydrogenation and aromatization over 4 wt% Mn/HZSM-5 in the absence of an oxidant*. Catalysis Letters, 2006. **112**(3-4): p. 239-245.
72. Xu, Y., et al., *Methane activation without using oxidants over Mo/HZSM-5 zeolite catalysts*. Catalysis Letters, 1994. **30**(1): p. 135-149.
73. Wang, L., R. Ohnishi, and M. Ichikawa, *Selective Dehydroaromatization of Methane toward Benzene on Re/HZSM-5 Catalysts and Effects of CO/CO<sub>2</sub> Addition*. Journal of Catalysis, 2000. **190**(2): p. 276-283.
74. Solymosi, F., A. Erdöhelyi, and A. Szöke, *Dehydrogenation of methane on supported molybdenum oxides. Formation of benzene from methane*. Catalysis Letters, 1995. **32**(1-2): p. 43-53.
75. Zhang, C.-L., et al., *Aromatization of methane in the absence of oxygen over Mo-based catalysts supported on different types of zeolites*. Catalysis Letters, 1998. **56**(4): p. 207-213.
76. Hongmei, L., *Investigation of bi- functional catalyst Mo/HZSM-5 in methane dehydro-aromatization system*, in *Dalian Institute of Chemical Physics Chinese Academy of Science*. 2004:

- Dalian.
77. Ma, D., et al., *Mo/MCM-22 Catalysts for Methane Dehydroaromatization: A Multinuclear MAS NMR Study*. The Journal of Physical Chemistry B, 2001. **105**(9): p. 1786-1793.
78. Bai, J., et al., *Shape Selectivity in Methane Dehydroaromatization Over Mo/MCM-22 Catalysts During a Lifetime Experiment*. Catalysis Letters, 2003. **90**(3-4): p. 123-130.
79. Rodrigues, A. and J.L. Monteiro, *CO<sub>2</sub> addition on the non-oxidative dehydro-aromatization of methane over MoMCM-22*. Catalysis Letters, 2007. **117**(3-4): p. 166-170.
80. Sobalík, Z., et al., *Acidic and catalytic properties of Mo/MCM-22 in methane aromatization: an FTIR study*. Applied Catalysis A: General, 2003. **253**(1): p. 271-282.
81. Ha, V.T.T., et al., *Aromatization of methane over zeolite supported molybdenum: active sites and reaction mechanism*. Journal of Molecular Catalysis A: Chemical, 2002. **181**(1-2): p. 283-290.
82. Wu, P., et al., *The synthesis of Mo/H-MCM-36 catalyst and its catalytic behavior in methane non-oxidative aromatization*. Catalysis Communications, 2005. **6**(7): p. 449-454.
83. Shu, Y., et al., *An MAS NMR Study on the Mo-modified Phosphoric Rare Earth (HZRP-1) Penta-Sil Zeolite Catalyst*. The Journal of Physical Chemistry B, 2000. **104**(34): p. 8245-8249.
84. Martínez, A., E. Peris, and G. Sastre, *Dehydroaromatization of methane under non-oxidative conditions over bifunctional Mo/ITQ-2 catalysts*. Catalysis Today, 2005. **107-108**(0): p. 676-684.
85. Xing, H., et al., *Detemplation with H<sub>2</sub>O<sub>2</sub> and characterization of MCM-56*. Catalysis Communications, 2008. **9**(2): p. 234-238.
86. Association, I.Z., *International Zeolite Association*. 1967.
87. Ma, S., et al., *Recent progress in methane dehydroaromatization: From laboratory curiosities to promising technology*. Journal of Energy Chemistry, 2013. **22**(1): p. 1-20.
88. Xu, Y., et al., *Interaction between ammonium heptamolybdate and NH<sub>4</sub>ZSM-5 zeolite: the location of Mo species and the acidity of Mo/HZSM-5*. Catalysis Letters, 1995. **35**(3-4): p. 233-243.
89. Chen, L.Y., et al., *Dehydro-oligomerization of Methane to Ethylene and Aromatics over Molybdenum/HZSM-5 Catalyst*. Journal of Catalysis, 1995. **157**(1): p. 190-200.
90. Wang, D., J.H. Lunsford, and M.P. Rosynek, *Catalytic conversion of methane to benzene over Mo/ZSM-5*. Topics in Catalysis, 1996. **3**(3): p. 289-297.
91. Wang, D., J.H. Lunsford, and M.P. Rosynek, *Characterization of a Mo/ZSM-5 Catalyst for the Conversion of Methane to Benzene*. Journal of Catalysis, 1997. **169**(1): p. 347-358.
92. Yuan, L., *Investigation of the interaction of Mo species with ZSM-5 and the carbon deposit in methane dehydro- aromatization*, in *Dalian Institute of Chemical Physics Chinese Academy of Science*. 1999: Dalian.
93. Zhang, J.-Z., M.A. Long, and R.F. Howe, *Molybdenum ZSM-5 zeolite catalysts for the conversion of methane to benzene*. Catalysis Today, 1998. **44**(1-4): p. 293-300.
94. Zhang, W., et al., *Methane Dehydro-aromatization over Mo/HZSM-5 in the Absence of Oxygen: A Multinuclear Solid-State NMR Study of the Interaction between Supported Mo Species and HZSM-5 Zeolite with Different Crystal Sizes*. Journal of Catalysis, 1999. **188**(2): p. 393-402.
95. Ma, D., et al., *MAS NMR, ESR and TPD studies of Mo/HZSM-5 catalysts: evidence for the migration of molybdenum species into the zeolitic channels*. Catalysis Letters, 2000. **66**(3): p. 155-160.
96. Ma, D., et al., *MAS NMR Studies on the Dealumination of Zeolite MCM-22*. The Journal of Physical Chemistry B, 2001. **105**(9): p. 1770-1779.

97. Ma, D., et al., *Methane Dehydro-aromatization under Nonoxidative Conditions over Mo/HZSM-5 Catalysts: EPR Study of the Mo Species on/in the HZSM-5 Zeolite*. *Journal of Catalysis*, 2000. **189**(2): p. 314-325.
98. Nagai, M., T. Nishibayashi, and S. Omi, *Molybdenum carbides and carbonaceous carbons on Mo/Al-FSM16 for methane conversion*. *Applied Catalysis A: General*, 2003. **253**(1): p. 101-112.
99. Tessonnier, J.-P., et al., *Quantitative Measurement of the Brønsted Acid Sites in Solid Acids: Toward a Single-Site Design of Mo-Modified ZSM-5 Zeolite*. *The Journal of Physical Chemistry B*, 2006. **110**(21): p. 10390-10395.
100. Tessonnier, J.-P., et al., *Methane dehydro-aromatization on Mo/ZSM-5: About the hidden role of Brønsted acid sites*. *Applied Catalysis A: General*, 2008. **336**(1-2): p. 79-88.
101. Zaikovskii, V.I., et al., *Properties and deactivation of the active sites of an MoZSM-5 catalyst for methane dehydroaromatization: Electron microscopic and EPR studies*. *Kinetics and Catalysis*, 2006. **47**(3): p. 389-394.
102. Sij, M., et al., *Thermally Stable Alkylidene Groups on the Surface of  $\beta$ -Mo<sub>2</sub>C: Relevance to Methane Aromatization and Olefin-Metathesis Catalysis*. *The Journal of Physical Chemistry C*, 2007. **111**(4): p. 1725-1732.
103. Solymosi, F., et al., *Aromatization of Methane over Supported and Unsupported Mo-Based Catalysts*. *Journal of Catalysis*, 1997. **165**(2): p. 150-161.
104. Wang, D., J. Lunsford, and M. Rosynek, *Catalytic conversion of methane to benzene over Mo/ZSM-5*. *Topics in Catalysis*, 1996. **3**(3-4): p. 289-297.
105. Weckhuysen, B., M. Rosynek, and J. Lunsford, *Characterization of surface carbon formed during the conversion of methane to benzene over Mo/H-ZSM-5 catalysts*. *Catalysis Letters*, 1998. **52**(1-2): p. 31-36.
106. Ma, D., et al., *On the Induction Period of Methane Aromatization over Mo-Based Catalysts*. *Journal of Catalysis*, 2000. **194**(1): p. 105-114.
107. Shu, Y., R. Ohnishi, and M. Ichikawa, *Stable and Selective Dehydrocondensation of Methane Towards Benzene on Modified Mo/MCM-22 Catalyst by the Dealumination Treatment*. *Catalysis Letters*, 2002. **81**(1-2): p. 9-17.
108. Szöke, A. and F. Solymosi, *Selective oxidation of methane to benzene over K<sub>2</sub>MoO<sub>4</sub>/ZSM-5 catalysts*. *Applied Catalysis A: General*, 1996. **142**(2): p. 361-374.
109. Solymosi, F., et al., *Aromatization of Methane over Supported and Unsupported Mo-Based Catalysts*. *Journal of Catalysis*, 1997. **165**(2): p. 150-161.
110. Dean, A.M., *Detailed kinetic modeling of autocatalysis in methane pyrolysis*. *The Journal of Physical Chemistry*, 1990. **94**(4): p. 1432-1439.
111. Li, L., R. W. Borry, and E. Iglesia, *Reaction-transport simulations of non-oxidative methane conversion with continuous hydrogen removal - homogeneous - heterogeneous reaction pathways*. *Chemical Engineering Science*, 2001. **56**(5): p. 1869-1881.
112. Li, Z., C. Kjolseth, and T. Haugrud, *numerical simulations of methane aromatization with and without a ceramic hydrogen separation membrane*. 2012.
113. Ding, W., et al., *Methane Conversion to Aromatics on Mo/H-ZSM5: Structure of Molybdenum Species in Working Catalysts*. *The Journal of Physical Chemistry B*, 2000. **105**(2): p. 506-513.
114. Kim, Y.-H., R.W. Borry lii, and E. Iglesia, *Genesis of methane activation sites in Mo-exchanged H-ZSM-5 catalysts*. *Microporous and Mesoporous Materials*, 2000. **35-36**(0): p. 495-509.
115. Li, W., et al., *Raman and X-Ray Absorption Studies of Mo Species in Mo/H-ZSM5 Catalysts for*

- Non-Oxidative CH<sub>4</sub> Reactions*. Journal of Catalysis, 2000. **191**(2): p. 373-383.
116. Wang, L., R. Ohnishi, and M. Ichikawa, *Novel rhenium based catalysts for dehydrocondensation of methane with CO/CO<sub>2</sub> towards ethylene and benzene*. Catalysis Letters, 1999. **62**(1): p. 29-33.
117. Liu, S., et al., *Bifunctional catalysis of Mo/HZSM-5 in the dehydroaromatization of methane with CO/CO<sub>2</sub> to benzene and naphthalene*. Kinetics and Catalysis, 2000. **41**(1): p. 132-144.
118. R., O., et al., *Catalytic dehydrocondensation of methane with CO and CO<sub>2</sub> toward benzene and naphthalene on Mo/HZSM-5 and Fe/Co-modified Mo/HZSM-5*. Vol. 182. 1999, Amsterdam, PAYS-BAS: Elsevier.
119. Liu, S., R. Ohnishi, and M. Ichikawa, *Promotional role of water added to methane feed on catalytic performance in the methane dehydroaromatization reaction on Mo/HZSM-5 catalyst*. Journal of Catalysis, 2003. **220**(1): p. 57-65.
120. Skutil, K. and M. Taniewski, *Some technological aspects of methane aromatization (direct and via oxidative coupling)*. Fuel Processing Technology, 2006. **87**(6): p. 511-521.
121. Osawa, T., I. Nakano, and O. Takayasu, *Dehydrogenation of Methane over Mo/ZSM-5. Effects of Additives in the Methane Stream*. Catalysis Letters, 2003. **86**(1-3): p. 57-62.
122. Liu, Z., M. Nutt, and E. Iglesia, *The Effects of CO<sub>2</sub>, CO and H<sub>2</sub> Co-Reactants on Methane Reactions Catalyzed by Mo/H-ZSM-5*. Catalysis Letters, 2002. **81**(3-4): p. 271-279.
123. Tan, P.L., et al., *Effects of Co-fed O<sub>2</sub> and CO<sub>2</sub> on the deactivation of Mo/HZSM-5 for methane aromatization*. Applied Catalysis A: General, 2003. **253**(1): p. 305-316.
124. Tan, P.L., et al., *Methane Aromatization over 2 wt% Mo/HZSM-5 in the Presence of O<sub>2</sub> and NO*. Catalysis Letters, 2002. **78**(1-4): p. 251-258.
125. Aritani, H., et al., *Methane dehydroaromatization over Mo-modified H-MFI for gas to liquid catalysts*. Journal of Environmental Sciences, 2009. **21**(6): p. 736-740.
126. Ma, H., R. Ohnishi, and M. Ichikawa, *Highly Stable Performance of Methane Dehydroaromatization on Mo/HZSM-5 Catalyst with a Small Amount of H<sub>2</sub> Addition into Methane Feed*. Catalysis Letters, 2003. **89**(1-2): p. 143-146.
127. Ma, H., et al., *Effective Coke Removal in Methane to Benzene (MTB) Reaction on Mo/HZSM-5 Catalyst by H<sub>2</sub> and H<sub>2</sub>O Co-addition to Methane*. Catalysis Letters, 2005. **104**(1-2): p. 63-66.
128. Li, Y., et al., *Combined Single-pass Conversion of Methane Via Oxidative Coupling and Dehydroaromatization*. Catalysis Letters, 2005. **105**(1-2): p. 77-82.
129. Li, Y., et al., *Combined Single-Pass Conversion of Methane Via Oxidative Coupling and Dehydroaromatization*. Catalysis Letters, 2003. **89**(3-4): p. 275-279.
130. Xu, Y., et al., *Methane activation without using oxidants over Mo/HZSM-5 zeolite catalysts*. Catalysis Letters, 1994. **30**(1-4): p. 135-149.
131. Solymosi, F., A. Szöke, and J. Cserényi, *Conversion of methane to benzene over Mo<sub>2</sub>C and Mo<sub>2</sub>C/ZSM-5 catalysts*. Catalysis Letters, 1996. **39**(3-4): p. 157-161.
132. Wang, L., et al., *Activity and stability enhancement of MoHZSM-5-based catalysts for methane non-oxidative transformation to aromatics and C<sub>2</sub> hydrocarbons: Effect of additives and pretreatment conditions*. Applied Catalysis A: General, 1997. **152**(2): p. 173-182.
133. Choudhary, V.R., A.K. Kinage, and T.V. Choudhary, *Low-Temperature Nonoxidative Activation of Methane over H-Galloaluminosilicate (MFI) Zeolite*. Science, 1997. **275**(5304): p. 1286-1288.
134. W. Borry, R., et al., *Non-oxidative catalytic conversion of methane with continuous hydrogen removal*, in *Studies in Surface Science and Catalysis*, A. Parmaliana, Editor. 1998, Elsevier. p.

- 403-410.
135. Liu, Z., L. Li, and E. Iglesia, *Catalytic Pyrolysis of Methane on Mo/H-ZSM5 with Continuous Hydrogen Removal by Permeation Through Dense Oxide Films*. *Catalysis Letters*, 2002. **82**(3-4): p. 175-180.
136. Li, L., R.W. Borry, and E. Iglesia, *Design and optimization of catalysts and membrane reactors for the non-oxidative conversion of methane*. *Chemical Engineering Science*, 2002. **57**(21): p. 4595-4604.
137. Wang, L., et al., *Production of ultra highly pure H<sub>2</sub> and higher hydrocarbons from methane in one step at mild temperatures and development of the catalyst under non-equilibrium reaction conditions*. *Chem Commun (Camb)*, 2001(19): p. 1952-3.
138. Larachi, F., et al., *Ru-Mo/HZSM-5 Catalyzed Methane Aromatization in Membrane Reactors*. *Catalysis Letters*, 2002. **84**(3-4): p. 183-192.
139. Rival, O., et al., *Oxygen-Free Methane Aromatization in a Catalytic Membrane Reactor*. *Industrial & Engineering Chemistry Research*, 2001. **40**(10): p. 2212-2219.
140. Iliuta, M.C., et al., *Methane Nonoxidative Aromatization over Ru-Mo/HZSM-5 in a Membrane Catalytic Reactor*. *Industrial & Engineering Chemistry Research*, 2002. **41**(10): p. 2371-2378.
141. Iliuta, M.C., B.P.A. Grandjean, and F. Larachi, *Methane Nonoxidative Aromatization over Ru-Mo/HZSM-5 at Temperatures up to 973 K in a Palladium-Silver/Stainless Steel Membrane Reactor*. *Industrial & Engineering Chemistry Research*, 2002. **42**(2): p. 323-330.
142. Yuan, S., et al., *The effect of oxygen on the aromatization of methane over the Mo/HZSM-5 catalyst*. *Catalysis Letters*, 1999. **63**(1-2): p. 73-77.
143. Zheng, H., et al., *Direct Observation of the Active Center for Methane Dehydroaromatization Using an Ultrahigh Field 95Mo NMR Spectroscopy*. *Journal of the American Chemical Society*, 2008. **130**(12): p. 3722-3723.
144. Liu, S., et al., *Catalytic dehydroaromatization of methane with CO/CO<sub>2</sub> towards benzene and naphthalene on bimetallic mo/zeolite catalysts: Bifunctional catalysis and dynamic mechanism, in Studies in Surface Science and Catalysis*. 1998, Elsevier. p. 241-246.
145. Liu, S. and Q. Dong, *Unique promotion effect of CO and CO<sub>2</sub> on the catalytic stability for benzene and naphthalene production from methane on Mo/HZSM-5 catalysts*. *Chemical Communications*, 1998(11): p. 1217-1218.
146. Sandler, S.I., *Chemical and Engineering Thermodynamics*. 1999, New York, USA: John Wiley & Sons.
147. Smith, J.M., H.C.V. Ness, and M. M.Abbott, *Introduction to Chemical Engineering Thermodynamics*. 2004, New Uork, USA: McGraw-Hill Companies
148. L.Yaws, C., *McGraw-Hill Handbooks, Chemical Properties Handbook*. McGraw-Hill Companies, Inc. 1999, Texas.
149. Missen, W.R.S.a.R.W., *Chemical reaction equilibrium analysis: Theory and algorithms*. 1982, New York: Wiley.
150. Guéret, C., M. Daroux, and F. Billaud, *Methane pyrolysis: thermodynamics*. *Chemical Engineering Science*, 1997. **52**(5): p. 815-827.
151. Shu, Y., et al., *Methane dehydro-aromatization over Mo/MCM-22 catalysts: a highly selective catalyst for the formation of benzene*. *Catalysis Letters*, 2000. **70**(1-2): p. 67-73.
152. Corma, A., V. Martínez-Soria, and E. Schnoefeld, *Alkylation of Benzene with Short-Chain Olefins over MCM-22 Zeolite: Catalytic Behaviour and Kinetic Mechanism*. *Journal of Catalysis*, 2000.



- 192**(1): p. 163-173.
153. Ma, D., *The structure - performance relationship of the methane dehydro- aromatization catalyst*, in *Dalian Institute of Chemical Physics Chinese Academy of Science*. 2001: Dalian.
154. Schüth, F., Engineered Porous Catalytic Materials. *Annual Review of Materials Research*, 2005. **35**(1): p. 209-238.
155. Tao, Y., et al., *Mesopore-Modified Zeolites: Preparation, Characterization, and Applications*. *Chemical Reviews*, 2006. **106**(3): p. 896-910.
156. Egeblad, K., et al., *Templating Mesoporous Zeolites*. *Chemistry of Materials*, 2007. **20**(3): p. 946-960.
157. Liu, L., et al., *Methane Dehydroaromatization on Mo/MCM-22 Catalysts: Effect of SiO<sub>2</sub>/Al<sub>2</sub>O<sub>3</sub> Ratio of MCM-22 Zeolite Supports*. *Catalysis Letters*, 2006. **108**(1-2): p. 25-30.
158. Graham, T., *On the law of the diffusion of gases*. *London-Edinburgh Philos. Mag. J. Sci.*, 1832. **3**: p. 8.
159. Barrer, R.M. and W. Jost, *A note on interstitial diffusion*. *Transactions of the Faraday Society*, 1949. **45**(0): p. 928-930.
160. van de Graaf, J.M., F. Kapteijn, and J.A. Moulijn, *Diffusivities of light alkanes in a silicalite-1 membrane layer*. *Microporous and Mesoporous Materials*, 2000. **35–36**(0): p. 267-281.
161. Wicke, E. and R. Kallenbach, *Die Oberflächendiffusion von Kohlendioxyd in aktiven Kohlen*. *Kolloid-Zeitschrift*, 1941. **97**(2): p. 135-151.
162. Missen, R.W., C.A. Mims, and B.A. Saville, *Introduction to chemical reaction engineering and kinetics*. 1999, Chichester, U.K.: John Wiley & Sons.
163. Trautz, M., *Das Gesetz der Reaktionsgeschwindigkeit und der Gleichgewichte in Gasen. Bestätigung der Additivität von Cv-3/2R. Neue Bestimmung der Integrationskonstanten und der Moleküldurchmesser*. *Zeitschrift für anorganische und allgemeine Chemie*, 1916. **96**(1): p. 1-28.
164. P.B.Weisz, *CHEMTECH*, 1992: p. 424.
165. Dittmeyer, R.a.C., J., *Catalytic Membrane Reactors. Handbook of Heterogeneous Catalysis*. . 2008, Weinheim: Wiley-VCH Verlag GmbH & Co. KGaA.
166. Sundmacher, K., A. Kienle, and A. Seidel-Morgenstern, *Integrated Chemical Processes: Synthesis, Operation, Analysis, and Control*. 2006: Wiley-VCH Verlag Weinheim, Germany.
167. Dittmeyer, R., V. Höllein, and K. Daub, *Membrane reactors for hydrogenation and dehydrogenation processes based on supported palladium*. *Journal of Molecular Catalysis A: Chemical*, 2001. **173**(1–2): p. 135-184.
168. Urbanczyk, D., Dittmeyer, R., Wolf, A., Warsitz, R., Fischer, G. and Voigt, I, *Evaluation of porous catalytic membranes operated in pore-flow-through mode for hydrogenation of  $\alpha$ -methylstyrene*. *Asia-Pacific Journal of Chemical Engineering*, 2010. **5**: p. 12-25.
169. Caro, J., Caspary, K. J., Hamel, C., Hoting, B., Kölsch, P., Langanke, B., *Catalytic Membrane Reactors for Partial Oxidation Using Perovskite Hollow Fiber Membranes and for Partial Hydrogenation Using a Catalytic Membrane Contactor*. *Industrial and Engineering Chemistry Research*, 2007. **46**(8): p. 2286-2294.
170. Seidel-Morgenstern, A., *New separation technique for the CPI*. *Chemical Engineering Progress*, 1968. **64**: p. 12.
171. G., D.A., *Recent research in catalytic inorganic membrane reactors*. *International Journal of Chemical Reaction Engineering*, 2003. **1**(6): p. 35.
172. Seidel-Morgenstern, A., *Analysis and experimental investigation of catalytic membrane*

- reactors*. 2005, New York: Wiley-VCH Verlag GmbH&Co. KGaA.
173. Saracco, G., et al., *High-temperature membrane reactors: potential and problems*. Chemical Engineering Science, 1999. **54**(13–14): p. 1997-2017.
174. H., S., *Review: Inorganic membranes synthesis, characteristics and applications*. 1991, New York: Van Nostrand Reinhold.
175. Seidel-Morgenstern, A., ed. *Membrane Reactors*. 2010, WILEY-VCH Verlag GmbH & Co.KGaA, Weinheim: Magdeburg.
176. Naibo Chu, J.Y., Gang Li, Suxia Yu, Jinming Lu, Jinqu Wang, *Methane non-oxidative dehydroaromatization in a SAPO-34 and SAPO-34/Pd membrane reactor*. 10th International Conference on Inorganic Membrane, 2008.
177. Ward, T.L. and T. Dao, *Model of hydrogen permeation behavior in palladium membranes*. Journal of Membrane Science, 1999. **153**(2): p. 211-231.
178. Govind, R. and D. Atnoor, *Development of a composite palladium membrane for selective hydrogen separation at high temperature*. Industrial & Engineering Chemistry Research, 1991. **30**(3): p. 591-594.
179. J. N, A., *ChemInform Abstract: Challenges in Membrane Catalysis*. ChemInform, 1993. **24**(5).
180. Guo, Y., et al., *Preparation and characterization of Pd–Ag/ceramic composite membrane and application to enhancement of catalytic dehydrogenation of isobutane*. Separation and Purification Technology, 2003. **32**(1–3): p. 271-279.
181. Ali, J.K., E.J. Newson, and D.W.T. Rippin, *Exceeding equilibrium conversion with a catalytic membrane reactor for the dehydrogenation of methylcyclohexane*. Chemical Engineering Science, 1994. **49**(13): p. 2129-2134.
182. Itoh, N., et al., *Hydrogen recovery from cyclohexane as a chemical hydrogen carrier using a palladium membrane reactor*. Catalysis Today, 2003. **82**(1–4): p. 119-125.
183. Sheintuch, M. and R.M. Dessau, *Observations, modeling and optimization of yield, selectivity and activity during dehydrogenation of isobutane and propane in a Pd membrane reactor*. Chemical Engineering Science, 1996. **51**(4): p. 535-547.
184. Gallucci, F. and A. Basile, *Pd-Cu membrane reactor for steam reforming reactions: A comparison between different fuels*. International Journal of Hydrogen Energy, 2008. **33**(6): p. 1671-1687.
185. Sá, S., et al., *Hydrogen production by methanol steam reforming in a membrane reactor: Palladium vs carbon molecular sieve membranes*. Journal of Membrane Science, 2009. **339**(1–2): p. 160-170.
186. Tong, J., et al., *Experimental Study of Steam Reforming of Methane in a Thin (6 μM) Pd-Based Membrane Reactor*. Industrial & Engineering Chemistry Research, 2005. **44**(5): p. 1454-1465.
187. Matsumura, Y. and J. Tong, *Methane Steam Reforming in Hydrogen-permeable Membrane Reactor for Pure Hydrogen Production*. Topics in Catalysis, 2008. **51**(1-4): p. 123-132.
188. Kikuchi, E., et al., *Membrane Reactor Using Microporous Glass-supported Thin Film of Palladium. Application to the Water Gas Shift Reaction*. Chemistry Letters, 1989. **18**(3): p. 489-492.
189. Basile, A., et al., *Membrane reactor for water gas shift reaction*. Gas Separation & Purification, 1996. **10**(4): p. 243-254.
190. Bi, Y., et al., *Water–gas shift reaction in a Pd membrane reactor over Pt/Ce<sub>0.6</sub>Zr<sub>0.4</sub>O<sub>2</sub> catalyst*. International Journal of Hydrogen Energy, 2009. **34**(7): p. 2965-2971.

191. Zhang, J., H. Xu, and W. Li, *High-purity CO<sub>x</sub>-free H<sub>2</sub> generation from NH<sub>3</sub> via the ultra permeable and highly selective Pd membranes*. Journal of Membrane Science, 2006. **277**(1–2): p. 85-93.
192. Fick, A., *Über diffusion*. Poggendorff's Annalen, 1855. **94**: p. 7.
193. Sing, K.S.W., *Reporting physisorption data for gas/solid systems with special reference to the determination of surface area and porosity (Provisional)*. Pure and Applied Chemistry, 2009. **54**(11): p. 2201-2218.
194. Gallucci, F., L. Paturzo, and A. Basile, *A simulation study of the steam reforming of methane in a dense tubular membrane reactor*. International Journal of Hydrogen Energy, 2004. **29**(6): p. 611-617.
195. van de Graaf, J.M., et al., *Application of a silicalite-1 membrane reactor in metathesis reactions*. Applied Catalysis A: General, 1999. **178**(2): p. 225-241.
196. Li, S., et al., *Methane Aromatization in the Absence of Oxygen Over Mo/HZSM-5 Catalysts*. Reaction Kinetics and Catalysis Letters, 2000. **70**(2): p. 349-356.
197. Ma, D., *Carbonaceous Deposition on Mo/MCM-22 Catalysts for Methane Aromatization: A TP Technique Investigation*. Journal of Catalysis, 2002. **208**(2): p. 260-269.
198. Liu, B.S., et al., *XPS, XAES, and TG/DTA characterization of deposited carbon in methane dehydroaromatization over Ga–Mo/ZSM-5 catalyst*. Applied Surface Science, 2007. **253**(11): p. 5092-5100.
199. Matus, E.V., et al., *Study of Methane Dehydroaromatization on Impregnated Mo/ZSM-5 Catalysts and Characterization of Nanostructured Molybdenum Phases and Carbonaceous Deposits*. Industrial & Engineering Chemistry Research, 2006. **46**(12): p. 4063-4074.
200. Chu, N., *Studies on Hierarchical Catalysts and Membrane Catalytic Reactor in Methane Dehydroaromatization*, in *Dalian University of Technology*. 2010, Dalian University of Technology: Dalian, Liaoning, China. p. 100.
201. Pio Forzatti, L.L., *Catalyst deactivation*. Catalysis Today, 1999. **52**: p. 165-181.
202. Bartholomew, C.H., *Mechanisms of catalyst deactivation*. Applied Catalysis A: General, 2001. **212**(1–2): p. 17-60.
203. Michel Guisne, F.R.R., *Deactivation and Regeneration of Zeolite Catalyst*. Catalytic Science Series, ed. G.J. Hutchings. 2011: World Scientific Pub Co.
204. John B. Butt, E.E.P., *Activation, deactivation, and Poisoning of Catalysts*. 1988, San Diego: Academic Press Inc.
205. Markos J., Ilavsky J., *Modelling of catalytic reactors with catalyst deactivation IV. Parameter estimation of the rate equations of heterogeneous catalyst deactivation* Chem. Papers, 1987. **41**(3): p. 375-393.
206. Gladys Jimenez-Garcia, R.Q.-S., Ricardo Aguilar-Lopez, Rafael Maya-Yescas, *Modelling Catalyst Deactivation by External Coke Deposition during Fluid Catalytic Cracking*. International Journal of Chemical Reaction Engineering, 2010. **8**(S2): p. 1-17.



## List of Figures

Figure 1. 1: Main processes and respectively products for methane processing.....	2
Figure 1.2: Comparison of oxidative and non-oxidative routes for methane conversion .....	5
Figure 1.3: Comparison of direct and indirect routes for methane conversion .....	6
Figure 1.4: Pore structure of MCM-22 zeolite [86] .....	10
Figure 1.5: Schematic representation of the MDA reaction over the Mo/HZSM-5 catalyst...	14
Figure 1.6: Schematic reaction network of the MDA reaction over the Mo/MCM-22 catalyst .....	16
Figure 2. 1: Schematic illustration of $\ln K_p$ versus $1/T$ plot.....	22
Figure 2. 2: Calculated equilibrium methane conversion at different temperatures [148]1 ....	26
Figure 2. 3: Thermodynamic equilibrium constants over different temperatures .....	27
Figure 2. 4: Calculated equilibrium methane conversion as a function of $H_2$ removal (%) during MDA, a: at 883K and 0.5 MPa [55]; b: at 973K and 0.1 MPa [148] .....	28
Figure 3. 1 SEM images of conventional zeolite MCM-22 .....	32
Figure 3. 2 SEM images of the zeolite MCM-22-HA.....	33
Figure 3. 3 TEM images of conventional zeolite MCM-22 .....	33
Figure 3. 4 TEM images of the zeolite MCM-22-HA.....	33
Figure 3. 5 Powder XRD patterns for MCM-22-HA, the conventional MCM-22 zeolites and Mo/MCM-22-HA catalyst.....	34
Figure 3. 6 Nitrogen adsorption and desorption isotherms for MCM-22-HA and the conventional MCM-22 zeolites.....	34
Figure 3. 7 $NH_3$ -TPD spectra of the MCM-22 (1), MCM-22-HA (2) zeolites, the calcined Mo/MCM-22 (3) and Mo/MCM-22-HA (4) catalysts.....	36
Figure 3. 8 TEM image and element distribution of the calcined Mo/MCM-22-HA catalyst	36
Figure 3. 9 The TG/DTG curves recorded from the coked conventional Mo/MCM-22 catalyst (1) and Mo/MCM-22-HA catalyst (2) being subjected to MDA reaction for 24h and 72h respectively .....	37
Figure 4. 1: Schematic diagram of experimental set-up.....	40
Figure 4. 2: Photograph of FBR set-up .....	41
Figure 4. 3: Schematic diagram of inner structure of FBR (L=250mm).....	42
Figure 4. 4: GC configuration (from the GC instruction manual, Agilent Germany) .....	42
Figure 4. 5: Set-up to study single component permeation through tubular membranes [160] .....	43
Figure 4. 6: Schematic diagram of experimental set-up for studying single gas permeation..	44
Figure 4. 7: Schematic diagram of experimental set-up for studying binary gas mixture permeation.....	45
Figure 4. 8: Schematic diagram of experimental set-up for studying ternary gas mixture permeation.....	45
Figure 4. 9: Schematic illustration of experiment set-up in membrane system .....	46
Figure 4. 10: Photograph of membrane system experimental set-up .....	46

Figure 4. 11: Schematic diagram of experimental set-up for membrane reactor of MDA.....	47
Figure 4. 12: Schematic illustration of applied membrane reactor .....	47
Figure 4. 13: Photograph of applied membrane reactor.....	48
Figure 4. 14: Micro GC photograph and configuration (from the GC instruction manual, Agilent Germany) .....	48
Figure 5. 1: Left: Benzene molar flow at different reaction temperatures (group A experiments, methane feed); Right: Schematic trend of three stages of produced benzene over reaction time following a proposal in the literature [91, 104, 105].....	55
Figure 5. 2: Schematic diagram of experiments in FBR .....	56
Figure 5. 3: Illustration of all groups (A,...,K) of experiments in FBR.....	57
Figure 5. 4: Methane conversion and benzene selectivity according to different temperature with $x_{0,CH_4}=90\%$ , $W/F=2160\text{kg}/\text{m}^3$ (group A) .....	58
Figure 5. 5: Ethylene selectivity and ethane selectivity according to different temperature with $x_{0,CH_4}=90\%$ , $W/F=2160\text{kg}/\text{m}^3$ (group A) .....	58
Figure 5. 6: Methane conversion and benzene selectivity according to stepwise temperature rising experiments with $x_{0,CH_4}=90\%$ , $W/F=2160\text{kg}/\text{m}^3$ (group A).....	59
Figure 5. 7: Ethylene selectivity and ethane selectivity according to stepwise temperature rising experiments with $x_{0,CH_4}=90\%$ , $W/F=2160\text{kg}/\text{m}^3$ (group A).....	59
Figure 5. 8: Average methane conversion and benzene selectivity comparison of single and stepwise experiment with $x_{0,CH_4}=90\%$ , $W/F=2160\text{kg}/\text{m}^3$ (group A).....	60
Figure 5. 9: Methane conversion and benzene selectivity according to different temperature with $x_{0,CH_4}=30\%$ , $W/F=720\text{kg}/\text{m}^3$ (group C) .....	60
Figure 5. 10: Ethylene selectivity and ethane selectivity according to different temperature with $x_{0,CH_4}=30\%$ , $W/F=720\text{kg}/\text{m}^3$ (group C) .....	61
Figure 5. 11: Methane conversion and benzene selectivity according to stepwise temperature rising experiments with $x_{0,CH_4}=30\%$ , $W/F=720\text{kg}/\text{m}^3$ (group C).....	61
Figure 5. 12: Ethylene selectivity and ethane selectivity according to stepwise temperature rising experiments with $x_{0,CH_4}=30\%$ , $W/F=720\text{kg}/\text{m}^3$ (group C).....	62
Figure 5. 13: Average methane conversion and benzene selectivity comparison of single and stepwise experiment with $x_{0,CH_4}=30\%$ , $W/F=720\text{kg}/\text{m}^3$ (group C).....	62
Figure 5. 14: Methane conversion and benzene selectivity for different temperature with $x_{0,CH_4}=30\%$ , $W/F=2160\text{kg}/\text{m}^3$ (group E) .....	63
Figure 5. 15: Ethylene selectivity and ethane selectivity for different temperature with $x_{0,CH_4}=30\%$ , $W/F=2160\text{kg}/\text{m}^3$ (group E) .....	63
Figure 5. 16: Methane conversion and benzene selectivity for stepwise temperature rising experiments with $x_{0,CH_4}=30\%$ , $W/F=2160\text{kg}/\text{m}^3$ (group E).....	64
Figure 5. 17: Ethylene selectivity and ethane selectivity for stepwise temperature rising experiments with $x_{0,CH_4}=30\%$ , $W/F=2160\text{kg}/\text{m}^3$ (group E).....	64
Figure 5. 18: Average methane conversion and benzene selectivity comparison of single and stepwise experiment with $x_{0,CH_4}=30\%$ , $W/F=2160\text{kg}/\text{m}^3$ (group E).....	64
Figure 5. 19: Methane conversion and benzene selectivity for different feed methane fraction with $T=700^\circ\text{C}$ , $W/F=2160\text{kg}/\text{m}^3$ (group B).....	65
Figure 5. 20: Ethylene selectivity and ethane selectivity for different feed methane fraction	

with $T=700^{\circ}\text{C}$ , $W/F=2160\text{kgs/m}^3$ (group B).....	66
Figure 5. 21: Average conversion and selectivity comparison of single experiments with $T=700^{\circ}\text{C}$ , $W/F=2160\text{kgs/m}^3$ (group B).....	66
Figure 5. 22: Methane conversion and benzene selectivity for different feed methane fraction with $T=700^{\circ}\text{C}$ , $W/F=720\text{kgs/m}^3$ (group D).....	67
Figure 5. 23: Ethylene selectivity and ethane selectivity for different feed methane fraction with $T=700^{\circ}\text{C}$ , $W/F=720\text{kgs/m}^3$ (group D).....	67
Figure 5. 24: Average conversion and selectivity comparison of single experiments with $T=700^{\circ}\text{C}$ , $W/F=720\text{kgs/m}^3$ (group D).....	67
Figure 5. 25: Methane conversion and benzene selectivity for different W/F with $x_{0,\text{CH}_4}=30\%$ , $T=700^{\circ}\text{C}$ : ■ for $719.81\text{ kgs/m}^3$ and ● for $2163.62\text{ kgs/m}^3$ (group H).....	68
Figure 5. 26: Ethylene and ethane selectivity for different W/F with $x_{0,\text{CH}_4}=30\%$ , $T=700^{\circ}\text{C}$ : ■ for $719.81\text{ kgs/m}^3$ and ● for $2163.62\text{ kgs/m}^3$ (group H).....	68
Figure 5. 27: Methane conversion and benzene selectivity for different W/F with $x_{0,\text{CH}_4}=50\%$ , $T=700^{\circ}\text{C}$ : ■ for $1201.63\text{ kgs/m}^3$ and ● for $2163.62\text{ kgs/m}^3$ (group F).....	69
Figure 5. 28: Ethylene and ethane selectivity for different W/F with $x_{0,\text{CH}_4}=50\%$ , $T=700^{\circ}\text{C}$ : ■ for $1201.63\text{ kgs/m}^3$ and ● for $2163.62\text{ kgs/m}^3$ (group F).....	69
Figure 5. 29: Methane conversion and benzene selectivity for different W/F with $x_{0,\text{CH}_4}=70\%$ , $T=700^{\circ}\text{C}$ : ■ for $1680.32\text{ kgs/m}^3$ and ● for $2163.62\text{ kgs/m}^3$ (group G).....	70
Figure 5. 30: Ethylene and ethane selectivity for different W/F with $x_{0,\text{CH}_4}=70\%$ , $T=700^{\circ}\text{C}$ : ■ for $1680.32\text{ kgs/m}^3$ and ● for $2163.62\text{ kgs/m}^3$ (group G).....	70
Figure 5. 31: Methane conversion and benzene selectivity for different W/F with $x_{0,\text{CH}_4}=90\%$ , $T=700^{\circ}\text{C}$ : ■ for $720.52\text{ kgs/m}^3$ and ● for $2163.62\text{ kgs/m}^3$ (group I).....	70
Figure 5. 32: Ethylene and ethane selectivity for different W/F with $x_{0,\text{CH}_4}=90\%$ , $T=700^{\circ}\text{C}$ : ■ for $720.52\text{ kgs/m}^3$ and ● for $2163.62\text{ kgs/m}^3$ (group I).....	71
Figure 5. 33: Methane conversion and benzene selectivity of stepwise experiments (group K).....	72
Figure 5. 34: Ethylene and ethane selectivity of stepwise experiments (group K).....	72
Figure 5. 35: Average methane conversion and benzene selectivity of stepwise experiments (group K).....	73
Figure 5. 36: Conversion and selectivity of W/F switching experiments (group J).....	73
Figure 5. 37: Average conversion and selectivity of W/F switching experiments (group J)...	74
Figure 5. 38: Ethylene conversion and benzene selectivity for different temperature with $x_{0,\text{C}_2\text{H}_4}=1\%$ , $W/F=54\text{kgs/m}^3$ (group A).....	75
Figure 5. 39: Ethane selectivity and methane selectivity for different temperature with $x_{0,\text{C}_2\text{H}_4}=1\%$ , $W/F=54\text{kgs/m}^3$ (group A).....	75
Figure 5. 40: Ethylene conversion and benzene selectivity for stepwise temperature rising experiments with $x_{0,\text{C}_2\text{H}_4}=1\%$ , $W/F=54\text{kgs/m}^3$ (group A).....	76
Figure 5. 41: Ethane selectivity and methane selectivity for stepwise temperature rising experiments with $x_{0,\text{C}_2\text{H}_4}=1\%$ , $W/F=54\text{kgs/m}^3$ (group A).....	76
Figure 5. 42: Average conversion and selectivity comparison of single and stepwise experiment with $x_{0,\text{C}_2\text{H}_4}=1\%$ , $W/F=54\text{kgs/m}^3$ (group A).....	77
Figure 5. 43: Conversion and selectivity comparison of activated and non-activated catalyst experiment with $x_{0,\text{C}_2\text{H}_4}=1\%$ , $W/F=54\text{kgs/m}^3$ (group A).....	78

Figure 5. 44: Ethylene conversion and benzene selectivity for different temperature with $x_{0,C_2H_4}=40\%$ , $W/F=2160\text{kg}/\text{m}^3$ (group B).....	78
Figure 5. 45: Ethane selectivity and methane selectivity for different temperature with $x_{0,C_2H_4}=40\%$ , $W/F=2160\text{kg}/\text{m}^3$ (group B).....	79
Figure 5. 46: Conversion and selectivity comparison of activated and non-activated catalyst experiment with $x_{0,C_2H_4}=40\%$ , $W/F=2160\text{kg}/\text{m}^3$ (group B).....	79
Figure 5. 47: Conversion and selectivity comparison of different ethylene feed volumetric fraction with $T=700^\circ\text{C}$ , $W/F=54\text{kg}/\text{m}^3$ (group C).....	80
Figure 5. 48: Ethylene conversion and benzene selectivity for different ethylene feed volumetric fraction with $T=700^\circ\text{C}$ (group D).....	81
Figure 5. 49: Ethane selectivity and methane selectivity for different ethylene feed volumetric fraction with $T=700^\circ\text{C}$ (group D).....	81
Figure 5. 50: Average conversion and selectivity comparison of different ethylene feed volumetric fraction with $T=700^\circ\text{C}$ (group D).....	81
Figure 5. 51: Carbon Balance of all the experiments.....	82
Figure 5. 52: Schematic illustration of PFTR.....	84
Figure 5. 53: Schematic diagram of steps of data analysis.....	87
Figure 5. 54: Experimental concentration time course.....	88
Figure 5. 55: Determination of the reaction order using differential method.....	88
Figure 5. 56: Determination of pre-exponential factor and activation energy by differential method.....	89
Figure 5. 57: Reaction network 1 with 3 reactions.....	90
Figure 5. 58: Simulation of reaction order of reaction network 1.....	91
Figure 5. 59: Simulation of pre-exponential factor and the activation energy of network 1...	92
Figure 5. 60: Comparison of simulated and stepwise experimental component molar flow rate.....	93
Figure 5. 61: Comparison of simulated and single experimental component molar flow rate	93
Figure 5. 62: Illustration of reaction network 2 with 5 reactions.....	94
Figure 5. 63: Illustration of sub-network 2 with 4 reactions ( $C_2H_4$ feed).....	94
Figure 5. 64: Estimation of reaction order of sub-network 2.....	95
Figure 5. 65: Estimation of pre-exponential factor and the activation energy of sub-network 2.....	96
Figure 5. 66: Comparison of simulated and experimental component molar flow rate.....	97
Figure 5. 67: Estimation of reaction order of reaction network 2.....	98
Figure 5. 68: Estimation of pre-exponential factor and the activation energy of reaction network 2.....	99
Figure 5. 69: Simulated and stepwise experimental benzene and methane molar flow rate.	100
Figure 5. 70: Simulated and stepwise experimental ethylene and ethane molar flow rate....	100
Figure 5. 71: Simulated and stepwise experimental coke molar formation rate and hydrogen molar flow rate.....	101
Figure 5. 72: Simulated and single experimental benzene and methane molar flow rate.....	101
Figure 5. 73: Simulated and single experimental ethylene and ethane molar flow rate.....	101
Figure 5. 74: Simulated and single experimental coke molar formation rate and hydrogen molar flow rate.....	102



---

Figure 5. 75: Illustration of reaction network 3 with 6 reactions .....	102
Figure 5. 76: Estimation of reaction order of reaction network 3 .....	103
Figure 5. 77: Estimation of pre-exponential factor and the activation energy of reaction network 3.....	104
Figure 5. 78: Simulated and stepwise experimental benzene and methane molar flow rate .	105
Figure 5. 79: Simulated and stepwise experimental ethylene and ethane molar flow rate....	106
Figure 5. 80: Simulated and stepwise experimental coke molar formation rate and hydrogen molar flow rate .....	106
Figure 5. 81: Simulated and single experimental benzene and methane molar flow rate .....	106
Figure 5. 82: Simulated and single experimental ethylene and ethane molar flow rate.....	107
Figure 5. 83: Simulated and single experimental coke molar formation rate and hydrogen molar flow rate .....	107
Figure 5. 84: Simulation performance evaluation compared with experimental performance .....	107
Figure 6. 1: Schematic diagram of retainment of homogeneous catalysts type .....	112
Figure 6. 2: Schematic diagram of “Contactor” .....	112
Figure 6. 3: Schematic diagram of extractor-type membrane reactor .....	113
Figure 6. 4: Schematic diagram of energetic coupling membrane reactor.....	113
Figure 6. 5: Schematic diagram of selectivity enhancement through withdrawal of a product .....	113
Figure 6. 6: Schematic diagram of distributor-type membrane reactor.....	114
Figure 6. 7: Transport mechanisms in porous media .....	118
Figure 6. 8: Components molar flow rates in FBR and “Pd MR” .....	120
Figure 6. 9: Comparison of component molar flow rates in FBR and “Pd MR” .....	120
Figure 6. 10: Comparison of methane conversion, benzene selectivity and yield in FBR and “Pd MR”.....	121
Figure 6. 11: Comparison of methane conversion, benzene selectivity and yield in FBR and “Pd MR” by varying $A_0$ .....	121
Figure 6. 12: Single gas permeation results for $N_2$ and He for each direction of flow .....	122
Figure 6. 13: Single gas permeation results for $H_2$ for each direction of flow .....	123
Figure 6. 14: Binary gas mixture diffusion experiment results for the pair He- $N_2$ .....	123
Figure 6. 15: Binary gas mixture diffusion experiment results for the pair $H_2$ - $N_2$ .....	124
Figure 6. 16: Binary gas mixture diffusion experiment results for the pair $CH_4$ - $N_2$ .....	124
Figure 6. 17: Binary gas mixture diffusion experiment results for the pair $CH_4$ -He.....	125
Figure 6. 18: Binary gas mixture diffusion experiment results for the pair $H_2$ - $CH_4$ .....	125
Figure 6. 19: Ternary gas mixture diffusion experiment results for the pair He + $N_2$ - $N_2$ .....	126
Figure 6. 20: Single gas permeation results at different temperatures for membrane No. 1 .	127
Figure 6. 21: Validation of diffusivities parameters at different temperatures for membrane No. 1.....	128
Figure 6. 22: Permeability and selectivity at different temperatures for membrane No. 1 ...	129
Figure 6. 23: Single gas permeation results at different temperatures for membrane No. 2 .	129
Figure 6. 24: Diffusivities parameter estimation at different temperatures for membrane No. 2 .....	130

Figure 6. 25: Validation of diffusivities parameters at different temperatures for membrane No. 2.....	131
Figure 6. 26: Permeability and selectivity at different temperatures for membrane No. 2 ...	131
Figure 6. 27: Comparison of the space time yield (STY) of typical large scale catalytic reactors (box) with area time yield (ATY) of several inorganic membranes [195] .....	132
Figure 6. 28: Predicted components molar flow rates in FBR and “carbon MR” .....	133
Figure 6. 29: Comparison of predicted component molar flow rates in FBR and “carbon MR” .....	133
Figure 6. 30: Comparison of predicted methane conversion, benzene selectivity and yield in FBR and “carbon MR” .....	133
Figure 6. 31: Methane conversion and benzene selectivity in “carbon MR” .....	134
Figure 6. 32: Ethylene and ethane selectivity in “carbon MR” .....	135
Figure 6. 33: Relative benzene and ethylene selectivity in “carbon MR” .....	135
Figure 6. 34: Relative ethane selectivity in “carbon MR” .....	136
Figure 6. 35: Benzene molar flow rate along with reaction time in “carbon MR” .....	136
Figure 6. 36: Comparison of methane and hydrogen molar flow rates in “carbon MR” at steady state .....	137
Figure 6. 37: Comparison of benzene, ethylene and nitrogen molar flow rates in “carbon MR” at steady state .....	137
Figure A. 1: Feed=CH <sub>4</sub> , T=650°C, feed volumetric fraction=90%, W/F=2166.91kgs/m <sup>3</sup> ....	161
Figure A. 2: Feed=CH <sub>4</sub> , T=675°C, feed volumetric fraction=90%, W/F=2165.67kgs/m <sup>3</sup> ....	161
Figure A. 3: Feed=CH <sub>4</sub> , T=700°C, feed volumetric fraction=90%, W/F=2207.86kgs/m <sup>3</sup> ....	161
Figure A. 4: Feed=CH <sub>4</sub> , T=725°C, feed volumetric fraction=90%, W/F=2166.53kgs/m <sup>3</sup> ....	161
Figure A. 5: Feed=CH <sub>4</sub> , T=750°C, feed volumetric fraction=90%, W/F=2166.49kgs/m <sup>3</sup> ....	162
Figure A. 6: Feed=CH <sub>4</sub> , T=700°C, feed volumetric fraction=30%, W/F=2162.28kgs/m <sup>3</sup> ....	162
Figure A. 7: Feed=CH <sub>4</sub> , T=700°C, feed volumetric fraction=50%, W/F=2163.62kgs/m <sup>3</sup> ....	162
Figure A. 8: Feed=CH <sub>4</sub> , T=700°C, feed volumetric fraction=70%, W/F=2163.74kgs/m <sup>3</sup> ....	162
Figure A. 9: Feed=CH <sub>4</sub> , T=700°C, feed volumetric fraction=90%, W/F=2167.24kgs/m <sup>3</sup> ....	162
Figure A. 10: Feed=CH <sub>4</sub> , T=700°C, feed volumetric fraction=30%, W/F=719.81kgs/m <sup>3</sup> ....	162
Figure A. 11: Feed=CH <sub>4</sub> , T=700°C, feed volumetric fraction=50%, W/F=1201.63kgs/m <sup>3</sup> ..	163
Figure A. 12: Feed=CH <sub>4</sub> , T=700°C, feed volumetric fraction=70%, W/F=1680.32kgs/m <sup>3</sup> ..	163
Figure A. 13: Feed=CH <sub>4</sub> , T=650°C, feed volumetric fraction=90%, W/F=2178.12kgs/m <sup>3</sup> ..	163
Figure A. 14: Feed=CH <sub>4</sub> , T=650°C, feed volumetric fraction=30%, W/F=720.26kgs/m <sup>3</sup> ....	163
Figure A. 15: Feed=CH <sub>4</sub> , T=675°C, feed volumetric fraction=30%, W/F=720.26kgs/m <sup>3</sup> ....	163
Figure A. 16: Feed=CH <sub>4</sub> , T=650°C, feed volumetric fraction=30%, W/F=2162.68kgs/m <sup>3</sup> ..	163
Figure A. 17: Feed=CH <sub>4</sub> , T=750°C, feed volumetric fraction=30%, W/F=2163.48kgs/m <sup>3</sup> ..	164
Figure A. 18: Feed=CH <sub>4</sub> , T=750°C, feed volumetric fraction=30%, W/F=720.19kgs/m <sup>3</sup> ....	164
Figure A. 19: Feed=CH <sub>4</sub> , T=700°C, feed volumetric fraction=90%, W/F=720.52kgs/m <sup>3</sup> ....	164
Figure A. 20: Feed=CH <sub>4</sub> , T=725°C, feed volumetric fraction=30%, W/F=720.30kgs/m <sup>3</sup> ....	164
Figure A. 21: Feed=CH <sub>4</sub> , T=650-750°C, feed volumetric fraction=30%, W/F=2162.37kgs/m <sup>3</sup> .....	164
Figure A. 22: Feed=CH <sub>4</sub> , T=650-750°C, feed volumetric fraction=30%, W/F=720.42kgs/m <sup>3</sup> .....	164

Figure A. 23: Feed=CH <sub>4</sub> , T=650-750 °C, feed volumetric fraction=90%, W/F=2166.06kgs/m <sup>3</sup> .....	165
Figure A. 24: Feed=CH <sub>4</sub> , T=700 °C, feed volumetric fraction=90%, W/F=1080.71- 2166.97kgs/m <sup>3</sup> .....	165
Figure A. 25: Feed=C <sub>2</sub> H <sub>4</sub> , T=650 °C, feed volumetric fraction=1%, W/F=53.93kgs/m <sup>3</sup> , Cat.=activated .....	165
Figure A. 26: Feed=C <sub>2</sub> H <sub>4</sub> , T=675 °C, feed volumetric fraction=1%, W/F=53.93kgs/m <sup>3</sup> , Cat.=activated .....	165
Figure A. 27: Feed=C <sub>2</sub> H <sub>4</sub> , T=700 °C, feed volumetric fraction=1%, W/F=74.90kgs/m <sup>3</sup> , Cat.=activated .....	166
Figure A. 28: Feed=C <sub>2</sub> H <sub>4</sub> , T=725 °C, feed volumetric fraction=1%, W/F=53.96kgs/m <sup>3</sup> , Cat.=activated .....	166
Figure A. 29: Feed=C <sub>2</sub> H <sub>4</sub> , T=750 °C, feed volumetric fraction=1%, W/F=53.95kgs/m <sup>3</sup> , Cat.=activated .....	166
Figure A. 30: Feed=C <sub>2</sub> H <sub>4</sub> , T=700 °C, feed volumetric fraction=40%, W/F=2161.69kgs/m <sup>3</sup> ,	166
Figure A. 31: Feed=C <sub>2</sub> H <sub>4</sub> , T=700 °C, feed volumetric fraction=1%, W/F=74.94kgs/m <sup>3</sup> ,.....	166
Figure A. 32: Feed=C <sub>2</sub> H <sub>4</sub> , T=700 °C, feed volumetric fraction=39.06%, W/F=2161.26kgs/m <sup>3</sup> , Cat.=not activated .....	166
Figure A. 33: Feed=C <sub>2</sub> H <sub>4</sub> , T=700 °C, feed volumetric fraction=0.5%, W/F=59.64kgs/m <sup>3</sup> , Cat.=activated .....	167
Figure A. 34: Feed=C <sub>2</sub> H <sub>4</sub> , T=700 °C, feed volumetric fraction=2.5%, W/F=149.74kgs/m <sup>3</sup> , Cat.=activated .....	167
Figure A. 35: Feed=C <sub>2</sub> H <sub>4</sub> , T=700 °C, feed volumetric fraction=21%, W/F=456.19kgs/m <sup>3</sup> , Cat.=activated .....	167
Figure A. 36: Feed=C <sub>2</sub> H <sub>4</sub> , T=750 °C, feed volumetric fraction=40%, W/F=2167.54kgs/m <sup>3</sup> , Cat.=activated .....	167
Figure A. 37: Feed=C <sub>2</sub> H <sub>4</sub> , T=750 °C, feed volumetric fraction=40%, W/F=2167.53kgs/m <sup>3</sup> , Cat.=activated .....	167
Figure A. 38: Feed=C <sub>2</sub> H <sub>4</sub> , T=650 °C, feed volumetric fraction=40%, W/F=2166.41kgs/m <sup>3</sup> , Cat.=activated .....	167
Figure A. 39: Feed=C <sub>2</sub> H <sub>4</sub> , T=700 °C, feed volumetric fraction=40%, W/F=2167.15kgs/m <sup>3</sup> , Cat.=activated .....	168
Figure A. 40: Feed=C <sub>2</sub> H <sub>4</sub> , T=650-750 °C, feed volumetric fraction=1%, W/F=53.94kgs/m <sup>3</sup> , Cat.=activated .....	168
Figure A. 41: Feed=CH <sub>4</sub> , T=700 °C, feed volumetric fraction=30%, SW=1 .....	168
Figure A. 42: Feed=CH <sub>4</sub> , T=700 °C, feed volumetric fraction=90%, SW=1 .....	168
Figure A. 43: Feed=CH <sub>4</sub> , T=700 °C, feed volumetric fraction=30%, SW=3 .....	168
Figure A. 44: Feed=CH <sub>4</sub> , T=650 °C, feed volumetric fraction=30%, SW=1 .....	168



## List of Tables

Table 1. 1: The catalytic results of methane dehydro-aromatization under non-oxidative condition over different catalysts [62] .....	8
Table 1. 2: Comparison of MDA activities of various supported metals on HZSM-5 zeolite ..	9
Table 1. 3: The effect of the zeolite supports on the catalytic performances of Mo-based catalysts in the methane dehydro-aromatization under non-oxidative condition [76] ..	10
Table 1. 4: Comparison of activities zeolite supports for Mo-based MDA catalyst [87] .....	11
Table 2. 1: The Gibbs enthalpy parameters of components [148].....	27
Table 3. 1 Materials and Reagents [45].....	31
Table 3. 2 BET surface areas, pore volumes and average pore diameters of traditional MCM-22 and MCM-22-HA .....	34
Table 3. 3 Results of XRF analysis of the Mo/MCM-22 and Mo/MCM-22-HA catalysts .....	35
Table 3. 4 Catalytic performance of various catalysts (Mo-based MCM-22 catalysts) being subjected to MDA reaction for 24 h.....	36
Table 4. 1: Chemicals for reactions.....	39
Table 4. 2: Parameters of the two carbon membranes provided by IKTS institute .....	39
Table 4. 3: Reaction conditions of methane experiments (feed 90%).....	49
Table 4. 4: Reaction conditions for fixed temperature experiments.....	50
Table 4. 5: Reaction conditions of ethylene experiments (feed 1%).....	50
Table 4. 6: Reaction conditions for fixed temperature experiments.....	51
Table 4. 7: Experiments for single gas permeation .....	52
Table 4. 8: Experimental plan for binary gas mixture permeation .....	52
Table 4. 9: Experimental plan for studying MDA in a MR.....	53
Table 5. 1: Different process parameters studied with CH <sub>4</sub> /N <sub>2</sub> feed mixtures in experiments	56
Table 5. 2: Influence of temperature and reaction time on conversion and selectivity .....	65
Table 5. 3: Influence of W/F and reaction time on conversion and selectivity .....	71
Table 5. 4: Different process parameters with C <sub>2</sub> H <sub>4</sub> /N <sub>2</sub> feed mixtures series experiments .....	74
Table 5. 5: Reaction orders for all the temperature for network 1.....	91
Table 5. 6: Pre-exponential factor and the activation energy of network 1 .....	92
Table 5. 7: Optimized estimation of parameters in reaction network 1 (eq. (5. 31)-(5. 33)).....	92
Table 5. 8: Pre-exponential factor and the activation energy of network 2.....	96
Table 5. 9: Optimized estimation of parameters in reaction network 2.....	97
Table 5. 10: Reaction orders for all the temperature for network 2 .....	98
Table 5. 11: Pre-exponential factor and the activation energy of network 2 .....	99
Table 5. 12: Optimized estimation of parameters in reaction network 2.....	100
Table 5. 13: Reaction orders for all the temperature for network 3 .....	104
Table 5. 14: Pre-exponential factor and the activation energy of network 3.....	104
Table 5. 15: Optimized estimation of parameters in reaction network 3.....	105

---

Table 6. 1: Linear regression of diffusivities for membrane No. 1 .....	127
Table 6. 2: Diffusivities parameters for membrane No. 1 .....	128
Table 6. 3: Linear regression of diffusivities for membrane No. 2 .....	130
Table 6. 4: Diffusivities parameters for membrane No. 2 .....	130
Table 7. 1: Exponential estimation results for deactivation .....	145
Table 7. 2: Preliminary estimation results for deactivation .....	145
Table 7. 3: Optimized estimation results for deactivation .....	146
Table 7. 4: Exponential estimation results for deactivation in “carbon MR” .....	150
Table 7. 5: Preliminary estimation results for deactivation in “carbon MR” .....	150
Table 7. 6: Optimized estimation results for deactivation in “carbon MR” .....	151

---

## Curriculum Vitae

### Personal Details:

Name: **Kaidi Gao**  
Nationality: Chinese  
Date of Birth: 10.10.1987 in China



### Education:

- Sep. 2011-now  
Otto-von-Guericke-University (OvGU) and Max Planck Institute, Faculty of Chemical Engineering, **Ph.D Studying** with Prof. Seidel-Morgenstern
- Oct. 2010-Jul. 2011  
Otto-von-Guericke-University (OvGU) and Max Planck Institute for Complex Dynamic Systems, **Master Thesis** Working with Prof. Seidel-Morgenstern
- Sep. 2008-Sep. 2010  
Dalian University of Technology, Graduate School, Institute of Adsorption and Inorganic Membrane (**Master Studying**)
- Sep. 2004-Jul. 2008  
Dalian University of Technology(DUT), Faculty of Chemical Engineering, Department of Chemical Engineering and Technology (**Bachelor Degree**)

### Experience:

- Secretary-General of Chinese Student Union of OvGU (2012)
- Magdeburg Chinese Spring Festival Party Organizer in OvGU (2011)
- New Year Party Organizer in the Institute of Adsorption and Inorganic Membrane (2009)
- 7-Days Internship in Dalian No. 7 Refinery (2007)
- Culture Minister of Faculty of Chemical Engineering (2006)
- 2-Days Practice in Factory for Synthetic Ammonia Chemistry of Dalian (2005)

### Award:

- Scholarship under the State Scholarship Fund from China Scholarship Council(2009)
- First-Class Scholarship of Graduate School, DUT(2008)
- Second-Class Scholarship of Graduates, DUT(2007)

